University of Southampton

Faculty of Engineering and Physical Sciences

School of Chemistry

Developing Nanocomposite Materials for Catalytic Applications

by

Evan William Lynch

ORCID: 0009-0007-6799-7457

Thesis for the degree of Doctor of Philosophy

April 2024

University of Southampton

Abstract

Faculty of Engineering and Physical Sciences

School of Chemistry

Doctor of Philosophy

Developing Nanocomposite Materials for Catalytic Applications

by

Evan William Lynch

In the field of nanoscale catalyst design, there are many parameters that must be carefully controlled to yield effective nanocomposite materials, such as physical properties, metal-support interactions, and experimental conditions. The development of reliable and accessible synthetic methods that can selectively and simultaneously modulate catalyst properties, such as through the local formation of interfaces, is integral to the continued development of advanced nanocatalysts.

The established sol-immobilisation method of preparing supported nanoparticles was extended to using metal-organic frameworks as a support, being employed to generate Pd/CuBTC nanoparticle-MOF composites. The possibilities of this method were further explored using water- and methanol-based sol-immobilisations, and an alternative CuTPA MOF support.

The limited stability of MOFs was exploited to reduce these NP-MOF composites into tailored nanocomposites, using a novel chemical-based method to generate PdCu/Cu_2O nanomaterials, in contrast to conventional thermal treatments that proceed via MOF pyrolysis. Characterisation with XRD, XAFS and HRTEM determined that it is possible to induce local Pd-Cu alloying within the Pd nanoparticles at room temperature, using an $NaBH_4$ reducing agent and an amine-based protecting agent. Additionally, precise control of reduction temperature, reductant concentration, and protecting agent concentration was demonstrated to allow various properties of the generated nanocomposites to be finely tuned, including the alloying extent, particle size, and support oxidation state. Furthermore, the catalytic performance of both the Pd/CuBTC composites and PdCu/Cu_2O nanocomposites was evaluated using the reduction of 4-nitrophenol and CO oxidation as model reactions, and the relative performances of the Pd and PdCu nanoparticles for both reactions are discussed.

The research presented in this thesis demonstrates new insight into the field of nanocomposite design via the development of a novel synthetic method, which has been demonstrated to generate alloyed nanoparticles and controlled nanocomposites under standard laboratory conditions.

Table of Contents

Table of Tables

Table of Tables

Table of Figures

Table of Figures

Table of Figures

Table of Figures

Table of Figures

Research Thesis: Declaration of Authorship

Print name: Evan William Lynch

Title of thesis: Developing Nanocomposite Materials for Catalytic Applications

I declare that this thesis and the work presented in it are my own and have been generated by me as the result of my own original research.

I confirm that:

1. This work was done wholly or mainly while in candidature for a research degree at this University;
2. Where any part of this thesis has previously been submitted for a degree or any other qualification at this University or any other institution, this has been clearly stated;
3. Where I have consulted the published work of others, this is always clearly attributed;
4. Where I have quoted from the work of others, the source is always given. With the exception of such quotations, this thesis is entirely my own work;
5. I have acknowledged all main sources of help;
6. Where the thesis is based on work done by myself jointly with others, I have made clear exactly what was done by others and what I have contributed myself;
7. None of this work has been published before submission.

Signature: ..... Date: 16/04/2024

Acknowledgements

First and foremost, I would like to express my profound gratitude to my academic supervisor, Dr. Peter Wells, whose consistent and unwavering support and patience enabled me to complete this research throughout significant adversity. All that follows is a credit to his careful guidance and compassion.

Thanks are also due to the past and present members of the Wells research group, including Dr. Marianna Casavola, who provided additional guidance and support during the first portion of my project. I would also like to particularly thank Donato, George, Rachel, Scott, Pip, Ellie, Khaled, and Kieran, who continually assisted me in overcoming the frequent challenges and pitfalls of academic research. The regular assistance from my Diamond-based co-supervisor Dr. Diego Gianolio and the other members of the B18 beamline is also greatly appreciated.

This project was supported by funding from the Engineering and Physical Sciences Research Council (EPSRC) and Diamond Light Source, whilst being based in the UK Catalysis Hub's laboratories in the Research Complex at Harwell, Oxfordshire. The support of all these institutions, as well as the people who keep them running, is greatly welcomed.

I would also like to express thanks to the UK Catalysis Hub, who provided an excellent working environment to be based at. The Hub functions as an interface for frequent collaboration between individuals who are part of different research groups at various institutions around the UK, and this network of exchanged ideas continues to be extremely valuable. I am grateful for the frequent motivation and assistance I received from my colleagues and fellow students there, particularly Monik, Jay, Emma, Andrea, Alex, Stefan, James, Lisa, Toni, and Daniela. Additionally, the support of the postdocs and staff both at the Hub and the Research Complex, especially from June, Alex, Josie, Alec, and Andy, was integral to helping me complete my research.

Finally, I am tremendously grateful to my parents and family, whose love and support, particularly in the final stages of the project, was foundational and unwavering.

Definitions and Abbreviations

4-AP	4-aminophenol
4-NP	4-nitrophenol
BCC	Body-centred cubic
BET	Brunauer-Emmett Teller (surface area isotherm)
BF	Bright-field (imaging)
BTC	Benzene-1,3,5-tricarboxylic acid (trimesic acid)
CCD	Charge-coupled device
CuBTC	Copper-trimesic acid metal-organic framework
DF	Dark-field (imaging)
DMF	N,N-dimethyl formamide
EDX	Energy-dispersive X-ray spectroscopy
ePSIC	electron Physical Science Imaging Centre
EXAFS	Extended X-ray absorption fine structure
FCC	Face-centred cubic
FT	Fischer-Tropsch
HRTEM	High-resolution transmission electron microscopy
MFC	Mass flow controller
MOF	Metal-organic framework
MP-AES	Microwave plasma atomic emission spectroscopy
MS	Mass spectrometry
m/z	Mass-to-charge ratio
NP	Nanoparticle
ORR	Oxygen reduction reaction
PID	Proportional-integral-derivative
PVA	Polyvinyl alcohol

Definitions and Abbreviations

PVP	Polyvinylpyrrolidone
QEXAFS	Quick-EXAFS
SBU	Secondary building unit
SEM	Scanning electron microscopy
SMSI	Strong metal-support interaction
TEM	Transmission electron microscopy
TGA	Thermogravimetric analysis
TOF	Turnover frequency
TPA	Terephthalic acid
UV/vis	Ultraviolet-visible spectroscopy
wt%	Weight percentage
XAFS	X-ray absorption fine structure
XANES	X-ray absorption near-edge spectroscopy
XAS	X-ray absorption spectroscopy
XRD	X-ray diffraction

Chapter 1 Introduction

1.1 Catalysis

1.1.1 Introduction to Catalysis

As human development, industrialisation, and globalisation begin to fundamentally alter our planet's environment and consume huge proportions of our non-renewable natural resources, significant efforts have been, and must continue to be, put into finding ways to mitigate the impact of human activity before the damage done becomes irreversible. Large-scale industrial processes can churn out pollutants on a grand scale if not implemented well, and the failure to check and prevent these emissions will have massive implications for the Earth's future on a very short and foreseeable timescale. One method of minimising the impact of these processes is through the development of effective catalysts, which by their presence alone can improve the efficiency of a chemical transformation through factors such as reduced energy consumption, lower temperature or pressure in operating conditions, or improved selectivity to favour the formation of a desired product, consequently minimising the generation of waste by-products.

The simplest definition of a catalyst is "a substance which speeds up a chemical reaction by lowering the activation energy for that reaction to occur, by providing an alternative mechanistic pathway for the reaction."[1] The catalyst must also be unaltered following the completion of the reaction, and consequently is reusable. This twin impact of increased efficiency and recyclability means that the field of catalyst design can play a large part in developing a sustainable economy and industry, either through developing a catalyst for an as-yet-unmodified process, or through using our understanding of the mechanism of a process to design an improved catalyst for an already-catalysed process. Possibly the most important illustration of both cases is the Haber-Bosch process for the synthesis of ammonia.

The Haber-Bosch process is essential for sustaining the still-rapidly-increasing human population, since it provides a synthetic alternative to natural fertilisers for crop growth, allowing a marked increase in the amount of crops that could be grown in a particular area and consequently stabilising the food supply for generations. Fritz Haber initially demonstrated that, in the presence of a suitable catalyst, small amounts of ammonia could be produced from combining nitrogen and hydrogen gases at 1000 °C;[2] development of the reaction to an industrial scale by Carl Bosch among others would show that an effective catalyst and the use of high pressure (around 20 MPa, or ~200 times atmospheric pressure) would reduce the ideal

operating temperature to around 500-600 °C.[3] Since then, the catalyst and industrial process have both evolved further, and the scale at which the process is used has grown to consuming between 1-2% of the global energy consumption.[4,5]

Another vital catalyst-driven industrial process is fluid catalytic cracking, in which a powdered zeolite catalyst is used to break down long-chain hydrocarbons refined from crude oil into lower-molecular-weight hydrocarbons more useful in fuels and industrial applications.[6] Prior to the development of the zeolites, this process was achieved by strong heating at very high pressures, but the addition of the catalyst both improves the energy efficiency of the process and increases the octane rating of the fuel products, which in turn increases that fuel's performance in a combustion engine.[7]

Catalysts are also essential in the Fischer-Tropsch (FT) process, which uses a transition metal catalyst to convert a mixture of carbon monoxide and hydrogen (known as syngas) into an array of liquid hydrocarbons.[8] The particular choice of catalyst for this reaction influences the distribution of products formed: whilst ruthenium is the most active catalyst, it is substantially more expensive than iron or cobalt-based catalysts, the efficiency of which can be improved using secondary promoters, which don't catalyse the reaction themselves, but can interact with the catalyst to alter its selectivity and mechanism.[9–11] A major difference between Fischer-Tropsch and refining from crude oil is that the FT products have fewer impurities (e.g., they are sulfur-free) and as such, the purification of the products is less involved, decreasing the necessary size and environmental impact of an FT refinery compared to a conventional crude oil refinery.[12]

It is clear, then, that for industrial processes of this large scale to continue to be feasible, further research on new and improved catalysts for these (or alternative) processes is vital, and to be able to achieve these improvements, we must first understand the fundamental mechanisms by which catalysis occurs, to be able to synthesise appropriate materials.

1.1.2 Heterogeneous Catalysis

The two main classes of catalysts are defined as homogeneous and heterogeneous; namely whether they exist in the same phase as the reactants (homogeneous) or a different phase (heterogeneous).[1] Homogeneous catalysts tend to be organometallic complexes, such as biological enzymes with metal cations at their active sites (e.g., carbonic anhydrase[13]), the rhodium-based Wilkinson's catalyst for the hydrogenation and hydroformylation of alkenes[14], and the iridium-based catalyst used in the Cativa process for the production of acetic acid from methanol[15]. Whilst these smaller catalysts are often more selective and easier to characterise under process conditions with temporal resolution, their limited thermal stability – even being

able to operate above 100 °C is considered stable - means they are not suitable for the sort of high-temperature reaction required by systems like the Haber process, and since they are soluble in the reaction medium by definition, they are difficult to separate from the products at the reaction's conclusion.[16]

Heterogeneous catalysts, however, are generally simpler to separate from reaction products, since they are usually solid-phase materials catalysing liquid or gas-phase reactions, and can often just be filtered from the reaction mixture in the former case.[17] A key example of a heterogeneous catalyst is the catalytic converter present in automobile exhausts, which usually consist of a mixture of platinum group metals (PGMs) including platinum itself, palladium, and/or rhodium, dispersed across a ceramic monolith. When the hot exhaust gases pass over the monolith, the precious metals on the surface act as catalysts for the oxidation of carbon monoxide (CO) to carbon dioxide (CO_2), the reduction of nitrogen monoxide (NO) to nitrogen (N_2), and the oxidation of hydrocarbons to water and CO_2.[18] These processes help prevent toxic gases, which in the case of nitrogen oxides cause acid rain[19], from being emitted into the atmosphere, and without these converters being present, air pollution would be markedly higher than the already-dangerous levels it can exist at.

There are three major mechanisms relevant to the study of heterogeneous catalysis: i) Langmuir-Hinshelwood; ii) Eley-Rideal and iii) Mars-van Krevelen. In the Langmuir-Hinshelwood mechanism, two reactant molecules adsorb on neighbouring catalytic sites and react together on the surface, with the product desorbing from the catalyst at the end of the reaction to leave the site free to repeat the cycle again. Examining the kinetics and rate law of this mechanism reveals that in the case of both molecules having a similar degree of adsorption, the order of the reaction is one with respect to each individual reactant (for an order of two overall), meaning that the rate of the reaction is proportional to the concentration of that reactant. This varies in cases where one reactant has a particularly strong or weak affinity for the catalyst substrate – if one reactant adsorbs much more strongly than the other, it can dominate the available catalytic sites, making it difficult for the other molecule to adsorb to an adjacent site and undergo reaction.[20]

The Eley-Rideal mechanism (sometimes called Langmuir-Rideal), on the other hand, only requires one of the two reactants to adsorb to the surface, with the second reactant molecule not adsorbing but interacting directly with the first adsorbed species from the gas phase. The kinetics here imply that the reaction order is one with respect to the gas-phase reactant, but the adsorbed species can have a reaction order of one at low concentrations, or zero at high concentrations - i.e. the rate of the reaction is not proportional to the concentration of the adsorbed species provided it is present in an initial sufficient quantity.[21] This is an important

consideration in catalyst design and reaction engineering, as one can tailor the affinity of a substrate for adsorption of a given compound or the relative amounts of reactants present for optimal performance.

Finally, the Mars-van Krevelen mechanism is often seen in the oxidation of compounds over noble metal catalysts, and unlike the preceding mechanisms, features incorporation of the lattice components into the catalysis products.[22–24] An example is in the oxidation of propene to acrolein, where the propene molecule adsorbs on to the catalyst surface, and the oxidation reaction proceeds using an oxygen atom from the surface layer of the catalyst. The subsequent desorption of the acrolein product leaves an oxygen vacancy in the catalyst's lattice, which is replenished by the dissociation of an O_2 molecule on the surface.[25]

Generally, then, the mechanism of heterogeneous catalysis requires a reactant to diffuse to an active site on the catalyst, adsorb to an appropriate surface facet, and react via the relevant catalytic mechanism, resulting in the formation of products on the surface that subsequently desorb and vacate the active site. Therefore, the activity of the catalyst is determined by the amount and availability of active sites, their selectivity towards the desired product above other alternatives, and their overall stability under operating conditions. The presence of other reactants or even molecules external to the reaction can block or alter the active site of the catalyst, which may result in the reduction of activity. This process is known as catalyst poisoning and must be avoided to maintain a high-performance catalyst. Since catalysts are required to be reusable, they must also be recoverable from the reaction mixture.[26,27]

1.1.3 Surfaces

Catalytic reactions at the surfaces of heterogeneous catalysts require the reactant molecules to adsorb to an active site on the surface. The sites available for adsorption have varying electronic properties influenced by the coordination number and geometry of a particular surface. For example, atoms at the (100), (110) and (111) surfaces of a face-centred cubic (FCC) crystal[28] (**Figure 1**) have different coordination numbers and adsorption sites:

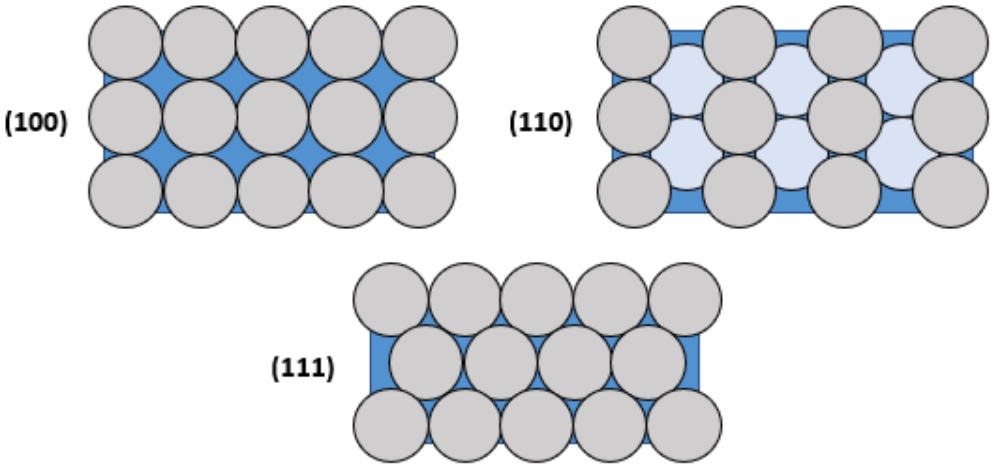

Figure 1: a) The (100) surface of a face-centred cubic crystal; b) the (110) surface of that crystal, with atoms in the layer below the surface shown as light blue circles; c) the (111) surface of the crystal.

It can be shown that the coordination number of atoms in the top layer of the (100), (110) and (111) surfaces are 8, 7 and 9 respectively, meaning they are all under-coordinated compared to the bulk FCC coordination number of 12, and can thus form bonds or chemical interactions with surface adsorbates. The possible adsorption sites for these surfaces are shown in **Figure 2**.

All these possible sites have different electronic environments due to the different coordination numbers of the atoms on the surface. This will alter their interactions with an adsorbate (i.e., the energy of adsorption for a molecule will vary with the site of adsorption) and in turn modulate the catalytic activity of that active site. For example, supported gold nanoparticle catalysts have shown unusual activity for low-temperature CO oxidation[29], and a proposed explanation for this involves the variation of CO binding strength both to different facets of the gold surface but also to different sites on each surface – computational studies have indicated that CO only has a very weak interaction with the Au(111) surface, but binds more strongly to the (100) surface and even more so to the (110) surface, specifically favouring the (110) short bridge site ahead of the top site and long bridge site.[30] All this is determined by subtle variations in the three-dimensional arrangement of neighbouring gold atoms[31], but even tiny changes like this can have dramatic consequences for catalytic performance.

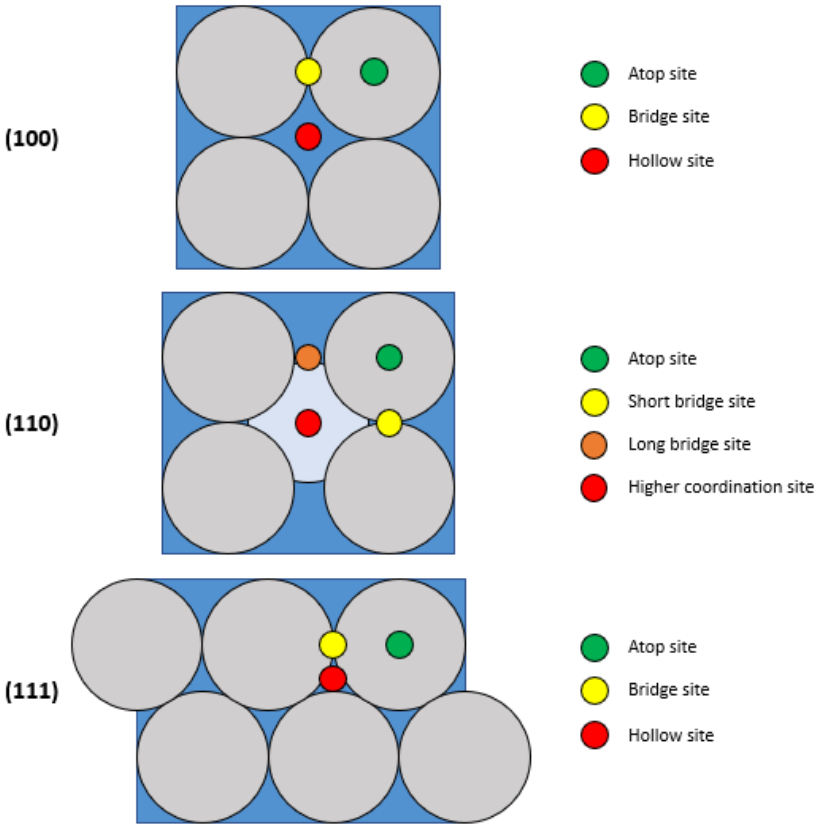

Figure 2: a) Adsorption sites on the (100) surface of a face-centred cubic crystal; b) adsorption sites on the (110) surface of the crystal; c) adsorption sites on the (111) surface of the crystal.

1.2 Metal Nanoparticles

Although the term "nanomaterials" has no consensus definition, in principle they are generally substances defined as "materials with a structural component smaller in size than 1 μm (10^{-6} m or 1000 nm) in one, two or three dimensions", and in practice they are often considered to have size dimensions of 1-100 nm.[32] However, the field of catalysis is more focused on metal nanoparticles (NPs) of dimensions of the order of 4 nanometres, since at this scale the surface area of the nanoparticulate catalyst becomes appropriately high for efficient catalysis and sufficiently-quick reaction rates. This extends to nanocomposites, which are multiphase substances where at least one phase is defined as a nanomaterial[33] – for example, small particles, of the order of 1-5 nm diameter, of palladium supported on larger discs of a metal oxide such as titania (TiO_2).

Since most metal NPs have an average size domain of between 1-50 nm, this implies a high surface-area-to-volume ratio, where a large proportion of atoms in a given nanoparticle are at the surface and are coordinated to fewer atoms than the maximum bulk coordination number, which for a typical face-centred cubic crystal is 12. This under-coordination allows surface

atoms in a nanoparticle cluster to interact with adsorbates, enabling the cluster's function as a catalyst.[34] A good surface-to-volume ratio is essential for an effective catalyst: to illustrate the relationship between particle size and available surface area, a cube of side length 1 μm would have a volume of 1 μm^3 and a surface area of 6 μm^2, but breaking that same volume down into a million cubes of side length 0.01 μm yields a total surface area of 600 μm^2. This relationship allows nanoparticulate materials to achieve surface areas of many square metres per gram and directly affects the rate of turnover of the catalyst.

1.2.1 Nanoparticle Structure

The size and shape of metal nanoparticles have a marked effect on their catalytic properties. A decrease in nanoparticle size causes a corresponding increase in the surface-area-to-volume ratio of the NPs, thus providing a greater proportion of under-coordinated atoms and more surface facets that can behave as catalytic active sites. This means that smaller nanoparticles will exhibit a higher catalytic activity, provided the adsorbates are bound to the active site sufficiently strongly to remain there long enough for the reaction to occur, but not so strongly that the reaction products cannot be easily released.[35] Therefore, nanoparticle size is a prime consideration when designing and tailoring NP-based catalysts.

However, particle size can only be decreased so far before an optimal size is reached, where further shrinking of the particles would actually yield a drop-off in effectiveness despite the increase in surface area. A good example of this was illustrated by Kinoshita, in summarising and rationalising the trends shown in literature of the oxygen reduction reaction (ORR) on the facets of Pt nanoparticles dispersed in acid electrolytes[36], and how the kinetics are affected by Pt particle size. It was demonstrated that the optimum particle size for the ORR was around 3-5 nm, and that decreasing below this particle size ultimately was an ineffective use of an expensive catalyst.

The reason for this is that the reaction is catalysed at the (100) and (111) facets of the cuboctahedral Pt nanoparticle, and the edge and corner sites on the nanoparticle are geometrically unfavourable for catalysis. Small particle size initially yielded a benefit, because the available surface area of those facets had increased, but then continuing past the peak of 3-5 nm size increased the proportion of edge and corner sites relative to the (100) and (111) facets, which are less accessible on a particle that is too small, so the activity decreased beyond this point.

The geometric shape of nanoparticles can also affect which facets are available for reactant adsorption. For cubic nanoparticles, only the (100) surface is presented, and for octahedral geometries only the (111) surface is available. Various shapes in-between those two geometries

can be utilised for a specific ratio of (100) to (111) surfaces, such as cuboctahedra, truncated cubes and truncated octahedra.[37,38]

It follows, therefore, that if a reaction proceeds most effectively at a given facet, then controlling the shape of a nanoparticle to only present that facet as available should have a positive effect on the catalytic performance. Chiu *et al.*[39] showed that controlling the available facets of CTAC-terminated gold nanocrystals affected their catalytic activity towards 4-nitroaniline reduction, with the Au(110) surface preferentially obtained via a rhombic dodecahedral morphology displaying higher activity than the Au(100) and Au(111) surfaces obtained from cubic and octahedral nanocrystals respectively. This was supported by density functional theory (DFT) calculations demonstrating that 4-nitroaniline had the highest binding energy to the Au(110) surface – however, the results also indicated that the (111) surface, whilst initially the least active, becomes more active than the (100) surface at increasing temperature, suggesting that the optimal choice of nanoparticle morphology for a given reaction is also dependent on the experimental conditions of the reaction itself. The various observed morphologies of the nanoparticles are depicted below in **Figure 3**.

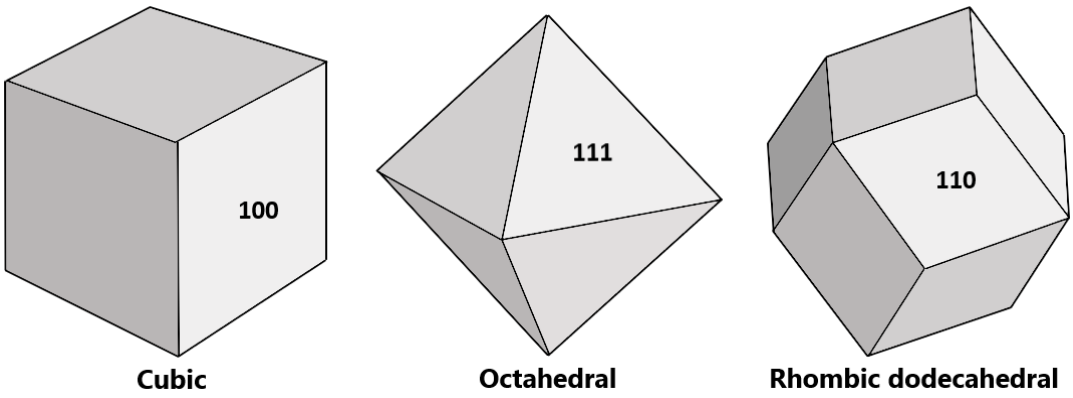

Figure 3: Schematic of various morphologies of gold nanoparticles synthesised by Chiu *et al.*[39] and observed by scanning electron microscopy, showing a) cubic NPs with {100} facets; b) octahedral NPs with {111} facets; c) rhombic dodecahedral NPs with {110} facets.

Narayanan and El-Sayed[40] used tetrahedral Pt nanoparticles capped with polyvinylpyrrolidone (PVP) and synthesised by H_2 reduction to demonstrate that, for the same size, nanoparticles with a higher proportion of corner and edge sites will be more catalytically active. The tetrahedral NPs had approximately 35% of the Pt atoms at corner and edge sites, and were 4-5 times more catalytically active for the reaction between hexacyanoferrate(III) ions and thiosulfate ions than cubic NPs with only 4% of Pt atoms at corners and edges. However, a large proportion of these tetrahedral nanoparticles were shown to be distorted during the reaction by dissolution of the Pt atoms at the edges, affecting their potential reusability.[41] Note how this

differs from Kinoshita's example presented earlier – in this case, the test reaction is catalysed at the corner and edge sites, rather than disfavoured at it as in the case of the oxygen reduction reaction, so the shape of the nanoparticle was tailored to a morphology that affords a higher proportion of these sites as a result.

These examples illustrate that the catalytic behaviour of nanoparticles is strongly influenced by their structure and morphology. In addition to controlling NP size, the shape and therefore the facets made available to adsorption must be an important consideration in catalyst design.

It is possible to influence which facets are present in a nanocrystal by using capping agents to influence crystal growth. Sun and Xia[42] used PVP to bind to the (100) surface of silver nanocrystals and hinder the growth rate in that crystallographic direction. This meant that the (111) facets grew preferentially, generating silver nanocubes where the (100) surface is prominent (**Figure 4**).

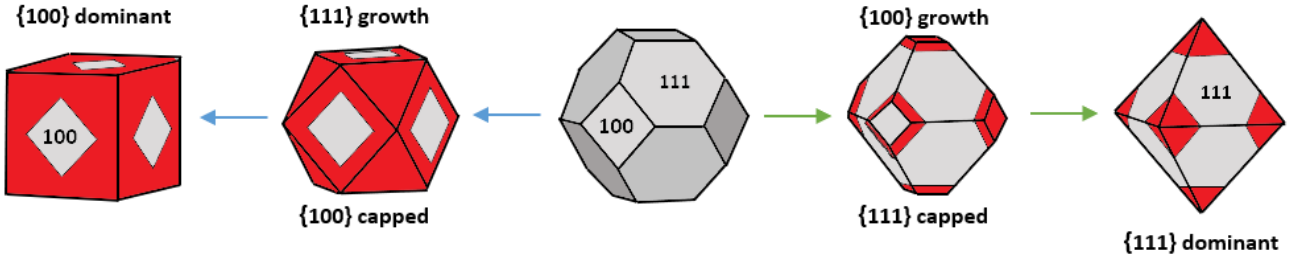

Figure 4: Schematic illustrating the control of nanoparticle shape via capping agents: capping the {100} surfaces to produce nanocubes and capping the {111} surfaces to produce octahedra. Capped facets are shown in grey, facets growing preferentially in red. Adapted from Roldan Cuenya *et al.*.[43]

1.2.2 Supported Nanoparticles

1.2.2.1 Strong Metal-Support Interactions

One persistent problem with using nanoparticles for catalysis is that free, colloidal nanoparticles have a tendency to aggregate, since the high surface area of nanoparticles implies a high surface energy.[44] Aggregation is favoured since it reduces the surface energy of the system, but therefore significantly reduces the nanoparticle surface area and catalytic effectiveness.[45] This issue can be mitigated by affixing the metal nanoparticles to a support, often metal oxides or carbon nanotubes.[46,47]

Interactions between supported metal particles and the support itself were discussed by Tauster *et al.*[48] in 1978, who noted that H_2 and CO adsorption were suppressed for noble metals supported on titania (TiO_2). This behaviour was ascribed to chemical interactions between the

support and noble metal, dubbed a "strong metal-support interaction" or SMSI. Initially, metal-metal bonding between the d orbitals of the noble metal and the vacant d orbitals of Ti^{4+} cations was proposed to explain this interaction, after encapsulation by the support and poisoning by impurities were dismissed.

However, further work on Pt/TiO_2 by Meriaudeau *et al.*[49] suggested that the SMSI was in fact caused by encapsulation by a suboxide of titanium (TiO_x, where $x < 2$), i.e., the Ti^{4+} cations were reduced before encapsulation. This hypothesis was adopted by Tauster *et al.* in 1987[50], after studies confirmed that TiO_x encapsulation was observed for Rh/TiO_2[51] and Pt/TiO_2[52]. Electron microscopy studies by Baker *et al.*[53] also indicated that the shape and size of Pt nanoparticles on titania could be reversibly altered by switching between reduction and oxidation, and that SMSI was observed after reduction of TiO_2 to Ti_4O_7 (as illustrated in **Figure 5**). Reduction in average nanoparticle size compared to Pt/SiO_2 (which does not exhibit any SMSI) after H_2 reduction of Pt/TiO_2 was also observed.[54]

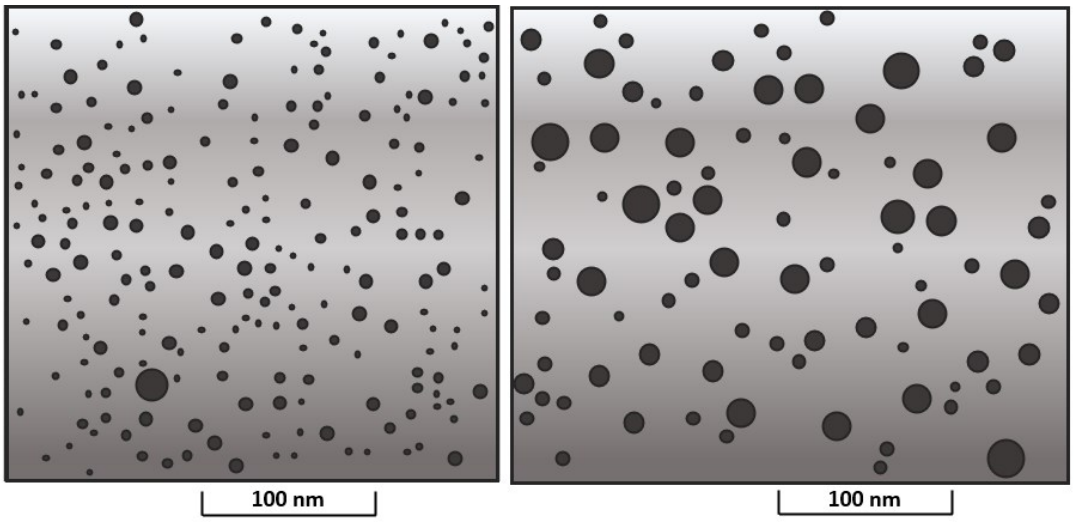

Figure 5: a) Schematic adapted from a TEM micrograph of platinum nanoparticles on titania after being exposed to H_2 at 875 K for 1 h to reduce TiO_2 to Ti_4O_7; b) Schematic adapted from a TEM micrograph of the previously-reduced platinum on titania sample after being heated in O_2 at 875 K for 1 h. The metal-support interactions induced by reduction of the underlying titania to Ti_4O_7 clearly reduce the average nanoparticle size and improve NP dispersion. Adapted from Baker *et al.*.[53]

These studies indicate that metal-support interactions are extremely influential in controlling the size and morphology of supported nanoparticles. The influence of these interactions on the catalytic behaviour are discussed in the next sections. SMSI effects are not limited to only titania; they have been reported for other metal oxide supports such as CeO_2[55] and Nb_2O_5.[56]

1.2.2.2 Additional active sites at the metal-support interface

As discussed in **Section 1.2.1**, the available facets and adsorption sites on nanoparticle surfaces affect their catalytic performance. Introducing those nanoparticles to a support necessarily creates an interface between the two species, giving rise to further active sites with their own unique structure and properties compared to those on a bare metal surface.

For example, Walker *et al.*[57] modelled the active sites of Pt/TiO_2 to investigate how the edge and corner sites of the Pt-TiO_2 interface (**Figure 6**) influence the mechanism of the water-gas shift reaction. They calculated that the edge site is more active than the corner site, and illustrated that a CO-promoted redox mechanism is more dominant than the classical redox mechanism at low temperatures. It was also demonstrated that at all temperatures, O-H bond dissociation at the Pt-TiO_2 interface is the rate-determining step of the reaction. Note how these sites differ from those at the edge and corner of an unsupported Pt nanoparticle (like those discussed in **Section 1.2.1**) – this is a new active site split between Pt and the oxygen atoms on the support's surface, and the interface is necessary for this site to exist.

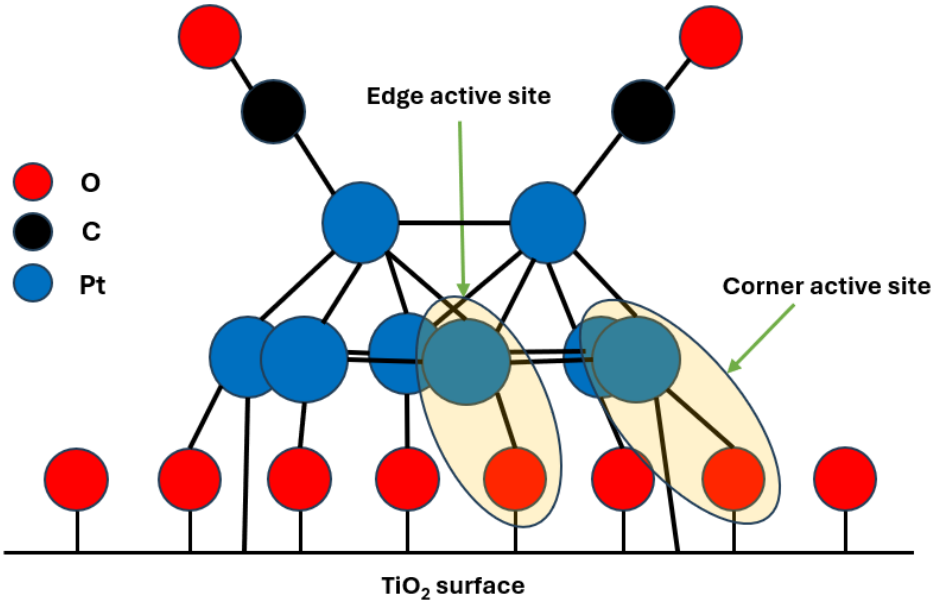

Figure 6: Representation of edge and corner active sites at the interface between Pt NPs and a titania support. Adapted from Walker *et al.*.[57]

Additionally, Bollinger and Vannice[58] explained the unusually high activity of Au/TiO_2 NP catalysts for low-temperature CO oxidation by proposing the existence of interfacial sites at the Au-TiO_x boundary, to which O_2 can bind and become activated before reacting with the CO adsorbed on an Au site. This is interesting because neither Au alone nor titania alone is an active catalyst for CO oxidation at the reaction temperature of 300 K. The combination of the two materials and the proximity of the sites adsorbing CO and O_2 at the interface – i.e., a metal-support interaction – is necessary for this material to be an active catalyst.

1.2.2.3 Charge Transfer between NP and support

The electronic interactions between the molecular orbitals of metal nanoparticle clusters and their supports lead to some degree of charge transfer between the NPs and the support, or vice versa. This leads to modulation of the oxidation states of atoms at the interface – for example partial oxidation of Au atoms following charge transfer at the interface to ceria[59] – and can accordingly influence catalytic behaviour.

Yoon *et al.*[60] calculated that the interaction between Pt NPs and the (001) surface of titania led to a higher degree of charge transfer from TiO_2 to Pt than for other facets. This extra degree of charge transfer was exploited to stabilise methyl formate as a reaction product when the sample was used to catalyse methanol oxidation, affording a significantly higher activity and selectivity than Pt NPs on other supports such as Co_3O_4 and ZnO (**Figure 7**), which collectively displayed behaviour similar to unsupported Pt NPs and favoured the production of CO_2 over methyl formate.

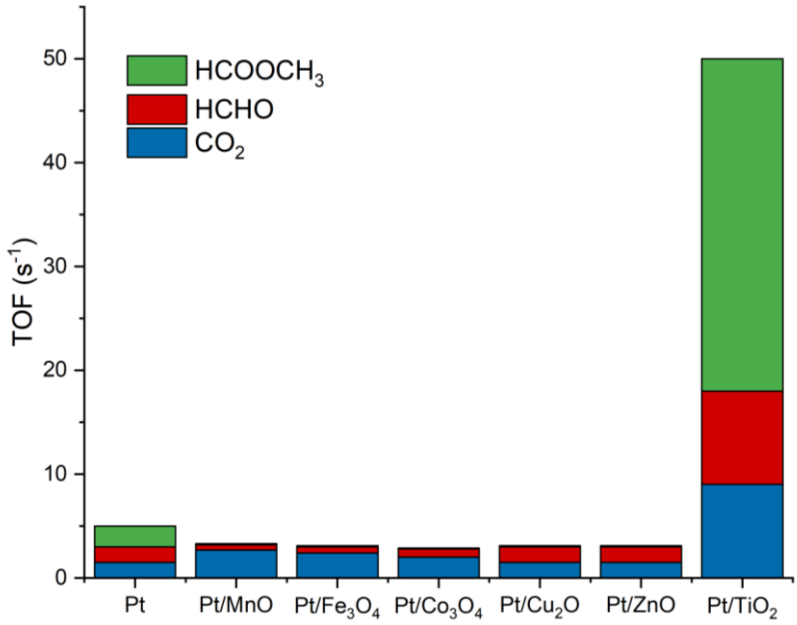

Figure 7: Plot of turnover frequencies and selectivities for methanol oxidation for platinum nanoparticle catalysts, both free and supported on various transition metal oxide supports, showing the relative amounts of the reaction products carbon dioxide (blue), formaldehyde (red), and methyl formate (green) arising from each catalyst. Based on data from Yoon *et al.*[60]

Similarly, Strayer *et al.*[61] demonstrated that charge transfer via the formation of mixed *d*-states between metal NPs (Ag, Cu, Ni, Co, Ir, Rh) and a niobate support reduced average nanoparticle size and inhibited sintering when compared to the same metal NPs supported on SiO_2, which does not generally display strong metal-support interactions.[62]

In summary, the interactions between a metal nanoparticle and its support are extremely influential on the catalytic behaviour of the nanocomposite as a whole, and the ability to control and tailor the extent of the interactions will be essential to designing the most effective catalysts for a given purpose. However, it is important to note that these metal-support interactions and their exhibited effects are a composite of multiple phenomena described above – dual-site catalytic mechanisms where one part of the reaction is catalysed on the metal and another on the support, charge transfer to and from the metal and the support, thermal stability and sintering resistance by encapsulation, and even restored catalytic activity from redispersion of an agglomerated catalyst powder are all causes and consequences which are commonly reported in literature under a single umbrella "SMSI" term, and it is important to properly investigate which of those effects are occurring in a given case rather than to wave it away under this broad terminology.

The magnitude and nature of these interactions in a given supported catalyst can be controlled using a range of preparation methods, which will now be discussed.

1.2.3 Preparation Methods for Metal Nanoparticles

1.2.3.1 Incipient Wetness Impregnation

One common but crude method for producing nanoparticles dispersed on suitable supports is to simply impregnate the support with a precursor solution containing atoms of the desired metal. If the volume of the solution used is less than or equal to the pore volume of the support, the method is termed incipient wetness impregnation.[63] In this instance, capillary action is exploited to draw the solution into the pores of the support. If the volume of the precursor solution is greater than the pore volume of the support, the effect of capillary action is limited, and the uptake of solution is diffusion-mediated and much slower. Controlling the volume of precursor solution is therefore necessary to prevent deposition of metal nanoparticles on the support surface rather than in the pores, and to decrease the time required for catalyst preparation.

After impregnation of the support, the sample is dried, calcined at high temperature (to drive off any volatile components of the metal precursor solution), or reduced, to yield metal nanoparticles on the support. It is also possible to modify the method with additional washing steps to remove components of the precursor solution, for example washing with ammonia to eliminate chloride ligands from precursors such as $HAuCl_4$ in the preparation of supported gold nanoparticles.[64] This method is also used to introduce metal nanoparticles to the pores of metal-organic frameworks, which is discussed in **Section 1.4.1**.

1.2.3.2 Sol-immobilisation

Sol-immobilisation is another common method for introducing metal NPs to a support. The method requires stabilising colloidal metal nanoparticles with a suitable capping agent and introducing them to a support under vigorous stirring conditions. This method has been shown to yield a suitable metal dispersion for catalysis.[65,66] The utility of the sol-immobilisation method was demonstrated by Rogers *et al.* in the preparation of Au/TiO_2 catalysts tested on the liquid phase oxidation of glycerol[67], and for Pd/TiO_2 catalysts used to hydrogenate furfural[68]. Those studies examined how temperature and solvent changes could be used to control nanoparticle sizes and the relative proportions of different active sites at the NP-support interface, which altered the activity and selectivity of the catalysts. Lopez-Sanchez *et al.*[69] had previously shown that sol-immobilisation of AuPd bimetallic NPs on a carbon support yielded catalysts that were more active for hydrogen peroxide synthesis and oxidation of benzyl alcohol when compared to AuPd/C catalysts produced by solution impregnation.

The sol-immobilisation method protects zero-valent metal nanoparticles in a colloidal solution via use of a capping agent, such as polyvinyl alcohol (PVA) or polyvinylpyrrolidone (PVP). These large polymer chains bind to the nanoparticles and stabilise them via steric interactions, as the hydrophobic carbon chains minimise their interaction with one another and thus prevent nanoparticle aggregation.[70,71]

However, the presence of another species at the nanoparticle surface must be accounted for, and any gains in catalytic activity from keeping nanoparticle size low could potentially be outweighed by a shielding effect where the large polymer chains of the capping agent ligands sterically hinder the approach of reactants and correspondingly reduce catalytic performance. This has been observed in glycerol oxidation on Au/TiO_2 nanoparticle catalysts, and it was determined that keeping the metal/PVA ratio high (i.e., a low quantity of capping agent compared to that of the metal) minimises this shielding effect whilst still yielding the stability benefits from using the capping agent in the first place.[72]

The capping agent can also be removed once the nanoparticles have been generated and successfully immobilised on a support. However, the conventional method for this has been thermal calcination to volatilise the ligands at temperatures beyond their boiling point[73], and it is evident that exposure to these high temperatures can induce the very sintering, aggregation, and shape modification effects that the capping agent was used to avoid in the first place.[74,75]

It is possible to remove the capping agent by oxidative methods such as ozone exposure, sometimes combined with an ultraviolet light source, which in tandem will oxidise the organic compounds of the capping agent into carbon dioxide and water. These methods were shown to

preserve the size, shape, and dispersion of the metal nanoparticles to a much greater extent than the thermal treatments[76,77], but Vidal-Iglesias *et al.*[78] demonstrated that there is an important distinction between shape and surface structure: even though electron microscopy indicated that NP shape had been preserved, structure-sensitive reactions that only proceed on selective facets (such as those discussed in **Section 1.2.1**) were used to illustrate that the oxidative treatment causes significant disordering of the atomic surface, in particular destroying the long-range ordered terraces of the Pt(100) and (111) facets. This suggests that oxidative methods are not quite the magic bullet they appear to be even on high-resolution imaging.

Recently, an alternative removal method involving solvent washing has been developed, where Au nanoparticles were stabilised with PVA and then supported on TiO_2 before being refluxed with warm water for varying time periods.[79] These catalysts were shown to have a higher activity than those that were dried and calcined in the conventional manner, whilst largely retaining their original morphology, but it is unclear whether or not surface disordering manifests in a similar manner to oxidative methods. The same idea has since been extended to attempting to remove the long-chain hydrocarbon capping agents by displacing them with excess small molecules with a similar capping ability[80] (e.g., displacing PVP with tert-butylamine[81]), and beyond that to a "surfactant-free method" where only small adsorbates such as DMF or melamine are used from the outset.[82]

In addition to these particle size and stability concerns addressed by the choices of capping agent and subsequent removal method, another key goal in the preparation of supported metal nanoparticles is to maximise the interfacial area between the NPs and the support, especially if they are to be used as catalysts for reactions which take place at the NP-support interface rather than at a nanoparticle surface facet. Whilst metal oxides such as titania and ceria (CeO_2) are the most common choice of support, due to their thermal and chemical stability and the ease of supporting NPs on them, other supports such as the high-surface area coordination polymers termed metal-organic frameworks have been investigated.

1.3 Metal-Organic Frameworks (MOFs)

1.3.1 MOF Structures

Metal-organic frameworks, or MOFs, are coordination polymers consisting of a lattice of metal ions or clusters connected to organic linkers by dative covalent bonds.[83] The organic linkers are commonly polydentate, which allows the formation of two- or three-dimensional crystal structures containing large pores (between 3-98 Å).[84] This ultrahigh porosity (BET surface area of 1000-10 000 $m^2 g^{-1}$) means that MOFs have been applied in a variety of uses, such as in

hydrogen storage[85], water desalination[86], and carbon capture[87]. Both the amount of surface area and pore size are highly tunable via differing synthetic routes and post-synthetic modifications.[88]

MOFs are often formed via hydrothermal or solvothermal (non-aqueous) synthesis, in which precursor compounds such as a metal salt and suitable organic linkers are heated in a pressurised steel autoclave, before self-assembling into the product framework.[89,90] A temperature gradient in the autoclave dissolves the precursor compounds in the hotter region, and allows nucleation and growth of the crystalline product in the cooler region.[91] Hydrothermal synthesis is the most common synthetic route to MOFs since it is reasonably practical and affords a highly crystalline product with a high specific surface area.[92]

Other routes for making MOFs include mechanochemical synthesis, in which the precursor materials undergo liquid-assisted grinding in a ball mill to induce crystal formation.[93] Microwave-assisted synthesis is also possible, and is often used to dissolve poorly-soluble precursors or offer a high-speed alternative to hydrothermal synthesis.[94] Finally, electrochemical synthesis can be used to avoid the incorporation of anions such as nitrates or chlorides from the precursor metal salts.[95] Electrodes of the desired metal ion are placed in a solution containing the organic linker and a conductive salt[96], but this generally leads to a lower-quality product than via alternative synthetic routes due to incorporation of the conductive salt into the MOF pores.[97]

One commonly-used variety of metal-organic framework is HKUST-1, or CuBTC (where BTC refers to benzene-1,3,5-tricarboxylic acid, or trimesic acid). This MOF has been used in the majority of work presented in this thesis, and here was produced via a hydrothermal synthetic method utilising copper(II) nitrate trihydrate as a precursor salt combined with a dissolved BTC organic linker.

The CuBTC MOF structure contains a Cu-Cu paddlewheel, as illustrated in **Figure 8**. This is an example of a secondary building unit (SBU), a complex or cluster used to predict the topology and structure of a MOF.[98] The carboxylate groups of four BTC linkers are the paddles of the wheel, coordinating to a central Cu-Cu ‘axle’.

Other frameworks based around the paddlewheel SBU include MOF-2, which whilst somewhat similar to CuBTC, is based around a terephthalic acid (TPA, **Figure 9a**) linker rather than trimesic acid (BTC, **Figure 9b**). The use of a bidentate TPA ligand rather than the tridentate BTC ligand leads to the formation of a layered structure with a lower surface area[99] – only ~360 $m^2 g^{-1}$ compared to the ~1050 $m^2 g^{-1}$ of CuBTC[85]. Whilst originally developed as a zinc-based MOF, MOF-2 also has a variant based around Cu(II) ions.[100]

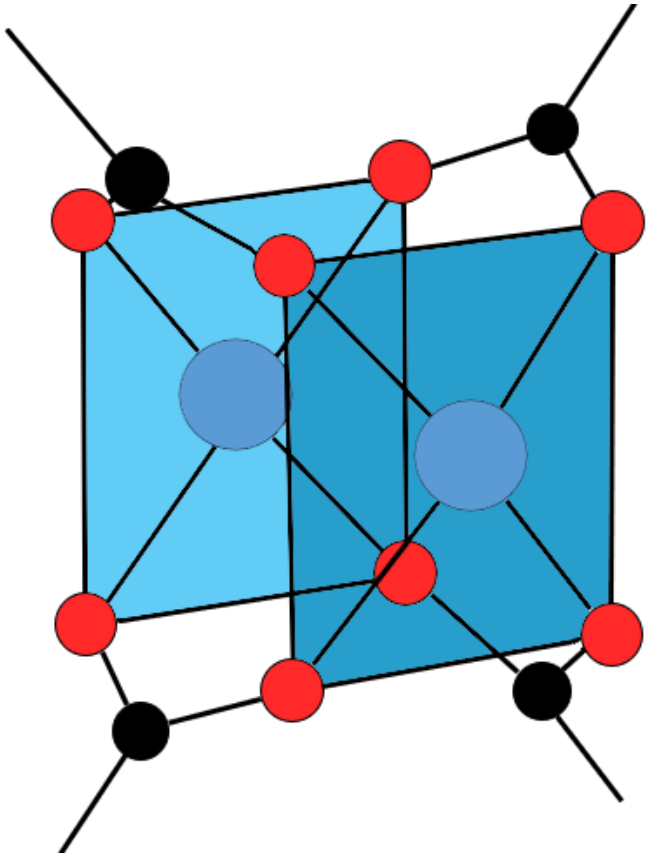

Figure 8: Schematic of a Cu-Cu paddlewheel secondary building unit from CuBTC MOF, adapted from a figure in Hendon *et al*.[101] Copper atoms are shown as blue circles, oxygen atoms as red circles, and carbon atoms as black circles. The rectangular faces of the paddlewheel are coloured in turquoise.

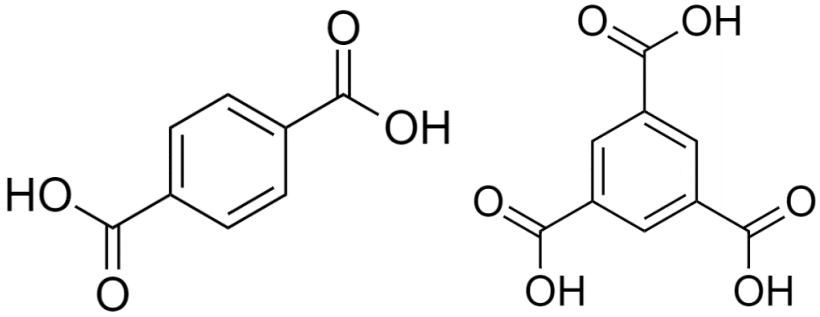

Figure 9: a) Terephthalic acid (TPA) ligand used in MOF-2 and MOF-5; b) trimesic acid (BTC) ligand used in CuBTC MOF.

Another MOF based around the TPA ligand is MOF-5, which is composed of a different secondary building unit to MOF-2 and yields remarkably different properties. The structures of MOF-2 and MOF-5 differ in the "knot" formed by a cluster of zinc atoms and coordinated linkers (**Figure 10**).[102] The four-handed knot for MOF-2 is a simple paddle-wheel, whereas the six-handed knot for MOF-5 is somewhat more complex and relies on a central, tetrahedral oxide coordinated by four Zn^{2+} ions, which in turn are bridged by six carboxylate groups.[103]

This difference in secondary building unit leads to a large difference in the available surface area of the MOF, due to the different crystal structures that MOF-2 and MOF-5 adopt (**Figure 11**). Whereas MOF-2 has a surface area of 200-300 $m^2 g^{-1}$, MOF-5 has been reported to have a surface area of up to 3900 $m^2 g^{-1}$, which makes it a much more useful basis for applications that use up a large quantity of specific surface area, such as gas storage.[104]

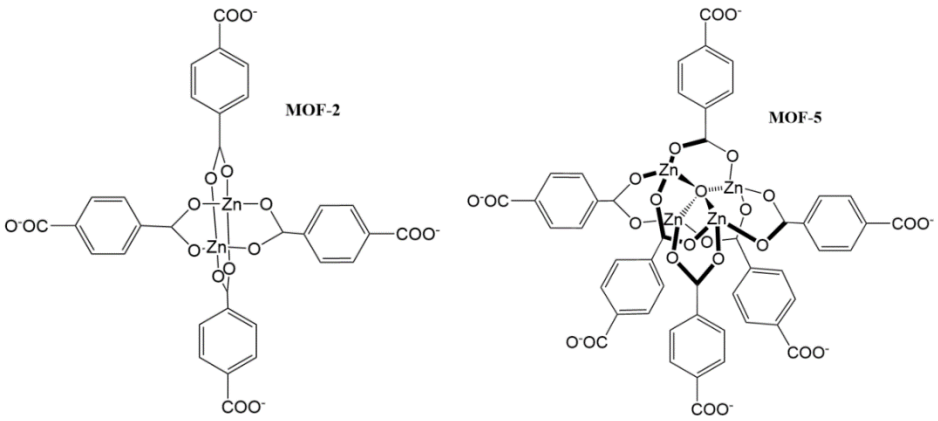

Figure 10: "Knots" formed by Zn and TPA linkers in MOF-2 and MOF-5. Adapted from Schweighauser *et al.*[102]

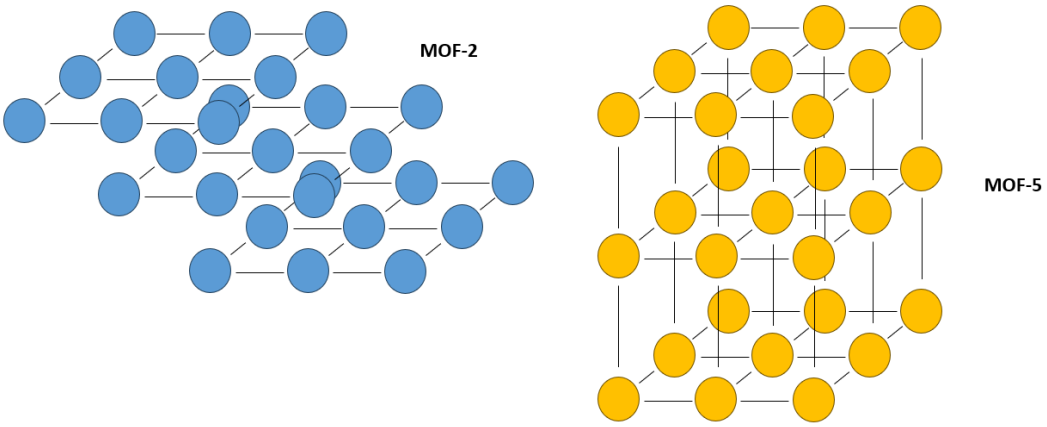

Figure 11: The layered and cubic crystal structures presented by MOF-2 and MOF-5 respectively. Adapted from Schweighauser *et al.*[102]

1.4 Using Metal-Organic Frameworks as a Nanoparticle Support

1.4.1 Nanoparticle-MOF Composites and MOF-derived Nanocomposites

The high porosity and specific surface area of metal-organic frameworks (MOFs) can be exploited for use as nanoparticle supports similar to the metal oxides and carbon supports discussed in **Section 1.2**. These NP-MOF composites have been demonstrated as active catalysts[105], and can be prepared by a range of methods, including solution impregnation,

chemical vapour deposition, and solid grinding.[106] The possible range and applications of these composites will be explored in detail in the introduction to Chapter 3.

Due to the limited stability of metal-organic frameworks,[107] they have also been utilised to derive tailored nanocomposite structures from an NP-MOF template.[108] The most popular method to achieve this is to use thermal treatments to pyrolyse the MOF support, carbonising or removing the organic ligands to yield nanoparticles supported on a carbon-based or metal oxide-based support, which itself is typically nanosized.[109,110] However, this type of method typically exhibits a lack of fine control over the physical and chemical properties of the nanocomposite[111], since there are limited experimental parameters that can be varied. The main options available in design of these nanocomposites are choices of overall calcination temperature, temperature ramp rate, and the atmosphere in which the nanocomposite is calcined.[112–114]

More recently, there have been some attempts to employ chemical methods as an alternative to pyrolysis, such as by using organic acids to etch away a MOF support[115], or by using a reducing agent like $NaBH_4$ to collapse the MOF structure.[116] A similar reducing agent-based approach is the focus of the work presented in this thesis, and the thermal and chemical methods of nanocomposite generation from NP-MOF templates will be discussed further in the introduction to Chapter 4.

1.5 PdCu Nanoparticles

Whilst palladium is one of the most popular elements used in supported nanoparticle catalysts[117–119], and Cu nanoparticles have been demonstrated as effective catalysts in their own right[120,121], there are additional benefits to producing alloyed bimetallic PdCu NPs, creating a local Pd-Cu interface within the nanoparticle.

Alloying copper to palladium can modulate the binding strength of molecules to the palladium surface, due to charge transfer between the alloyed Pd and Cu atoms. A computational study by Tang *et al.*[122] showed that Pd-to-Cu charge transfer both lowers the energy of the electronic *d*-band of Pd and correspondingly induces a raise in the *d*-band of Cu, calculating that this increases the binding strength of oxygen to Cu. The Pd-O binding strength was demonstrated to decrease by a higher magnitude than the increase in Cu-O binding strength, due to increased overlap between the *d*-states of Pd and the molecular orbitals of O_2.

Additionally, Pd atoms bind carbon monoxide ligands more strongly than Cu atoms, and it has been demonstrated that the CO binding energy for PdCu alloys decreases linearly with increasing Cu composition.[123] This decreased binding strength has tangible implications for

PdCu-based catalysts, since one weakness of Pd-based nanoparticle catalysts is their propensity to be poisoned by tightly-bound CO ligands, diminishing their catalytic activity[124].

To obtain these charge-transfer effects in bimetallic PdCu nanoparticles, the Pd and Cu atoms must remain in close proximity to one another, rather than segregating into separate phases. Shan *et al.*[125] demonstrated that PdCu nanoalloys form two different structure types: an ordered phase with interpenetrating Pd and Cu body-centred-cubic (BCC) lattices, and a disordered face-centred-cubic (FCC) phase with Pd and Cu intermixed randomly at the lattice sites. Samples with a 50:50 Pd:Cu composition were shown to phase-segregate into domains of these two types, whereas samples with a higher proportion of one metal exhibited a single phase. It was demonstrated that alloying of Pd and Cu into the ordered BCC phase occurred at 300 °C, before a phase transition into the disordered FCC phase began at 450 °C – although the transformation remained incomplete at 700 °C. Importantly for their catalytic applications, no change in nanoparticle size was observed during the heat treatment. PdCu/C samples with these phase structures were tested for CO oxidation[125], and it was determined that samples of 50:50 Pd/Cu composition were most effective for CO oxidation, supporting the results of computational studies[126]. Presence of the disordered FCC phase in those samples was shown to increase catalytic activity – however, if the nanoalloy significantly phase-separates into separate domains of the BCC and FCC phases, the separation will diminish this observed synergy between the Pd and Cu atoms.

Whilst CO oxidation is a useful test reaction for PdCu nanoparticles, they have been evaluated for a range of other reactions. For example, Mori *et al.*[127] demonstrated that PdCu nanoparticles embedded in a resin were more active for the decomposition of formic acid than PdAg- and PdAu-based catalysts, which exclusively use precious metals and are therefore more expensive. A catalyst that can achieve the selective decomposition of formic acid (HCOOH) to H_2 and CO_2 rather than H_2O and CO makes formic acid useful as a medium for hydrogen storage[128], which ultimately has the potential to serve as a replacement for fossil fuels.[129] Since the reaction is not perfectly selective, the PdCu NPs synthesised by Mori *et al.*[127] were shown to outperform Pd NPs alone due to their improved resistance to CO poisoning.

Another catalytic reaction with potential environmental impacts is the denitrification of groundwater, since nitrate ions that become part of drinking water are transformed into the toxic nitrite ion within the human body.[130] Lim *et al.*[131] prepared ordered and disordered examples of PdCu-alloyed electrocatalysts for this reaction, demonstrating that 91% selectivity for N_2 was achieved by the ordered catalyst, in contrast to the disordered catalyst, which was both non-selective and unstable.

These examples all demonstrate how the ability to engineer a specific bimetallic interface within a nanoparticle can have significant impacts on its catalytic properties, with improvements including preferential selectivity, increased stability, and poisoning resistance. Additionally, the PdCu nanocatalysts described above have often out-performed counterparts made exclusively from Pd or other precious metals. Exploiting the electronic benefits of alloying Pd to Cu could lead to the development of catalysts that have a lower overall amount of palladium, decreasing cost and increasing sustainability.[132,133] Therefore, the possibility of creating a controlled Pd-Cu interface within nanoparticle catalysts will be explored in this project.

1.6 Project Summary

In summary, metal nanoparticle catalysts have been demonstrated to be highly useful and versatile. Phenomena such as charge transfer and suboxide encapsulation contribute towards strong metal-support interactions, which can be exploited to modulate catalytic activity and selectivity. Various experimental methods such as incipient wetness impregnation and sol-immobilisation can be used to control the properties of the supported NP catalysts. The high surface area per unit mass of metal-organic frameworks can be utilised as a support for metal nanoparticles, and these NP-MOF composites can also be used as catalysts in the same fashion as nanoparticles supported on metal oxides or carbon-based supports.

Pyrolysing the NP-MOF composites has been discussed as an alternative preparation to produce oxide- or carbon-supported NP catalysts, since most MOFs have only a limited range of thermal stability. However, the products of destroying the framework via chemical methods, as opposed to annealing, and the potential catalytic utilities of those products, have not been widely investigated.

Therefore, this project aims to exploit the careful control of nanoparticle size and dispersion afforded by a sol-immobilisation method, as described in **Section 1.2.3.2**, to produce catalytically-active nanoparticle-MOF composites, before using them as a sacrificial template in a novel chemical reduction method, to produce nanocomposite catalysts with well-defined and controllable properties. This thesis will:

(1) Extend the sol-immobilisation method to prepare Pd/CuMOF composites based on different carboxylate ligands, using both water-based and methanol-based immobilisations,
(2) Demonstrate how the limited stability of these Pd/CuMOF templates can be selectively exploited to form controlled nanocomposite materials via a novel chemical reduction method,
(3) Assess the impacts of various reaction parameters on the structure and properties of the synthesised nanocomposites, including Pd loading, reduction temperature and reductant concentration,
(4) Use *ex situ* X-ray absorption spectroscopy studies to investigate Pd-Cu alloying in the formation of bimetallic PdCu NPs,
(5) Evaluate the catalytic performances of the Pd/CuMOF composites and reduced PdCu/Cu_2O nanocomposites, through use of 4-nitrophenol reduction and CO oxidation as test reactions, to determine how the inducement of Pd-Cu alloying influences catalytic activity.

1.7 References

1 I. Chorkendorff and J. W. Niemantsverdriet, *Concepts of Modern Catalysis and Kinetics*, Wiley-VCH, 3rd edn., 2017.

2 V. Smil, *Enriching the Earth: Fritz Haber, Carl Bosch, and the Transformation of World Food Production*, MIT Press, 2001.

3 G. Ertl, *J. Vac. Sci. Technol. A*, 1983, **1**, 1247–1253.

4 V. Kyriakou, I. Garagounis, A. Vourros, E. Vasileiou and M. Stoukides, *Joule*, 2020, **4**, 142–158.

5 J. Humphreys, R. Lan and S. Tao, *Adv. Energy Sustain. Res.*, 2021, **2**, 2000043.

6 E. T. C. Vogt and B. M. Weckhuysen, *Chem. Soc. Rev.*, 2015, 44, 7342–7370.

7 J. Biswas and I. E. Maxwell, *Appl. Catal.*, 1990, **58**, 1–18.

8 B. Shi, Y. Liao and J. L. Naumovitz, in *Fischer-Tropsch Synthesis, Catalysts and Catalysis: Advances and Applications*, eds. B. H. Davis and M. L. Occelli, CRC Press, 2016, pp. 165–181.

9 E. Iglesia, S. L. Soled and R. A. Fiato, *J. Catal.*, 1992, **137**, 212–224.

10 J. Xie, J. Yang, A. I. Dugulan, A. Holmen, D. Chen, K. P. De Jong and M. J. Louwerse, *ACS Catal.*, 2016, **6**, 3147–3157.

11 S. Iqbal, T. E. Davies, J. S. Hayward, D. J. Morgan, K. Karim, J. K. Bartley, S. H. Taylor and G. J. Hutchings, *Catal. Today*, 2016, **272**, 74–79.

12 A. de Klerk, *Green Chem.*, 2007, **9**, 560–565.

13 A. M. Wright, Z. Wu, G. Zhang, J. L. Mancuso, R. J. Comito, R. W. Day, C. H. Hendon, J. T. Miller and M. Dincă, *Chem*, 2018, **4**, 2894–2901.

14 C. K. Brown and G. Wilkinson, *J. Chem. Soc. A Inorganic, Phys. Theor. Chem.*, 1970, 2753–2764.

15 A. Haynes, P. M. Maitlis, G. E. Morris, G. J. Sunley, H. Adams, P. W. Badger, C. M. Bowers, D. B. Cook, P. I. P. Elliott, T. Ghaffar, H. Green, T. R. Griffin, M. Payne, J. M. Pearson, M. J. Taylor, P. W. Vickers and R. J. Watt, *J. Am. Chem. Soc.*, 2004, **126**, 2847–2861.

16 P. W. N. M. van Leeuwen and J. C. Chadwick, *Homogeneous Catalysts: Activity - Stability - Deactivation*, Wiley-VCH, 2011.

17 A. Corma, *Angew. Chemie - Int. Ed.*, 2016, 55, 6112–6113.

18 K. Taylor, *Catal. Rev.*, 1993, **35**, 457–481.

19 Z. Hong, Z. Wang and X. Li, *Catal. Sci. Technol.*, 2017, 7, 3440–3452.

20 J. Hagen, *Industrial Catalysis: A Practical Approach*, Wiley-VCH, 2015.

21 R. Prins, *Top. Catal.*, 2018, **61**, 714–721.

22 P. Mars and D. W. van Krevelen, *Chem. Eng. Sci.*, 1954, **3**, 41–59.

23 C. Doornkamp and V. Ponec, *J. Mol. Catal. A Chem.*, 2000, **162**, 19–32.

24 E. J. Grootendorst, Y. Verbeek and V. Ponec, *J. Catal.*, 1995, **157**, 706–712.

25 Z. Zhai, X. Wang, R. Licht and A. T. Bell, *J. Catal.*, 2015, **325**, 87–100.

26 P. Munnik, P. E. De Jongh and K. P. De Jong, *Chem. Rev.*, 2015, 115, 6687–6718.

27 P. Forzatti and L. Lietti, *Catal. Today*, 1999, **52**, 165–181.

28 G. Attard and C. Barnes, *Surfaces (Oxford Chemistry Primer)*, Oxford University Press, 1998.

29 M. Haruta, S. Tsubota, T. Kobayashi, H. Kageyama, M. J. Genet and B. Delmon, *J. Catal.*, 1993, **144**, 175–192.

30 Y. Wang, B. Xu and W. Shen, *Adsorpt. Sci. Technol.*, 2013, **31**, 823–828.

31 K. Sun, M. Kohyama, S. Tanaka and S. Takeda, *J. Comput. Chem.*, 2011, **32**, 3276–3282.

32 D. R. Boverhof, C. M. Bramante, J. H. Butala, S. F. Clancy, W. M. Lafranconi, J. West and S. C. Gordon, *Regul. Toxicol. Pharmacol.*, 2015, **73**, 137–150.

33 F. De Clippel, M. Dusselier, S. Van De Vyver, L. Peng, P. A. Jacobs and B. F. Sels, *Green Chem.*, 2013, 15, 1398–1430.

34 A. Z. Moshfegh, *J. Phys. D. Appl. Phys.*, 2009, **42**, 233001.

35 G. C. Bond, *Surf. Sci.*, 1985, **156**, 966–981.

36 K. Kinoshita, *J. Electrochem. Soc.*, 1990, **137**, 845–848.

37 Y. Chen, X. Gu, C. G. Nie, Z. Y. Jiang, Z. X. Xie and C. J. Lin, *Chem. Commun.*, 2005, 4181–4183.

38 A. Umar, J. Lee, J. Dey and S. M. Choi, *Chem. Mater.*, 2016, **28**, 4962–4970.

39 C. Y. Chiu, P. J. Chung, K. U. Lao, C. W. Liao and M. H. Huang, *J. Phys. Chem. C*, 2012, **116**, 23757–23763.

40 R. Narayanan and M. A. El-Sayed, *Nano Lett.*, 2004, **4**, 1343–1348.

41 R. Narayanan and M. A. El-Sayed, *J. Phys. Chem. B*, 2004, **108**, 5726–5733.

42 Y. Sun and Y. Xia, *Science*, 2002, **298**, 2176–2179.

43 B. Roldan Cuenya and F. Behafarid, *Surf. Sci. Rep.*, 2015, **70**, 135–187.

44 Q. L. Zhu and Q. Xu, *Chem*, 2016, 1, 220–245.

45 W. Zhang, *Adv. Exp. Med. Biol.*, 2014, **811**, 20–43.

46 M. J. Loedolff, B. M. Goh, G. A. Koutsantonis and R. O. Fuller, *New J. Chem.*, 2018, **42**, 14894–14900.

47 F. Morales-Lara, V. K. Abdelkader-Fernández, M. Melguizo, A. Turco, E. Mazzotta, M. Domingo-García, F. J. López-Garzón and M. Pérez-Mendoza, *J. Mater. Chem. A*, 2019, **7**, 24502–24514.

48 S. J. Tauster, S. C. Fung and R. L. Garten, *J. Am. Chem. Soc.*, 1978, **100**, 170–175.

49 P. Meriaudeau, J. F. Dutel, M. Dufaux and C. Naccache, *Stud. Surf. Sci. Catal.*, 1982, **11**, 95–104.

50 S. J. Tauster, *Acc. Chem. Res.*, 1987, **20**, 389–394.

51 H. R. Sadeghi and V. E. Henrich, *J. Catal.*, 1984, **87**, 279–282.

52 D. N. Belton, Y. M. Sun and J. M. White, *J. Phys. Chem.*, 1984, **88**, 5172–5176.

53 R. Baker, E. Prestridge and R. Garten, *J. Catal.*, 1979, **59**, 293–302.

54 R. Baker, E. Prestridge and R. Garten, *J. Catal.*, 1979, **56**, 390–406.

55 A. Datye, D. Kalakkad, M. Yao and D. Smith, *J. Catal.*, 1995, 155, 148–153.

56 J. C. Matsubu, S. Zhang, L. DeRita, N. S. Marinkovic, J. G. Chen, G. W. Graham, X. Pan and P. Christopher, *Nat. Chem.*, 2017, **9**, 120–127.

57 E. A. Walker, D. Mitchell, G. A. Terejanu and A. Heyden, *ACS Catal.*, 2018, **8**, 3990–3998.

58 M. A. Bollinger and M. A. Vannice, *Appl. Catal. B Environ.*, 1996, **8**, 417–443.

59 Y. G. Wang, D. Mei, V. A. Glezakou, J. Li and R. Rousseau, *Nat. Commun.*, 2015, **6**, 6511.

60 S. Yoon, K. Oh, F. Liu, J. H. Seo, G. A. Somorjai, J. H. Lee and K. An, *ACS Catal.*, 2018, 8 (6), 5391–5398.

61 M. E. Strayer, T. P. Senftle, J. P. Winterstein, N. M. Vargas-Barbosa, R. Sharma, R. M. Rioux, M. J. Janik and T. E. Mallouk, *J. Am. Chem. Soc.*, 2015, **137**, 16216–16224.

62 B. K. Min, A. K. Santra and D. W. Goodman, *Catal. Today*, 2003, 85, 113–124.

63 J. A. Schwarz, C. Contescu and A. Contescu, *Chem. Rev.*, 1995, **95**, 477–510.

64 L. Delannoy, N. El Hassan, A. Musi, N. N. Le To, J.-M. Krafft and C. Louis, *J. Phys. Chem. B*, 2006, **110**, 22471–22478.

65 L. Prati, A. Villa, C. E. Chan-Thaw, R. Arrigo, D. Wang and D. S. Su, *Faraday Discuss.*, 2011, **152**, 353–365.

66 F. Porta, L. Prati, M. Rossi, S. Coluccia and G. Martra, *Catal. Today*, 2000, **61**, 165–172.

67 S. M. Rogers, C. R. A. Catlow, C. E. Chan-Thaw, D. Gianolio, E. K. Gibson, A. L. Gould, N. Jian, A. J. Logsdail, R. E. Palmer, L. Prati, N. Dimitratos, A. Villa and P. P. Wells, *ACS Catal.*, 2015, **5**, 4377–4384.

68 S. M. Rogers, C. R. A. Catlow, C. E. Chan-Thaw, A. Chutia, N. Jian, R. E. Palmer, M. Perdjon, A. Thetford, N. Dimitratos, A. Villa and P. P. Wells, *ACS Catal.*, 2017, **7**, 2266–2274.

69 J. A. Lopez-Sanchez, N. Dimitratos, P. Miedziak, E. Ntainjua, J. K. Edwards, D. Morgan, A. F. Carley, R. Tiruvalam, C. Kiely and G. J. Hutchings, *Phys. Chem. Chem. Phys.*, 2008, **10**, 1921–1930.

70 B. Ajitha, Y. A. Kumar Reddy, P. S. Reddy, H. J. Jeon and C. W. Ahn, *RSC Adv.*, 2016, **6**, 36171–36179.

71 K. M. Koczkur, S. Mourdikoudis, L. Polavarapu and S. E. Skrabalak, *Dalt. Trans.*, 2015, **44**, 17883–17905.

72 A. Villa, D. Wang, G. M. Veith, F. Vindigni and L. Prati, *Catal. Sci. Technol.*, 2013, **3**, 3036–3041.

73 J. D. Grunwaldt, M. Maciejewski, O. S. Becker, P. Fabrizioli and A. Baiker, *J. Catal.*, 1999, **186**, 458–469.

74 S. Campisi, M. Schiavoni, C. E. Chan-Thaw and A. Villa, *Catalysts*, 2016, **6**, 1–21.

75 G. Collins, F. Davitt, C. O'Dwyer and J. D. Holmes, *ACS Appl. Nano Mater.*, 2018, **1**, 7129–7138.

76 L. D. Menard, F. Xu, R. G. Nuzzo and J. C. Yang, *J. Catal.*, 2006, **243**, 64–73.

77 C. Aliaga, J. Y. Park, Y. Yamada, H. S. Lee, C. Tsung, P. Yang and G. a Somorjai, *J. Phys. Chem. C*, 2009, **113**, 6150–6155.

78 F. J. Vidal-Iglesias, J. Solla-Gullón, E. Herrero, V. Montiel, A. Aldaz and J. M. Feliu, *Electrochem. commun.*, 2011, **13**, 502–505.

79 J. A. Lopez-Sanchez, N. Dimitratos, C. Hammond, G. L. Brett, L. Kesavan, S. White, P. Miedziak, R. Tiruvalam, R. L. Jenkins, A. F. Carley, D. Knight, C. J. Kiely and G. J. Hutchings, *Nat. Chem.*, 2011, **3**, 551–556.

80 Z. Niu and Y. Li, *Chem. Mater.*, 2014, **26**, 72–83.

81 N. Naresh, F. G. S. Wasim, B. P. Ladewig and M. Neergat, *J. Mater. Chem. A*, 2013, **1**, 8553–8559.

82 Y. Imura, S. Furukawa, K. Ozawa, C. Morita-Imura, T. Kawai and T. Komatsu, *RSC Adv.*, 2016, **6**, 17222–17227.

83 Y. R. Lee, J. Kim and W. S. Ahn, *Korean J. Chem. Eng.*, 2013, **30**, 1667–1680.

84 Y. V. Kaneti, J. Tang, R. R. Salunkhe, X. Jiang, A. Yu, K. C. W. Wu and Y. Yamauchi, *Adv. Mater.*, 2017, **29**, 1604898.

85 K.-S. Lin, A. K. Adhikari, C.-N. Ku, C.-L. Chiang and H. Kuo, *Int. J. Hydrogen Energy*, 2012, **37**, 13865–13871.

86 M. Kadhom and B. Deng, *Appl. Mater. Today*, 2018, **11**, 219–230.

87 C. A. Trickett, A. Helal, B. A. Al-Maythalony, Z. H. Yamani, K. E. Cordova and O. M. Yaghi, *Nat. Rev. Mater.*, 2017, **2**, 17045.

88 H. C. Zhou, J. R. Long and O. M. Yaghi, *Chem. Rev.*, 2012, **112**, 673–674.

89 O. M. Yaghi and H. Li, *J. Am. Chem. Soc.*, 1995, **117**, 10401–10402.

90 D. Biswal and P. G. Kusalik, *ACS Nano*, 2017, **11**, 258–268.

91 N. Stock and S. Biswas, *Chem. Rev.*, 2012, 112, 933–969.

92 J. L. Crane, K. E. Anderson and S. G. Conway, *J. Chem. Educ.*, 2015, **92**, 373–377.

93 M. Klimakow, P. Klobes, A. F. Thünemann, K. Rademann and F. Emmerling, *Chem. Mater.*, 2010, **22**, 5216–5221.

94 S. H. Jhung, J. Lee and J.-S. Chang, *Bull. Korean Chem. Soc.*, 2005, **26**, 880–881.

95 K. Pirzadeh, A. A. Ghoreyshi, M. Rahimnejad and M. Mohammadi, *Korean J. Chem. Eng.*, 2018, **35**, 1–10.

96 U. Mueller, M. Schubert, F. Teich, H. Puetter, K. Schierle-Arndt and J. Pastré, in *Journal of Materials Chemistry*, 2006, vol. 16, pp. 626–636.

97 M. Schlesinger, S. Schulze, M. Hietschold and M. Mehring, *Microporous Mesoporous Mater.*, 2010, **132**, 121–127.

98 M. Eddaoudi, D. B. Moler, H. Li, B. Chen, T. M. Reineke, M. O'Keeffe and O. M. Yaghi, *Acc. Chem. Res.*, 2001, **34**, 319–330.

99 N. Getachew, Y. Chebude, I. Diaz and M. Sanchez-Sanchez, *J. Porous Mater.*, 2014, **21**, 769–773.

100 H. K. Kim, W. S. Yun, M. B. Kim, J. Y. Kim, Y. S. Bae, J. D. Lee and N. C. Jeong, *J. Am. Chem. Soc.*, 2015, **137**, 10009–10015.

101 C. H. Hendon and A. Walsh, *Chem. Sci.*, 2015, **6**, 3674–3683.

102 L. Schweighauser, K. Harano and E. Nakamura, *Inorg. Chem. Commun.*, 2017, **84**, 1–4.

103 A. Schoedel and O. M. Yaghi, in *Macrocyclic and Supramolecular Chemistry: How Izatt–Christensen Award Winners Shaped the Field*, John Wiley & Sons, Ltd., First Edit., 2016.

104 D. J. Tranchemontagne, J. R. Hunt and O. M. Yaghi, *Tetrahedron*, 2008, **64**, 8553–8557.

105 W. Xiang, Y. Zhang, H. Lin and C. Liu, *Molecules*, 2017, **22**, 2103.

106 L. Jiao, Y. Wang, H. L. Jiang and Q. Xu, *Adv. Mater.*, 2018, **30**, 1703663.

107 H. L. Wang, H. Yeh, Y. C. Chen, Y. C. Lai, C. Y. Lin, K. Y. Lu, R. M. Ho, B. H. Li, C. H. Lin and D. H. Tsai, *ACS Appl. Mater. Interfaces*, 2018, **10**, 9332–9341.

108 L. Oar-Arteta, T. Wezendonk, X. Sun, F. Kapteijn and J. Gascon, *Mater. Chem. Front.*, 2017, **1**, 1709.

109 J. Zhang, B. An, Y. Hong, Y. Meng, X. Hu, C. Wang, J. Lin, W. Lin and Y. Wang, *Mater. Chem. Front.*, 2017, **1**, 2405.

110 L. Hu, W. Li, L. Wang and B. Wang, *EnergyChem*, 2021, **3**, 100056.

111 C. Singh, S. Mukhopadhyay and I. Hod, *Nano Converg.*, 2021, **8**, 1–10.

112 Q. Wang and D. Astruc, *Chem. Rev.*, 2020, **120**, 1438–1511.

113 V. P. Santos, T. A. Wezendonk, J. J. D. Jaén, A. I. Dugulan, M. A. Nasalevich, H. U. Islam, A. Chojecki, S. Sartipi, X. Sun, A. A. Hakeem, A. C. J. Koeken, M. Ruitenbeek, T. Davidian, G. R. Meima, G. Sankar, F. Kapteijn, M. Makkee and J. Gascon, *Nat. Commun.*, 2015, **6**, 6451.

114 H. Niu, S. Liu, Y. Cai, F. Wu and X. Zhao, *Microporous Mesoporous Mater.*, 2016, **219**, 48–53.

115 R. Li, S. Wu, X. Wan, H. Xu and Y. Xiong, *Inorg. Chem. Front.*, 2016, **3**, 104–110.

116 Y. Fu, X. Zhai, S. Wang, L. Shao, X. Bai, Z. Su, Y. Liu, L. Zhang and J. Chen, *Inorg. Chem.*, 2021, **60**, 16447–16454.

117 A. Chen and C. Ostrom, *Chem. Rev.*, 2015, **115**, 11999–12044.

118 N. Joudeh, A. Saragliadis, G. Koster, P. Mikheenko and D. Linke, *Front. Nanotechnol.*, 2022, **4**, 1–24.

119 J. I. Ayogu and E. A. Onoabedje, *ChemistryOpen*, 2021, **10**, 430–450.

120 M. B. Gawande, A. Goswami, F. X. Felpin, T. Asefa, X. Huang, R. Silva, X. Zou, R. Zboril and R. S. Varma, *Chem. Rev.*, 2016, **116**, 3722–3811.

121 G. Totarella, R. Beerthuis, N. Masoud, C. Louis, L. Delannoy and P. E. De Jongh, *J. Phys. Chem. C*, 2021, **125**, 366–375.

122 W. Tang, L. Zhang and G. Henkelman, *J. Phys. Chem. Lett.*, 2011, **2**, 1328–1331.

123 N. Lopez and J. K. Nørskov, *Surf. Sci.*, 2001, **477**, 59–75.

124 F. Schiller, M. Ilyn, V. Pérez-Dieste, C. Escudero, C. Huck-Iriart, N. Ruiz Del Arbol, B. Hagman, L. R. Merte, F. Bertram, M. Shipilin, S. Blomberg, J. Gustafson, E. Lundgren and J. E. Ortega, *J. Am. Chem. Soc.*, 2018, **140**, 16245–16252.

125 S. Shan, V. Petkov, B. Prasai, J. Wu, P. Joseph, Z. Skeete, E. Kim, D. Mott, O. Malis, J. Luo and C. J. Zhong, *Nanoscale*, 2015, **7**, 18936–18948.

126 W. Zhang, S. Shan, J. Luo, A. Fisher, J.-F. Chen, C.-J. Zhong, J. Zhu and D. Cheng, *J. Phys. Chem. C*, 2017, **121**, 11010–11020.

127 K. Mori, H. Tanaka, M. Dojo, K. Yoshizawa and H. Yamashita, *Chem. - A Eur. J.*, 2015, **21**, 12085–12092.

128 D. Wei, R. Sang, P. Sponholz, H. Junge and M. Beller, *Nat. Energy*, 2022, **7**, 438–447.

129 M. R. Usman, *Renew. Sustain. Energy Rev.*, 2022, **167**, 112743.

130 M. Duca and M. T. M. Koper, *Energy Environ. Sci.*, 2012, **5**, 9726–9742.

131 J. Lim, D. A. Cullen, E. Stavitski, S. W. Lee and M. C. Hatzell, *ACS Energy Lett.*, 2023, **8**, 4746–4752.

132 J. Zheng, H. Zeng, C. Tan, T. Zhang, B. Zhao, W. Guo, H. Wang, Y. Sun and L. Jiang, *ACS Sustain. Chem. Eng.*, 2019, **7**, 15354–15360.

133 S. McCarthy, D. C. Braddock and J. D. E. T. Wilton-Ely, *Coord. Chem. Rev.*, 2021, **442**, 213925.

Chapter 2 Methods

This chapter will discuss the various experimental methods and analytical techniques used throughout this report, beginning with the hydrothermal synthesis of metal-organic frameworks, the sol-immobilisation method used to prepare Pd/CuBTC composites, and the reduction method used to generate $PdCu/Cu_2O$ nanocomposites. Following this, the various spectroscopic and analytical techniques used to characterise the prepared samples will be examined, including XRD, electron microscopy, TGA, MP-AES, X-ray absorption spectroscopy, and UV/vis spectroscopy. Finally, the techniques used to test the catalytic activity of the synthesised nanocomposites, including the reduction of 4-nitrophenol and microreactor-based CO oxidation, will be discussed.

2.1 Synthetic Methods

2.1.1 MOF synthesis

One common method of synthesis for porous structures such as metal-organic frameworks is hydrothermal synthesis, in which high pressure and temperature is used to force crystals of a material to nucleate and grow.[1,2] The reaction components are dissolved in a solvent mixture which is then placed in an stainless steel autoclave and heated beyond the boiling point of the solvent.[3] Dimethyl formamide, or DMF, is a common solvent in MOF synthesis, since it can dissolve many different organic linkers and metal precursor salts.[4] However, it also occupies the pores and channels within the MOF structure following synthesis, often proving difficult to remove. The slow process of solvent exchange can be used to remove this solvated DMF, by stirring the MOF in a solution of another solvent such as dimethyl ether or ethanol, which gradually replaces the DMF within the framework.[5,6]

The CuBTC MOF[7] prepared throughout this project was synthesised as follows: 1,3,5-benzenetricarboxylic (BTC) acid (1.0 g) was dissolved in 30 mL of a 1:1 (by volume) mixture of ethanol and N,N-dimethylformamide (DMF). Copper (II) nitrate trihydrate (2.077 g) was dissolved in a separate solution of 15 mL water. The two solutions were mixed together, and stirred for 10 minutes, before the resulting solution was transferred into a Teflon-lined stainless steel autoclave and heated at 393 K for 10 h. The reaction vessel was then allowed to cool to room temperature and the resulting blue crystals were isolated by filtration, washed with DMF (100 mL g^{-1} of MOF), and extracted with methanol overnight (200 mL g^{-1}) to remove solvated DMF.[8] The similar CuTPA MOF[9] was synthesised in an analogous manner, but using 1.0 g of 1,4-benzenedicarboxylic acid (BDC) in place of BTC.

2.1.2 The sol-immobilisation method

As discussed in **Section 1.2.3.2**, the sol-immobilisation method is a popular colloid-based approach for introducing stabilised nanoparticles to a support.[10] The method generates zero-valent metal ions in solution, stabilising them with a capping agent such as polyvinyl alcohol (PVA) or polyvinylpyrrolidone (PVP), which allows the generation of small metal nanoparticles below 10 nm in diameter. This stabilisation is achieved through steric interactions, as the large polymer chains of PVA chains bind to the colloidal nanoparticles and then spread out in solution. Nanoparticle aggregation is then discouraged by clashes between the PVA chains as particles approach one another.[11] While current studies of sol-immobilisation have mainly focused on the use of metal oxide-based supports[12,13] or activated carbon[14], this project extended the sol-immobilisation to metal-organic frameworks, since they have a high surface area that can act as a nanoparticle support.

The Pd/MOF composites synthesised in this report were prepared as follows: Potassium tetrachloropalladate(II) (K_2PdCl_4) was used to prepare an aqueous solution of the desired palladium concentration (1.26×10^{-4} M), to which a solution of polyvinyl alcohol (molecular weight = 9000–10 000 g mol^{-1}, 80% hydrolysed, PVA/Pd wt. ratio = 0.65) was added. A fresh solution of $NaBH_4$ (0.1 M, $NaBH_4$/Pd molar ratio = 5) was prepared and added dropwise to the solution of K_2PdCl_4 and PVA with stirring. After a period of 30 minutes, to ensure the complete reduction of Pd, a CuBTC MOF powder was added under vigorous stirring conditions to immobilise the nanoparticles on the MOF surface. The amount of support material required was calculated to yield metal loadings of 0.25, 0.5 and 1 wt % Pd, and the mixture was subsequently stirred for 60 min. The solution was filtered, and the collected solid was washed thoroughly with 2 L of deionised water (18.2 MΩ cm^{-1}) and 200 mL of ethanol to remove soluble impurities, and dried overnight at room temperature.

2.1.3 Reduction of Pd/CuMOF composites

The chemical reduction method developed in Chapter 4 of this work adapts the conditions experienced by Pd/CuBTC composites during the *in situ* reduction of 4-nitrophenol, which is discussed in **Section 2.7.1**.

The PdCu/Cu_2O nanocomposites prepared in this work were generated by reduction of Pd/CuBTC composites using excess $NaBH_4$ in the presence of 4-nitrophenol, which is itself reduced to 4-aminophenol during the reaction. 500 mg of Pd/CuBTC was added to a 70 mL aqueous solution of 0.00018 M 4-nitrophenol before adding 100 mL of 0.0397 M $NaBH_4$ in H_2O, which yields a minimum $NaBH_4$/metal molar ratio of 1.5:1. After a minimum of 30 minutes, at which point generated hydrogen bubbles had dissipated, the samples were collected by

centrifugation at 3500 rpm for six minutes in Falcon centrifuge tubes, washed thoroughly with H_2O, centrifuged again under the same conditions, and then dried at 80 °C overnight. PdCu/CuO samples were also prepared in the same manner but without the addition of 4-nitrophenol. Any additional variations in experimental method, such as for optimisation of nanocomposite properties, are documented in Chapter 4.

2.2 X-Ray Diffraction (XRD)

X-ray diffraction (XRD) is an extremely useful technique to determine the crystal structure of a sample. X-rays incident on the sample are scattered elastically by electrons (Thomson scattering), and the reflected waves interfere with the incident waves. Most of the interference is destructive, but it can be shown that in certain directions the waves constructively interfere to give points of maximum intensity, which appear as spots on an X-ray diffraction pattern.

These points of constructive interference are given by Bragg's Law, depicted graphically in **Figure 12**:

$$n\lambda = 2d_{hkl}\sin\theta \tag{1}$$

where d_{hkl} is the spacing between adjacent planes with Miller indices (*hkl*), θ is the incident angle, λ is the wavelength of the incident X-rays and *n* is any integer.[15] XRD is a non-destructive and highly informative technique which requires only a small amount of material to perform, so it is extremely useful for catalyst characterisation.

The Scherrer equation[16] is used to estimate the average size of a crystallite in a measured phase in powder X-ray diffraction. The equation is as follows:

$$< L > = \frac{K\lambda}{\beta\cos\theta} \tag{2}$$

where <*L*> is the average crystallite size, λ the X-ray wavelength, θ the Bragg angle, β the full width at half-maximum (FWHM) of the Bragg peak being investigated, and K a "crystallite shape factor" often taken as equal to 0.9.[17]

X-ray diffraction patterns measured in Chapter 3 were recorded on a Bruker D8 diffractometer with a Ge(220) primary beam monochromator and a Vantec detector using low background Si sample holders. The patterns were recorded across a range of $2\theta = 5°{-}80°$ with a step size of 0.0109°.

All other diffraction patterns were recorded on a Rigaku Miniflex diffractometer at the Material Characterisation Laboratory, Harwell, using aluminium sample holders. The patterns were recorded across a range of $2\theta = 5° - 80°$ with a step size of 0.02°.

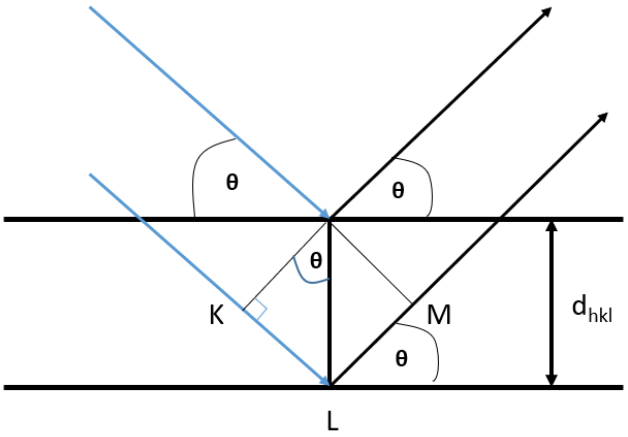

$$n\lambda = KL + LM$$

$$KL = LM = d_{hkl} \sin\theta$$

$$n\lambda = 2d_{hkl} \sin\theta$$

Figure 12: Schematic of the Bragg condition for constructive interference in X-ray diffraction.

2.3 Electron Microscopy (SEM/TEM)

The physicist Ernst Abbe demonstrated[18] that, for coherent imaging methods, the highest resolution d_{min} attainable using visible light is given by:

$$d_{min} = \frac{\lambda}{2n \sin\alpha} = \frac{\lambda}{2NA} \tag{3}$$

where n is the refractive index of the medium, λ the wavelength of the incident light, α the angle of the incident light to the axis and NA the numerical aperture of the lens. For a typical visible light ray in ideal conditions this calculates as a resolution limit of around 250 nanometres, and experimental conditions, optical aberrations, and lens quality often decrease this resolution further.[19]

Since metal nanoparticles by definition have an upper size limit of at most 50-100 nm[20], alternative methods to conventional optical microscopy must be used to image them. Due to the quantum mechanical principle of wave-particle duality, electrons behave as a wave with a characteristic de Broglie wavelength[21]:

$$\lambda_{DB} = \frac{h}{m_e v} \tag{4}$$

where h is Planck's constant, and m_e and v are the mass and velocity of the electron respectively. It can be shown that for an electron accelerated by a potential of 30 kilovolts (kV), the de Broglie wavelength is equal to 7.08 x 10^{-12} m; ignoring relativistic effects and assuming an

angle of 10^{-2} radians, the highest resolution theoretically obtainable approaches 0.4 nm.[22] This increases to 0.2 nm for a potential of 100 kV. Therefore, imaging using electrons rather than visible light will be an effective method to resolve individual metal nanoparticle clusters.

The chosen accelerating voltages used above are typical values used in two types of electron microscopy: scanning electron microscopy (SEM, usually up to 30 kV) and transmission electron microscopy (TEM, up to 300 kV). A schematic of a scanning electron microscope is shown in **Figure 13**. Thermal excitation of a suitable filament (e.g., tungsten or LaB_6) causes thermionic emission of electrons, which are attracted to the anode by an applied potential difference. Various condenser lenses are used to focus the electron beam, and the scanning coils are used to raster the beam across the surface of the sample.[23]

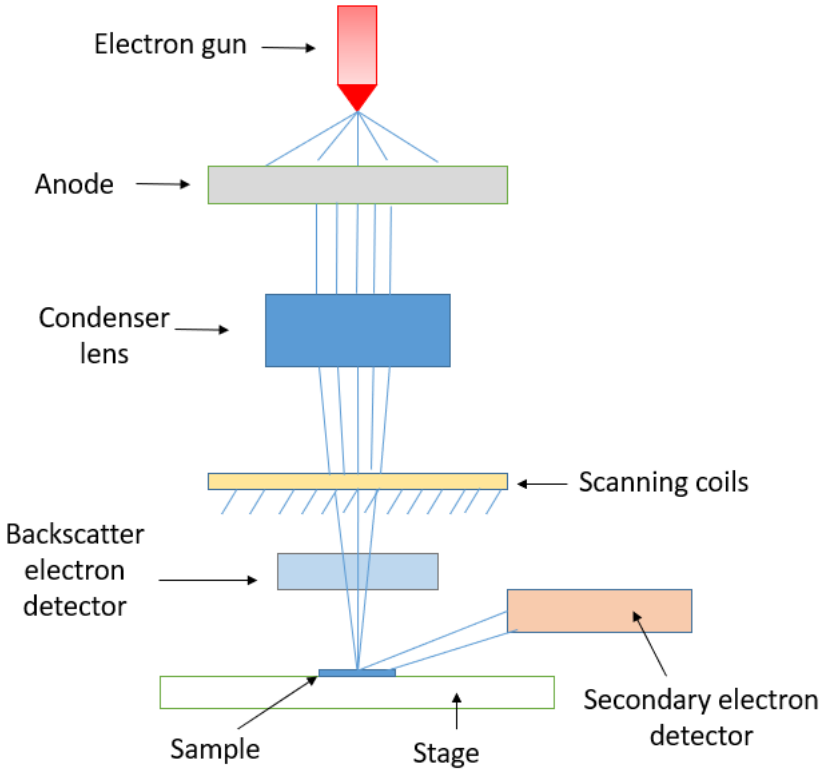

Figure 13: Schematic of a scanning electron microscope (SEM), showing the electron gun, condenser lens, scanning coils, sample stage, and both backscatter and secondary electron detectors.

When the electron beam collides with the sample, scattering events occur. Some electrons are elastically scattered back towards the beam source and picked up by the backscatter electron detector. These backscattered electrons are useful for distinguishing different phases in a material, since atoms of heavier elements (with a correspondingly larger electron cloud) backscatter more strongly and thus appear brighter in the transcribed image (see **Figure 14** below).

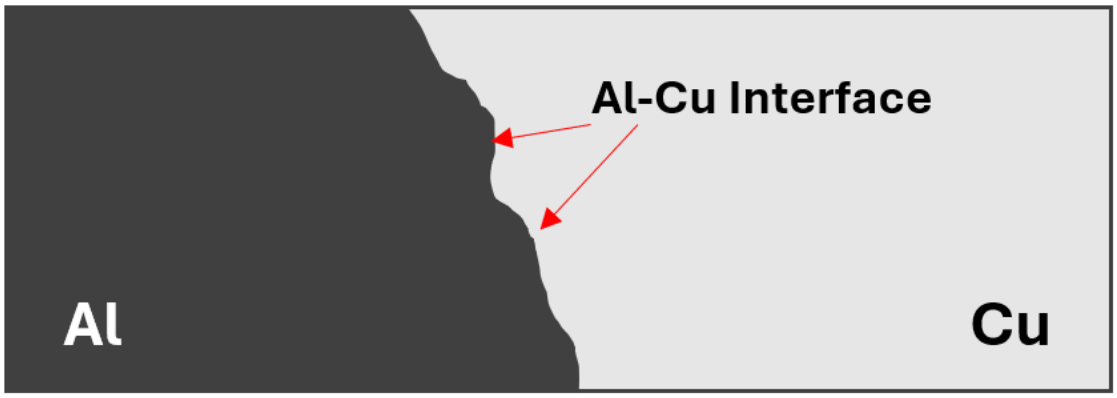

Figure 14: Schematic of a backscatter electron SEM image of an Al-Cu alloy, adapted from work by Xue et al.[24] The Cu section appears brighter on the micrograph due to increased backscatter of electrons.

Secondary electrons are those emitted from the *k*-orbitals of atoms in the sample due to inelastic scattering events. They have low kinetic energies, of the order of tens of eV, and thus originate from atoms close to the sample surface. Detection of these electrons allows clear imaging of surface topography and is usually facilitated by a scintillator-photomultiplier Everhart-Thornley detector.[25]

Although similar to SEM, transmission electron microscopy (TEM) is a separate technique which affords higher magnification of a sample. Rather than scanning across a sample, TEM uses a static beam of electrons to penetrate a very thin (<100 nm) sample.[26] TEM generally uses higher accelerating voltages and consequently can achieve resolutions on the order of angstroms, and even single atoms.[27] Both SEM and TEM imaging are performed under vacuum to prevent scattering of the electron beam by gas molecules in the air.[26]

The internal workings of a TEM differ somewhat from that of an SEM, and are illustrated in **Figure 15**. The electron beam is focused by multiple sets of condenser lenses, transmitted through the sample, and is focused on to a fluorescent screen by the objective and projective lenses, where the transmitted electrons can be detected by a charge-coupled device (CCD) camera and processed to create the electron image.[28] The imaging modes possible for TEM include bright-field (BF) and dark-field (DF). In bright-field imaging, the electrons transmitted directly through the sample are preferentially collected and used to form the image, whereas in dark-field imaging, electrons scattered away from the sample at higher angles are collected.[29] These provide two different levels of contrast and yield complementary information about the structure of a sample.[30]

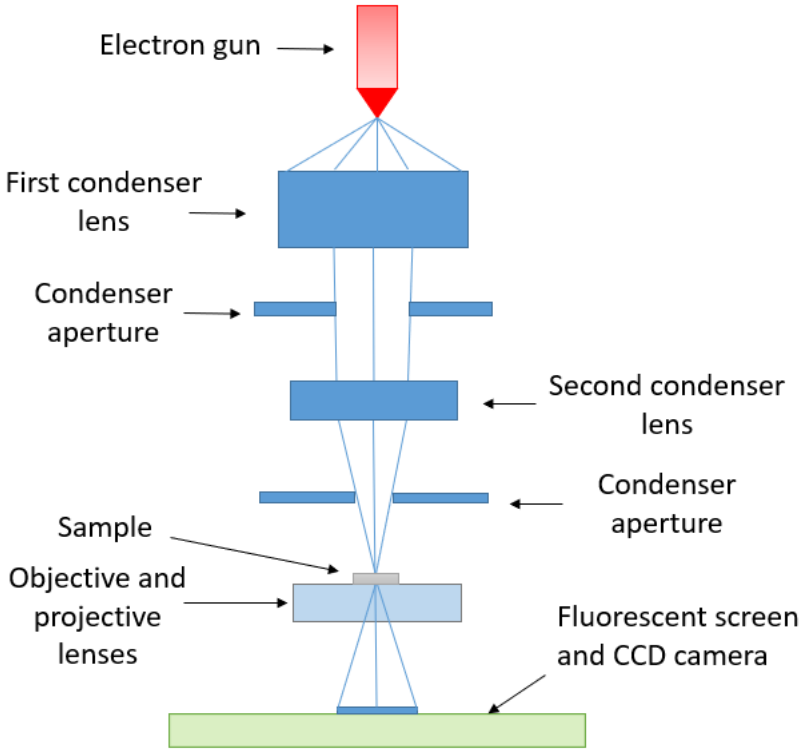

Figure 15: Schematic of a transmission electron microscope, showing the electron gun, condenser lenses and apertures, sample holder, objective lenses, and fluorescent screen.

Scanning electron microscope micrographs in this work were recorded using a JEOL JSM-6610LV microscope with a tungsten filament and energy of 30 kV, with subsequent EDX and elemental mapping carried out via AZtec software (Oxford Instruments).

Transmission electron micrographs in this work were recorded using a JEOL JEM 2100 with a lanthanum hexaboride (LaB_6) filament at 200 kV. Samples were prepared by being dispersed on holey carbon TEM grids. High-resolution TEM was performed on a JEOL ARM200F at the electron Physical Sciences Imaging Centre (ePSIC) at Diamond Light Source, also at an accelerating voltage of 200 kV.

2.4 Thermogravimetric Analysis (TGA)

The technique of thermogravimetric analysis (TGA) focuses on measuring the weight of a sample whilst it is being heated.[31] Increasing the temperature of a sample can cause components within the sample to be driven off as gases, such as adsorbed water. This vaporisation causes a corresponding mass loss which is measured by a sensitive balance within the instrument. At higher temperatures, the thermal decomposition of a sample can be evaluated. For example, metal-organic frameworks (as discussed in **Section 1.3**) often

decompose at temperatures of 200-500 °C, depending on their structure.[32] The organic ligands are generally converted to carbon, with the metal ions forming metal oxide nanoparticles both on and around the amorphous carbon structure.

Inert gases such as Ar or N_2 can be flowed into the furnace and across the sample during the measurement to prevent any mass gain from oxidation. However, oxidative and reductive atmospheres (e.g., O_2 and H_2 respectively) can also be used to examine the redox behaviour of the sample at high temperature.[33] For example, oxidation of a metal would cause an increase in mass as oxygen atoms from the gas flow are captured.

TGA analysis in this report was performed using a TA Instruments Thermogravimetric Analyzer with a platinum pan. N_2 was flowed across the samples at a rate of 60 mL min^{-1}, with a corresponding balance gas flow rate of 40 mL min^{-1} N_2. Temperature was ramped at a rate of 20 °C min^{-1} up to 1000 °C.

2.5 Microwave Plasma Atomic Emission Spectroscopy (MP-AES)

The loading of specific elements on a catalyst can be determined using atomic emission spectroscopy, which typically uses an intense burst of energy to vaporise a sample. The energy input causes the atoms in the sample to emit radiation at a series of characteristic wavelengths that represent electron energy level transitions within that specific element, and the intensities of these spectral lines correspond to the proportion of that element present in the sample.[34] Microwave plasma atomic emission spectroscopy has detection limits down to parts-per-million (ppm), which allows accurate determination of nanoparticle loading on a catalyst support.[35] Samples studied in this report were analysed using an Agilent 4100 spectrometer, which uses a plasma generated from nitrogen gas to initiate the electronic transitions. Samples were digested in 10% aqua regia with an Anton Paar Multiwave 3000 digester and diluted with deionised water to a 0.1 wt% solution. Standard solutions were prepared from Pd and Cu atomic absorption standards of 1000 μg mL^{-1}, with 0.1, 0.5, 1.0, 5, and 10 ppm solutions prepared for Pd, and 0, 10, 25, 50, 100, and 200 ppm solutions prepared for Cu. Calibrations were performed at wavelengths of 324.754 nm and 510.554 nm for Cu, and 340.458 nm and 360.955 nm for Pd, as shown in **Figure 16**.

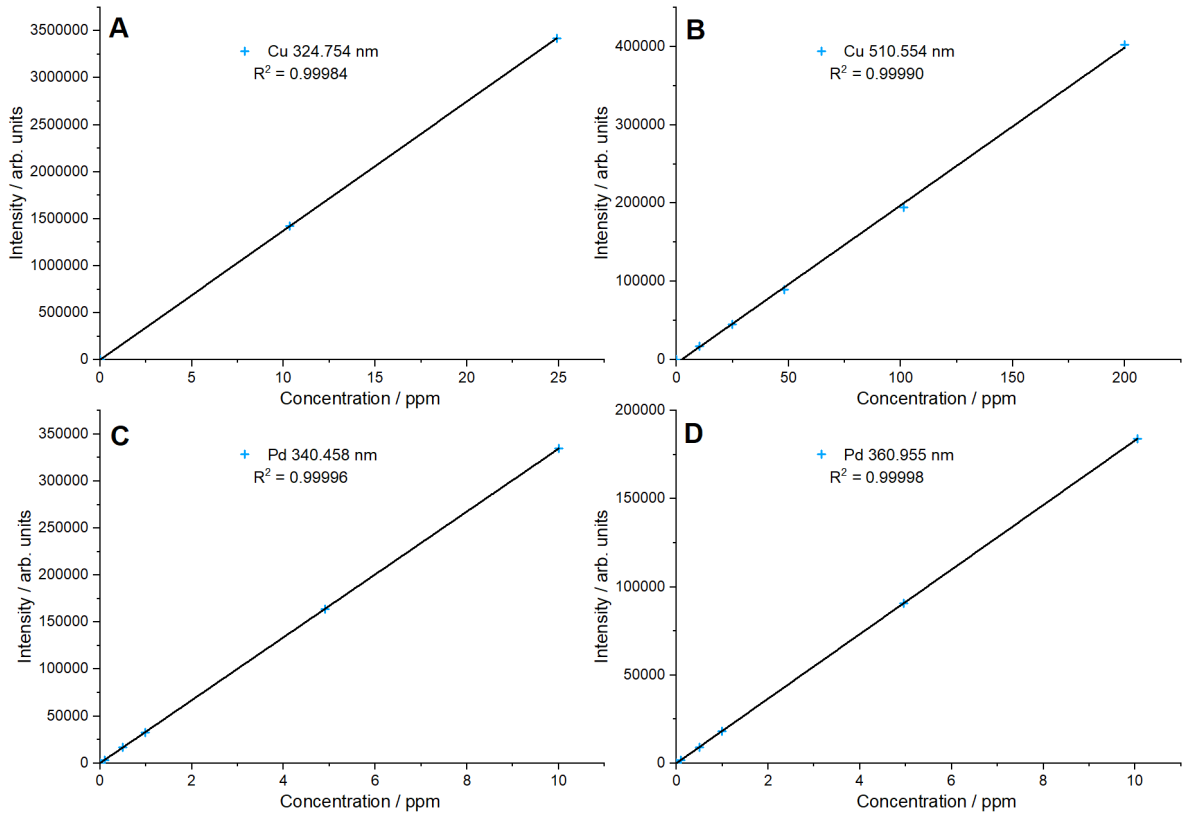

Figure 16: Calibration curves for MP-AES spectroscopy, measured at wavelengths of 324.754 nm and 510.554 nm for Cu, and at 340.458 nm and 360.955 nm for Pd.

2.6 X-Ray Absorption Spectroscopy (XAS)

2.6.1 Background

X-ray Absorption Spectroscopy (XAS) is an intricate spectroscopic technique which provides quantitative information on the structural and electronic properties of a material.[36] The many applications of XAS include examining the effects of dopants on the electronic properties of semiconductors[37], investigating the structure and nature of active sites in a catalyst[38], and quantifying the local lattice distortions arising from alloying in the crystal structure of a metal.[39]

A sample is illuminated with a monochromatic X-ray beam and the change in X-ray absorption coefficient with energy is measured. X-rays are absorbed by a sample if the energy of the incident photons is sufficient to promote an electron from a bound core state into an unoccupied electronic state above the Fermi level, via the photoelectric effect, as seen in **Figure 17**.

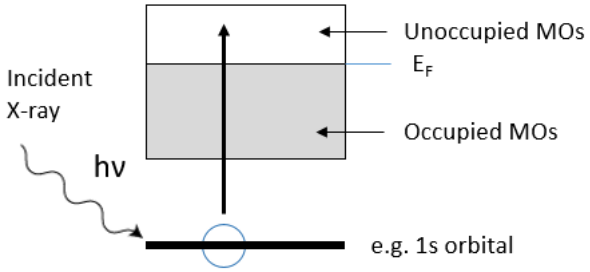

Figure 17: Schematic of X-ray absorption by an atom. An incident X-ray of energy $h\nu$ is absorbed by a core electron and promoted into a suitable unoccupied molecular orbital.

The emission of a photoelectron leaves a hole in the core electronic state, leaving the atom as a whole in an excited state. There are two modes of relaxation back to the ground state: X-ray fluorescence and the Auger effect. In X-ray fluorescence (**Figure 18a**), an electron from a higher-energy core state drops down energy levels to fill the created core-hole, and an X-ray with energy equivalent to the energy gap between those two core states is emitted. In the Auger effect (**Figure 18b**), an electron from a higher core state drops down into the core-hole and a second electron from the higher core state is emitted into the continuum. Both these processes have well-defined energy levels which allow simple identification of both the element and the precise energy level involved in absorption.[40]

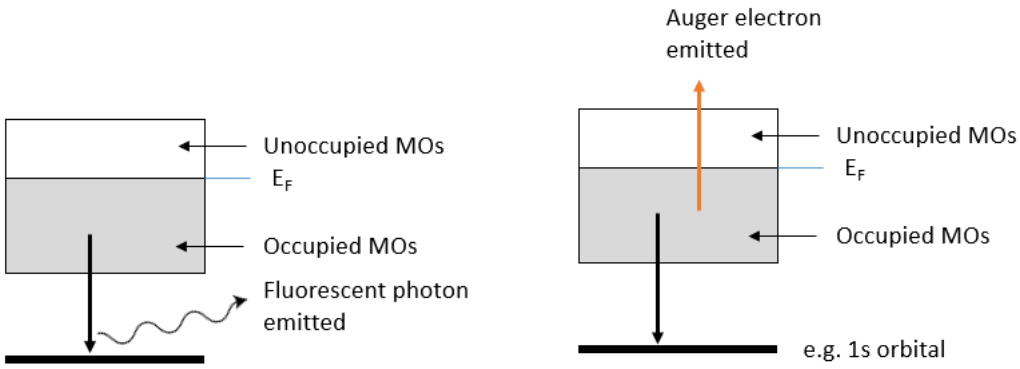

Figure 18: a) Schematic of X-ray fluorescence; b) Schematic of the Auger effect.

2.6.2 The XAS Spectrum

An XAS spectrum shows a series of 'edge steps' in the absorption coefficient, which each correspond to photoelectron emission from deeper core electronic states when the X-ray energy meets a threshold equivalent to the energy of that core state[41] – for example, the Cu K edge (corresponding to exciting electrons from the Cu 1s atomic orbital) becomes accessible at an energy of ~8979 eV.[42] XAS spectra show characteristic oscillations of the absorption coefficient around each edge step, collectively referred to as X-Ray Absorption Fine Structure (XAFS) (**Figure 19**).

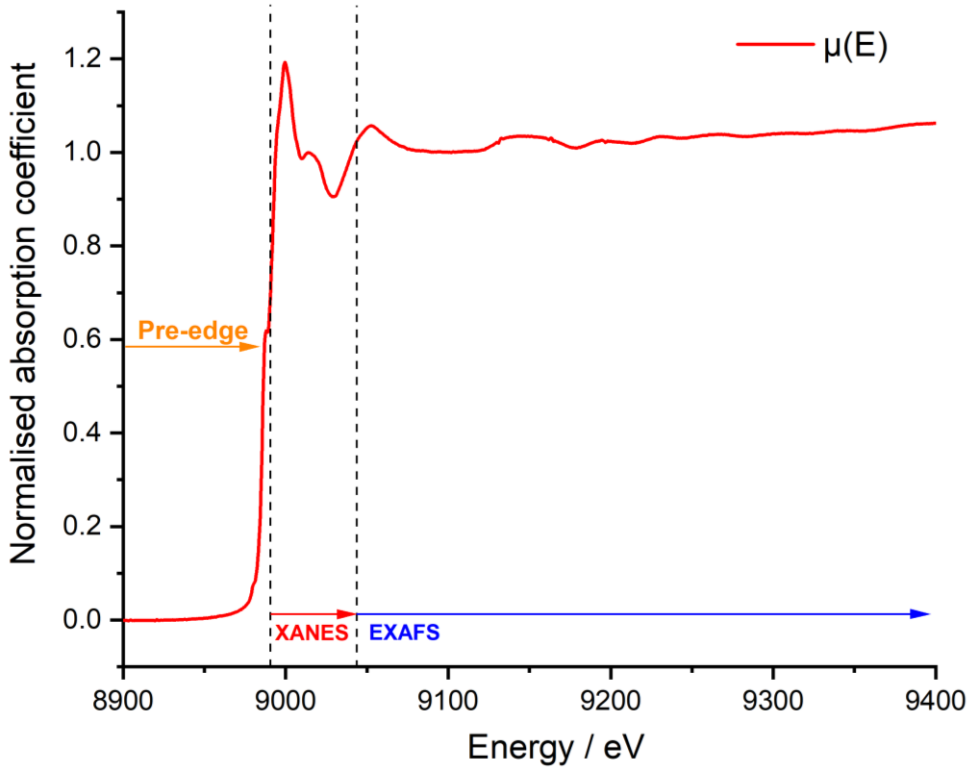

Figure 19: Example illustration of the change in X-ray absorption coefficient at an edge step, using a spectrum of copper(II) oxide (CuO) recorded at the Cu K edge. The pre-edge, XANES, and EXAFS regions are marked.

The oscillations around the edge step are a direct consequence of the wave-like nature of the emitted photoelectron. In condensed matter, upon X-ray absorption by an atom, the emitted photoelectron (modelled as a wave) will be scattered by the neighbouring atoms in the crystal lattice, and some of the wave will be scattered back towards the absorbing atom. That backscattered wave will interfere with the emitted photoelectron wave either constructively or destructively, causing a corresponding increase or decrease in the wavefunction of the emitted photoelectron and a measurable change in the X-ray absorption coefficient. The collective interference from many different scattering paths in a substance combines to produce the observed oscillations.[43]

2.6.3 The XAS Experiment

XAS studies require the X-ray beam to exhibit high stability and intensity across a large energy range, making synchrotron light sources the optimum choice of light source for XAS experiments. Modern synchrotrons operate by accelerating electrons close to the speed of light before containing them in a storage ring. Unfortunately, beamtime is expensive, oversubscribed, and difficult to obtain, which means XAS must be used somewhat sparingly and in conjunction with other characterisation techniques.

2.6.4 Transmission and Fluorescence Measurements

The most common method for performing XAS studies on a sample is to pass the X-ray beam directly through the sample in 'transmission' mode. This works for liquids of known concentration and for solid samples pressed into homogeneous pellets. The intensity of the X-ray beam (I_t) after passing through a sample of thickness x is given by the equation[44]:

$$I_t = I_0 e^{-\mu x} \tag{5}$$

where μ is the absorption coefficient and I_0 is the original intensity of the beam. This rearranges to give the XAS signal μx as:

$$\mu x = -\ln \frac{I_t}{I_0} \tag{6}$$

The intensity of the incident X-ray beam is determined at three points by passing through a sequence of ion chambers. The X-rays passing through the ion chambers ionise some of the inert gas atoms, which are attracted to a charged metal plate. The resultant current can be used to determine the flux of X-rays at that point. The ion chambers measure the intensity of the X-ray beam before it passes through the sample (I_0), after it has passed through the sample (I_t), and after it has passed through both the sample and a reference metal foil (I_{ref}).

The process of X-ray fluorescence is described in **Section 2.6.1**. If the sample being measured has a low loading of the atom being investigated, or if the surrounding material is strongly absorbing, it can become impossible to collect measurements in transmission mode. It is possible to overcome this by collecting in fluorescence mode, in which a solid-state detector is positioned at 90° to the incident X-ray path to collect emitted photons from X-ray fluorescence. However, since fluorescence is an isotropic process, and the detector only covers a small angle of the photons being emitted, the detected flux is much lower than in transmission mode, and thus XAS spectra have to be collected for a longer time to yield an appropriate signal-to-noise ratio.[45]

2.6.5 XANES and EXAFS

The fine structure observed around the edge step can be considered as two regions: X-Ray Absorption Near-Edge Structure (XANES) and Extended X-Ray Absorption Fine Structure (EXAFS). There is no clear boundary between the regions, although XANES is predominantly the peaks and shoulders near the edge step, up to around 50 eV away from the edge, and EXAFS is the oscillations beyond that point as the signal decays.[46] Analysis of the XANES region allows determination of the oxidation state of a sample and the symmetry of the coordination

environment.[47] EXAFS is more useful for quantitative determination of sample geometry, and is discussed in the next section.

2.6.6 The EXAFS Equation

Through a series of approximations, it is possible to mathematically derive an expression for the change in signal caused by an individual scattering atom[48]:

$$\chi_\Gamma(k) = \frac{S_0^2 N_\Gamma F_\Gamma(k)}{2kR_\Gamma^2} e^{-2k^2\sigma_\Gamma^2} e^{-R_\Gamma/\lambda_\Gamma(k)} \sin(2kR_\Gamma + \delta_\Gamma(k)) \quad (7)$$

Consequently, the total calculation for a material is the sum over all possible scattering atoms and paths:

$$\chi(k) = \sum_\Gamma \chi_\Gamma(k) \quad (8)$$

The derivation of the above EXAFS equation requires first modelling the emitted photoelectron as a plane wave scattering off a soft boundary, then modelling as a spherical wave and incorporating a series of additional factors such as the scattering probability $F_\Gamma(k)$, the phase shift from scattering $\delta_\Gamma(k)$, and the amplitude reduction factor S_0^2, an empirical parameter which accounts for multiple electron excitations at the same atom and often lies between 0.8 and 0.9.[49] The Debye-Waller factor σ_Γ^2 is also introduced, which models the mean square radial displacement between the absorbing atom and the scattering atom, essentially accounting for various forms of crystal disorder.[46]

Through computer modelling and knowledge of the scattering amplitude $\chi(k)$ and the phase shift $\delta_\Gamma(k)$, it is possible to use the EXAFS equation to determine the parameters N_Γ, R_Γ and σ_Γ^2: the number of neighbouring atoms, the distance to the neighbouring atoms, and the mean square radial displacement respectively. These parameters can be determined by "fitting" a theoretically-calculated EXAFS signal to the experimentally-determined signal.[48] FEFF is the most widely-used package for fitting EXAFS signals, and works by expanding the Green's function for a muffin-tin potential in terms of the one-electron propagator and the single-term scattering matrix.[50] This allows consideration of all the paths of a given order (e.g., scattering from exactly two atoms in the cluster).[51]

2.6.7 Data Reduction

Acquired XAFS spectra must be processed to aggregate them into a presentable form, which is performed here using the Demeter software package, in which the ATHENA program is used to process the data and analyse the XANES region, and the ARTEMIS program is used to produce

models to fit the EXAFS region of the spectra.[52] The same data reduction procedure was used for all XAFS data presented in this report. Firstly, measured X-ray intensities are converted to absorption coefficient μ(E) and plotted against X-ray energy in eV. The data is then deglitched, removing intensity errors that can arise from small errors in the monochromator. Multiple spectra recorded for a sample can then be averaged into a single spectrum, before the X-ray background is removed using subtraction of pre-edge and post-edge background functions. The value of E_0 for the data is calibrated by examining the first derivative of the absorption coefficient, with the largest value of the derivative indicating the steepest slope of the absorption coefficient and therefore the X-ray edge.[40]

The data is then transformed into *k*-space, showing oscillations in the absorption coefficient as a function of the X-ray wavenumber. Oscillations at higher values of *k* can be amplified using *k*-weighting, where the value of $\chi(k)$ is multiplied by functions of *k*, typically k^2. Applying the Fourier transform to this *k*-space data yields an approximation of the radial distribution of nearest neighbours around the absorbing atom; however, this data must be phase-corrected to yield the true scattering distances; the non-phase-corrected plot will have a systematic error in distances.

The EXAFS region can then be fitted using the ARTEMIS program, using crystallographic information files representing the composition of the sample and any possible scattering paths within the crystal lattice. The amplitude reduction factor S_0^2 is determined using a fit of a reference foil for the absorbing atom. The fitting procedure in Artemis typically yields values of coordination number for each scattering distance in the model, along with variations in bond length compared to the reference crystal lattice, the Debye-Waller factor σ^2, and an R-factor that measures the quality of a fit.[53]

2.6.8 Synchrotrons as an X-ray Source

The quality of data collected during an XAFS experiment is directly affected by the quality of the incident X-rays. Early XAFS experiments used vacuum discharge tubes to generate their X-rays[54], but the technique of XAFS as a whole reached greater prominence during the 1970s, when synchrotron radiation was employed to generate intense, collimated X-ray beams with high brilliance, greatly improving the signal-to-noise ratio of the data.[55]

In the Diamond Light Source synchrotron, located in Harwell, Oxfordshire, a high energy electron beam is produced to generate the X-rays, beginning with thermionic emission of electrons from a high-voltage cathode. These electrons are first accelerated to a potential of 90 keV, then to 100 MeV through use of a linear accelerator, before being injected into a “booster ring”, a small synchrotron inset within the main storage ring of the facility. Bending magnets

within this booster ring gradually accelerate the electrons to an energy of 3 GeV, the operating energy for the main synchrotron. Finally, the 3 GeV electrons are themselves injected into the main storage ring, which has a circumference of 560 metres. This produces a final electron beam that is curved around the facility through the use of fifty more bending magnets. The energy of the beam can be consistently maintained by frequent "topping-up" of electrons through further injection.[56]

When an electron beam is forced to curve away from its straight path, through application of a magnetic field, it will emit electromagnetic radiation in the form of photons, and at the high speeds observed within the storage ring, this is referred to as "synchrotron radiation".[57] The EM radiation generated within Diamond Light Source is in the X-ray range, and can be filtered and focused by an array of optics within beamlines placed around the storage ring, generating intense, well-defined X-ray beams of known energies. This allows a precise variation of energy that enables the absorption edges for an atom to be accurately measured.[44]

If an experiment requires X-rays of increased intensity, this can be achieved by another type of magnetic device known as an insertion device, placed on the straight sections of the storage ring between bending magnets. These insertion devices are typically divided into two types named "wigglers" and "undulators", which use rapidly-alternating magnetic poles to force the electron beam to oscillate sinusoidally. Depending on the configuration of magnets within the insertion device, an X-ray beam of higher energy, flux, or brilliance can be generated compared to those produced at a bending magnet.[58]

All XAFS studies in this work were undertaken on the B18 beamline at Diamond Light Source, Harwell, UK, which uses a double crystal monochromator to access X-ray edges from 2-35 keV.[59] The monochromator is quickly rotated through the Bragg angles for each data point, exploiting the intensity of synchrotron radiation to still obtain a high signal-to-noise ratio for each data point, known as the Quick-EXAFS, or QEXAFS, technique.[60] The Si(111) facet of the monochromator was used for measurements at the Cu K edge, and the Si(311) facet was used for the Pd K edge. All samples were prepared as pellets, and the samples measured in transmission mode were diluted with cellulose to optimise the edge step of the particles.

2.7 Ultraviolet-visible spectroscopy (UV/vis)

UV/vis spectroscopy is a technique used to determine the presence of electronic transitions in a sample via the absorption of light in the ultraviolet and visible ranges of the electromagnetic spectrum.[61] Systems of conjugated double bonds in molecules such as aromatics essentially form a quantum-mechanical particle-in-a-box, in which electrons can be excited to higher energy levels via the absorption of a photon with a suitable energy (and consequently wavelength). When a chemical reaction interferes with the conjugated system in a molecule, the length of the "box", or potential well, is altered, consequently affecting the energy levels, and thus changing the wavelengths of light absorbed by the sample. This makes UV/vis spectroscopy an excellent technique for tracking the rate of chemical reactions.[62]

2.7.1 Reduction of 4-nitrophenol to 4-aminophenol

One such reaction that can be investigated in real-time is the reduction of 4-nitrophenol to 4-aminophenol. The reaction can be easily achieved using sodium borohydride ($NaBH_4$) as a reducing agent, and the reaction scheme is depicted in **Figure 20**.

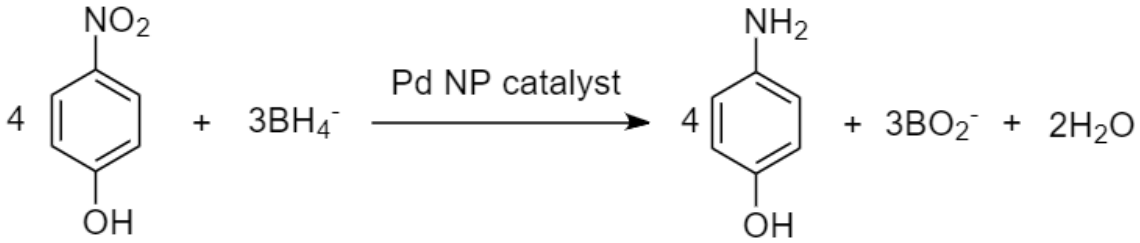

Figure 20: Reaction scheme of the reduction of 4-nitrophenol with borohydride ions to yield 4-aminophenol.

Upon contact with $NaBH_4$, the borohydride ions immediately deprotonate the phenol group, generating the 4-nitrophenolate ion, which has a bright yellow colour and displays a clear absorbance at $\lambda = 400\ \mathrm{nm}$, which can easily be tracked by UV/vis spectroscopy.[63] As the 4-nitrophenol is converted into 4-aminophenol, the peak at $\lambda = 400\ \mathrm{nm}$ will slowly decrease, with a corresponding increase being observed in a peak at $\lambda = 300\ \mathrm{nm}$ that corresponds to the absorbance of 4-aminophenol. Repeated scanning over time allows a kinetic analysis to be performed on the reaction.

Using an excess of $NaBH_4$ as a reducing agent allows the assumption that its concentration is constant over the timescale of the reaction, which makes the reaction pseudo-first-order with respect to the concentration of 4-nitrophenol.[64] Therefore, a plot of $ln(C_t/C_0)$ against time,

where C_0 is the initial concentration of 4-nitrophenol and C_t the concentration at time *t*, gives a linear plot with a gradient of *–k*, where *k* is the rate constant for the reaction.

The concentration of 4-nitrophenol at a given time can be determined from the absorbance of the peak at $\lambda = 400\ \mathrm{nm}$ by the Beer-Lambert law, which relates the absorbance of a sample to the path length of the attenuated light and the concentration of the absorbing species[65]:

$$log_{10}(I_0/I) = A = \varepsilon lc \quad (9)$$

where I_0 is the initial intensity of the light being absorbed by a sample, I is its measured intensity after passing through the sample across a known path length l, A is the absorbance of the sample, which measures the amount of attenuation of the light passing through it, and ε is the molar extinction coefficient, which has units of $mol^{-1}\ dm^3\ cm^{-1}$, and for this 4-NP assay has been calibrated as 18873 $mol^{-1}\ dm^3\ cm^{-1}$.[66]

All UV/vis spectra in this report were recorded using a Shimadzu UV-1800 spectrophotometer, using polystyrene cuvettes with a path length of 1 cm. 0.3 mL of 0.0397 M $NaBH_4$ was added to 1 mg of PdCu/Cu_2O catalyst, before 2.7 mL of 0.00018 M 4-nitrophenol solution was added. Scans from 600-300 nm were repeated every 15 seconds until the reaction was observed to be complete.

2.8 Adsorption Isotherms and Surface Area Analysis (BET)

Adsorption is the adhesion of molecules to a surface or interface via the formation of a chemical bond (chemisorption) or van der Waals interaction (physisorption) between the adsorbate and the surface.[67] Adsorption can occur in single-layer or multi-layered forms, the latter of which sees the first layer of adsorbate either physisorbed or chemisorbed to the surface, and successive layers physisorbed by weaker non-covalent interactions.[68,69]

Isotherms are theories used to explain adsorption as a function of surface coverage at a fixed temperature. Multi-layer adsorption is commonly characterised by the Brunauer-Emmett-Teller (BET) isotherm[70], which assumes that multiple layers of adsorbates can all be modelled by the simpler Langmuir isotherm, used to characterise monolayer surface coverage.[71] There are some limitations to the BET model, since the theory assumes that the surface of the material is entirely homogeneous, that all adsorption sites on the surface of the material are equivalent, and that exactly one molecule adsorbs per possible adsorption site, none of which are strictly true in practice.[72,73]

The form of the BET isotherm can be seen in the following equation:

$$\frac{X}{X_m} = \frac{C(p/p_0)}{(1 - p/p_0)\,(1 + (C - 1)\,p/p_0)} \tag{10}$$

where X and X_m are the total mass adsorbed and the monolayer mass adsorbed at a relative vapour pressure of p/p_0 respectively. C is the BET constant, which indicates the relative lifetimes of molecules in the first layer to those in successive layers, and is equivalent to:

$$C = \exp\left(\frac{E_1 - L}{RT}\right) \tag{11}$$

where E_1 is the heat of adsorption in the first layer, L is the latent heat of condensation, T is the temperature, and R is the ideal gas constant.

Equation 10 can be rewritten as the following:

$$\frac{1}{v[(p_0/p) - 1]} = \frac{C - 1}{v_m C}\left(\frac{p}{p_0}\right) + \frac{1}{v_m C} \tag{12}$$

where v and v_m are the total and monolayer volumes of gas adsorbed respectively. The expression in Equation 12 is plotted on the y-axis against the relative vapour pressure in a BET plot. From the gradient m and y-intercept b of a suitable linear regression line taking the form $y = mx + b$, the values of v_m and the BET constant C can be derived as follows:

$$v_m = \frac{1}{m - b} \tag{13}$$

$$C = 1 + \frac{m}{b} \tag{14}$$

Finally, the total BET surface area S_{tot} is given by:

$$S_{tot} = \frac{v_m N s}{V} \tag{15}$$

where s is the adsorption cross-section of the adsorbate gas, V the adsorbate's molar volume, and N is Avogadro's constant.

Highly porous materials such as metal-organic frameworks are often characterised by their BET surface area, which can be thousands of square metres per gram of material.[74] The measurement conventionally uses a simple molecule as an adsorbate, such as N_2 or CO_2.[75] For nitrogen adsorption measurements, the sample is immersed in liquid nitrogen to hold it at 77 K, the boiling point of N_2, maintaining a constant temperature to record the isotherm.[74]

All MOF samples analysed in this work were degassed at 423 K overnight with a FloVAC Degasser before BET surface area measurements were obtained via nitrogen adsorption at 77 K with a Quantachrome Quadrasorb analyser.

2.9 Microreactor-based Catalytic Testing

2.9.1 CATLAB Microreactor

Catalytic testing of the nanocomposites synthesised in this work was performed using a Hiden CATLAB microreactor connected to a Hiden Analytical QGA mass spectrometer, allowing samples to undergo a pre-set temperature profile whilst reactant gases are flowed across the catalyst surface. The mass spectrometer allows *in situ* monitoring of the output gases from the catalyst bed, enabling quantification of reaction conversion and selectivity. A schematic of the microreactor, mass flow controllers (MFCs), and the mass spectrometer is shown in **Figure 21**.

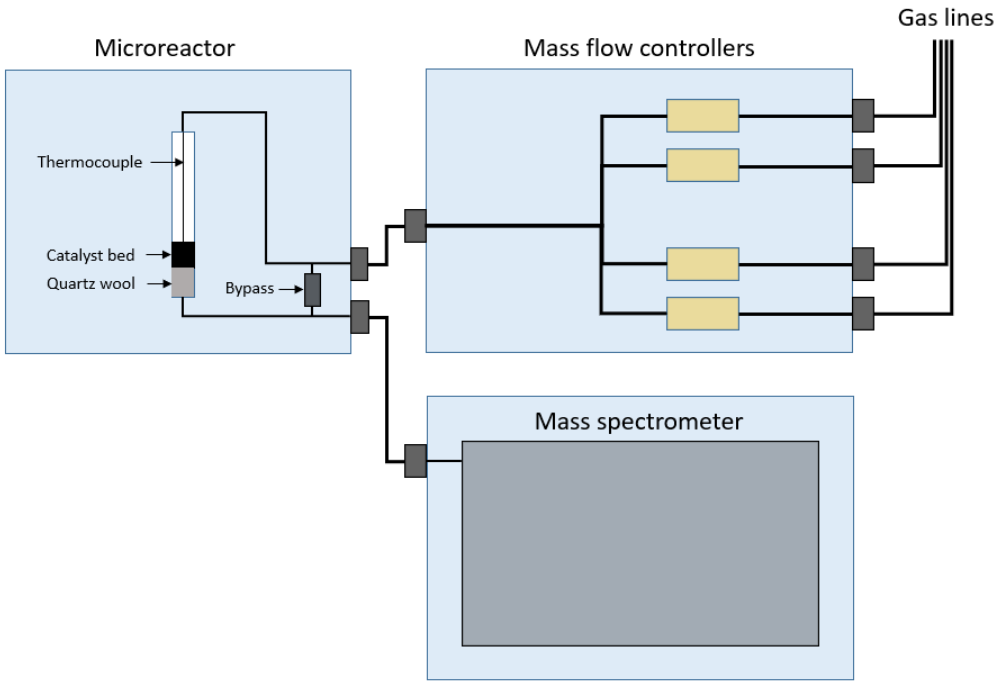

Figure 21: Schematic of the CATLAB microreactor setup, showing the catalyst bed with quartz wool packing and a thermocouple, the mass flow controllers, and the mass spectrometer used to analyse the resultant gas stream.

The mass flow controllers are employed to react to the pressure from a gas line input and use a proportional control valve to provide a pre-set and steady flow of gas. The flow rates can be adjusted during testing, for example to change the composition of the testing atmosphere. When active testing is not taking place, a constant flow rate of inert gas such as helium or argon is maintained throughout the system. Within the microreactor, the sample to be tested is loaded into a quartz capillary, the base of which is packed with quartz wool to keep the catalyst bed in place. The catalyst bed itself is ground into small particles, with a series of sieves used to obtain a fixed mass of sample with a set distribution of particle diameters, such as the range

125 – 250 µm. This ensures that gas flows as evenly as possible through the catalyst bed and that the whole catalyst comes into contact with the reactant gases.

The furnace in the microreactor can produce temperatures of up to 1000 °C, at temperature ramp rates of 0.1-20 °C min^{-1}. The temperature of the system is set using a proportional-integral-derivative (PID) controller connected to a thermocouple in contact with the catalyst bed, allowing precise control of the experimental conditions. The microreactor also features a bypass setting that can be used to switch gas flow away from the catalyst bed when necessary.

In this work, the Pd/CuBTC composites produced in Chapter 3 and the PdCu/Cu_2O nanocomposites synthesised in Chapter 4 were investigated as catalysts for CO oxidation using the CATLAB setup. A 5 °C min^{-1} temperature ramp rate was employed across the range 40-200 °C for the PdCu/Cu_2O nanocomposites, and across the range 40-350 °C for the Pd/CuBTC composites. A pellet press and sieve set were used to obtain 100 mg of catalyst in the 125 – 250 µm sieve fraction, which was used to form a catalyst bed in a quartz capillary packed at both ends with quartz wool. Catalytic testing was performed using a total gas flow rate of 70 mL min^{-1}, with 50 mL min^{-1} of 10% CO/He, an excess of 5 mL min^{-1} O_2, and 15 mL min^{-1} Ar. Exhaust gases were fed into a Hiden QGA mass spectrometer, allowing tracking of outlet composition for CO at m/z = 28, O_2 at m/z = 32, Ar at m/z = 40, He at m/z = 4, and CO_2 at m/z = 44.

2.9.2 Mass Spectrometry (MS)

Mass spectrometry (MS) is a common analytical technique that is used here to quantify the composition of the gas stream output from the CATLAB microreactor. The gases are fed into the spectrometer, and the molecules are ionised via bombardment of electrons from a tungsten filament, accelerated using an electric field, and passed into a quadrupole mass analyser.[76] The quadrupole setup uses an array of four parallel metal rods to generate an oscillating electric field, which can be calibrated such that only ions with a specific mass-to-charge (m/z) ratio can successfully match the oscillations of the field and pass through the quadrupolar array to the detector. Variation of the electric field then allows detection at all desired m/z values.[77] One weakness of this setup is that only pre-set m/z values are analysed; a mass spectrometer based on deflection using a magnetic field would instead scan through the whole m/z range.[78]

2.10 References

1 O. M. Yaghi and H. Li, *J. Am. Chem. Soc.*, 1995, **117**, 10401–10402.

2 W. Chen, L. Du and C. Wu, in *Metal-Organic Frameworks for Biomedical Applications*, Elsevier Inc., 2020, pp. 141–157.

3 J. L. Crane, K. E. Anderson and S. G. Conway, *J. Chem. Educ.*, 2015, **92**, 373–377.

4 R. A. Dodson, A. P. Kalenak and A. J. Matzger, *J. Am. Chem. Soc.*, 2020, **142**, 20806–20813.

5 K. R. Wright, K. Nath and A. J. Matzger, *Angew. Chemie - Int. Ed.*, 2022, **61**, 1–5.

6 H. Woo, A. M. Devlin and A. J. Matzger, *J. Am. Chem. Soc.*, 2023, **145**, 18634–18641.

7 K.-S. Lin, A. K. Adhikari, C.-N. Ku, C.-L. Chiang and H. Kuo, *Int. J. Hydrogen Energy*, 2012, **37**, 13865–13871.

8 J. Bae, J. S. Choi, S. Hwang, W. S. Yun, D. Song, J. Lee and N. C. Jeong, *ACS Appl. Mater. Interfaces*, 2017, **9**, 24743–24752.

9 R. Adams, C. Carson, J. Ward, R. Tannenbaum and W. Koros, *Microporous Mesoporous Mater.*, 2010, **131**, 13–20.

10 S. Rogers, R. Catlow, D. Gianolio, P. Wells and N. Dimitratos, *Faraday Discuss.*, 2018, 1–12.

11 R. Javed, M. Zia, S. Naz, S. O. Aisida, N. ul Ain and Q. Ao, *J. Nanobiotechnology*, 2020, **18**, 1–15.

12 A. Villa, D. Wang, G. M. Veith, F. Vindigni and L. Prati, *Catal. Sci. Technol.*, 2013, **3**, 3036–3041.

13 G. F. Tierney, S. Alijani, M. Panchal, D. Decarolis, M. B. de Gutierrez, K. M. H. Mohammed, J. Callison, E. K. Gibson, P. B. J. Thompson, P. Collier, N. Dimitratos, E. C. Corbos, F. Pelletier, A. Villa and P. P. Wells, *ChemCatChem*, 2021, **13**, 5121–5133.

14 J. A. Lopez-Sanchez, N. Dimitratos, P. Miedziak, E. Ntainjua, J. K. Edwards, D. Morgan, A. F. Carley, R. Tiruvalam, C. Kiely and G. J. Hutchings, *Phys. Chem. Chem. Phys.*, 2008, **10**, 1921–1930.

15 M. Birkholz, in *Thin Film Analysis by X-Ray Scattering*, Wiley-VCH, 2006.

16 A. L. Patterson, *Phys. Rev.*, 1939, **56**, 978–982.

17 U. Holzwarth and N. Gibson, *Nat. Nanotechnol.*, 2011, **6**, 534.

18 A. Lipson, S. G. Lipson and H. Lipson, *Optical Physics*, Cambridge University Press, 4th ed., 2011.

19 R. Heintzmann and G. Ficz, *Briefings Funct. Genomics Proteomics*, 2006, **5**, 289–301.

20 I. Khan, K. Saeed and I. Khan, *Arab. J. Chem.*, 2019, **12**, 908–931.

21 D. J. Griffiths, *Introduction to Quantum Mechanics*, Prentice-Hall, 1995.

22 S. Amelinckx, D. van Dyck, J. van Landuyt and G. van Tendeloo, *Electron Microscopy: Principles and Fundamentals*, Wiley-VCH, 1997.

23 J. Goldstein, D. E. Newbury, D. C. Joy, C. E. Lyman, P. Echlin, E. Lifshin, L. Sawyer and J. R. Michael, *Scanning Electron Microscopy and X-ray Microanalysis*, 2003, vol. 44.

24 P. Xue, B. L. Xiao, D. R. Ni and Z. Y. Ma, *Mater. Sci. Eng. A*, 2010, **527**, 5723–5727.

25 W. Zhou, R. Apkarian, Z. L. Wang and D. Joy, in *Scanning Microscopy for Nanotechnology*, Springer-Verlag New York, 2007.

26 Z. Luo, *A Practical Guide to Transmission Electron Microscopy - Volume 1: Fundamentals*, Momentum Press Engineering, New York, 2016.

27 A. V Crewe, J. Wall and J. Langmore, *Science (80-.).*, 1970, **168**, 1338–1340.

28 B. Fultz and J. Howe, *Transmission Electron Microscopy and Diffractometry of Materials*, Springer, Heidelberg, 2012.

29 N. D. Klein, K. R. Hurley, Z. V. Feng and C. L. Haynes, *Anal. Chem.*, 2015, **87**, 4356–4362.

30 Z. Liu, L. Tian, S. Liu and L. Waller, *J. Biomed. Opt.*, 2014, **19**, 1.

31 A. E. . Newkirk, *Anal. Chem.*, 1960, **32**, 1558–1563.

32 C. Healy, K. M. Patil, B. H. Wilson, L. Hermanspahn, N. C. Harvey-Reid, B. I. Howard, C. Kleinjan, J. Kolien, F. Payet, S. G. Telfer, P. E. Kruger and T. D. Bennett, *Coord. Chem. Rev.*, 2020, **419**, 213388.

33 M. Athar, P. Rzepka, D. Thoeny, M. Ranocchiari and J. Anton Van Bokhoven, *RSC Adv.*, 2021, **11**, 38849–38855.

34 H. G. Joosten, A. Golloch, J. Flock and S. Killewald, *Atomic Emission Spectrometry: AES - Spark, Arc, Laser Excitation*, 2020.

35 V. Balaram, *Microchem. J.*, 2020, **159**, 105483.

36 E. D. Crozier, *Nucl. Instruments Methods Phys. Res. Sect. B Beam Interact. with Mater. Atoms*, 1997, **133**, 134–144.

37 M. D. Watson, J. Collins-Mcintyre, L. R. Shelford, A. I. Coldea, D. Prabhakaran, S. C. Speller, T. Mousavi, C. R. M. Grovenor, Z. Salman, S. R. Giblin, G. Van Der Laan and T. Hesjedal, *New J. Phys.*, 2013, **15**, 103016.

38 F. M. F. De Groot, *Top. Catal.*, 2000, **10**, 179–186.

39 H. S. Oh, D. Ma, G. P. Leyson, B. Grabowski, E. S. Park, F. Kormann and D. Raabe, *Entropy*, 2016, **18**, 1–9.

40 M. Newville, *Fundamentals of XAFS*, University of Chicago, 2004.

41 Y. Joly and S. Grenier, in *X-Ray Absorption and X-Ray Emission Spectroscopy: Theory and Applications*, eds. J. A. van Bokhoven and C. Lamberti, John Wiley and Sons, 2016.

42 A. Gaur, D. Shrivastava and K. Joshi, in *Journal of Physics: Conference Series*, 2009, vol. 190.

43 D. C. Koningsberger, B. L. Mojet, G. E. Van Dorssen and D. E. Ramaker, *Top. Catal.*, 2000, **10**, 143–155.

44 D. Gianolio, in *X-Ray Absorption and X-Ray Emission Spectroscopy: Theory and Applications*, eds. J. A. van Bokhoven and C. Lamberti, John Wiley and Sons, 2016.

45 M. Newville, *Rev. Mineral. Geochemistry*, 2014, **78**, 33–74.

46 S. Calvin, *XAFS for Everyone*, CRC Press, 2014.

47 Y. Iwasawa, K. Asakura and M. Tada, *XAFS Techniques for Catalysts, Nanomaterials, and Surfaces*, 2017.

48 B. Ravel, in *X-Ray Absorption and X-Ray Emission Spectroscopy: Theory and Applications*, eds. J. A. van Bokhoven and C. Lamberti, 2016.

49 G. Vlaic and L. Olivi, *Croat. Chem. Acta*, 2004, **77**, 427–433.

50 B. Ravel, *J. Synchrotron Radiat.*, 2015, **22**, 1258–1262.

51 J. J. Rehr, R. C. Albers and S. I. Zabinsky, *Phys. Rev. Lett.*, 1992, **69**, 3397–3400.

52 B. Ravel and M. Newville, *J. Synchrotron Radiat.*, 2005, **12**, 537–541.

53 H. Husain, M. Sulthonul, B. Hariyanto, C. Cholsuk and S. Pratapa, *Mater. Today Proc.*, 2020, **44**, 3296–3300.

54 H. Fricke, *Phys. Rev.*, 1920, **16**, 202–215.

55 F. W. Lytle, *J. Synchrotron Radiat.*, 1999, **6**, 123–134.

56 G. Materlik, T. Rayment and D. I. Stuart, *Philos. Trans. R. Soc. A Math. Phys. Eng. Sci.*, 2015, **373**, 20130161.

57 C. J. Rhodes, *Sci. Prog.*, 2015, **98**, 192–200.

58 K. Wille, *Cern Accel. Sch.*, 1996, 61–75.

59 A. J. Dent, G. Cibin, S. Ramos, A. D. Smith, S. M. Scott, L. Varandas, M. R. Pearson, N. A. Krumpa, C. P. Jones and P. E. Robbins, *J. Phys. Conf. Ser.*, 2009, **190**, 1–5.

60 M. Nachtegaal, O. Müller, C. König and R. Frahm, in *X-Ray Absorption and X-Ray Emission Spectroscopy: Theory and Applications*, 2015, vol. 1–2, pp. 155–183.

61 H.-H. Perkampus, in *UV-VIS Spectroscopy and Its Applications*, Springer-Verlag, Heidelberg, 1992, pp. 3–10.

62 H.-H. Perkampus, in *UV-VIS Spectroscopy and Its Applications*, Springer-Verlag, Heidelberg, 1992, pp. 165–214.

63 R. D. Neal, Y. Inoue, R. A. Hughes and S. Neretina, *J. Phys. Chem. C*, 2019, **123**, 12894–12901.

64 J. Feng, L. Su, Y. Ma, C. Ren, Q. Guo and X. Chen, *Chem. Eng. J.*, 2013, **221**, 16–24.

65 T. G. Mayerhöfer, S. Pahlow and J. Popp, *Chemphyschem*, 2020, **21**, 2029–2046.

66 S. M. Rogers, *Designing Metal Nanoparticles for Catalysis*, University College London, 2017.

67 P. Atkins and J. De Paula, *Physical Chemistry: Thermodynamics, Structure, and Change*, Oxford University Press, 10th ed., 2014.

68 F. B. Scheufele, A. N. Módenes, C. E. Borba, C. Ribeiro, F. R. Espinoza-Quiñones, R. Bergamasco and N. C. Pereira, *Chem. Eng. J.*, 2016, **284**, 1328–1341.

69 D. J. Lavrich, S. M. Wetterer, S. L. Bernasek and G. Scoles, *J. Phys. Chem. B*, 1998, **102**, 3456–3465.

70 G. Fagerlund, *Matériaux Constr.*, 1973, **6**, 239–245.

71 I. Langmuir, *J. Am. Chem. Soc.*, 1918, **40**, 1361–1403.

72 W. G. McMillan and E. Teller, *J. Phys. Chem.*, 1951, **55**, 17–20.

73 K. S. W. Sing, *Adv. Colloid Interface Sci.*, 1998, **76–77**, 3–11.

74 K. S. Walton and R. Q. Snurr, *J. Am. Chem. Soc.*, 2007, **129**, 8552–8556.

75 F. Ambroz, T. J. Macdonald, V. Martis and I. P. Parkin, *Small Methods*, 2018, **2**, 1–17.

76 E. de Hoffmann and V. Stroobant, in *Mass Spectrometry: Principles and Applications*, John Wiley & Sons, Ltd, Chichester, 3rd ed., 2007, pp. 88–99.

77 R. E. March, *J. Mass Spectrom.*, 1997, **32**, 351–369.

78 E. de Hoffmann and V. Stroobant, in *Mass Spectrometry: Principles and Applications*, John Wiley & Sons, Ltd, Chichester, 2007, pp. 143–157.

Chapter 3 Preparation of Nanoparticle-MOF Composites

3.1 Introduction

Supported metal nanoparticles and metal-organic frameworks both have highly tunable properties and catalytic applications. Consequently, there has been substantial research into the use of MOFs as nanoparticle supports in their own right. This combination is often termed a nanoparticle-MOF (NP-MOF) composite, and multiple synthetic methods have been developed to finely control the subsequent nanocomposites and their catalytic behaviours.

We can consider the "ship-in-a-bottle" approach, named because of its analogy to the popular modelling hobby. This method focuses on synthesising unsupported metal nanoparticles, then adding a combination of metal ions and ligands to grow a MOF around the nanoparticles, effectively encapsulating them within the highly-porous MOF structure.[1] This encapsulation method also allows fine control over the resultant crystal size by using a monodentate capping reagent, or modulator, to control the nucleation rate of the MOF. For example, Wang *et al*.[2] used acetic acid to compete with the dicarboxylic acid linkers in the UiO-66 MOF, as part of the synthesis of Pt@UiO-66 nanocomposites (where the @-sign specifically indicates the encapsulation of Pt within the MOF pores). They reported that controlling crystallite size through modulation predictably facilitates a shorter diffusion path for reactant molecules, which led to enhanced catalytic performance for the production of imines from nitrobenzene, but the encapsulation of the nanoparticles within the MOF also allows exploitation of the MOF's ability to act as a molecular sieve. This provides simultaneous control of reaction selectivity[3,4], so both parts of the NP-MOF composite are contributing to beneficial catalytic behaviour.

An alternate school of NP-MOF nanocomposite synthesis is the "bottle-around-ship" approach, where the MOF is prepared initially, then a metal nanoparticle precursor is introduced to form the NPs either on the MOF surface or within its cavities. Various approaches within this framework include solution methods, chemical vapour deposition[5,6] and solid grinding[7,8]. Two main solution methods are used: solution impregnation, where the MOF is mixed with a solution of metal nanoparticles or their precursors and the metal is deposited on the surface or in the pores; and a double-solvent approach, which uses a small volume of aqueous metal precursor solution and a large amount of organic solvent, utilising capillary pressure and hydrophilic interactions to introduce the metal precursor into the pores of the MOF rather than on the

surface. Once immobilised on or in the MOF, the metal precursor compounds can be further reduced (e.g., using H_2) to yield metal NPs.[9]

Due to the high pore volumes of metal-organic frameworks, incipient wetness impregnation, as described in **Section 1.2.3.1**, is a common method in the preparation of NP-MOF composites. Sabo *et al.*[10] added dropwise a solution of $Pd(acac)_2$ in chloroform to MOF-5 before reducing under hydrogen to yield a Pd/MOF-5 composite that functions as a reusable catalyst for styrene hydrogenation. The catalyst was able to adsorb more hydrogen than MOF-5 alone, and displayed a higher activity for the reaction than Pd NPs on an activated carbon support.

Cao *et al*.[11] used a similar method with aqueous solutions of $NiCl_2$ and K_2PtCl_6 to synthesise bimetallic NiPt NPs in the pores of MIL-101 for use in the dehydrogenation of hydrazine. Various Ni:Pt ratios were investigated, with a $Ni_{88}Pt_{12}$@MIL-101 composition yielding the highest activity for any catalyst then reported for hydrazine dehydrogenation.

Aijaz *et al.*[12] used the double-solvent approach to synthesise ultrafine Pt NPs inside MIL-101 MOF, using aqueous H_2PtCl_6 and *n*-hexane as the organic solvent before reducing in H_2/He at 200 °C. These Pt NPs had an average size of 1.8 nm, and were therefore sufficiently small to fit into the pores of MIL-101 (2.9-3.4 nm)[13]. This method was shown to minimise nanoparticle aggregation, and very few NPs were observed on the surface of the MOF rather than in the pores. These composites were demonstrated to be active for CO oxidation with no structural change following the reaction.

Zhu *et al.*[14] also used the double-solvent approach to produce bimetallic AuNi nanoparticles in MIL-101, producing the NPs via reduction with $NaBH_4$ rather than H_2. They showed that a high concentration of $NaBH_4$ was required to avoid agglomeration of NPs on the surface of the MOF: 0.6 M $NaBH_4$ was required to avoid metal NP precursor molecules diffusing out of the pores and on to the surface. These samples were tested for catalytic hydrolysis of ammonia borane (NH_3BH_3), which is a common method of hydrogen generation[15]. Due to lower amounts of agglomeration leading to a smaller average NP size, the samples with AuNi NPs confined to the MOF pores were significantly more active than the samples with NPs on the surface. The bimetallic NPs also displayed a higher activity than either Au@MIL-101 or Ni@MIL-101 samples, indicating that synergistic effects between the Au and Ni elements in the bimetallic NPs are contributing to increased catalytic performance.

As well as these two-step methods, where the MOF and the NPs are produced separately, there have been multiple successful applications of a “one-pot” method for the generation of NP-MOF composites, where the precursor solutions are all directly mixed, and the structure self-assembles accordingly. For example, He *et al.*[16] combined $HAuCl_4$, zinc nitrate

hexahydrate, and a benzene-dicarboxylic acid linker in a mixture of polyvinylpyrrolidone, DMF, and ethanol to synthesise what are effectively core-shell nanoparticles of Au encapsulated by MOF-5. Control of reaction conditions allowed the gold nanoparticles to be swiftly formed by reduction with DMF, and then be capped and stabilised by the PVP present. The presence of ethanol caused a change in metal coordination to encourage MOF-5 to preferentially nucleate on the surface of the PVP-capped Au NPs, to produce an outer shell that could be varied in thickness from ~3-69 nm, before the PVP and DMF were removed to yield an Au@MOF-5 nanocomposite that served as a highly-specific sensor for CO_2 molecules in surface-enhanced Raman scattering.

A similar idea is seen in work by Kuo *et al.*[17], where Pd nanoparticles were coated with a sacrificial layer of Cu_2O to form initial core-shell nanoparticles, with this Cu_2O layer both providing a clean surface for the formation of a ZIF-8 MOF, and subsequently being etched away by the protons that form during the ZIF-8 growth, leaving another "yolk-shell" type nanocomposite of Pd@ZIF-8, but here without the complication of polymeric capping agents such as PVP, which generally require careful removal during nanocomposite synthesis. This nanocomposite was then applied as a catalyst for the hydrogenations of ethylene, cyclohexene and cyclooctene, with the size of the ZIF-8 shell acting as a control for size selectivity in the reaction products.

The above examples ultimately demonstrate the broad scope within the field of NP-MOF composites: providing a means to utilise the varied catalytic properties of monometallic and bimetallic nanoparticles through use of a versatile and tweakable support structure. The precise location of the nanoparticles on or within the MOF support has a tangible effect on reaction rate and selectivity, and the small dimensions of both the NPs and the MOF crystals allows both structures to be involved in reaction mechanisms, e.g., via the molecular sieving of reactant or product molecules using a porous MOF structure whilst the molecules diffuse to a catalytic nanoparticle site.

In this chapter, composites based on Pd nanoparticles and CuBTC MOF are synthesised via an adapted sol-immobilisation method. The resultant composites are characterised by a range of techniques, including X-ray absorption spectroscopy, to investigate the structures of both the nanoparticles and the support material. The synthetic method is then varied to generate similar Pd/CuMOF composites both by using a methanol-based synthesis and an alternative CuTPA MOF support.

3.2 Experimental Details

Preparation of CuBTC MOF: 1,3,5-benzenetricarboxylic (BTC) acid (1.0 g) was dissolved in 30 mL of a 1:1 (by volume) mixture of ethanol and N,N-dimethylformamide (DMF). Copper (II) nitrate trihydrate (2.077 g) was dissolved in a separate solution of 15 mL water. The two solutions were mixed together, and stirred for 10 minutes, before the resulting solution was transferred into a Teflon-lined stainless steel autoclave and heated at 393 K for 10 h. The reaction vessel was then allowed to cool to room temperature and the resulting blue crystals were isolated by filtration, washed with DMF (100 mL g^{-1} of MOF), and extracted with methanol overnight (200 mL g^{-1}) to remove solvated DMF.[18] CuTPA MOF was synthesised in an analogous manner but using 1.0 g of 1,4-benzenedicarboxylic acid (BDC) in place of BTC.

Preparation of Pd/CuBTC MOF template: A standard sol-immobilization method was employed in the preparation of supported Pd nanoparticles. Potassium tetrachloropalladate(II) (K_2PdCl_4) was used to prepare aqueous solutions in H_2O of the desired palladium concentration (1.26×10^{-4} M), to which solutions of polyvinyl alcohol (PVA, 1 wt. % solution, Aldrich, M_w = 9000–10 000 g mol^{-1}, 80% hydrolysed, PVA/Pd wt. ratio = 0.65) were added. Fresh solutions of $NaBH_4$ (0.1 M, >96%, Aldrich, $NaBH_4$/Pd molar ratio = 5) were prepared and added dropwise to each with stirring to form a dark brown solution. After the complete reduction of Pd over 30 minutes, the CuBTC MOF was added under vigorous stirring conditions for nanoparticle immobilisation. The amount of support material required was calculated so as to give a final Pd metal loading of 1 wt. %, and the mixture was stirred for 60 min. The slurry was filtered, and the resulting solid was washed thoroughly with distilled water (2 L of 18.2 MΩ cm^{-1} water) and ethanol to remove soluble impurities, and dried overnight at room temperature.

XRD: X-ray diffraction patterns were recorded on a Bruker D8 diffractometer with Ge(220) primary beam monochromator and a Vantec detector using low background Si sample holders. The patterns were recorded across a range of $2\theta = 5° - 80°$ with a step size of 0.0109°.

XAFS: Cu K and Pd K edge XAFS data were acquired using the B18 beamline at Diamond Light Source synchrotron, located at the Rutherford Appleton Laboratory, Harwell. Measurements were performed using the QEXAFS setup with a Si (111) (for Cu K) / Si (311) (Pd K) monochromator and ion chamber detectors, at a time resolution of 1 min per spectrum. Measurements were performed in transmission mode, using 13 mm pellets made with a cellulose binder, with the pellet loading calculated to obtain an optimal absorbance edge step of approximately 1.

BET: Samples were degassed at 423 K overnight with a FloVAC Degasser before BET surface area measurements were obtained via nitrogen adsorption at 77 K with a Quantachrome Quadrasorb analyser.

MP-AES: MP-AES spectra were recorded on an Agilent 4100 spectrometer. Samples were digested in an aqueous solution of 10% aqua regia. The instrument was calibrated using Pd and Cu atomic absorption standards of 1000 µg / mL, using wavelengths of 324.754 nm and 510.554 nm for Cu, and 340.458 nm and 360.955 nm for Pd.

SEM/EDX: Scanning electron microscope micrographs were recorded using a JEOL JSM-6610LV microscope with a tungsten filament and energy of 30 kV. EDX and elemental mapping was carried out via AZtec software (Oxford Instruments).

TEM: Transmission electron micrographs were recorded using a JEOL JEM 2100 with a lanthanum hexaboride (LaB_6) filament at an accelerating voltage of 200 kV. Samples were prepared by being dispersed on holey carbon TEM grids. High-resolution TEM was performed on a JEOL ARM200F at the electron Physical Sciences Imaging Centre (ePSIC) at Diamond Light Source, also at an accelerating voltage of 200 kV.

TGA: Thermogravimetric analysis was performed using a TA Instruments Thermogravimetric Analyzer, using a platinum pan, a sample gas rate of 60 mL min^{-1} N_2, a balance gas rate of 40 mL min^{-1} N_2, and a ramp rate of 20 °C per minute up to 1000 °C. Each measurement used ~10 mg of sample.

3.3 Synthesis of CuBTC MOF and Pd/CuBTC composites

3.3.1 Synthesis and characterisation of CuBTC MOF

The initial goal of this project was to synthesise a composite of Pd NPs and the CuBTC MOF (also known as HKUST-1). Adopting a variant of the many solution methods used in the "bottle-around-ship" school of NP-MOF composite design, the Pd NPs are introduced using a sol-immobilisation method more commonly seen in supporting metal NPs on a metal oxide support, as discussed in **Section 1.2.3.2**.

However, the first step towards this goal was to confirm a reproducible synthesis of the CuBTC MOF itself, which was produced via hydrothermal synthesis using a solvent mixture of 1:1:1 ratio H_2O:DMF:EtOH. The resulting product was characterised by X-ray diffraction and BET surface area measurements.

The powder X-ray diffraction pattern of the synthesised CuBTC MOF is seen in **Figure 22** below and compared to a simulated reference pattern generated using the Mercury crystal structure visualisation tool produced by the Cambridge Crystallographic Data Centre. The .cif file used to generate the pattern was sourced from the Crystallography Open Database (entry #2300380, from Yakovenko *et al.*[19]).

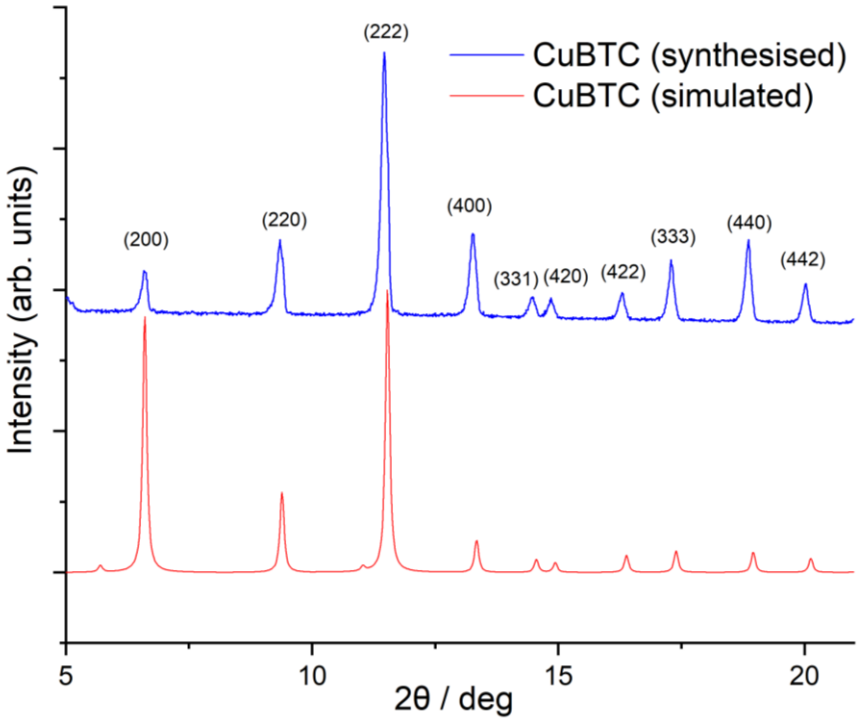

Figure 22: Synthesised and simulated X-ray diffraction patterns for CuBTC MOF, with peaks indexed to the corresponding families of lattice planes.

The high level of agreement between the patterns for the synthesised and simulated MOF indicates that CuBTC has successfully been prepared, and this pattern also correlates well with those obtained by others in the literature.[20–22] The intensities of the characteristic triad of peaks corresponding to the (220), (222) and (400) planes between 9-13° 2θ are similar across all the examples – however the observed difference in intensities seen for the (200) plane is most likely due to a loss of perfect crystallinity due to absorbed water vapour, since CuBTC is water-sensitive.[23] The small artefacts observed shortly before the (200) and (222) planes in the simulated sample are reflections of very weak intensity corresponding to the (111) and (113) planes, which are not observed experimentally.

It is apparent that the two diffraction patterns do not precisely align; applying the Bragg equation (**Section 2.2**) to the diffraction angles for the most intense peak, the (222) reflection, suggests an increase in cubic unit cell parameter of approximately 0.4 Å (26.3 Å simulated, 26.7 Å synthesised) from the simulated sample to the synthesised sample. However, this variation is expected, as analysis of the literature reveals that the cubic unit cell parameter is generally dependent on the choice of synthetic protocol. For example, Cortes-Suarez *et al.*[24] synthesised a sample of CuBTC MOF with a similar cell parameter of 26.67 Å, which then contracted to 26.14 Å upon compositing that MOF with a single-walled carbon nanotube. Investigation of the Computation-Ready, Experimental (CoRE) MOF Database, a collection of thousands of experimentally-synthesised MOFs[25], indicates that there are over 50 reported examples of the CuBTC MOF structure displaying these small variations.[26]

The lattice expansion is most likely another consequence of the hydrophilicity of the MOF, specifically from water's strong affinity for the Cu^{2+} metal ions within the structure.[27,28] The choice of a 1:1:1 H_2O:DMF:EtOH solvent mixture, where the water is used to dissolve the copper nitrate precursor, will allow the water to contribute to a slight breakdown of the MOF structure through ligand displacement and hydrolysis, and will allow some Cu atoms to leach from the MOF.[29] This can ultimately affect composites produced from this MOF and will be considered further both in this chapter and Chapter 4.

Measurement of BET surface area was also used to confirm that CuBTC MOF was prepared correctly, with the BET plot shown in **Figure 23** above. The gradient and *y*-intercept of the BET plot can be used as shown in **Section 2.8** to calculate the BET surface area of the produced CuBTC MOF as 1053 $m^2\ g^{-1}$, which compares favourably to the 1055 $m^2\ g^{-1}$ reported for samples prepared using similar hydrothermal synthetic methods.[30]

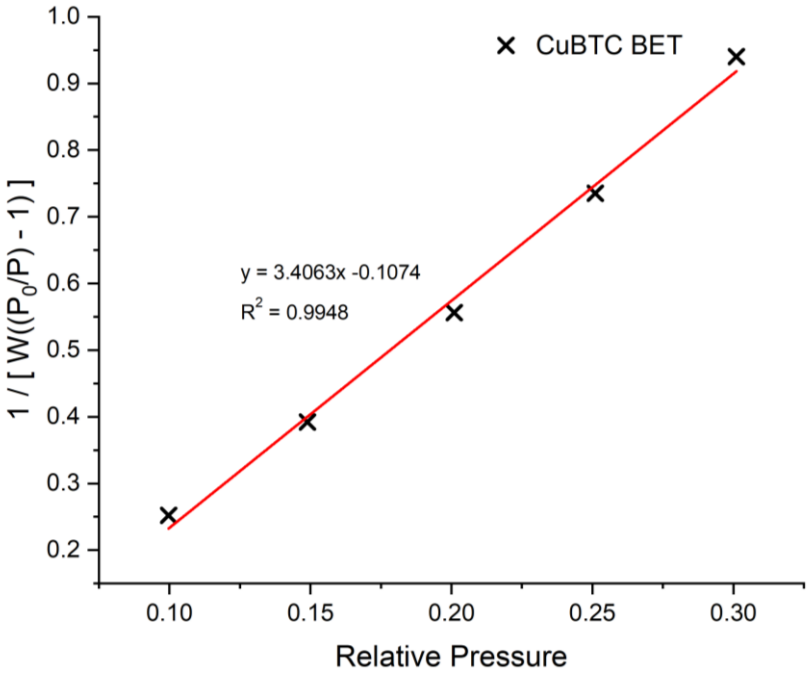

Figure 23: BET plot of CuBTC MOF, relative pressure range 0.05 - 0.35.

3.3.2 Synthesis and characterisation of Pd/CuBTC MOF composite

The synthesised CuBTC MOF was then used as the support in the sol-immobilisation technique for supporting metal nanoparticles (**Section 1.2.3.2)**. Comparison of the X-ray diffraction patterns for CuBTC and the resultant NP-MOF composite Pd/CuBTC (as seen in **Figure 24** below) indicates that the crystal structure has been retained following immobilisation of the Pd NPs. The slight broadening of the peaks in Pd/CuBTC indicates a further loss of crystallinity from the sample's exposure to water during the sol-immobilisation process, most evident from the low-angle shoulder of the (220) peak at 9.0° and the faint introduction of two further reflections, seen at 7.7° and 11.9°. Indeed, these new reflections likely indicate the presence of a new phase formed by water-based degradation of the CuBTC MOF. Decoste *et al*.[31] investigated the stability of CuBTC MOF by aging it for 28 days at 40 °C and 90% relative humidity, after which the XRD pattern of the MOF structure displayed similar reflections at these values of 2θ. Their subsequent analysis via IR spectroscopy suggested that a new MOF structure was formed after the aging process, where the carboxylate groups in the MOF are protonated by water to yield carboxylic acid groups, but without the whole structure completely degrading into its constituent components. Whilst it is hard to clearly observe these reflections in the sample of CuBTC presented here, due to the reflections' lower intensities and the sample's limited amount of aging in comparison to the Decoste study, the immersion of the sample to water during the sol-immobilisation process is likely to produce a similar, and even possibly accelerated, effect to keeping the sample in a high-humidity environment.

This observed degradation again neatly demonstrates the instability of the MOF precursor, a property which will be exploited later to produce NP-metal oxide nanocomposites. The full view of the powder pattern supports this, showing that the crystal structure is broadly retained during the sol-immobilisation process, albeit with some slight deviations.

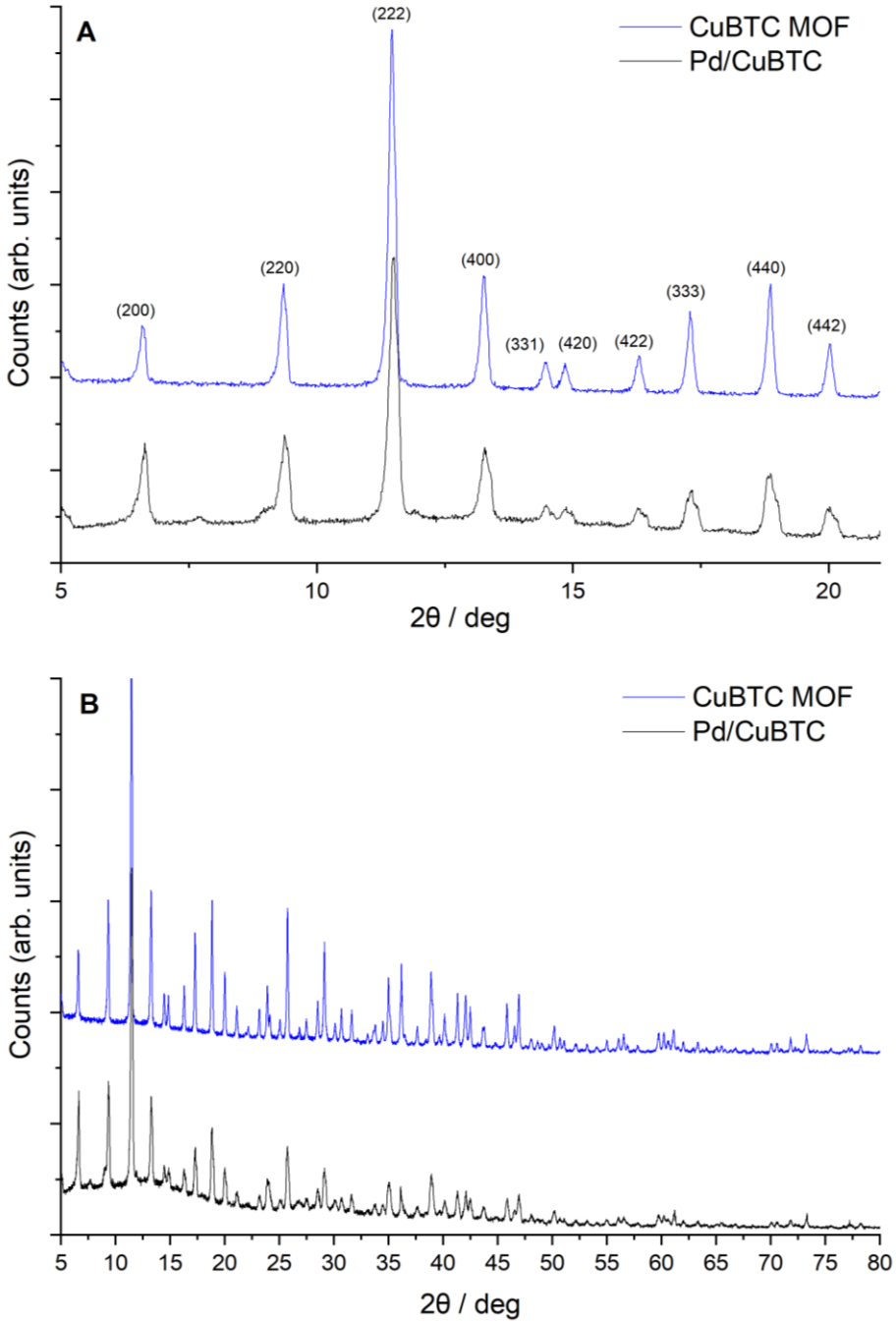

Figure 24: X-ray diffraction patterns of CuBTC MOF and Pd/CuBTC, a) showing the region 5-20° 2θ, and b) the region 5-80° 2θ.

The degradation of the sample due to water exposure is more apparent when looking at the higher angle range in more detail, as shown in **Figure 25**. Many small, disordered peaks are

visible, indicating some breakdown in crystallinity, but amongst these, some of the more intense peaks resemble the diffraction pattern for Cu_2O. The Cu_2O reference pattern is obtained from work by Wang *et al.*[32] published on the Inorganic Crystal Structure Database (ICSD-180846).

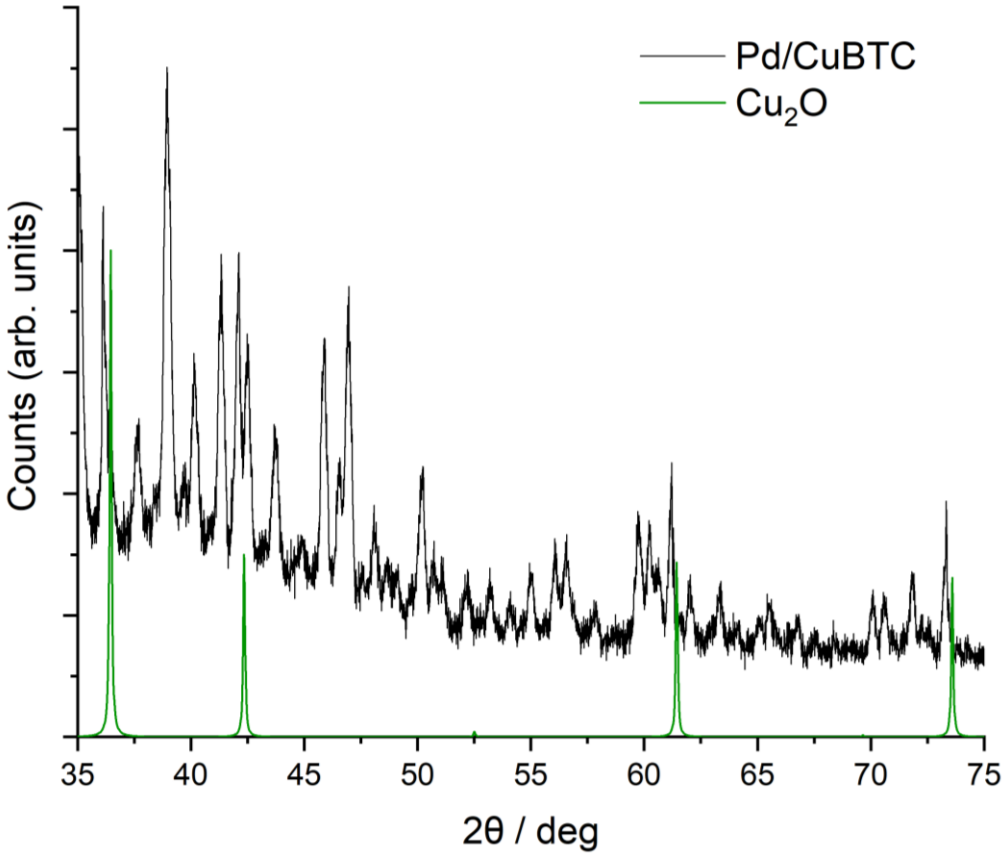

Figure 25: X-ray diffraction pattern of Pd/CuBTC composite showing a range from 35-75° 2θ, plotted against a Cu_2O reference pattern.

The Cu_2O pattern is shifted by approximately 0.2 degrees, which can be explained by a small difference in cell parameter between the measured sample and the reference. The presence of Cu_2O is expected to arise from copper atoms being removed from the MOF during the sol-immobilisation process, and is discussed in further detail in **Section 3.3.4**.

The BET surface area of the Pd/CuBTC composite was measured as ~900 $m^2 g^{-1}$, which is a reduction on the 1053 $m^2 g^{-1}$ observed for the bare CuBTC MOF. This reduction is expected due to the immobilisation of the Pd nanoparticles upon the surface, and due to the observed slight water-induced breakdown of the high-surface-area MOF after further exposure to water during the sol-immobilisation process, and therefore helps to confirm that the immobilisation was successful.

Multiple methods were used to investigate the ability of the sol-immobilisation method to achieve an accurate 1.0 wt% Pd loading on the CuBTC support. Both SEM/EDX and MP-AES were employed, with varying degrees of accuracy.

The EDX spectrum of the Pd/CuBTC sample was recorded during SEM imaging. The obtained spectra is shown in **Figure 26** below.

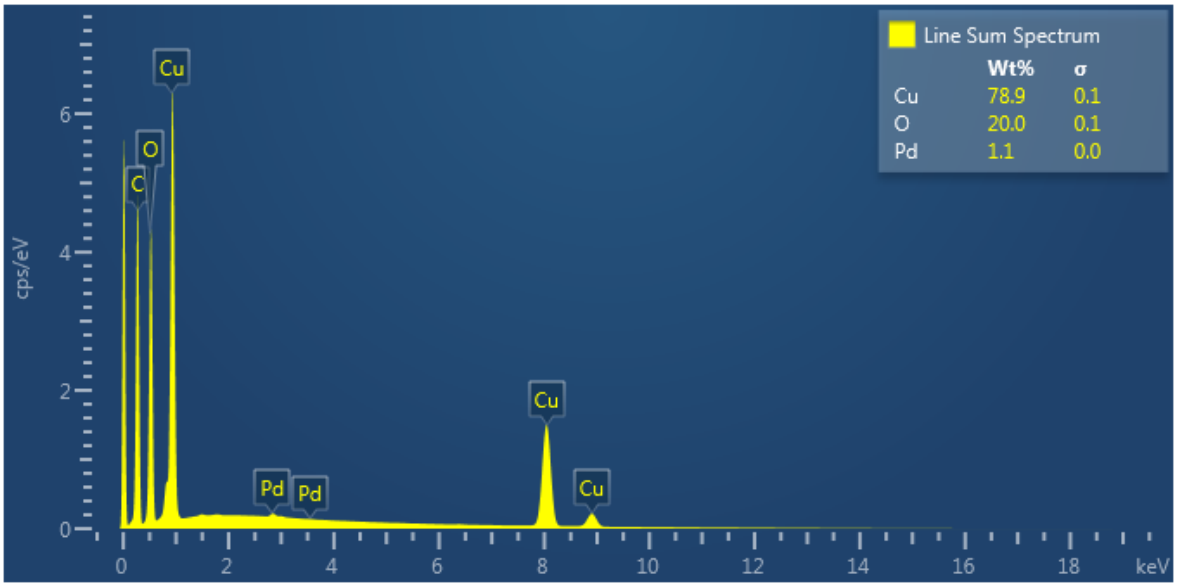

Figure 26: EDX spectrum of Pd/CuBTC composite, illustrating estimated Pd, Cu, and O loadings.

Unfortunately, EDX is not very accurate at measuring carbon content due to high contamination of samples with carbon from the SEM vacuum chamber itself. This makes the weight percentages given in **Figure 26** unreliable, even though the Pd loading is recorded as being close to the expected value of 1.0 wt %. Additionally, the Cu wt % is recorded as 78.9%, but the actual weight percentage of Cu in bare CuBTC MOF is only 33.9 wt%, calculated from the molecular formula $C_{18}H_6Cu_3O_{12}$.[33] This anomalous result likely indicates that the sample holder used for the experiment itself contains copper, and all this combined suggests that an alternate method is preferable for determining Pd loading. Therefore, MP-AES analysis of the Pd weight percentage was performed, calibrated by the 340.458 and 360.955 nm spectral lines of palladium. Analysis of the results indicated that Pd/CuBTC samples calculated to be 1 wt% Pd displayed true Pd loadings of between 0.90 and 0.99 wt%.

Transmission electron microscopy (TEM) of the Pd/CuBTC precursor was performed, and micrographs are shown below in **Figure 27** and **Figure 28**.

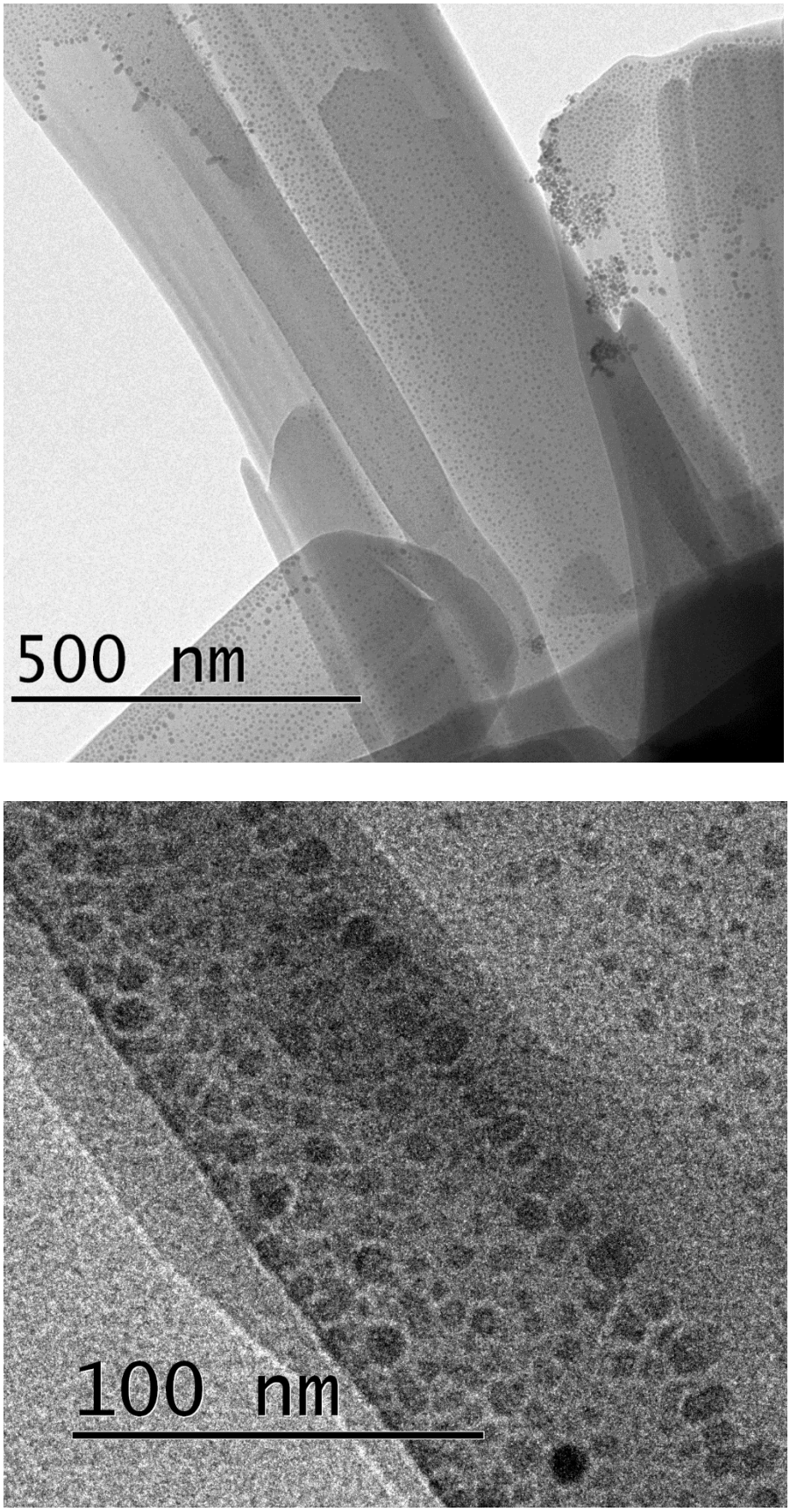

Figure 27: Transmission electron micrographs of 1 wt% Pd/CuBTC, showing Pd NPs dispersed across rods of CuBTC MOF, at scales of a) 500 nm and b) 100 nm respectively.

The TEM micrographs clearly show the two main components of the Pd/CuBTC composite structure, with rod-like crystallites of CuBTC supporting a fine dispersion of Pd nanoparticles. The top right of the 500-nm-scale image also shows the beginnings of some larger aggregations of nanoparticles (visible as darker clusters). Sample preparation requires great care to ensure that the nanoparticles are generated evenly and capped by PVA to minimise this agglomeration. Examining the TEM micrographs in more detail indicates that the supported Pd NPs are generally 5-10 nm in diameter, which is somewhat larger than the 2-5 nm observed for Pd NPs supported on titania.[34] Being able to control the dispersion of the nanoparticles in this manner is crucial, since it will both allow this composite to function as a catalyst, and ensure that a maximal amount of Pd and Cu are in contact for later composite reduction and potential alloying.

Figure 28 shows a high-resolution TEM image of the Pd/CuBTC composite recorded at the electron Physical Science Imaging Centre (ePSIC) at Diamond Light Source. The Pd nanoparticles here have diameters of ~5-7 nm and can be seen clustered together on the edge of a rod of CuBTC MOF.

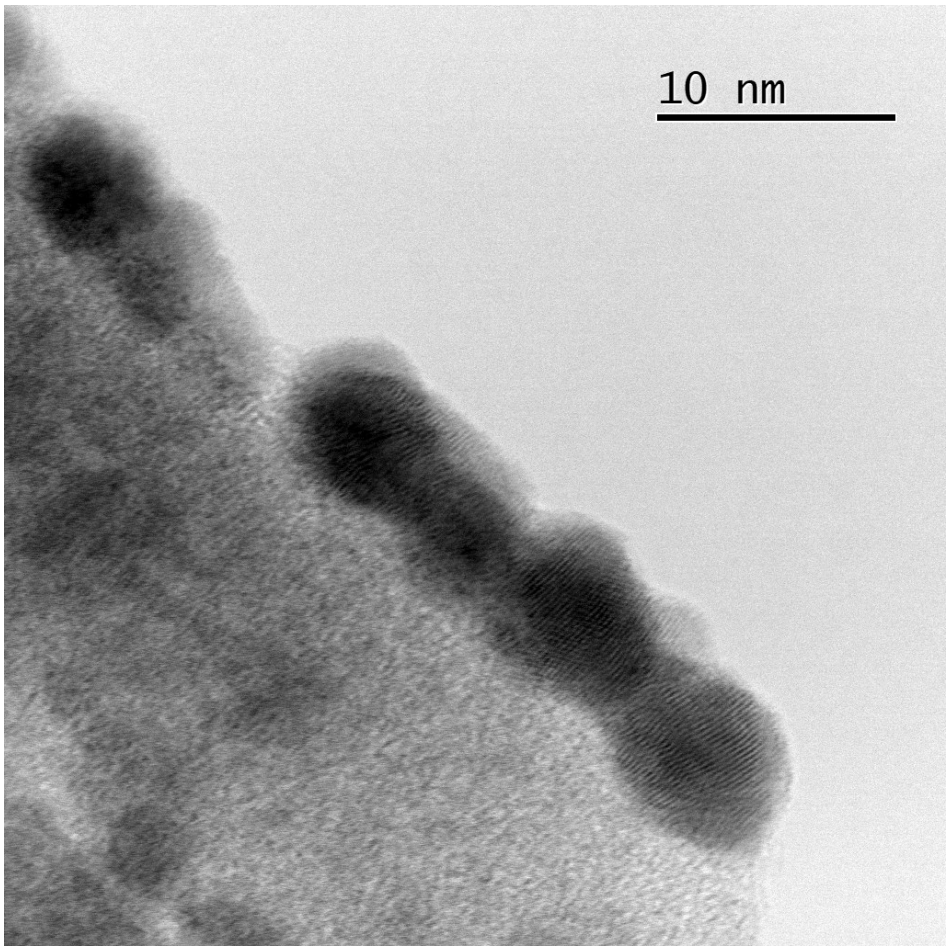

Figure 28: HRTEM image of Pd/CuBTC, showing Pd nanoparticles (dark) dispersed on CuBTC MOF substrate (lighter).

3.3.3 XAFS Analysis of CuBTC and Pd/CuBTC

XAFS analysis was undertaken on the prepared samples of CuBTC MOF and the Pd/CuBTC composite on the B18 beamline at Diamond Light Source. The results are displayed below in **Figure 29**. Initial comparison of the XANES spectra for the two samples, shown in **Figure 29a** and **Figure 29e** for CuBTC and Pd/CuBTC respectively, clearly shows that the overall structure of the material has remained intact during immobilisation of the nanoparticles. However, a deeper analysis of the derivatives of the XANES spectra, shown in **Figure 29b** and **Figure 29f**, indicates some more subtle changes.

The XANES spectrum for the CuBTC MOF demonstrates a small pre-edge feature beginning at 8979 eV, which is characteristic of a 1s to 3d electronic transition that ordinarily is forbidden in a case of perfect octahedral symmetry. However, this transition is well-documented to occur in transition metal oxides due to a mixing of the 3d and 4p electronic states in cases where centrosymmetry is broken.[35,36] Comparison of the XANES spectra for CuBTC to reference standards of Cu^0, Cu(I) oxide, and Cu(II) oxide, as seen in **Figure 30**, shows this pre-edge feature in all of CuBTC, Pd/CuBTC and Cu(II) oxide. Furthermore, the similarity of the white line feature at ~8996 eV for both CuBTC and Pd/CuBTC also indicates that these samples are largely composed of Cu(II) ions.

Comparison of the derivatives of the XANES spectra also shows that an extra feature is apparent in the XANES spectrum of the Pd/CuBTC MOF, a small rising-edge feature at ~8985 eV. This occurs in the same region as a distinct shoulder on the Cu(II) oxide XANES spectrum, and is considered to be indicative of a square planar Cu environment[26], which matches the geometry of copper in bulk copper(II) oxide (CuO).

The non-phase-corrected Fourier transform of the EXAFS spectrum, displayed for the two samples in **Figure 29d** and **Figure 29h**, shows a dominant scattering path followed by smaller scattering features at and above 2 Å. The coordination environment of the copper atoms can be further explored by fitting the EXAFS data using the Artemis program from the Demeter software package.

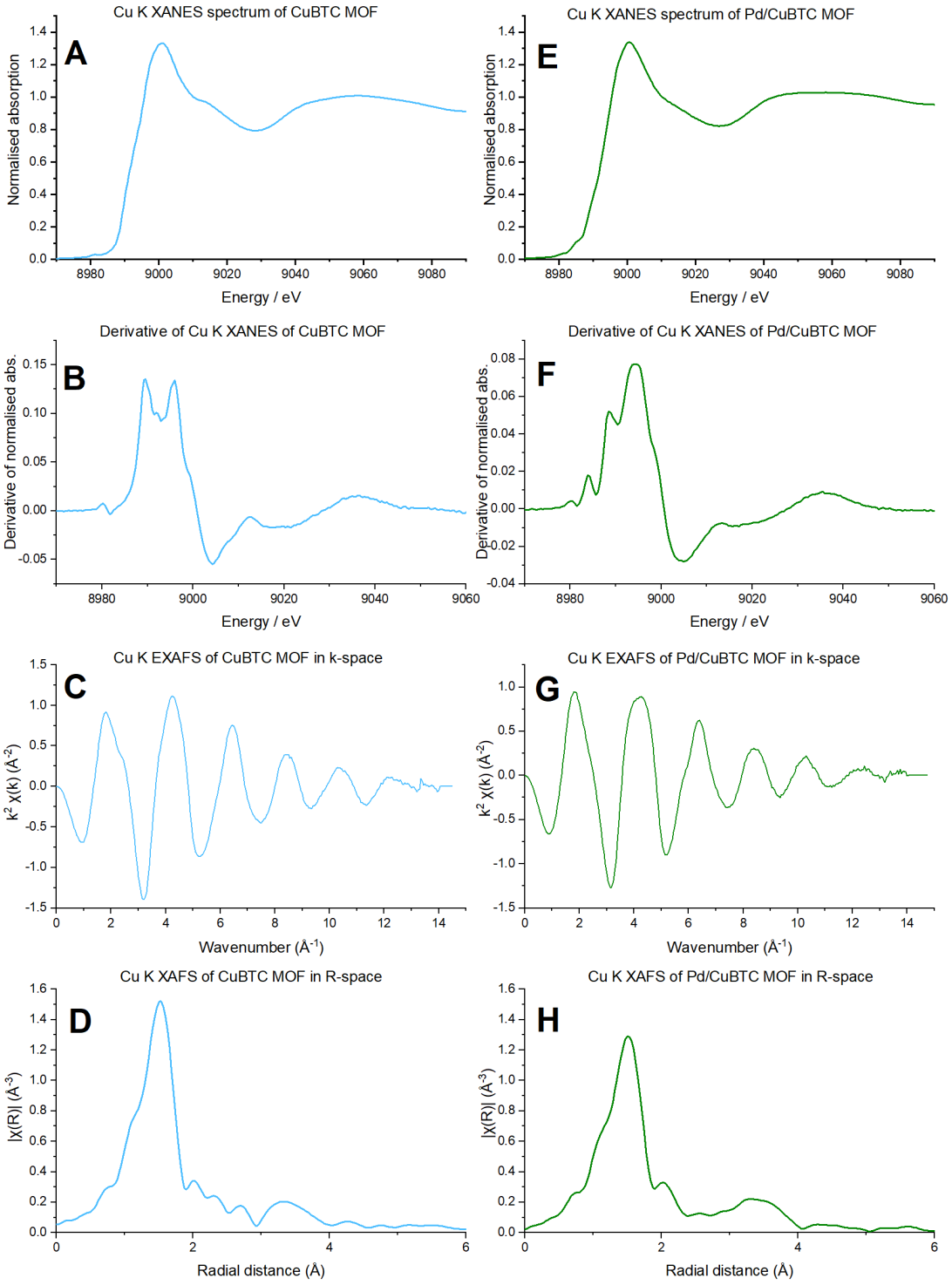

Figure 29: Cu K edge XAFS spectra for CuBTC MOF (blue) and Pd/CuBTC MOF composite (green); where figures A-D represent for the CuBTC MOF a) the normalised absorption coefficient at the Cu K X-ray edge after background subtraction; b) the first derivative of that absorption coefficient; c) the transformation of the absorption signal into *k*-space, weighted by a k^2-term; and d) the Fourier transform of the k^2-weighted *k*-space function into *R*-space; figures E-H are analogous to figures A-D but for the Pd/CuBTC composite.

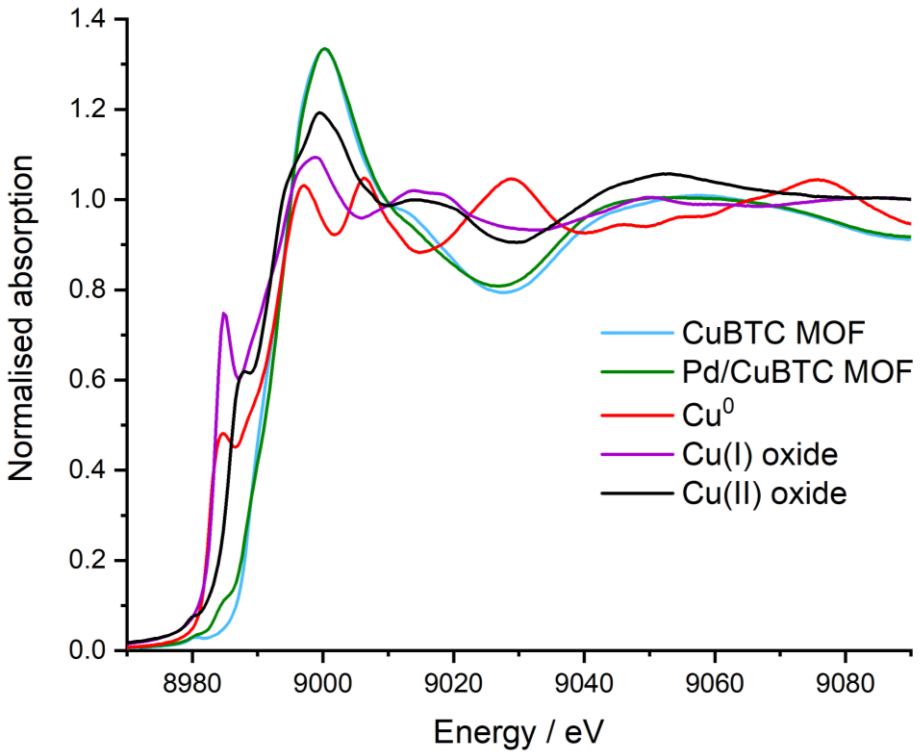

Figure 30: Normalised Cu K XANES spectra for CuBTC and Pd/CuBTC MOF, plotted with Cu^0, Cu(I) oxide and Cu(II) oxide standard references.

The EXAFS fits for CuBTC and Pd/CuBTC were performed using a quick first shell model to estimate the Cu-O scattering. The resulting fits are displayed below in **Figure 31**, with the fitting parameters listed in **Table 1**. The fits suggest that the copper atoms in CuBTC and Pd/CuBTC are coordinated to five oxygen atoms, in a distorted square-based pyramid arrangement. The first Cu-O scattering path at 1.94 Å reflects coordination to four oxygen atoms from two BTC ligands, with an additional scattering path indicating coordination to a more loosely-bound water ligand, at a distance of ~2.2 Å. The higher value of the σ^2 Debye-Waller factor for this second scattering path supports this since it suggests a higher amount of disorder. This model is supported by other synthesised examples of CuBTC in the literature[26,30], and further demonstrates that the underlying metal-organic framework is largely unchanged following Pd nanoparticle immobilisation. However, the previously-mentioned rising-edge feature at ~8985 eV in the XANES spectrum perhaps suggests a small presence of copper oxide in Pd/CuBTC. It is hypothesised that the additional exposure to water during the sol-immobilisation process has abstracted a small amount of copper from the framework, which remains present in the square planar coordination geometry of bulk CuO, which would cause the rising-edge feature. Since XAFS is an averaging technique and the overall amount is only very slight, this can explain the slight changes in the spectra between CuBTC and Pd/CuBTC, and fits with discussion of CuBTC's water stability in **Section 3.3.1**.

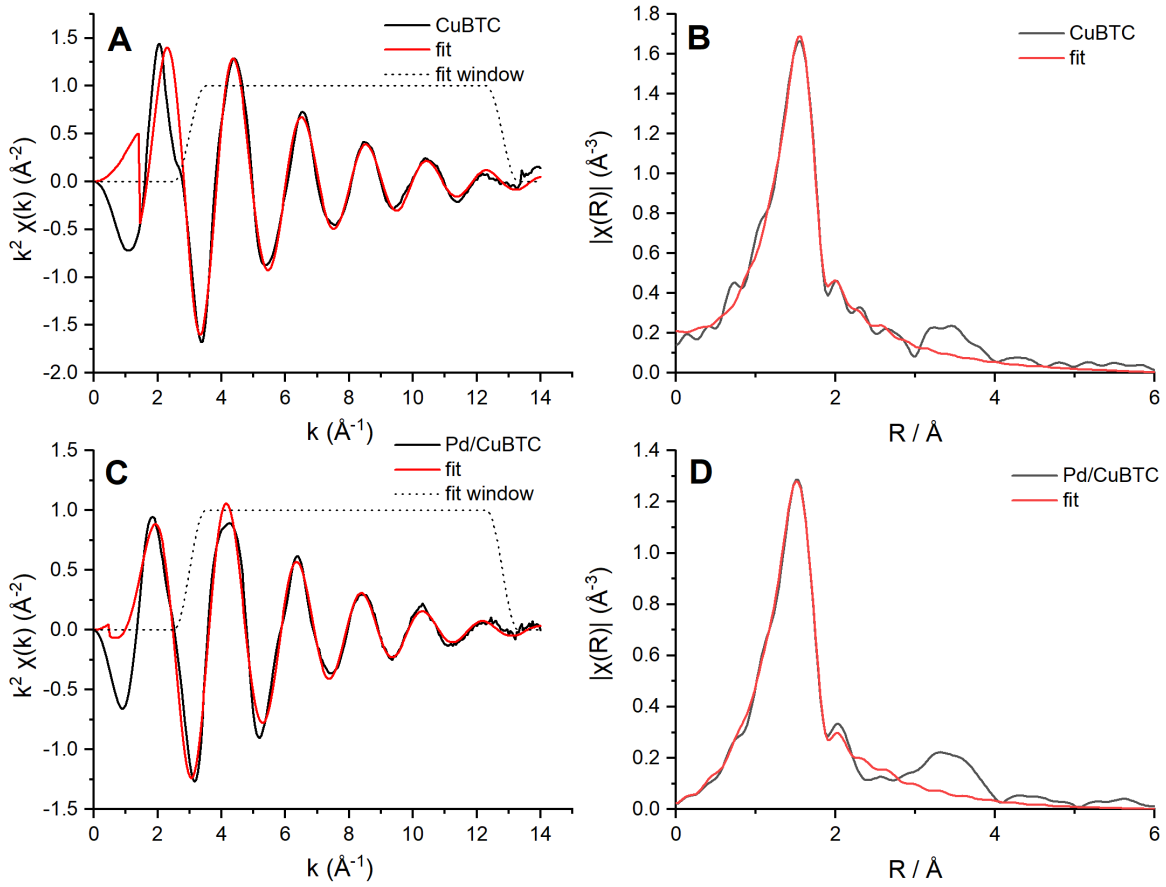

Figure 31: Fits of Cu K EXAFS data for CuBTC showing for a) the k^2-weighted EXAFS signal (black) with a corresponding fit (red) and fit window (black dots); and b) the magnitude of the k^2-weighted non-phase-corrected Fourier transformed signal (black) with a corresponding fit (red). Figures c) and d) are analogous to a) and b) respectively, but for the Pd/CuBTC composite.

Table 1: EXAFS fitting parameters for the Cu K edge for CuBTC and Pd/CuBTC composites. Fitting parameters: $S_0^2 = 0.92$, determined from a fit of Cu foil; fit range $3 < k < 12.8$ and $1.0 < R < 2.5$. Spectra fitted using 9 independent points. The values for coordination number and E_0 were fixed with no associated error.

Sample	Bond (Absorber-scatterer)	Coordination number (C.N.)	E_0 (eV)	σ^2 / Å^2	R / Å	R-factor
CuBTC	Cu-O1	4	-7.5	0.005(1)	1.94(1)	0.002
	Cu-O2	1		0.019(4)	2.23(3)	
Pd/CuBTC	Cu-O1	4	1	0.006(3)	1.95(2)	0.003
	Cu-O2	1		0.016(3)	2.26(2)	

The Pd K edge for the Pd/CuBTC sample was also measured, to examine the nature of the interface between the Pd nanoparticles and the underlying CuBTC framework. The XANES spectrum, XANES derivative and the corresponding transformations to *k*-space and *R*-space are displayed in **Figure 32a-d**. The Fourier transform indicates two distinct scattering paths at around 2.0 and 2.5 Å. To investigate their possible origins, the XANES spectrum and Fourier transform were also compared to reference standards for Pd^0, PdO (Pd^{2+}), and PdC_x, as shown in **Figure 33**. As seen in **Figure 33b**, the scattering path at ~2.5 Å (non-phase-corrected) very closely resembles that for Pd^0, suggesting a Pd-Pd scattering distance; however, the other scattering path at ~2.0 Å is less clear. Whilst formation of a PdO surface layer on Pd nanoparticles is reasonably common[37,38], there is not much similarity between the XANES spectra of PdO and Pd/CuBTC. However, both the XANES and Fourier transform data are reasonably similar to a reference of Pd carbide formed in a Pd/SiO_2 catalyst[39].

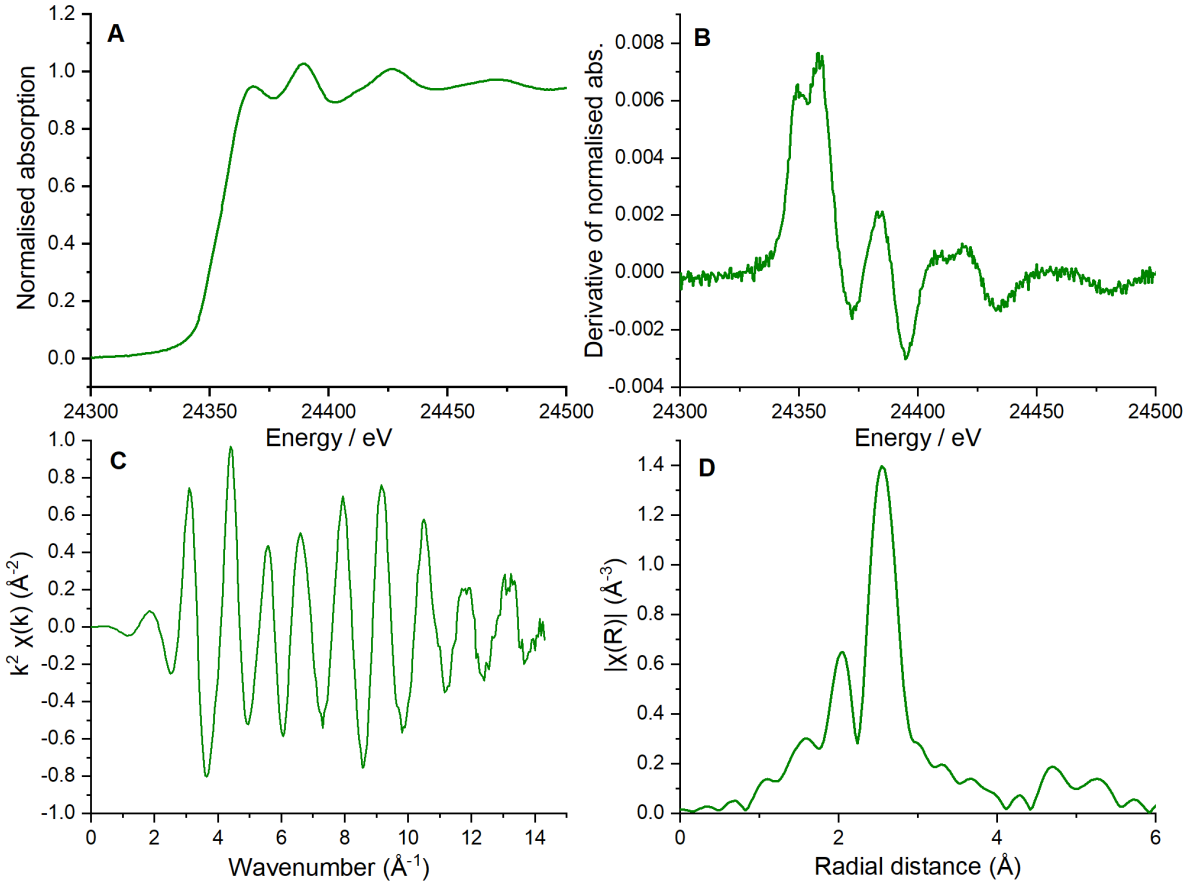

Figure 32: Pd K edge XAFS spectra for Pd/CuBTC MOF composite; where figures A-D represent a) the normalised absorption coefficient at the Cu K X-ray edge after background subtraction; b) the first derivative of that absorption coefficient; c) the transformation of the absorption signal into *k*-space, weighted by a k^2-term; and d) the Fourier transform of the k^2-weighted *k*-space function into *R*-space.

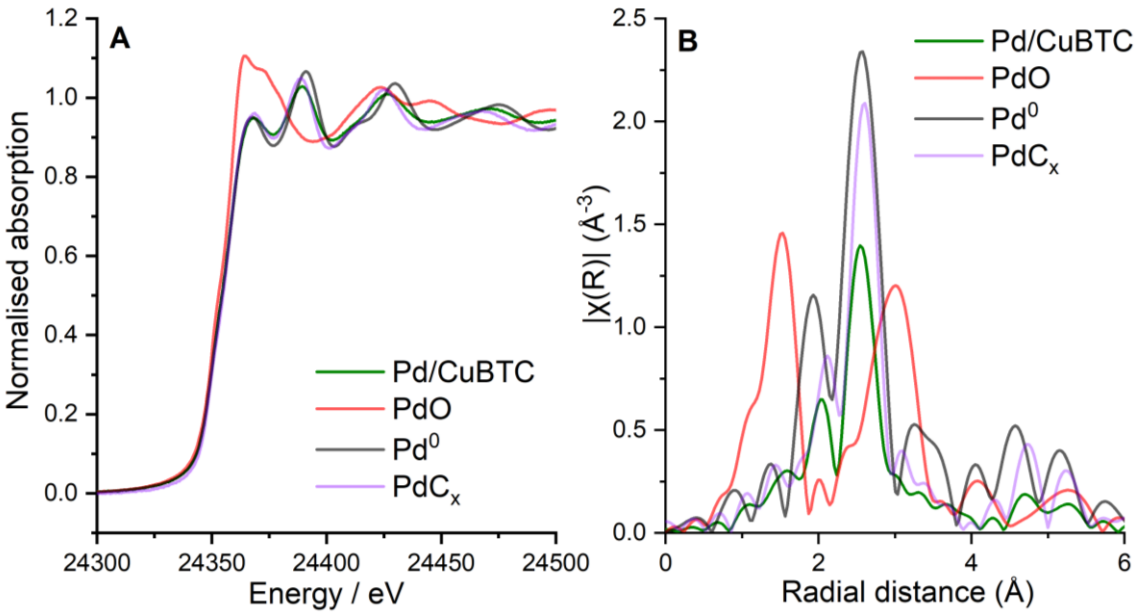

Figure 33: a) Normalised Pd K XANES spectra for Pd/CuBTC MOF, plotted with PdO (Pd^{2+}), Pd^0 and PdC_x references; b) k^2-weighted non-phase-corrected Fourier transform of Pd/CuBTC XANES spectrum, plotted with corresponding Fourier transforms for PdO (Pd^{2+}), Pd^0 and PdC_x references.

In particular, when compared to Pd^0, the XANES spectrum of Pd/CuBTC exhibits a slight broadening and positive energy shift at the first XANES feature at ~24368 eV (**Figure 34**), and also a slight negative energy shift at the second main XANES feature at ~24390 eV. The combination of both of these features is highly suggestive of a carbide rather than another interstitial structure such as a hydride, as reported by Bugaev *et al.* in Pd K XAFS investigations of Pd carbides and hydrides both at the surface and in the bulk of Pd nanoparticles,[40,41] where the hydride XANES spectrum does not produce the same broadening and positive shift in the feature at ~24368 eV. Furthermore, palladium hydride forms reversibly and requires a H_2 environment to remain stable; upon exposure to air or even after replacing the atmosphere with an inert gas, it will decompose back to Pd^0.[42] The stronger bonds formed between palladium and carbon allow the carbide to persist in the structure, and the source of the carbon in many reported palladium carbides is the organic reagents used in sample preparation.[43,44] Example carbon sources in the synthesis of Pd/CuBTC could include the PVA capping agent for the nanoparticles, the BTC ligands used as linkers in the MOF, and solvated MeOH in the MOF pores introduced via solvent exchange of DMF in the MOF synthesis. The overall evidence thus favours carbidisation over hydride formation, but this will be explored further by fitting the EXAFS spectrum of Pd/CuBTC.

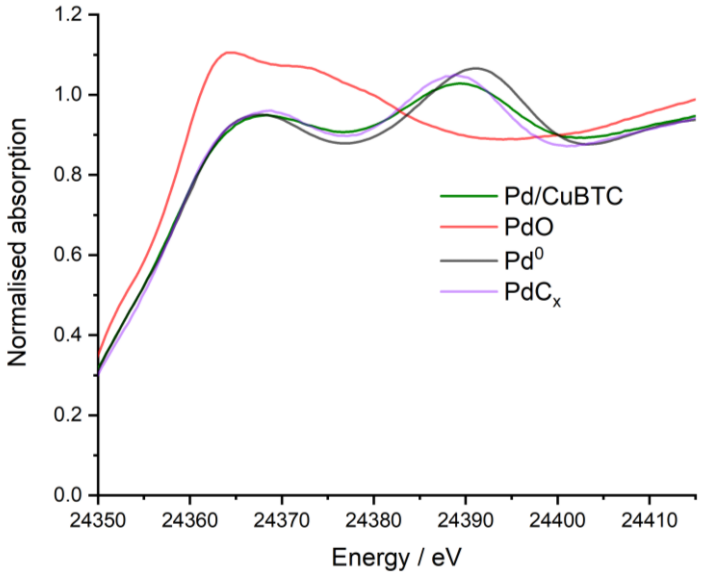

Figure 34: A closer look at the initial XANES spectra of Pd/CuBTC with Pd^0, PdO and PdC_x references, highlighting the two main features at ~24368 eV and ~24389 eV.

To investigate the carbidisation, a first-shell fit of the EXAFS spectrum of the Pd K edge Pd/CuBTC was performed, with the results displayed in **Figure 35** and associated fitting parameters listed in **Table 2**. Fits of the reference compounds Pd^0, PdO, and PdC_x are also included. It is clear that the fit for Pd/CuBTC accurately models the primary peak in the Fourier transform data, at ~2.5 Å, but there is still some discrepancy around the feature at ~2.0 Å. Attempts to incorporate a Pd-O scattering distance did not resolve this, and EXAFS cannot accurately measure a possible quantity of carbon within the lattice via use of a Pd-C scattering distance.[39] Due to the similarity between the XANES spectra of Pd/CuBTC and the carbide reference, it is hypothesised that a small amount of PdC_x has formed during the immobilisation process – the carbidic shifts in the XANES are noticeable but also smaller in magnitude than the PdC_x reference.

Carbidisation is also supported by the slight expansion of the Pd-Pd coordination distance, moving from 2.75 Å in Pd^0 to 2.77 Å in the fitted Pd/CuBTC composite. The PdC_x reference, which displays larger shifts in the XANES region than Pd/CuBTC, exhibits a Pd-Pd distance of 2.80 Å upon fitting, indicating that a larger quantity of interstitial carbon causes further disruption in the Pd nanoparticle lattice and increases the interatomic spacing. This PdC_x reference was estimated[39] to have the composition $PdC_{0.28}$, and the smaller lattice expansion in Pd/CuBTC suggests that the nanoparticles in the composite contain somewhat less carbon than this amount.

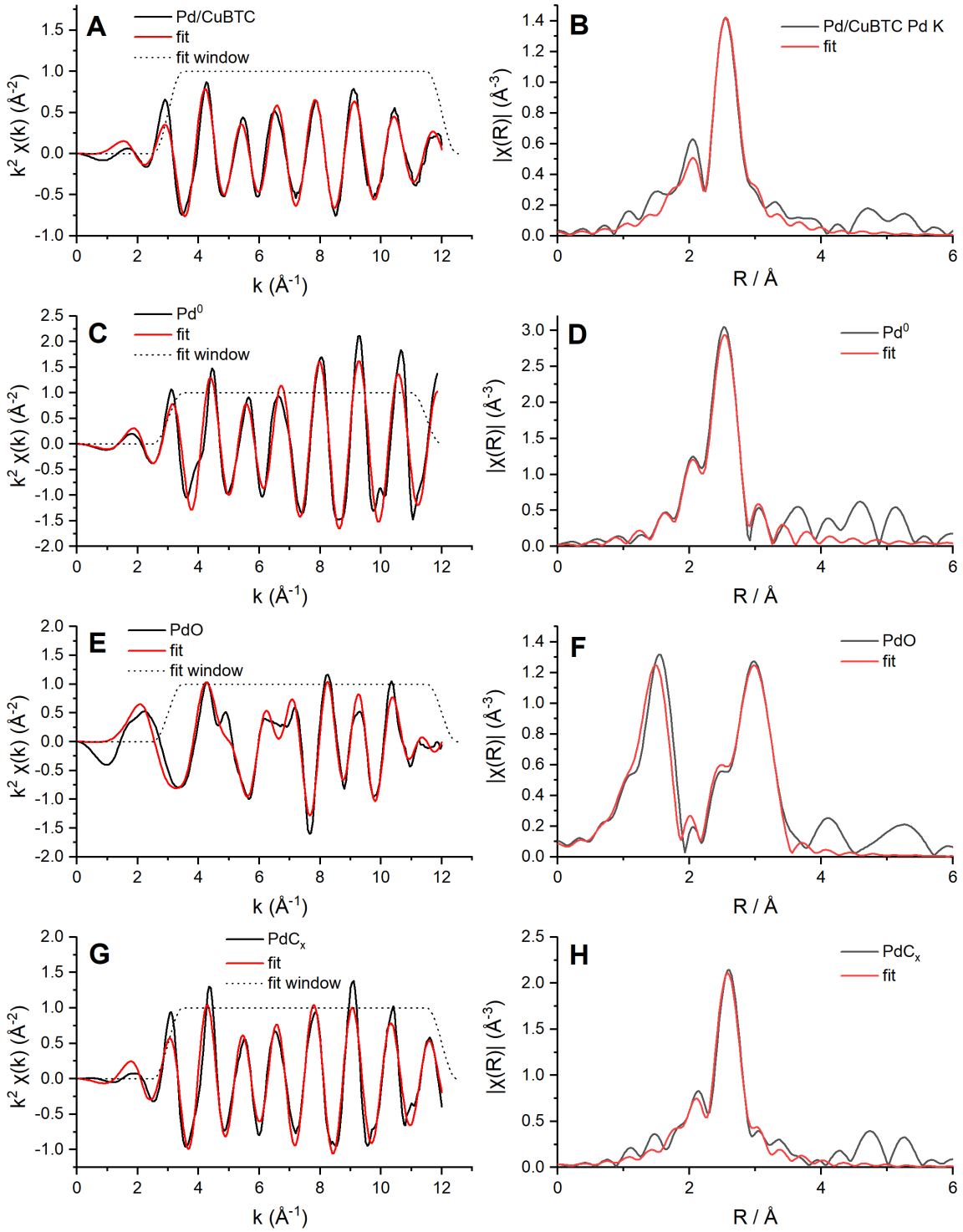

Figure 35: Fits of Pd K EXAFS data for Pd/CuBTC showing for a) the k^2-weighted EXAFS signal (black) with a corresponding fit (red) and fit window (black dots); and b) the magnitude of the k^2-weighted non-phase-corrected Fourier transformed signal (black) with a corresponding fit (red). Figures c) and d) are analogous to a) and b) respectively, but for a Pd^0 reference; in the same manner, figures e) and f) represent a PdO reference and figures g) and h) represent a PdC_x reference.

Table 2: EXAFS fitting parameters for the Pd K edge for the Pd/CuBTC composite and reference compounds Pd^0, PdO and PdC_x. Fitting parameters: $S_0^2 = 0.85$, determined from a fit of Pd foil; fit range $3 < k < 12$ and $1.0 < R < 3.0$, with the exception of the PdO fit, which used the range $1.0 < R < 3.5$. Spectrum fitted using 12 independent points. The values of E_0 and σ^2 were fixed with no associated error.

Sample	Bond (Absorber-scatterer)	Coordination number (C.N.)	E_0 (eV)	σ^2 / Å^2	R / Å	R-factor
Pd/CuBTC	Pd-Pd1	8.8(3)	-5	0.009	2.77(2)	0.02
Pd^0	Pd-Pd1	12.1(5)	0	0.006	2.75(1)	0.01
PdO	Pd-O1	4.7(4)	-3	0.004	1.99(1)	0.03
	Pd-Pd1	2.3(4)		0.003	3.02(1)	
	Pd-Pd2	7.4(9)		0.005	3.41(1)	
PdC_x	Pd-Pd1	11.6(5)	-0.3	0.008	2.80(1)	0.02

There is also the possibility that some small amount of abstracted copper from the water-induced breakdown of the CuBTC MOF has contributed to a small amount of Pd-Cu alloying – incorporating a Pd-Cu scattering distance in the EXAFS fit was similarly unsuccessful as Pd-O, but a very small amount would be sufficient to subtly distort the XAFS signal whilst remaining hard to quantify. This Pd-Cu alloying behaviour will be discussed further in Chapter 4.

To further confirm the possibility of PdC_x formation, a linear combination analysis was performed on the Pd/CuBTC XANES data, comparing it to both the Pd^0 and PdC_x references, shown in **Figure 36**. The resulting fit suggested proportions of 39% for the Pd^0 reference and 61% for the carbide reference, indicating the nanoparticle structure likely features some amount of carbidisation.

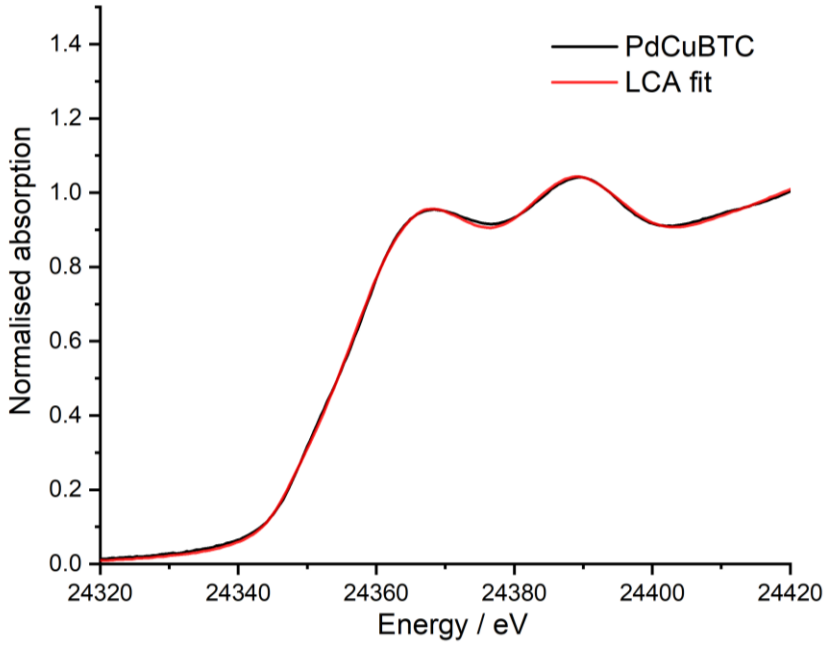

Figure 36: Linear combination analysis fit for the Pd/CuBTC composite, using Pd^0 and PdC_x as reference materials.

3.3.4 Varying the loading of Pd immobilised on the MOF

The effect of changing the loading of Pd nanoparticles on the CuBTC MOF was also investigated. In addition to the 1 wt% Pd loading already examined, samples with 0.5 and 0.25 wt% Pd were prepared. Examination of the powder XRD patterns of these samples (**Figure 37**) indicate that the 5-20° region of 2θ appears broadly the same but with a significant broadening of the (220) peak at 9.4°, even more so than that observed in **Figure 24a**. The faint reflections at 7.7° and 11.9° also observed there are much more prominent here for the lower wt% samples, suggesting further degradation of the MOF structure than was observed for the 1 wt% sample. This is corroborated by the extra reflections around 30° that appear for the 0.25 wt% sample, and it is clear that the overall crystallinity of the sample is decreasing with decreasing Pd loading, and it is likely that the alternative MOF structure with protonated carboxylic acid groups, as opposed to the initial carboxylate groups, is forming during this process, as proposed by Decoste et al.[31] and discussed in **Section 3.3.2**.

The presence of a Cu_2O phase, in a small quantity for the 0.5 wt% sample and more significantly for the 0.25 wt% sample, is also apparent from the sharp peaks at 36.4° and 42.3°. This is attributed to copper ions being abstracted from the MOF lattice, potentially due to reaction with trace $NaBH_4$ remaining active in the solution used for the sol-immobilisation process, producing zero-valent Cu NPs followed by oxidation to Cu(I) in air to produce Cu_2O. Although there is a waiting period of 30 minutes implemented in the procedure, and $NaBH_4$ is readily reactive with water, this remains a possibility; a more likely alternative is that copper is being removed from the lattice through reaction with water, as CuBTC MOF is not especially stable in water. In either case, this suggests that significant amounts of copper could be deliberately abstracted from the lattice and be available for alloying with Pd upon reduction. The Cu_2O reference pattern is again taken from the Inorganic Crystal Structure Database (ICSD-180846).

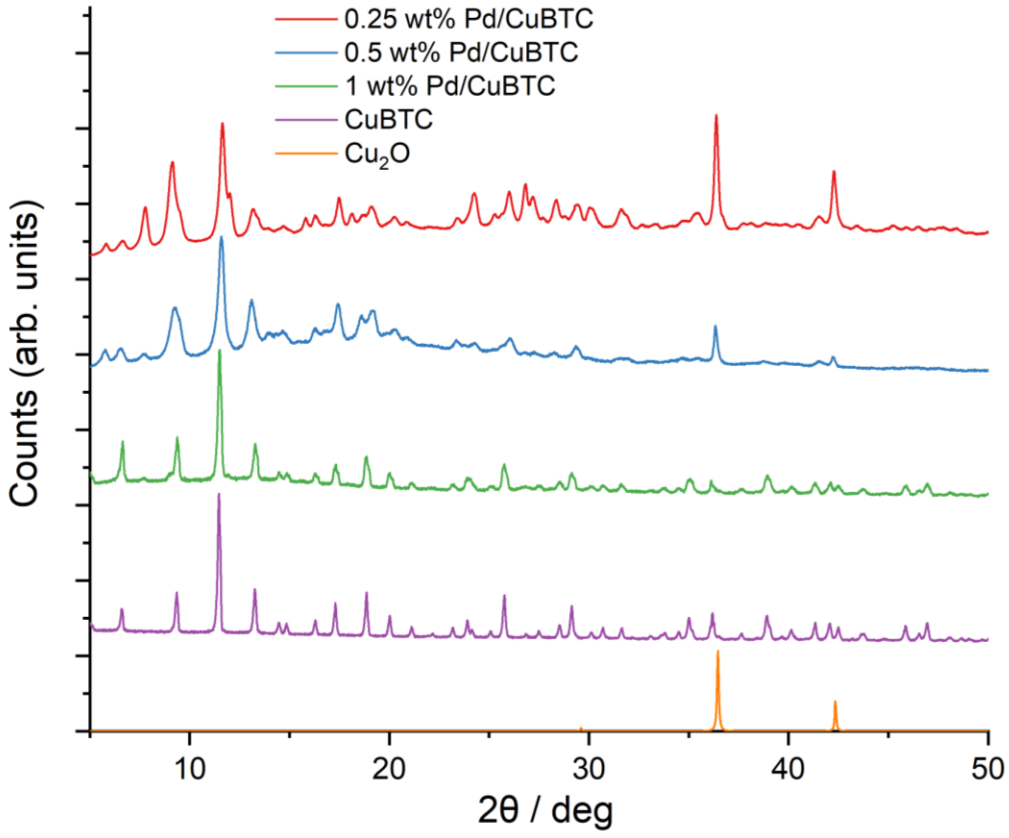

Figure 37: XRD patterns of the Pd/CuBTC composites of approximately 0.25, 0.5 and 1.0 wt% loading of Pd NPs, and those patterns compared to those of CuBTC MOF and a Cu_2O reference pattern.

3.3.5 Extending the sol-immobilisation method to CuTPA

To examine the applicability of this sol-immobilisation method to producing composites of Pd nanoparticles and other metal-organic frameworks, terephthalic acid (TPA) was also used as a ligand and combined with a copper nitrate salt to yield a CuTPA metal-organic framework. This ligand is well-studied as a MOF linker, although its most usual application is in the structure of MOF-5, in which it links together Zn_4O clusters.[45] The analogous CuTPA MOF has been reported as a high-porosity framework produced by conventional MOF synthetic methods[46,47], and here it was synthesised using the same approach as for the CuBTC MOF. The TPA ligand differs from the BTC ligand in that it has only two carboxylic acid groups, in positions 1 and 4 on the benzene ring, rather than in positions 1, 3, and 5.

This sample had Pd NPs immobilised on its surface in two different loadings, 0.25 wt% and 1 wt%. Whilst the XRD patterns (**Figure 38**) for the original MOF and the Pd-loaded samples appear broadly similar below 30°, the region 35-80° indicates that there is clearly a large amount of Cu_2O present in the original framework. The fact that these reflections do not exist in the Pd/CuTPA composites derived from that original material suggests that the CuTPA sample has degraded after synthesis but prior to measurement, and has done so independently of the Pd-loaded samples. This is supported by the extra features observed at around 10° and 18° in the CuTPA sample. The 0.25 wt% and 1 wt% Pd samples have a very strong correspondence, suggesting that the sol-immobilisation procedure again does not significantly affect the structure of the underlying MOF, notwithstanding the anomalous results exhibited by CuTPA. Due to the limited info on CuTPA MOF in the literature, there does not appear to have been significant studies undertaken into its stability in water, but MOFs MIL-101 (chromium-based[48]), MOF-74 (zinc-based[49]) and UiO-66 (zirconium-based[50]) all use TPA as a ligand and have been reported as showing some degree of resistance to hydrolysis.[51]

The 1 wt% and 0.25 wt% Pd samples also show some evidence of degradation into Cu_2O, but on a small scale. Ultimately, the overall goal of this project is to exploit the instability of metal-organic frameworks to produce controlled nanocomposites, and the presence of some degradation here implies that CuTPA also has the potential to produce nanocomposite catalysts.

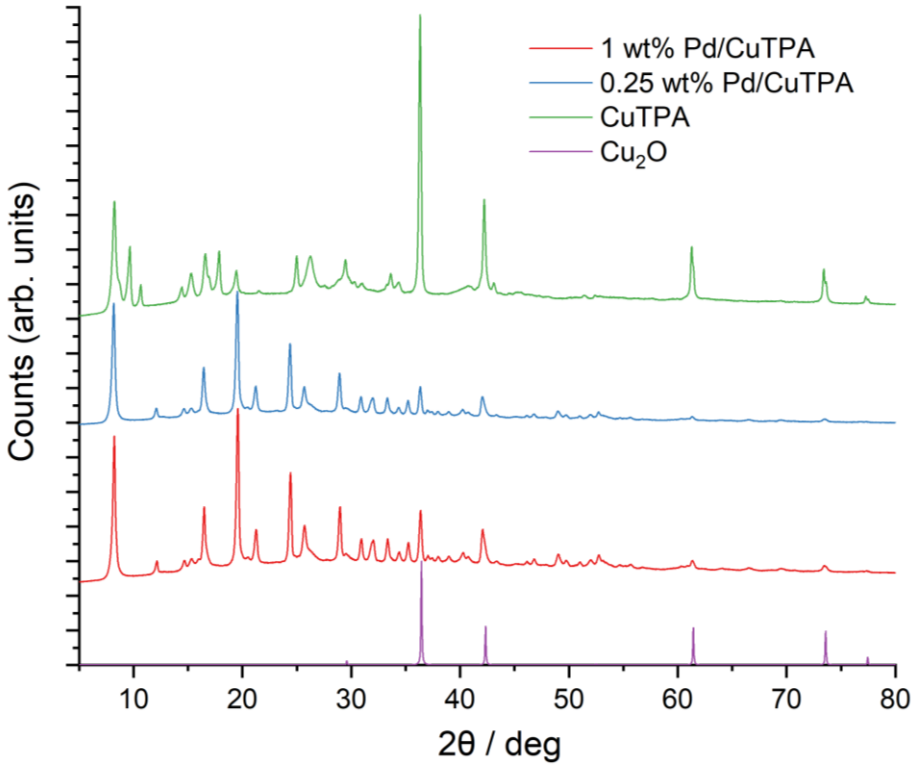

Figure 38: XRD patterns for CuTPA MOF (green) and both 0.25 wt% (blue) and 1 wt% (red) loadings of Pd/CuTPA compared to a Cu_2O reference pattern.

3.3.6 Alternative preparation of Pd/CuBTC using methanol

Although the sol-immobilisation method generally uses water as a solvent, an alternative method using methanol as a solvent was explored, based on work by other members of the research group. Unfortunately, the PVA polymer used to cap the metal nanoparticles is insoluble in MeOH, so it cannot be used to stabilise the Pd NPs, but stabilising effects via interactions with the methanol solvent molecules themselves have been determined by Tierney *et al.*.[52] The results of this capping method compared to those achieved using water and PVA will be discussed further via EXAFS analysis in **Section 0**; however, comparison of the XRD patterns of the H_2O- and MeOH-prepared samples (**Figure 39**) indicates that the MeOH-prepared samples retain the CuBTC crystal structure in the same fashion as those prepared with water.

Since the entire solvent for the sol-immobilisation process has been altered, the CuBTC MOF prepared in MeOH does not exhibit degradation in the same manner seen for the H_2O preparation. Each peak in the XRD pattern is sharper, suggesting that the crystalline structure is significantly more intact following the immobilisation. Additionally, the higher-order peaks above 30° 2θ do not correspond to reference patterns for Cu_2O, CuO or Cu^0, further indicating a lack of degradation and differing from both the CuBTC and CuTPA samples prepared in water, which showed signs of small amounts of Cu_2O being present.

While this may prove useful for the synthesis of nanocomposite catalysts where the MOF remains intact during a reaction, the goal of this project remains to exploit the water-induced MOF degradation, so it may be more challenging to produce alloyed PdCu catalysts from samples prepared in MeOH, since copper is not abstracted from the framework in sufficient quantities.

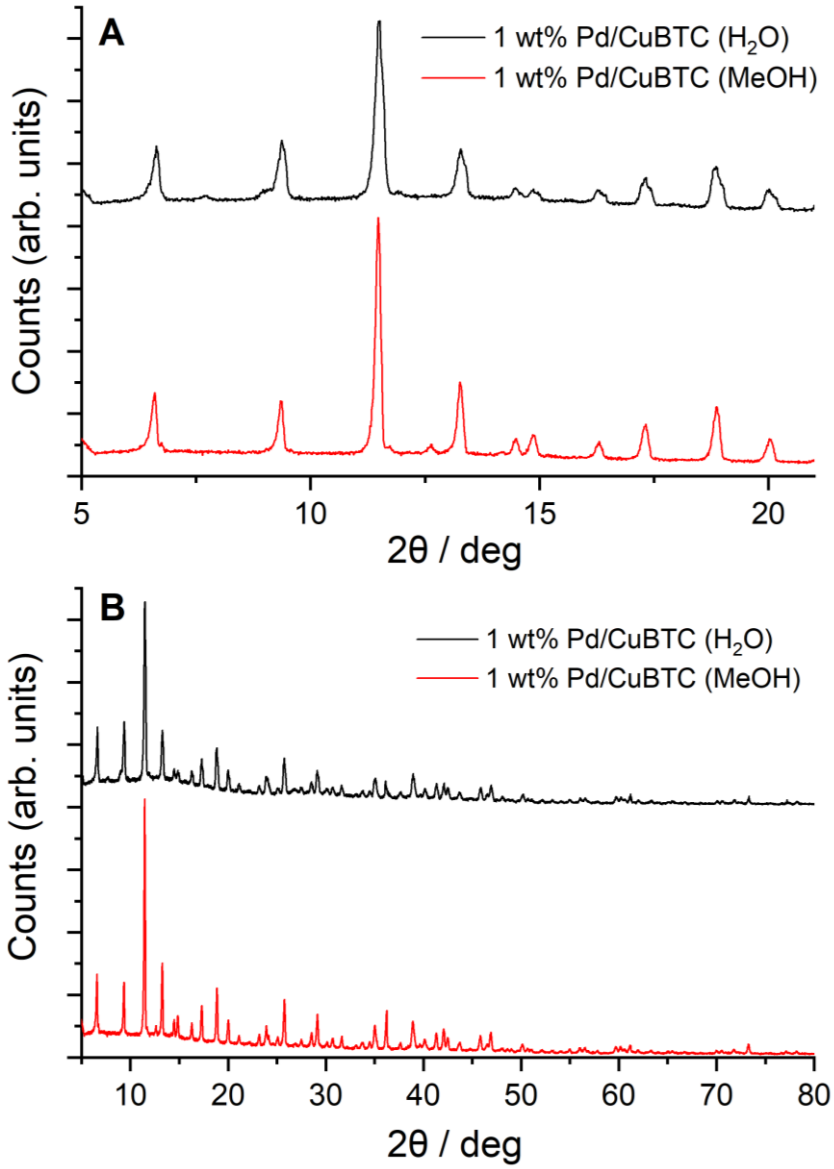

Figure 39: XRD patterns of 1 wt% Pd/CuBTC composites prepared via sol-immobilisation using water and methanol as a solvent respectively, shown in a) 5-20 degrees 2θ; b) 5-80 degrees 2θ.

3.3.7 Thermal stability of CuBTC and CuTPA MOFs

Thermogravimetric analysis was performed on CuBTC, 1 wt% Pd/CuBTC, CuTPA and 1 wt% Pd/CuTPA, with the results displayed in **Figure 40**. The results illustrate that a significant quantity of water is adsorbed into CuBTC, evidenced by a drop of up to a third of the sample weight by 200 °C, which is a sufficient temperature to release adsorbed water within the MOF pores. Both CuBTC and Pd/CuBTC have very similar thermal stabilities (**Figure 40a**) and begin to thermally decompose above 300 °C, with a sharp drop at ~360 °C ascribed to the BTC ligands decomposing, leaving carbon and CuO as residue. Literature suggests that the fact that CuBTC adsorbs a large amount of water is actually detrimental to its thermal stability, since the removal of the water leaves a large quantity of coordinatively-unsaturated copper sites, which are fundamentally less stable than the saturated sites seen in other, more stable, MOFs.[53]

This may explain the additional thermal stability of CuTPA compared to CuBTC (**Figure 40c**). The CuTPA sample loses less than 10% of its weight as water, and the sharp drop for thermal decomposition of the sample is observed at a slightly higher temperature than for CuBTC. The reduced water loss also suggests that the CuTPA MOF has a substantially lower surface area on which to adsorb water molecules. This lowered surface area may also explain why there is a more noticeable difference in thermal stability between CuTPA and Pd/CuTPA (**Figure 40b**) – water is lost more slowly, which could be due to Pd nanoparticles occupying a relatively-larger amount of the available surface area, whereas for Pd/CuBTC, the proportion of the overall surface area occupied by the Pd nanoparticles will be substantially smaller.

The thermal stability of these frameworks is relevant to their potential applications as catalysts. It is clear that NP-MOF composites will only be applicable as catalysts to reactions within a limited temperature window, since they will irreversibly decompose at what are relatively low temperatures for some types of catalytic reaction. For instance, CO oxidation often takes place at high temperatures, such as in car exhausts, although one focus of supported nanoparticle and nanocomposite research has been to develop catalysts that function under 200 °C, some even operating as low as 100 °C[54] or at room temperature.[55] However, there have been many examples of using heat treatments or alternative methods to decompose these nanocomposites into new species that are also catalytically-active, and this will be a focus of this study and explored further in the next chapter.

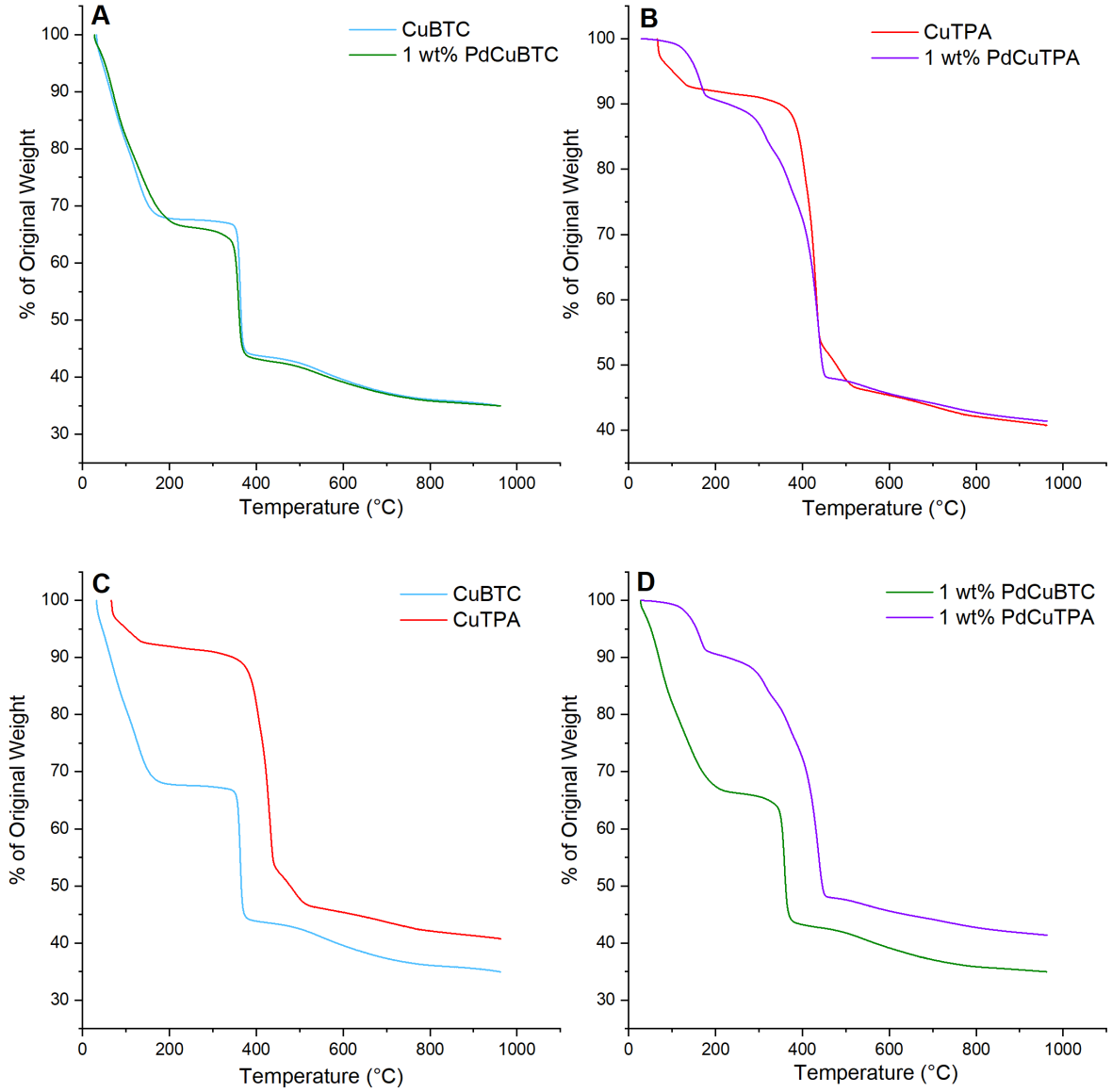

Figure 40: Results for thermogravimetric analysis on CuBTC, 1 wt% Pd/CuBTC, CuTPA and 1 wt% Pd/CuTPA, displayed as a) CuBTC and 1 wt% Pd/CuBTC; b) CuTPA and 1 wt% Pd/CuTPA; c) CuBTC and CuTPA; and d) 1 wt% Pd/CuBTC and 1 wt% Pd/CuTPA, for straightforward comparison.

3.4 Conclusions

A composite of Pd nanoparticles and the CuBTC metal-organic framework was produced via hydrothermal synthesis of CuBTC and sol-immobilisation of PVA-capped Pd nanoparticles on to the CuBTC surface. X-ray diffraction indicated that the CuBTC framework remains mostly intact during the immobilisation of the nanoparticles, with the exception of some loss of crystallinity and formation of Cu_2O from abstracted copper atoms. The loading of the Pd NPs was confirmed via energy dispersive X-ray analysis (EDX) and microwave plasma atomic emission spectroscopy (MP-AES). Transmission electron micrographs of the Pd/CuBTC composite determined that the composite features rods of CuBTC with Pd nanoparticles well dispersed across the rod surfaces, with typical nanoparticle diameters of 5-10 nm. This demonstrates that the sol-immobilisation method can be successfully extended to using metal-organic frameworks as a nanoparticle support.

XAFS analysis of the Cu K edge for CuBTC and Pd/CuBTC was used to confirm the slight degradation of the sample during sol-immobilisation and elucidate the local coordination environment of the Cu atoms in the framework. Examining the Pd K edge for the nanoparticles in Pd/CuBTC suggested that an interstitial carbide is forming in the nanoparticles during the immobilisation process, although only to a small degree. This was supported by a slight expansion in Pd-Pd scattering distance upon EXAFS fitting.

Varying the loading of the Pd NPs on the MOF was shown to be possible across a range of 0.25-1 wt% Pd. Changing the loading of the Pd NPs did not significantly alter the structure of the MOF, but XRD analysis suggests that a lower nanoparticle loading leads to faster degradation of the MOF crystal structure when exposed to water, causing increased Cu_2O formation.

The synthesis method for the Pd/CuBTC composites was extended to other MOFs, using the example of CuTPA, which demonstrates similar behaviour to CuBTC, including some degradation in water during immobilisation. Additionally, a synthesis of the Pd/CuBTC composite using a MeOH-based sol-immobilisation rather than the conventional water-based method was also demonstrated. The resultant composites exhibited greater crystallinity and stability compared to their analogues prepared in water, which will have an impact on the type of nanocomposite catalysts they can be modified into. Finally, the thermal stability of the CuBTC and CuTPA MOFs was investigated, since their observed lack of stability at high temperatures directly affects the range of reactions their derivative catalysts can be applied to.

3.5 References

1 W. Xiang, Y. Zhang, H. Lin and C. Liu, *Molecules*, 2017, **22**, 2103.

2 B. Wang, W. Liu, W. Zhang and J. Liu, *Nano Res.*, 2017, **10**, 3826–3835.

3 Q. Yang, W. Liu, B. Wang, W. Zhang, X. Zeng, C. Zhang, Y. Qin, X. Sun, T. Wu, J. Liu, F. Huo and J. Lu, *Nat. Commun.*, 2017, **8**, 1–9.

4 K. Na, K. M. Choi, O. M. Yaghi and G. A. Somorjai, *Nano Lett.*, 2014, **14**, 5979–5983.

5 S. Hermes, M. K. Schroeter, R. Schmid, L. Khodeir, M. Muhler, A. Tissler, R. W. Fischer and R. A. Fischer, *Angew. Chemie - Int. Ed.*, 2005, **44**, 6237–6241.

6 F. Schröder, D. Esken, M. Cokoja, M. W. E. Van Den Berg, O. I. Lebedev, G. Van Tendeloo, B. Walaszek, G. Buntkowsky, H. H. Limbach, B. Chaudret and R. A. Fischer, *J. Am. Chem. Soc.*, 2008, **130**, 6119–6130.

7 T. Ishida, M. Nagaoka, T. Akita and M. Haruta, *Chem. - A Eur. J.*, 2008, **14**, 8456–8460.

8 T. Ishida, N. Kawakita, T. Akita and M. Haruta, *Gold Bull.*, 2009, **42**, 267–274.

9 Q. Yang, Q. Xu and H. L. Jiang, *Chem. Soc. Rev.*, 2017, 46, 4774–4808.

10 M. Sabo, A. Henschel, H. Fröde, E. Klemm and S. Kaskel, *J. Mater. Chem.*, 2007, **17**, 3827–3832.

11 N. Cao, L. Yang, H. Dai, T. Liu, J. Su, X. Wu, W. Luo and G. Cheng, *Inorg. Chem.*, 2014, **53**, 10122–10128.

12 A. Aijaz, A. Karkamkar, Y. J. Choi, N. Tsumori, E. Rönnebro, T. Autrey, H. Shioyama and Q. Xu, *J. Am. Chem. Soc.*, 2012, **134**, 13926–13929.

13 D. Y. Hong, Y. K. Hwang, C. Serre, G. Férey and J. S. Chang, *Adv. Funct. Mater.*, 2009, **19**, 1537–1552.

14 Q. L. Zhu, J. Li and Q. Xu, *J. Am. Chem. Soc.*, 2013, **135**, 10210–10213.

15 A. Rossin and M. Peruzzini, *Chem. Rev.*, 2016, **116**, 8848–8872.

16 L. He, Y. Liu, J. Liu, Y. Xiong, J. Zheng and Y. Liu, *Angew. Chemie - Int. Ed.*, 2013, **52**, 3741–3745.

17 C. Kuo, Y. Tang, L. Chou, B. T. Sneed, C. N. Brodsky and Z. Zhao, *J. Am. Chem. Soc*, 2012, **134**, 14345–14348.

18 J. Bae, J. S. Choi, S. Hwang, W. S. Yun, D. Song, J. Lee and N. C. Jeong, *ACS Appl. Mater. Interfaces*, 2017, **9**, 24743–24752.

19 A. A. Yakovenko, J. H. Reibenspies, N. Bhuvanesh and H. C. Zhou, *J. Appl. Crystallogr.*, 2013, **46**, 346–353.

20 T. Toyao, K. Liang, K. Okada, R. Ricco, M. J. Styles, Y. Tokudome, Y. Horiuchi, A. J. Hill, M. Takahashi, M. Matsuoka and P. Falcaro, *Inorg. Chem. Front*, 2015, **2**, 434.

21 B. Panella, M. Hirscher, H. Pütter and U. Müller, *Adv. Funct. Mater.*, 2006, **16**, 520–524.

22 N. Al-Janabi, P. Hill, L. Torrente-Murciano, A. Garforth, P. Gorgojo, F. Siperstein and X. Fan, *Chem. Eng. J.*, 2015, **281**, 669–677.

23 K. Tan, N. Nijem, Y. Gao, S. Zuluaga, J. Li, T. Thonhauser and Y. J. Chabal, *CrystEngComm*, 2015, **17**, 247–260.

24 J. Cortes-Suarez, V. Celis-Arias, H. I. Beltran, A. Tejeda-Cruz, I. A. Ibarra, J. E. Romero-Ibarra, E. Sanchez-Gonzalez and S. Loera-Serna, *ACS Omega*, 2019, **4**, 5275–5282.

25 Y. G. Chung, E. Haldoupis, B. J. Bucior, M. Haranczyk, S. Lee, H. Zhang, K. D. Vogiatzis, M. Milisavljevic, S. Ling, S. Camp, B. Slater, J. I. Siepmann, D. S. Sholl and R. Q. Snurr, *J. Chem. Eng. Data*, 2019, **64**, 5985–5998.

26 A. Gainanova, G. Kuz, A. Mushtakov, Q. Nguyen, I. Akin, E. Khramov, A. Zhukova, E. Markova, R. Terekhova and D. Zhukov, *J. Phys. Chem. C*, 2023, **127**, 18365–18377.

27 J. M. Castillo, T. J. H. Vlugt and S. Calero, *J. Phys. Chem. C*, 2008, **112**, 15934–15939.

28 D. Kim, I. J. Kim, H. T. Kwon, K. Paeng and H. Lee, *ACS Omega*, 2023, **8**, 14900–14906.

29 P. Goyal, A. Paruthi, D. Menon, R. Behara, A. Jaiswal, K. V, A. Kumar, V. Krishnan and S. K. Misra, *Chem. Eng. J.*, 2022, **430**, 133088.

30 K.-S. Lin, A. K. Adhikari, C.-N. Ku, C.-L. Chiang and H. Kuo, *Int. J. Hydrogen Energy*, 2012, **37**, 13865–13871.

31 J. B. Decoste, G. W. Peterson, B. J. Schindler, K. L. Killops, M. A. Browe and J. J. Mahle, *J. Mater. Chem. A*, 2013, **1**, 11922–11932.

32 W. Wang, Z. Liao, Y. Wang, X. Wu, F. Qu and X. Zhang, *Cryst. Res. Technol.*, 2011, **46**, 300–304.

33 S.S.Y. Chui, S.M.F. Lo, J.P.H. Charmant, A.G. Orpen and I.D. Williams, *Science (80-.).*, 1999, **283**, 1148.

34 S. M. Rogers, C. R. A. Catlow, C. E. Chan-Thaw, A. Chutia, N. Jian, R. E. Palmer, M. Perdjon, A. Thetford, N. Dimitratos, A. Villa and P. P. Wells, *ACS Catal.*, 2017, **7**, 2266–2274.

35 N. C. Tomson, K. D. Williams, X. Dai, S. Sproules, S. Debeer, T. H. Warren and K. Wieghardt, *Chem. Sci.*, 2015, **6**, 2474–2487.

36 F. De Groot, G. Vankó and P. Glatzel, *J. Phys. Condens. Matter*, 2009, **21**, 104207.

37 C. Popa, T. Zhu, I. Tranca, P. Kaghazchi, T. Jacob and E. J. M. Hensen, *Phys. Chem. Chem. Phys.*, 2015, **17**, 2268–2273.

38 P. Wu, Y. Cao, L. Zhao, Y. Wang, Z. He, W. Xing, P. Bai, S. Mintova and Z. Yan, *J. Catal.*, 2019, **375**, 32–43.

39 W. Jones, P. P. Wells, E. K. Gibson, A. Chutia, I. P. Silverwood, C. R. A. Catlow and M. Bowker, *ChemCatChem*, 2019, **11**, 4219–4442.

40 A. L. Bugaev, O. A. Usoltsev, A. A. Guda, K. A. Lomachenko, I. A. Pankin, Y. V. Rusalev, H. Emerich, E. Groppo, R. Pellegrini, A. V. Soldatov, J. A. Van Bokhoven and C. Lamberti, *J. Phys. Chem. C*, 2018, **122**, 12029–12037.

41 A. L. Bugaev, A. A. Guda, K. A. Lomachenko, L. A. Bugaev and A. V. Soldatov, *Bull. Russ. Acad. Sci. Phys.*, 2015, **79**, 1180–1185.

42 T. Xie and R. M. Rioux, *Catal. Today*, 2021, **371**, 29–39.

43 N. K. Nag, *J. Phys. Chem. B*, 2001, **105**, 5945–5949.

44 S. B. Ziemecki, G. A. Jones, D. G. Swartzfager, R. L. Harlow and J. Faber, *J. Am. Chem. Soc.*, 1985, **107**, 4547–4548.

45 D. J. Tranchemontagne, J. R. Hunt and O. M. Yaghi, *Tetrahedron*, 2008, **64**, 8553–8557.

46 B. Zhang, Y. Luo, K. Kanyuck, G. Bauchan, J. Mowery and P. Zavalij, *J. Agric. Food Chem.*, 2016, **64**, 5164–5170.

47 R. Adams, C. Carson, J. Ward, R. Tannenbaum and W. Koros, *Microporous Mesoporous Mater.*, 2010, **131**, 13–20.

48 S. Bhattacharjee, C. Chen and W. S. Ahn, *RSC Adv.*, 2014, **4**, 52500–52525.

49 H. Kim and C. S. Hong, *CrystEngComm*, 2021, **23**, 1377–1387.

50 J. Winarta, B. Shan, S. M. McIntyre, L. Ye, C. Wang, J. Liu and B. Mu, *Cryst. Growth Des.*, 2020, **20**, 1347–1362.

51 B. Liu, K. Vikrant, K. H. Kim, V. Kumar and S. K. Kailasa, *Environ. Sci. Nano*, 2020, **7**, 1319–1347.

52 G. F. Tierney, S. Alijani, M. Panchal, D. Decarolis, M. B. de Gutierrez, K. M. H. Mohammed, J. Callison, E. K. Gibson, P. B. J. Thompson, P. Collier, N. Dimitratos, E. C. Corbos, F. Pelletier, A. Villa and P. P. Wells, *ChemCatChem*, 2021, **13**, 5121–5133.

53 C. Healy, K. M. Patil, B. H. Wilson, L. Hermanspahn, N. C. Harvey-Reid, B. I. Howard, C. Kleinjan, J. Kolien, F. Payet, S. G. Telfer, P. E. Kruger and T. D. Bennett, *Coord. Chem. Rev.*, 2020, **419**, 213388.

54 A. Lin, A. A. Ibrahim, P. Arab, H. M. El-Kaderi and M. S. El-Shall, *ACS Appl. Mater. Interfaces*, 2017, **9**, 17961–17968.

55 S. Gatla, D. Aubert, G. Agostini, O. Mathon, S. Pascarelli, T. Lunkenbein, M. G. Willinger and H. Kaper, *ACS Catal.*, 2016, **6**, 6151–6155.

Chapter 4 Generation of PdCu Nanocomposites

4.1 Introduction

Whilst the previous chapter focused on the generation of composite materials from Pd nanoparticles and Cu-based metal-organic frameworks, this chapter will focus on destroying the porous MOF structure in these composites to yield nanocomposite materials. Within the field of NP-MOF composites, a popular approach has been to exploit the relative instability of metal-organic frameworks[1] to derive nanoparticle structures from an NP-MOF template. The methods involved in a transformation can be broadly divided into thermal methods, where the composite is heated to very high temperatures (typically 700-1000 °C)[2] to induce thermal decomposition; and chemical methods, where a reducing agent is employed to break down the framework.[3]

4.1.1 Thermal Methods of Nanocomposite Generation

Thermal treatments have been extensively used to produce these nanocomposites[4], pyrolysing the MOF lattice to produce nanoparticles on a metal oxide or carbon support. For example, Zhang et al[5] used pyrolysis of CuBTC MOF at 500 °C to generate Cu NPs stabilised in a carbon matrix (Cu@C), and also doped the copper-containing MOF with zinc to produce the bimetallic Cu/Zn@C system. The support interactions from the carbon matrix were used to stabilise the Cu NPs at sufficiently high temperatures for them to effectively catalyse CO_2 hydrogenation via the reverse water-gas shift reaction, since Cu NPs tend to aggregate above 300 °C[6], reducing their surface area and catalytic effectiveness. Jagadeesh *et al.*[7] also used pyrolysis of a cobalt-based MOF to synthesise Co NPs and cobalt/cobalt-oxide core-shell NPs in a carbon matrix, for use as amination catalysts.

MOF pyrolysis is not limited to producing nanocomposites with a carbon matrix. Zamaro *et al.*[8] used thermal treatments to produce CuO NPs and CuO/CeO_2 systems, with the ceria being impregnated on to the MOF prior to pyrolysis. These systems were demonstrated as being active for CO oxidation, with the ceria-supported nanoparticles being significantly more active than the bare CuO NPs. Similarly, Liu *et al.*[9] impregnated the pores of MOF-5 with $PtCl_4$ before heating at 600 °C to yield Pt/ZnO nanocomposites, which were seen to be twice as active for CO oxidation than Pt/ZnO samples produced via conventional methods.[10]

However, these thermal treatment methods have generally been considered to afford a lack of control in the structure of the product, since pyrolysis is inherently a brute-force process. The

organic linkers can either be evaporated or carbonised locally[11], which generates the carbon matrices seen in previous examples, but there are limited parameters with which to control the nanostructure. Santos *et al.*[12] used a slow temperature ramp to encapsulate iron atoms from FeBTC MOF into a carbon matrix, with an additional carbon source from furfuryl alcohol, using the heating parameters to generate their desired carbon-based nanostructure. Additionally, Jalal *et al.*[13] varied the overall temperature of pyrolysis to vary the defect density within their carbon support, demonstrating that increasing the pyrolysis temperature beyond 800 °C produced nanocomposite catalysts that remained stable for hydrogenation of butadiene over a longer period than those produced at 400 °C. Absolute temperature and ramp rate therefore afford some limited control over the properties of the resultant nanocomposites, but this project aims to explore alternative methods for achieving this transformation that yield a finer level of modulation.

One other important consideration for the pyrolysis method is the concepts of the Tammann and Hüttig temperatures. The Tammann temperature for a metal is estimated at half the metal's melting point in Kelvin, and is the point at which bulk atoms begin to diffuse significantly.[14] Similarly, the Hüttig temperature describes the point at which atoms at the surface achieve significant mobility, and is generally estimated as 30% of a metal's melting point in Kelvin.[15] Using the example of copper metal, which has a melting point around 1356 K[16], the Tammann and Hüttig temperatures would be 405 °C and 134 °C respectively[17,18], or well within the range of the pyrolysis temperatures discussed in this section. The effects of high-temperature MOF pyrolysis therefore become clear: nanoparticles on the surface will likely achieve mobility during the process, which can lead to aggregation and sintering in the resulting nanocomposite.[19] There are methods that can limit this aggregation for NP-based catalysts, such as by using ultrahigh pressures during pyrolysis[20], or by exploiting strong metal-support interactions[21,22] to encourage the nanoparticles to remain in place, but generally this remains a significant concern for the thermal method that must be at least mitigated.

4.1.2 Chemical Methods of Nanocomposite Generation

The use of chemical methods to reduce MOFs, such as via reducing agents like sodium borohydride ($NaBH_4$), has been generally unexplored. In one early example, Li *et al.*[23] combined calcination with etching by ascorbic acid of CuBTC MOF to produce Cu NPs inside octahedral shells of TiO_2 for use as photocatalysts. Simultaneous etching by ascorbic acid and reduction of the Cu^{2+} cations released by etching was shown to effectively produce $Cu@TiO_2$ nanocomposites that were active for photocatalytic hydrogen production, with the Cu co-catalyst enhancing charge separation. In contrast, the sample produced via calcination was

significantly less active, which was attributed to increased Cu particle size and the presence of carbon residues generated by the calcination.

More recently, Fu *et al.*[24] examined $NaBH_4$ as a reducing agent for MOFs, using a slow catalytic reduction using ethanol as a solvent to reduce CuBTC MOF, producing Cu NPs whilst partly retaining the original MOF structure. Their rationale for this was that reduction with water as a solvent leads to a significantly faster rate of dissociation for the reducing agent, destroying the framework entirely, but the slower rate obtained with ethanol allows the delicate porosity of the MOF to be maintained. It is a broadly-similar approach to that reported in this chapter, but focuses on the reduction of bare CuBTC MOF rather than a Pd/CuBTC nanocomposite, and prioritises retention of the base structure rather than a transformation to a metal oxide-based support.

The general paucity of research in this area presents an interesting opportunity: is there a way to exploit a chemical-based method, operating at room temperature and pressure and therefore possible on a laboratory bench, to synthesise nanocomposites derived from NP-MOF composite structures, whilst also retaining control over their physical properties in a manner that a pyrolysis-based method cannot?

This chapter will explore how the Pd/CuBTC nanocomposites derived in the previous chapter can be used as a sacrificial template, using reduction via $NaBH_4$ to yield PdCu-based nanocomposites supported on a mixed copper oxide support. Whilst the reduction reaction can be carried out at room temperature, it generates a significant amount of local heat, which is hypothesised to allow local diffusion of Cu atoms, with the help of coordination to 4-aminophenol produced via the *in situ* reduction of 4-nitrophenol, facilitating alloying to produce bimetallic PdCu nanoparticles. Additionally, the oxidation state of the copper oxide support, and the extent of Pd-Cu alloying within the nanoparticles, are demonstrated to be controlled using simple variation of parameters in the reduction reaction.

4.2 Experimental Details

Synthesis of Pd/MOF composites: All CuBTC and CuTPA MOFs used to produce the Pd/CuBTC composites used in this chapter were synthesised via the 1:1:1 DMF:H_2O:EtOH hydrothermal synthesis method outlined in Chapter 3. The Pd/CuBTC and Pd/CuTPA composites were produced via the water-based sol-immobilisation method, using PVA as a capping agent, also outlined in Chapter 3, with the exception of the MeOH-based composites studied in **Section 4.3.2.1**, which used only MeOH as a solvent and no associated capping agent.

Reduction of Pd-CuMOF composites: PdCu/Cu_2O nanocomposites were generated by reduction of Pd/CuBTC composites using excess $NaBH_4$ in the presence of 4-nitrophenol, which is itself reduced to 4-aminophenol during the reaction. 500mg of Pd/CuBTC was added to a 70 mL aqueous solution of 0.00018 M 4-nitrophenol before adding 100 mL of 0.0397 M $NaBH_4$ in H_2O, which yields a minimum $NaBH_4$/metal molar ratio of 1.5:1. After a minimum of 30 minutes, at which point generated hydrogen bubbles had dissipated, the samples were collected by centrifugation at 3500 rpm for six minutes in Falcon centrifuge tubes, washed thoroughly with H_2O, centrifuged again under the same conditions, and then dried at 80 °C overnight.

For the optimised sample series discussed in **Section 4.3.3**, samples were prepared at reduced $NaBH_4$ concentrations of 0.0036 M, 0.0049 M, and 0.0085 M to test variation in that parameter. For the samples testing a variation in reduction temperature, the water used to dissolve the $NaBH_4$ was held at temperatures of 1 °C, 25 °C, 50 °C and 75 °C respectively, with the Pd/CuBTC powder and 4-NP solutions added and brought to that temperature, before the final addition of $NaBH_4$ to begin the reduction. Finally, nanocomposites were prepared using increased 4-NP concentrations of 0.001 M, 0.005 M, and 0.01 M to examine variation.

XRD: X-ray diffraction patterns were recorded on a Rigaku Miniflex diffractometer at the Material Characterisation Laboratory, Harwell, using aluminium sample holders. The patterns were recorded across a range of $2\theta = 5° - 80°$ with a step size of 0.02° and a scan speed of 5° min^{-1}.

XAFS: Pd K edge XAFS data was acquired using the B18 beamline at Diamond Light Source synchrotron, located at the Rutherford Appleton Laboratory, Harwell. Measurements were performed using the QEXAFS setup with a Si (311) monochromator and ion chamber detectors.

For the experiment in **Section 0**, measurements were performed in fluorescence mode using a 36-element Ge detector. Samples were prepared as pellets with 8 mm diameter using a cellulose binder. For the experiment in **Section 4.3.4**, measurements were performed in transmission mode, using 13 mm pellets, again using a cellulose binder, with the pellet loading calculated to obtain an optimal absorbance edge step of approximately 1.

TEM: Transmission electron micrographs were recorded using a JEOL JEM 2100 with a lanthanum hexaboride (LaB_6) filament at an accelerating voltage of 200 kV. Samples were prepared by being dispersed on holey carbon TEM grids. High-resolution TEM was performed on a JEOL ARM200F at the electron Physical Sciences Imaging Centre (ePSIC) at Diamond Light Source, also at an accelerating voltage of 200 kV.

4.3 Results and Discussion

4.3.1 Formation of a copper oxide substrate

4.3.1.1 Nanocomposites derived from Pd/CuBTC

As an initial test of whether a chemical method could successfully produce nanocomposites with controllable physical properties, the Pd/CuBTC composites produced and characterised in the previous chapter were treated with sodium borohydride ($NaBH_4$) at room temperature, in the presence of 4-nitrophenol. Cu^{2+} ions, the dominant species in the CuBTC MOF support, react with $NaBH_4$ and are reduced to copper metal, which is then able to re-oxidise in air to produce Cu_2O.[25] This reaction has itself been employed to generate Cu nanoparticles[26], although the aim in this project is to generate PdCu alloyed nanoparticles supported on a copper oxide substrate. The use of 4-nitrophenol in the reduction stems from the use of nitroarene reduction as a model reaction for the testing of nanoparticle catalysts[27] – many noble metals, including Pd, display catalytic activity for the reduction of 4-nitrophenol to 4-aminophenol with $NaBH_4$, and this chapter will discuss the influence that the organic compound has on the resulting structure of the nanocomposites.

The reduction products for Pd/CuBTC samples with 1 wt%, 0.5 wt% and 0.25 wt% Pd loading were analysed by X-ray diffraction, with the resulting patterns displayed in **Figure 41**. These patterns show a mixture of Cu_2O and Cu^0 phases, most clearly illustrated by the peaks at 36.3° and 42.3°, which correspond to the (111) and (200) reflections for body-centred cubic cuprite[28] (Cu_2O); and by the peaks at 43.3 and 50.4 degrees, which are caused by the reflections from the (111) and (200) planes of face-centred cubic metallic Cu.[29]

Because of the presence of these mixed phases in the support, sample nomenclature will use "PdCu/Cu_2O" to indicate a nanocomposite formed by reduction of the Pd/CuMOF composites; however, the presence of other copper oxide phases in the support will be discussed when relevant. Additionally, it should be noted that the reduction process removes the organic ligands attached to the Cu^{2+} ions in the MOF, which is a significant proportion of its weight. Consequently, for simplicity, sample nomenclature will refer to a weight-percentage loading as the calculated loading for the original Pd/CuMOF composite, as the relative weight percentage of Pd in the reduced nanocomposites increases during reduction.

Figure 41 shows how the mixed Cu^0/Cu_2O structure of the reduced Pd/CuBTC samples does not change significantly when varying the weight percentage of Pd on the original composite. However, the 0.5 wt% Pd sample is observed to have a higher proportion of Cu_2O than the other two samples, as evidenced by an increase in intensity of the corresponding reflections.

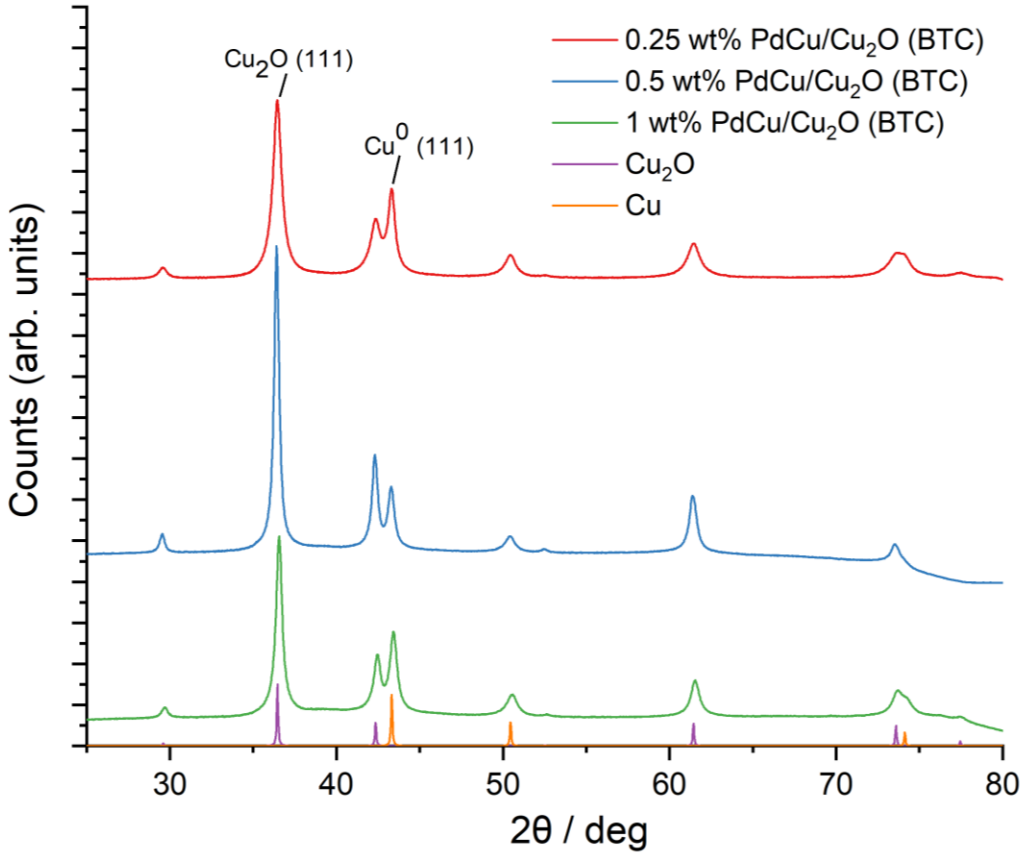

Figure 41: X-ray diffraction patterns of Pd/CuBTC samples with loadings of 1 wt%, 0.5 wt% and 0.25 wt% Pd, after reduction with $NaBH_4$ in the presence of 4-NP to yield $PdCu/Cu_2O$.

The crystallite size of the reduced nanocomposites can be calculated by the Scherrer equation (**Section 2.2**). Using the common approximation of 0.9 for the shape factor[30], and examining the most significant peaks for each copper phase, estimated crystallite sizes for each nanocomposite loading are listed in **Table 3**.

Given the 0.25 wt% sample displays the smallest copper oxide crystallites for both phases, it is possible that a consequent decreased Pd coverage on the CuBTC MOF surface in the sample with lower loading facilitates the access of $NaBH_4$ to the MOF's Cu^{2+} ions, which could create more nucleation sites for the copper oxide phases, leading to a corresponding decrease in crystallite size.

Table 3: Estimated crystallite sizes for 1 wt%, 0.5 wt% and 0.25 wt% PdCu/Cu_2O nanocomposites, using the Scherrer equation, taking the shape factor to be 0.9, and examining the Cu_2O (111) and Cu^0 (111) reflections.

Sample ID	Cu_2O crystallite size estimate / nm	Cu^0 crystallite size estimate / nm
PdCu/Cu_2O 1 wt%	36.4	30.5
PdCu/Cu_2O 0.5 wt%	44.0	34.2
PdCu/Cu_2O 0.25 wt%	26.1	26.7

The effect of reducing the Pd/CuBTC composite with $NaBH_4$ without the presence of 4-nitrophenol is illustrated in **Figure 42**. The diffraction pattern is observed to be significantly more complex, but can be resolved into patterns corresponding to Cu^0, Cu_2O and CuO species. The most intense peaks at 35.5° and 38.6° suggest that this nanocomposite is mostly dominated by CuO, but the remainder of the pattern indicates that there are also significant amounts of Cu_2O and zero-valent copper metal present.

This demonstrates that 4-nitrophenol, or the reduced product 4-aminophenol, is influencing the formation and resulting oxidation state of the copper oxide support, since CuO is not observed at all when 4-NP is added before reduction with $NaBH_4$. The different ratio of Cu_2O:Cu^0 phases observed for the 0.5 wt% sample in **Figure 41** could therefore potentially be ascribed to a slight difference in the amount of 4-nitrophenol present during the reduction.

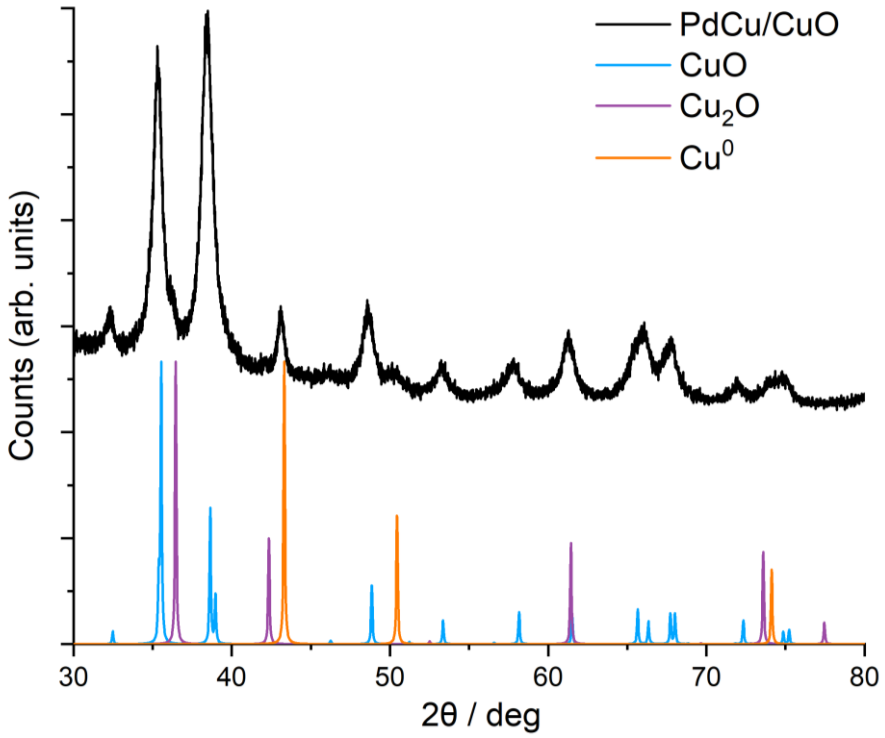

Figure 42: X-ray diffraction pattern of PdCu/CuO, produced by reducing 1 wt% Pd/CuBTC with $NaBH_4$ without the presence of 4-nitrophenol.

Repetition of the reduction of the 1 wt% Pd/CuBTC composite in the presence of 4-aminophenol and ethanolamine (**Figure 43**) suggests that coordination of amine groups to the copper species during reduction is the dominant factor controlling the oxidation state of the resultant copper support, since reduction with these compounds present produces similar nanocomposites to those produced with 4-nitrophenol (**Figure 41**). It is also notable that the XRD pattern produced by the sample reduced in the presence of 4-aminophenol displays greatly-reduced intensities for the Cu^0 peaks relative to the Cu_2O peaks (e.g., the (200) peak at 50.4° is almost absent), suggesting that that sample is predominantly based on Cu_2O.

The use of these amine ligands is the first step towards being able to control the physical properties of the reduced nanocomposite. Destroying the MOF structure by thermal decomposition would not allow fine-tuning of the oxidation state of the copper substrate, but this chemical approach allows the elimination of a CuO phase from the support to leave a mixed Cu_2O and Cu^0 structure. Optimisation of this preparation method to allow fine-grained control over the Cu_2O/Cu^0 ratio, among other properties, will be discussed further in **Section 4.3.3**.

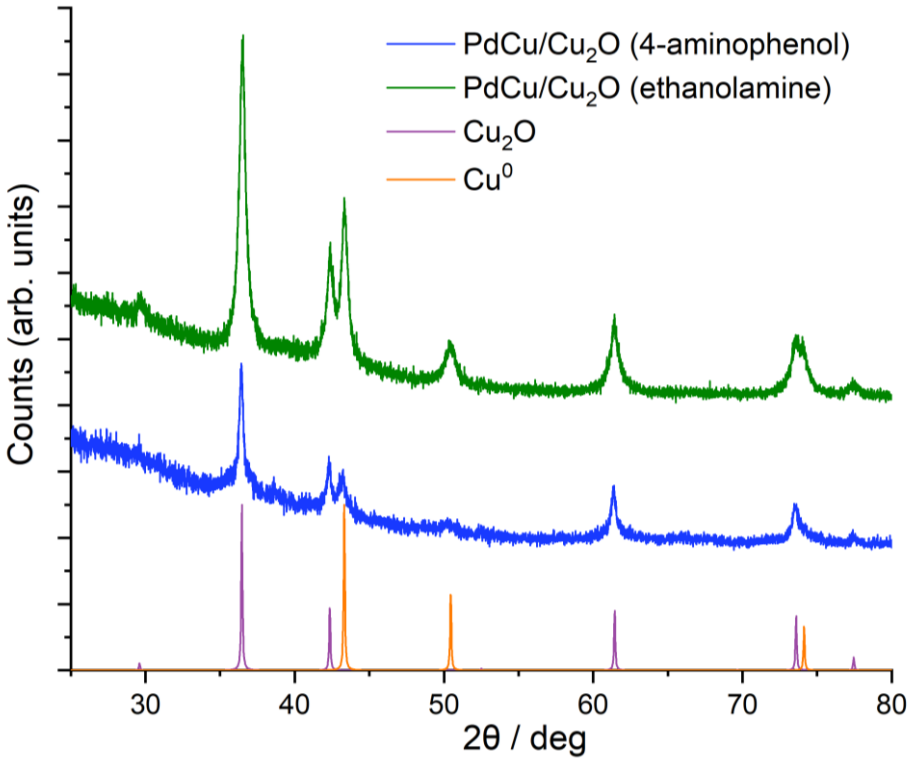

Figure 43: X-ray diffraction patterns of the PdCu/Cu_2O nanocomposites produced following $NaBH_4$ reduction in the presence of 4-aminophenol and ethanolamine, plotted with Cu_2O and Cu^0 reference standards.

4.3.1.2 Nanocomposites derived from Pd/CuTPA

PdCu-based nanocomposites were also produced by the reduction of the Pd/CuTPA MOF discussed in **Section 3.3.5**, using the same reduction method as for the Pd/CuBTC composites above, including the presence of 4-nitrophenol. Nanocomposites with an initial Pd loading of 1 wt% and 0.25 wt% on the MOF were characterised by XRD, with the results displayed in **Figure 44a**. The XRD pattern for the 1 wt% nanocomposite was also compared to a Pd/CuBTC-derived nanocomposite of the same loading, depicted in **Figure 44b**.

It is apparent from **Figure 44a** that the loading of Pd/CuTPA does not significantly influence the balance of Cu^0 and Cu_2O phases present in the final nanocomposite, as the intensity ratios between the various peaks remain approximately the same. This is the same observation as for the 0.25 wt% and 1 wt% BTC-derived samples. The direct comparison between the two choices of MOF in **Figure 44b** demonstrates that PdCu/Cu_2O samples produced from reduction of Pd/CuTPA composites have a very similar structure to those produced from Pd/CuBTC, indicating that either choice of framework ligand would be suitable to synthesise this class of PdCu nanocomposites.

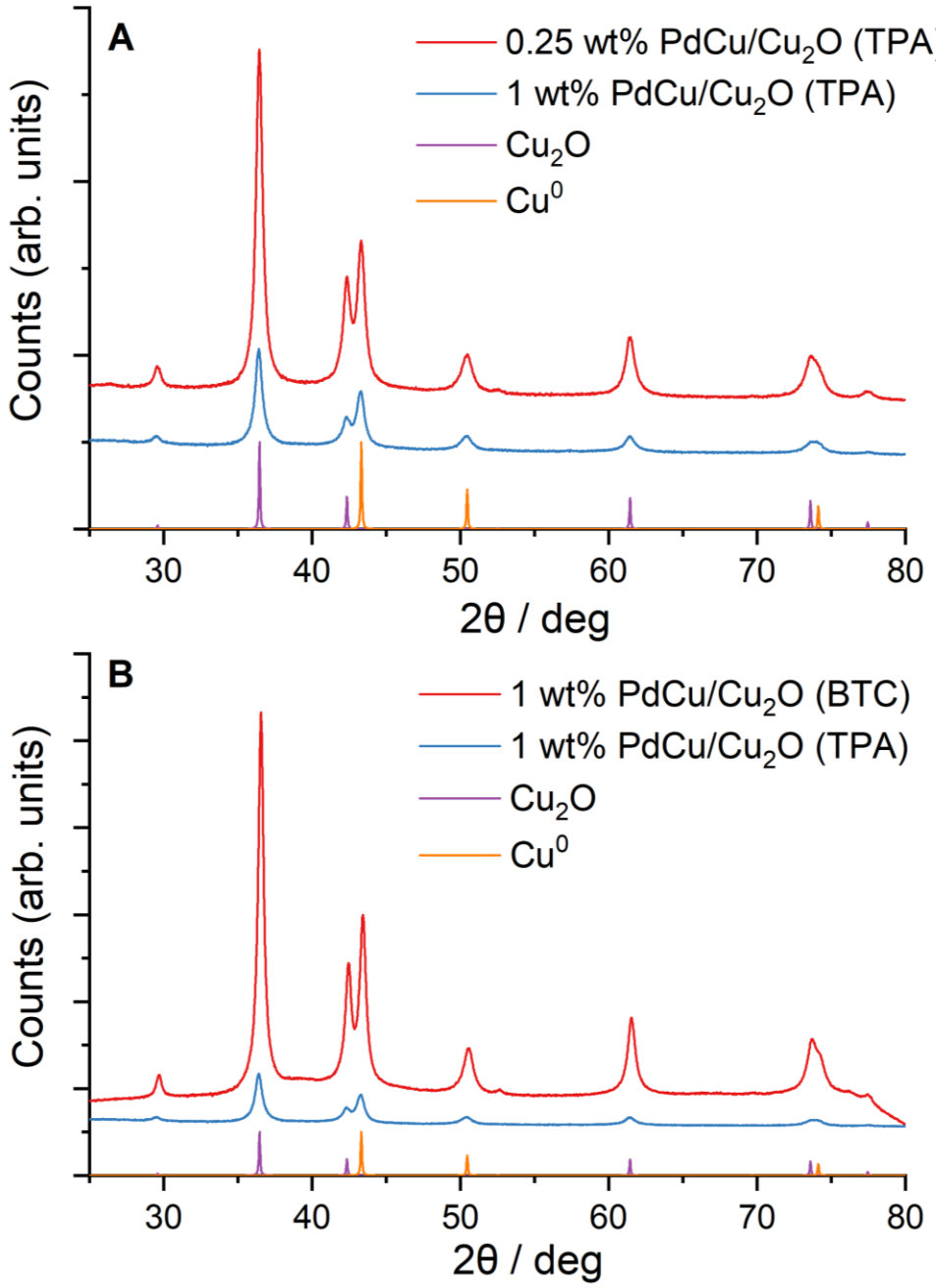

Figure 44: a) X-ray diffraction patterns of 0.25 wt% and 1 wt% $PdCu/Cu_2O$ samples produced from reducing Pd/CuTPA composites with $NaBH_4$ and 4-NP, plotted with reference standards of Cu_2O and Cu^0; b) Comparison of XRD patterns for 1 wt% $PdCu/Cu_2O$ produced from reducing 1 wt% Pd/CuBTC and Pd/CuTPA respectively, under the same conditions as for a).

4.3.2 XAS of PdCu nanocomposites

An X-ray absorption spectroscopy (XAS) study was performed on six nanocomposite samples on beamline B18 at Diamond Light Source, examining the Pd K edge at 24.35 keV. The experiment was designed to test the effects of changing the sol-immobilisation solvent, the presence of 4-nitrophenol during reduction, and the concentration of the $NaBH_4$ reducing agent. The relevant experimental details for the samples are summarised in **Table 4**.

Four of the samples, here labelled as PdCu-reduced A, B, E, and F, were prepared using the standard water-based sol-immobilisation method. The first two samples examined (A and B) were both exposed to 4-NP, but sample A was dried after being placed in 4-NP solution, before being reduced. The second water-based sample (B) was reduced using $NaBH_4$ in the presence of 4-NP.

Additionally, two samples, labelled PdCu-reduced C and D, were prepared using methanol as the solvent for sol-immobilisation, as discussed in **Section 3.3.6**. The additional stabilising effects determined for the Pd NPs during the sol-immobilisation process[31], in addition to the increased stability of the CuBTC MOF in the methanol solvent, provide an interesting comparison to the inherent instability of the water-based preparation method.

Finally, the remaining two samples of the four (samples E and F) produced using the water-based method were produced without any exposure to 4-NP at all, but instead using increased concentrations of $NaBH_4$ in the nanocomposite reduction step, of 0.1 M and 1.0 M respectively. The standard concentration of $NaBH_4$ in the reduction step is 0.0397 M, which matches the concentration of $NaBH_4$ used in the reduction of 4-nitrophenol to 4-aminophenol by Pd/CuBTC, and this concentration was retained for the reduction of the other samples.

Table 4: Summary of the PdCu-based nanocomposites analysed using XAS, and their corresponding production methods. All sample loadings were calculated to be 1 wt% Pd during preparation.

Sample ID	Sol-immobilisation solvent	4-Nitrophenol present during reduction?	Reduction conditions	$NaBH_4$ concentration / mol dm^{-3}
PdCu-reduced A	H_2O	No	Exposed to 4-NP, dried, then reduced using $NaBH_4$.	0.0397
PdCu-reduced B	H_2O	Yes	Reduced using $NaBH_4$ with 4-NP present.	0.0397
PdCu-reduced C	MeOH	No	Exposed to 4-NP, dried, then reduced using $NaBH_4$.	0.0397
PdCu-reduced D	MeOH	Yes	Reduced using $NaBH_4$ with 4-NP present.	0.0397
PdCu-reduced E	H_2O	No	Reduced using $NaBH_4$, no exposure to 4-NP.	0.1
PdCu-reduced F	H_2O	No	Reduced using $NaBH_4$, no exposure to 4-NP.	1.0

4.3.2.1 Pd K edge EXAFS and fitting

The PdCu nanocomposites were measured at the Pd K edge in fluorescence mode. The XANES spectra, XANES derivative, and transformations into *k*-space and *R*-space (k^2-weighted, non-phase corrected) for samples A and B are shown in **Figure 45**.

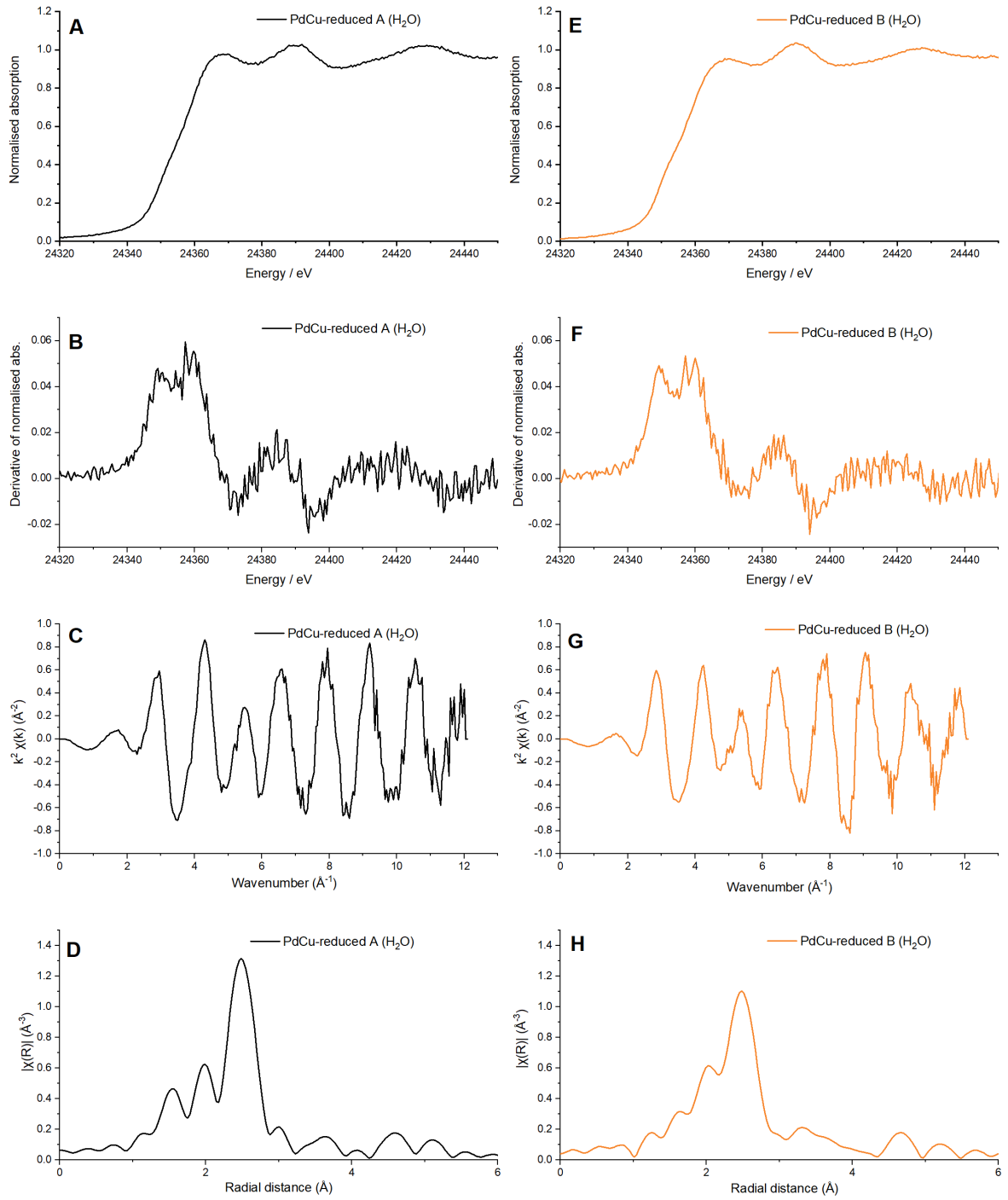

Figure 45: Pd K edge XAFS spectra for sample IDs PdCu-reduced A (black) and Pd-reduced B (orange); where figures A-D represent for the sample PdCu-reduced A a) the normalised absorption coefficient at the Pd K X-ray edge after background subtraction; b) the first derivative of that absorption coefficient; c) the transformation of the absorption signal into *k*-space, weighted by a k^2-term; and d) the Fourier transform of the k^2-weighted *k*-space function into *R*-space; figures E-H are analogous to figures A-D but for the PdCu-reduced B sample.

Whilst the spectra appear very similar, there are some subtle differences that have substantial implications for the local structure of the Pd nanoparticles. When comparing the samples

directly in *k*-space, as seen in **Figure 46a**, there is a slight phase shift in the oscillations towards lower wavenumber for the B sample, prepared by reduction of Pd/CuBTC in the presence of 4-NP. This shift could be explained by comparing the non-phase-corrected Fourier transform data in **Figure 46b**, as there is a raised feature for sample B at ~2.2 Å, in between the two peaks at 2.0 Å and 2.5 Å, effectively appearing as a shoulder on the 2.5 Å peak. It is hypothesised that this is due to the presence of an additional scattering distance in the local coordination environment of the Pd atoms – an additional scatterer would also explain the shift in oscillations in *k*-space, since a modification to the Pd lattice will alter Pd-Pd spacing and change the phase of the oscillations.[32] Considering the possible candidate atoms for scattering and examining the literature, Islam *et al*.[33] reported a similar feature below the main Pd-Pd scattering feature as being evidence of Pd-Cu alloying in their synthesis of PdCu nanoparticles supported on alumina, corroborated by other examples elsewhere.[34,35]

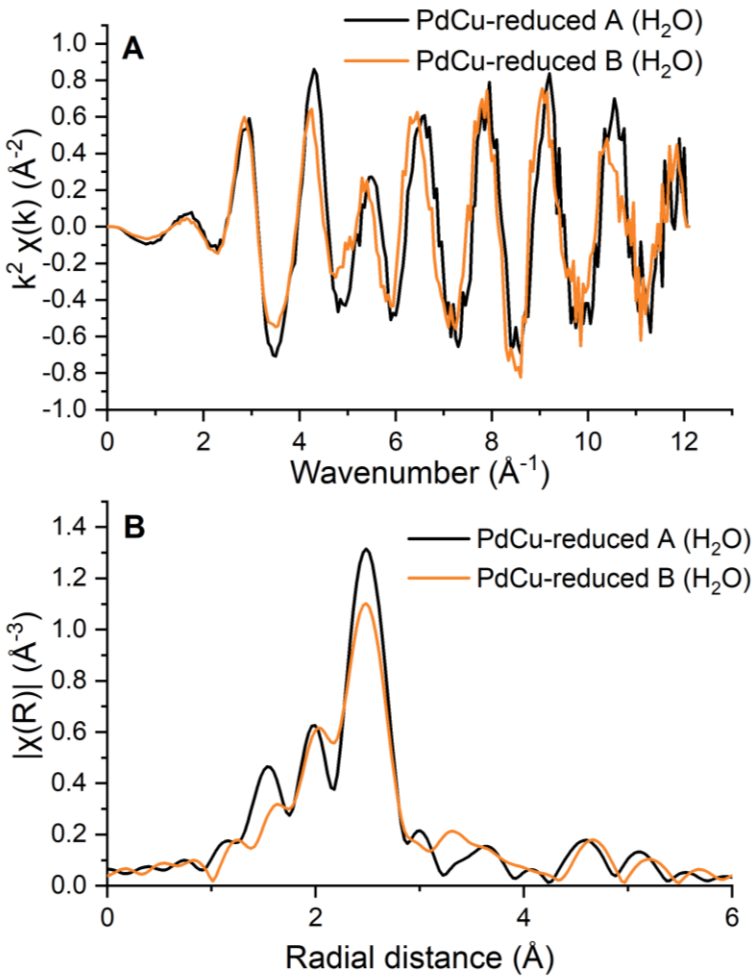

Figure 46: a) Comparisons of the k^2-weighted *k*-space functions of the Pd K edge XAFS spectra for PdCu-reduced samples A and B; b) comparisons of the non-phase-corrected Fourier transform XAFS data at the Pd K edge for PdCu-reduced samples A and B.

To examine the source of this scattering distance, fits of the EXAFS data for both samples A and B were calculated using the program Artemis in the Demeter software package, and are displayed in **Figure 47**. The associated fitting parameters are listed in **Table 5**. The fit for each sample was performed using a simple first-shell model of the coordination environment to minimise the number of free parameters. This choice of model was effective for obtaining an appropriate fit in the window $1.0 < R < 3.0$. The amplitude reduction factor S_0^2 was estimated as 0.85 from a fit of a Pd foil reference standard, and then kept fixed throughout the fitting procedure. This is due to S_0^2 being multiplied by coordination number in the numerator of the EXAFS equation (see **Section 2.6.6**), preventing it from being determined independently for a single shell fit with unknown coordination number.[36]

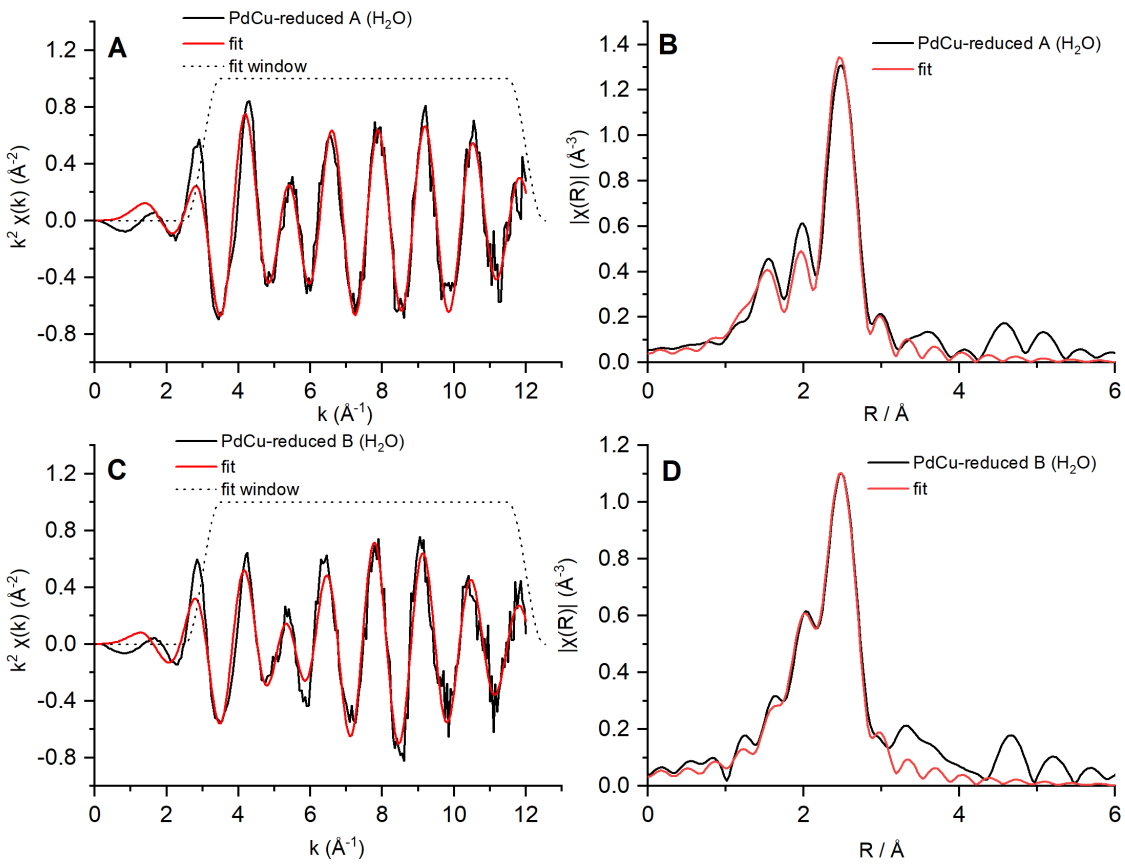

Figure 47: Fits of Pd K EXAFS data for the reduced nanocomposite sample PdCu-reduced A (H_2O prep, no 4-NP at reduction), showing a) the k^2-weighted EXAFS signal (black) with a corresponding fit (red) and fit window (black dots); and b) the magnitude of the k^2-weighted non-phase-corrected Fourier transformed signal (black) with a corresponding fit (red). Figures c) and d) are analogous to a) and b) respectively, but for the reduced nanocomposite sample PdCu-reduced B (H_2O prep with 4-NP at reduction).

Sample A was modelled using Pd-O and Pd-Pd scattering distances in the window $1.0 < R < 3.0$. Whilst the fit struggles to precisely replicate the features at 1.6 Å and 2.0 Å (non-phase-

corrected), the central feature corresponding to Pd-Pd scattering at 2.5 Å and the subsequent feature at 3.0 Å are well-aligned with the fit. The fitted coordination numbers are a Pd coordination of 7.0 (indicating that each Pd atom is on average coordinated to seven other Pd atoms) and a small average oxygen coordination of 0.7, perhaps suggesting reasonably large Pd NPs with a small oxidic surface layer.

The fit for Sample B appears to more accurately model all the features present in the fitting window of the non-phase-corrected Fourier transform, including the unusual shoulder feature at ~2.2 Å. This was achieved by replacing the Pd-O scattering distance used for the previous sample with a Pd-Cu scattering path. The fitting model suggests an average Pd-Pd coordination of 7.3 per atom, with an additional small coordination of 1.4 to neighbouring Cu atoms.

Table 5: EXAFS fitting parameters for the Pd K edge for samples PdCu-reduced A and PdCu-reduced B. Fitting parameters: $S_0^2 = 0.85$, determined from a fit of Pd foil; fit range $3 < k < 12$ and $1.0 < R < 3.0$. Spectra fitted using 9 independent points. The values for E_0 and σ^2 were fixed with no associated error.

Sample	Bond (Absorber-scatterer)	Coordination number (C.N.)	E_0 (eV)	σ^2 / Å^2	R / Å	R-factor
A	Pd-O1	0.7(2)	-7.5	0.002	1.96(2)	0.02
	Pd-Pd1	7.0(4)		0.008	2.73(1)	
B	Pd-Cu1	1.4(2)	-7.5	0.005	2.60(1)	0.02
	Pd-Pd1	7.3(5)		0.010	2.76(1)	

The presence of this Pd-Cu scattering distance in the fit suggests that local Pd-Cu alloying has occurred in the Pd nanoparticles. The previous chapter discussed how the water-based preparation for sol-immobilisation of Pd nanoparticles on to the CuBTC MOF leads to some degradation of the framework itself, causing some Cu_2O to be produced. It was not possible to successfully fit a Pd-Cu scattering distance to the Pd K EXAFS data for the Pd/CuBTC composites; however, shifts in the XANES and a slight lattice expansion hinted at the possibility of a slight amount of Pd-Cu alloying in the samples following the sol-immobilisation method.

After the reduction with $NaBH_4$, comparison of the non-phase-corrected Fourier transform data for the PdCu-reduced sample B and the original Pd/CuBTC nanocomposite, as shown in **Figure 48**, further confirms that a change in structure has taken place during the reduction process, with the increase in signal at ~2.2 Å following the reduction demonstrating the Pd-Cu alloying.

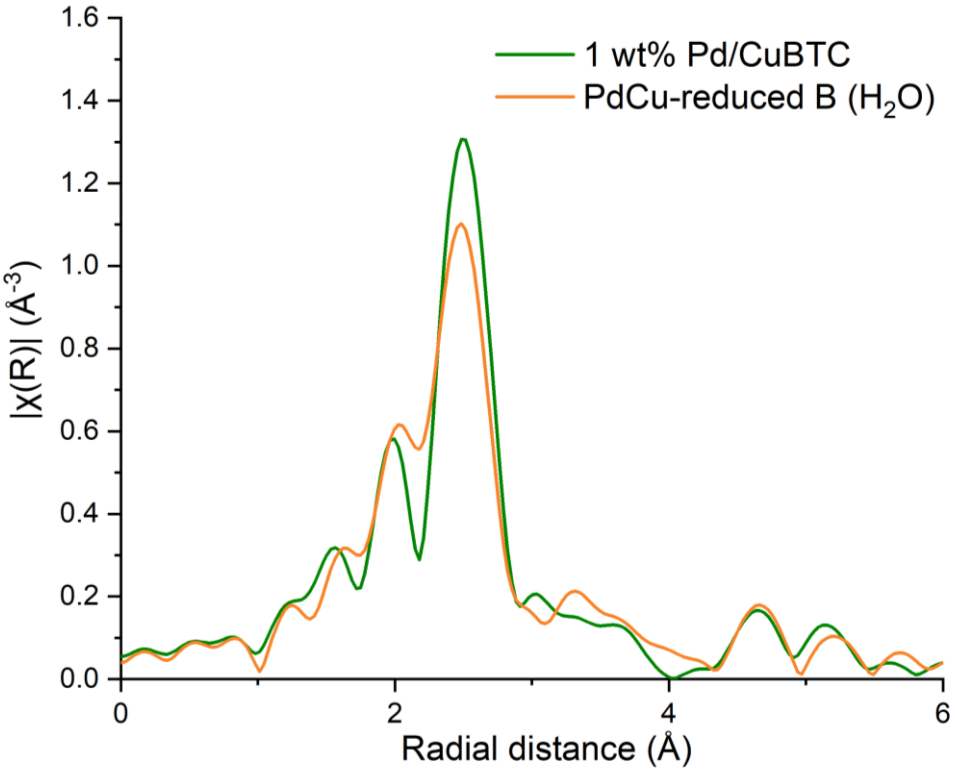

Figure 48: Comparison of non-phase-corrected Fourier transformed Pd K EXAFS spectra for the Pd/CuBTC composite and the PdCu-reduced sample B (H_2O prep, 4-NP present at reduction).

The role of 4-nitrophenol in influencing the oxidation state of the support has already been discussed (**Section 4.3.1.1**), where it was demonstrated that reduction without the presence of 4-nitrophenol produces a nanoparticle support dominated by CuO, with the additional presence of Cu^0 and Cu_2O phases. For this example, given that the key difference between the PdCu-reduced samples A and B is the exposure of B to 4-NP during the reduction, it is likely that 4-NP or its reduced counterpart 4-aminophenol is also influencing local Pd-Cu alloying in the nanoparticles themselves.

Incorporating the fact that reduction in the presence of either ethanolamine or 4-aminophenol produces similar nanocomposites with mixed Cu^0/Cu_2O oxidation states in the supports, along with the fact that reduction with the sheer amount of $NaBH_4$ needed to reduce the copper in the MOF produces a significant amount of local heat, despite the reaction being carried out in a room-temperature solution; it is hypothesised that the copper abstracted from the MOF lattice by degradation from contact with water during sol-immobilisation is able to easily diffuse under the local high temperature of the reduction reaction. If these copper atoms are sufficiently close to a Pd nanoparticle on the MOF surface, they could be coordinated by 4-aminophenol produced by the reduction of 4-NP on that Pd nanoparticle, and brought in proximity to alloy into

the nanoparticle. However, the precise mechanism of the alloying is currently unclear, and would require further beamline XAFS studies to determine.

To examine the influence of the sol-immobilisation solvent and to confirm if water-induced degradation of the MOF is contributing to PdCu alloying, two samples were prepared using methanol as a solvent, and again had their Pd K edge measured in fluorescence mode. The XANES spectra, XANES derivative, and transformations into *k*-space and *R*-space (k^2-weighted, non-phase corrected) for samples C and D are shown in **Figure 49a-d**.

Initial analysis of the spectra suggests there is not a significant difference in structure between samples C and D – both the XANES and the XANES derivative are in general agreement. This is a contrast from the water-prepared samples, where the sample reduced with 4-NP was noticeably different. Comparing the *k*-space and *R*-space data for the water- and methanol-prepared samples indicates that samples C and D have significant commonalities with sample A, as shown in **Figure 50**.

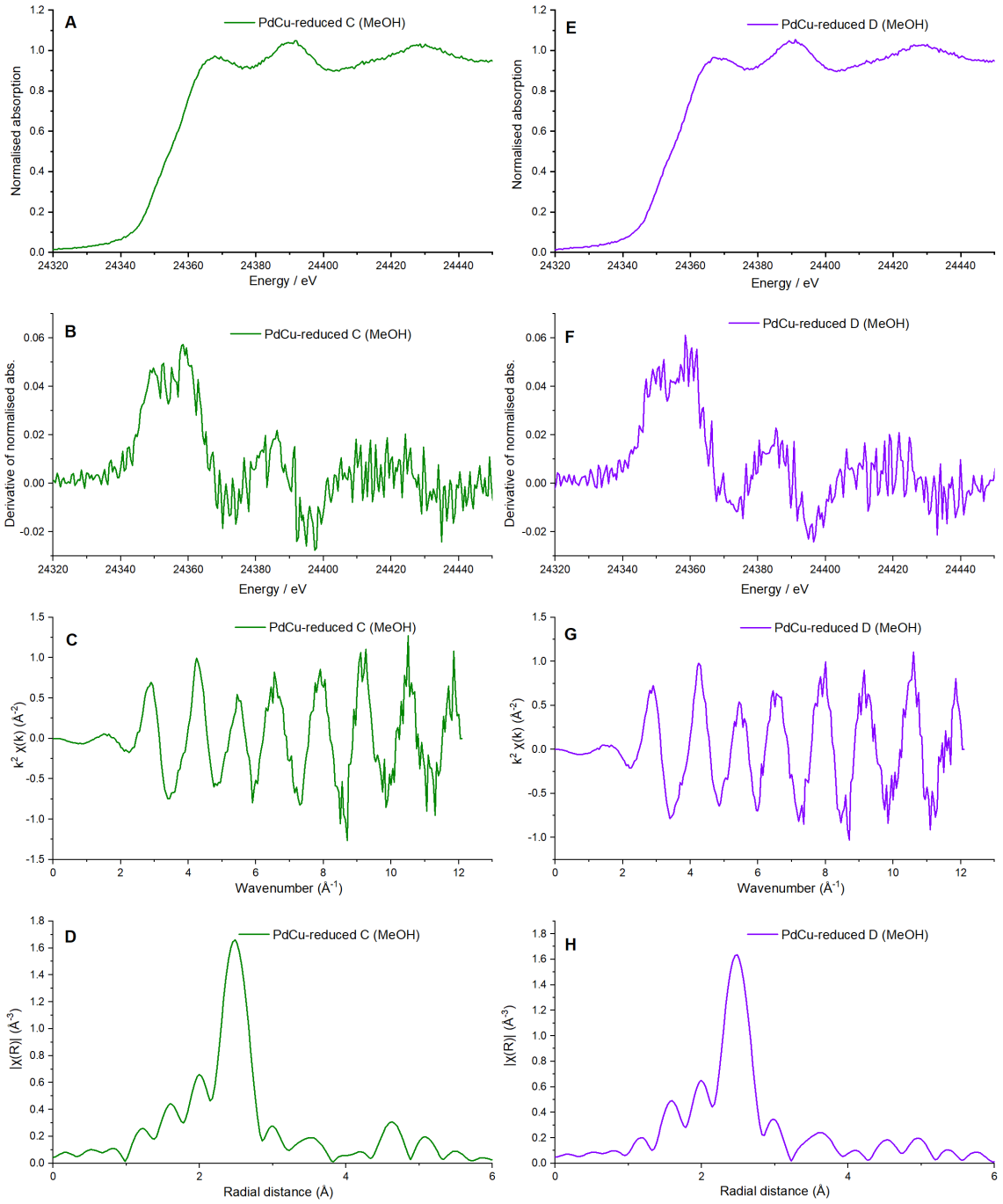

Figure 49: Pd K edge XAFS spectra for sample IDs PdCu-reduced C (green) and Pd-reduced D (violet); where figures A-D represent for the sample PdCu-reduced C a) the normalised absorption coefficient at the Pd K X-ray edge after background subtraction; b) the first derivative of that absorption coefficient; c) the transformation of the absorption signal into *k*-space, weighted by a k^2-term; and d) the Fourier transform of the k^2-weighted *k*-space function into *R*-space; figures E-H are analogous to figures A-D but for the PdCu-reduced D sample.

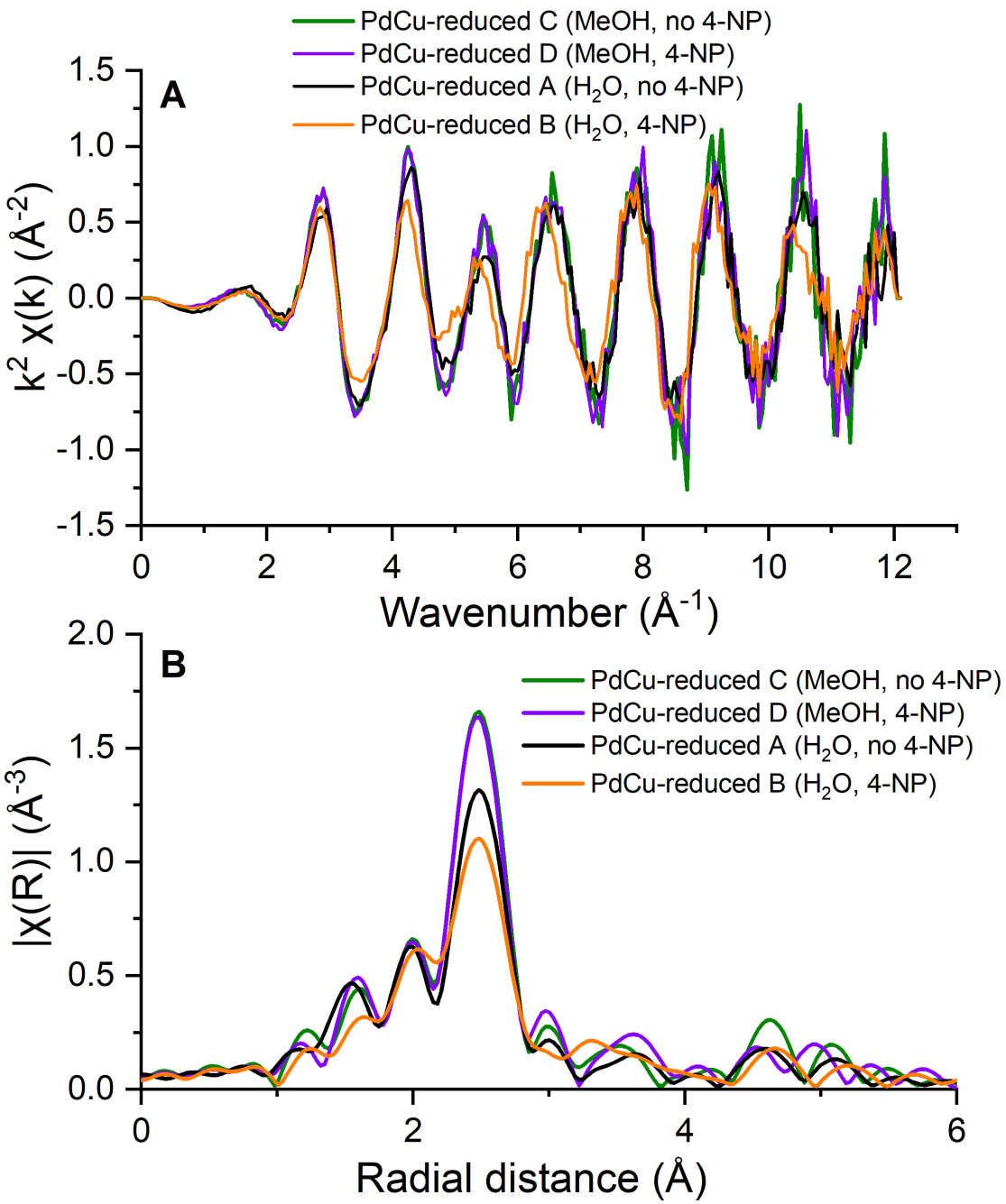

Figure 50: a) Comparisons of the k^2-weighted k-space functions of the Pd K edge XAFS spectra for PdCu-reduced samples C, D, A, and B; b) comparisons of the non-phase-corrected Fourier transform XAFS data at the Pd K edge for PdCu-reduced samples C, D, A, and B.

A simple first shell model was again employed to fit the EXAFS spectra of samples C and D using the Artemis software. The resulting fits are displayed in **Figure 51**, with the calculated fitting parameters listed in **Table 6**. As with the fit for sample A, it has been challenging to model the first two notable features in the Fourier transform data, at around 1.6 Å and 2.0 Å (non-phase-corrected). Using a Pd-O scattering distance yields a very low coordination number with a reasonable margin of error, but models without that Pd-O distance do not yield a reasonable fit.

Additionally, attempting to replace the distance with a Pd-Cu scattering distance does not model the data well, and the absence of the extra shoulder-like feature at 2.2 Å suggests that there is not a significant amount of Pd-Cu alloying in these nanoparticles.

The main difference in the fitting parameters between the methanol-prepared samples and sample A is that the Pd coordination number has increased for the samples produced in methanol, rising from 7.0 for sample A to 9.0 and 9.4 for samples C and D respectively.

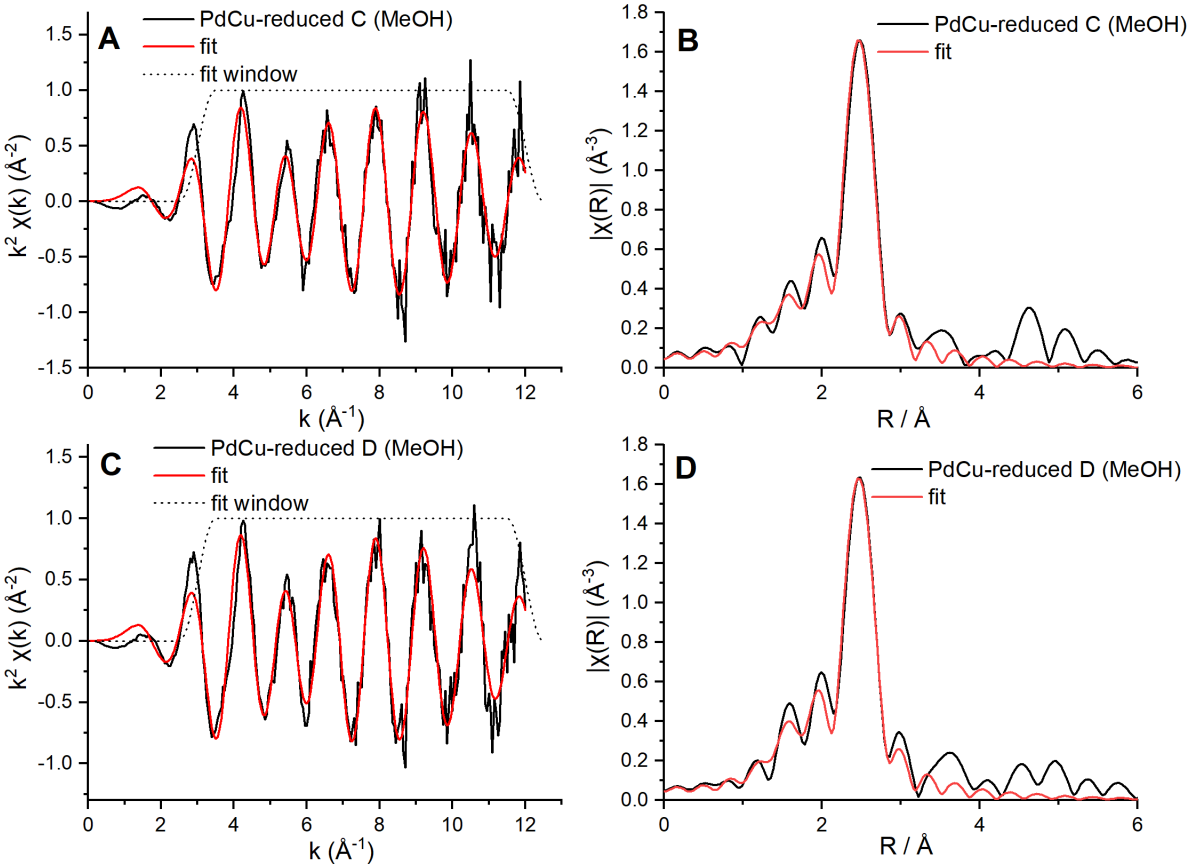

Figure 51: Fits of Pd K EXAFS data for the reduced nanocomposite sample PdCu-reduced C (MeOH prep, no 4-NP at reduction), showing a) the k^2-weighted EXAFS signal (black) with a corresponding fit (red) and fit window (black dots); and b) the magnitude of the k^2-weighted non-phase-corrected Fourier transformed signal (black) with a corresponding fit (red). Figures c) and d) are analogous to a) and b) respectively, but for the reduced nanocomposite sample PdCu-reduced D (MeOH prep with 4-NP at reduction).

Table 6: EXAFS fitting parameters for the Pd K edge for samples PdCu-reduced C and PdCu-reduced D. Fitting parameters: $S_0^2 = 0.85$, determined from a fit of Pd foil; fit range $3 < k < 12$ and $1.0 < R < 3.0$. Spectra fitted using 9 independent points. The values for E_0 and σ^2 were fixed with no associated error.

Sample	Bond (Absorber-scatterer)	Coordination number (C.N.)	E_0 (eV)	σ^2 / Å^2	R / Å	R-factor
C	Pd-O1	0.5(3)	-7.5	0.005	1.95(4)	0.02
	Pd-Pd1	9.0(4)		0.008	2.74(1)	
D	Pd-O1	0.4(3)	-7.5	0.004	1.99(1)	0.02
	Pd-Pd1	9.4(5)		0.008	2.74(1)	

In the water-prepared samples, PVA is used to cap the Pd nanoparticles during their synthesis from K_2PdCl_4 reduction in the first step of sol-immobilisation, to prevent their aggregation into bulk Pd^0. However, it is insoluble in methanol, so cannot be used in the preparation of samples C and D, with the alternative mechanism preventing NP aggregation being stabilising effects arising from the methanol molecules themselves.[31] However, in this case, the increase in Pd coordination number is attributed to the stabilising effects from the MeOH molecules not being as effective against aggregation as the steric effect from polymer chains of PVA. Aggregation causes the coordination number to increase since in a larger Pd nanoparticle, a lower proportion of Pd atoms are present at the surface to be undercoordinated.[37]

This change in solvent for the sol-immobilisation step from water to methanol has clearly had an influence on the properties of the nanocomposites produced, since the Pd-Cu alloying is only noticeable in the *k*-space and *R*-space data for sample B, from the phase shift of the *k*-space oscillations and the shoulder feature at ~2.2 Å (non-phase corrected) in *R*-space. In addition to the particle size effects from the lack of PVA capping agent and limited stabilisation from MeOH, it is clear that the presence of 4-nitrophenol is not causing alloying to occur by itself. The key behind this is the stability of CuBTC MOF in methanol. For example, methanol is used to remove solvated DMF from the pores of CuBTC via solvent exchange after synthesis, and Yang *et al*.[38] report that the use of methanol in CuBTC MOF synthesis in fact yields a highly-crystalline example of the MOF with a greater pore volume and adsorption capacity than those produced via other solvents, including water. In contrast, Chapter 3 discussed how extended exposure to water, even through atmospheric humidity, causes the MOF's carboxylate groups to protonate and causes the MOF to degrade over time. This provides a local source of copper around the Pd nanoparticles in Pd/CuBTC that can be used in Pd-Cu alloying upon reduction with $NaBH_4$. In

the nanocomposites produced via a methanol-based sol-immobilisation, however, the MOF is not immersed in water for a long period, and will maintain stability, as seen in **Section 3.3.6**. This lack of abstraction of copper from the MOF lattice is the reason why sample D, produced by $NaBH_4$ reduction in the presence of 4-NP, does not exhibit Pd-Cu alloying compared to its counterpart sample B. The combination of a water-based sol-immobilisation step and the presence of 4-nitrophenol/4-aminophenol, or a suitable other capping agent like ethanolamine, is required to initiate Pd-Cu alloying via this process, since the copper must first be abstracted for it to be available to be coordinated by the capping agent and brought into proximity with the Pd nanoparticle for alloying.

Finally, the two samples produced using higher concentrations of $NaBH_4$ in the reduction of the Pd/CuBTC composites were again studied at the Pd K edge in fluorescence mode. The XANES spectra, XANES derivative, and transformations into *k*-space and *R*-space (k^2-weighted, non-phase corrected) for samples E and F are shown in **Figure 52a-d**. There is a clear similarity between both of the first-derivative XANES spectra, and these two samples consequently have very similar XANES spectra.

These samples are largely similar in preparation method to sample A, with the only differences being the concentration of $NaBH_4$ in the Pd/CuBTC reduction, and the fact that the Pd/CuBTC composite used to produce sample A was exposed to 4-NP before being dried, then reduced with $NaBH_4$; samples E and F had no exposure to 4-NP throughout the synthetic procedure. The *k*-space and *R*-space data for these three samples are therefore compared together in **Figure 53**. All samples display the same features at approximately 1.6, 2.0 and 2.5 Å in the non-phase-corrected Fourier transform, albeit at varying amplitudes. This is attributed to particle size effects arising from the variation in $NaBH_4$ concentration, since the amplitude of the central peak at 2.5 Å decreases in the samples reduced at higher concentrations, suggesting an overall reduction in Pd-Pd scattering and smaller Pd nanoparticles. These smaller nanoparticles would also exhibit an increased amount of Pd-O scattering, which is evidenced by the changes in amplitude of the smaller peaks in the Fourier transform, and by a slight increase in Pd-O coordination number in the EXAFS analysis.

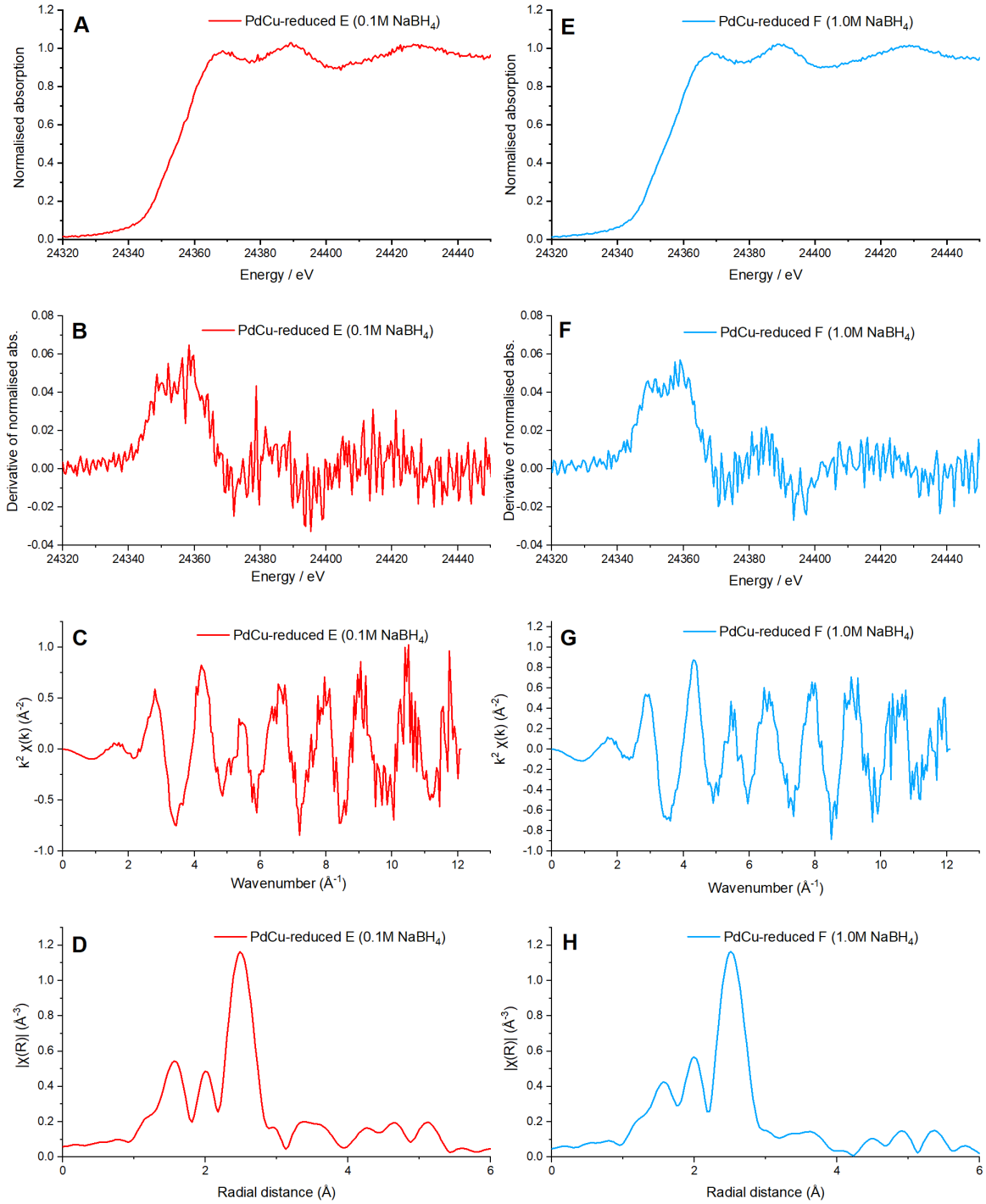

Figure 52: Pd K edge XAFS spectra for sample IDs PdCu-reduced E (red) and PdCu-reduced F (blue); where figures A-D represent for the sample PdCu-reduced E a) the normalised absorption coefficient at the Pd K X-ray edge after background subtraction; b) the first derivative of that absorption coefficient; c) the transformation of the absorption signal into *k*-space, weighted by a k^2-term; and d) the Fourier transform of the k^2-weighted *k*-space function into *R*-space; figures E-H are analogous to figures A-D but for the PdCu-reduced F sample.

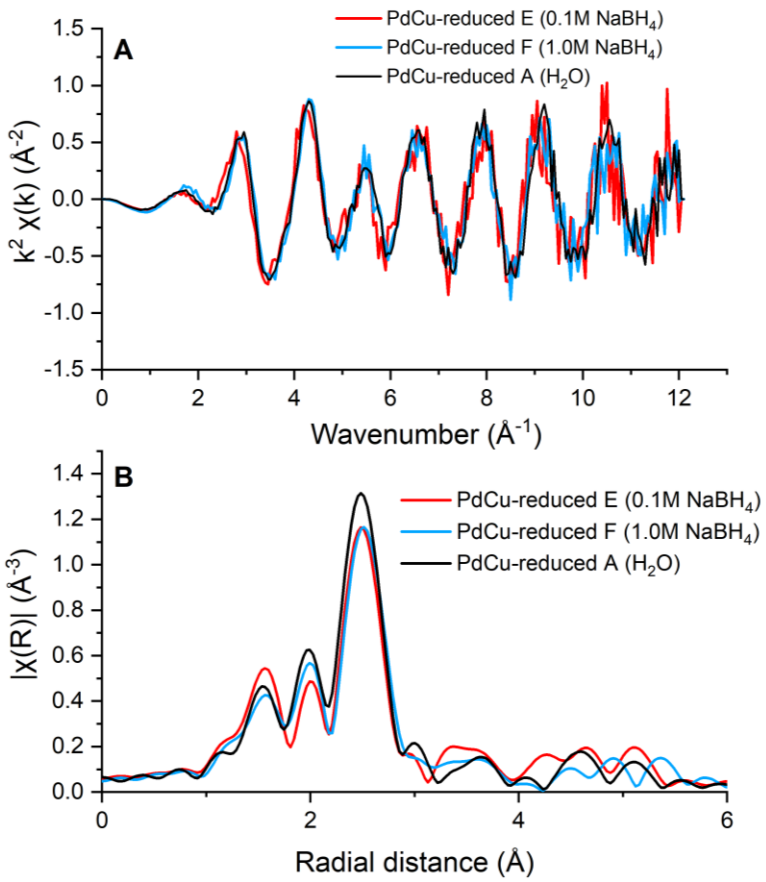

Figure 53: a) Comparisons of the k^2-weighted k-space functions of the Pd K edge XAFS spectra for PdCu-reduced samples E, F and A; b) comparisons of the non-phase-corrected Fourier transform XAFS data at the Pd K edge for PdCu-reduced samples E, F and A.

Using the same simple first shell method as the previous samples, the EXAFS data was fitted and is displayed in **Figure 54**, with associated fitting parameters in **Table 7**. The fitting process is again similar to that of sample A, with an imperfect modelling of the first two smaller features in the Fourier transform, but a well-modelled main peak for the Pd-Pd scattering. Similarly to samples A, C, and D, the two smaller features in the FT cannot be modelled using a Pd-Cu scattering distance, and instead are rendered using a small contribution from a Pd-O scattering distance, which indicates that local Pd-Cu alloying in these samples is either absent or insignificant.

Sample E displays the lowest Pd-Pd coordination number of the samples in this dataset, with a value of 6.8, compared to 7.0-7.3 for the first batch of water-prepared samples A and B, and 9.0-9.4 for the methanol-prepared samples C and D. Sample F's value of 7.2 also brings it in line with the other water-prepared samples. There is quite a high associated error in coordination number, of a minimum of ±0.4, so the four water-prepared samples all lie within a standard deviation of one another; and it is worth noting that the increased $NaBH_4$ concentration applies to the reduction step for the overall Pd/CuBTC composite, rather than the formation of the Pd nanoparticles during sol-immobilisation.

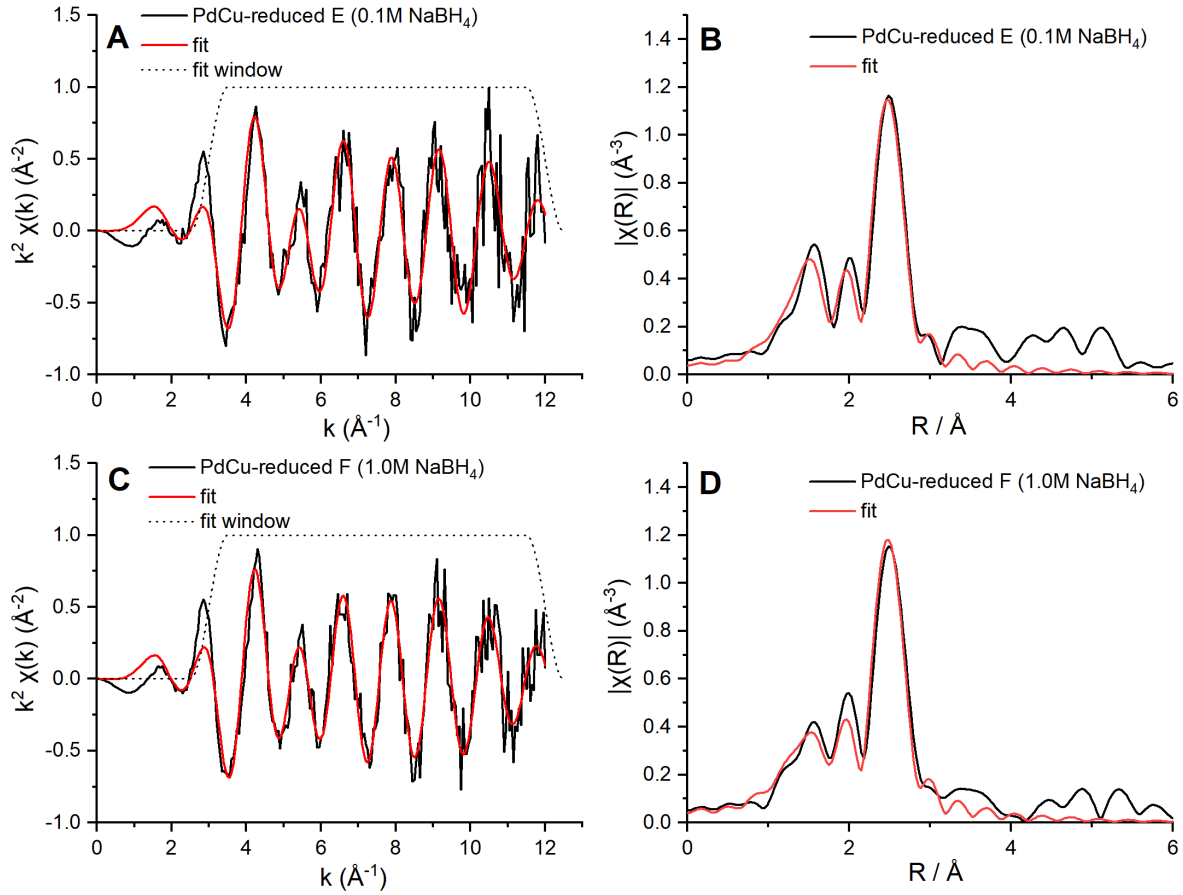

Figure 54: Fits of Pd K EXAFS data for the reduced nanocomposite sample PdCu-reduced E (0.1 M $NaBH_4$), showing a) the k^2-weighted EXAFS signal (black) with a corresponding fit (red) and fit window (black dots); and b) the magnitude of the k^2-weighted non-phase-corrected Fourier transformed signal (black) with a corresponding fit (red). Figures c) and d) are analogous to a) and b) respectively, but for the reduced nanocomposite sample PdCu-reduced F (1.0 M $NaBH_4$).

Table 7: EXAFS fitting parameters for the Pd K edge for samples PdCu-reduced E and PdCu-reduced F. Fitting parameters: $S_0^2 = 0.85$, determined from a fit of Pd foil; fit range $3 < k < 12$ and $1.0 < R < 3.0$. Spectra fitted using 9 independent points. The values for E_0 and σ^2 were fixed with no associated error.

Sample	Bond (Absorber-scatterer)	Coordination number (C.N.)	E_0 (eV)	σ^2 / Å^2	R / Å	R-factor
E	Pd-O1	1.1(2)	-7.5	0.002	1.97(2)	0.02
	Pd-Pd1	6.8(4)		0.009	2.75(1)	
F	Pd-O1	0.9(2)	-7.5	0.004	1.96(2)	0.02
	Pd-Pd1	7.2(4)		0.009	2.75(1)	

To summarise, this XAS study has elucidated several different method-dependent effects on the overall structure of the nanocomposites produced from the reduction of Pd/CuBTC by $NaBH_4$. Firstly, a strict and specific set of experimental conditions are required to cause Pd-Cu alloying and produce bimetallic PdCu NPs supported on Cu_2O: namely, a sol-immobilisation preparation method based on water, which will abstract sufficient amounts of copper from the MOF lattice for alloying to be possible; and for 4-nitrophenol to be present during the reduction, so that the 4-aminophenol product can influence the formation of a Cu_2O support and potentially direct the alloying itself. Lack of 4-nitrophenol during the Pd/CuBTC reduction step shifts the oxidation state of the support in favour of CuO rather than Cu_2O, as discussed in **Section 4.3.1.1**, and does not produce local PdCu alloying.

Changing the sol-immobilisation solvent to methanol does not yield PdCu alloying either, even when 4-nitrophenol is present. This is attributed to a lack of abstraction of copper from degradation of the MOF during the sol-immobilisation process, due to CuBTC MOF's increased stability in methanol. Additionally, the methanol-based method produces nanoparticles with a higher Pd coordination, likely representing increased aggregation during the initial nanoparticle preparation due to a lack of PVA capping agent.

Finally, changing the concentration of $NaBH_4$ used for the reduction of Pd/CuBTC does not cause Pd-Cu alloying in its own right; the presence of 4-nitrophenol is still the determining factor.

4.3.3 Optimisation of the PdCu/Cu_2O nanocomposite properties

So far, this chapter has established that production of bimetallic PdCu-alloyed nanocomposites on a copper oxide support is possible with the reduction of a Pd/CuBTC composite using a mixture of $NaBH_4$ and 4-nitrophenol, or its derivative 4-aminophenol. However, the nanocomposites produced still have other variables in their structure, such as the oxidation state of the copper oxide support. Therefore, a series of experiments were carried out to optimise the preparation method and investigate whether variation of specific reaction conditions could allow tight control over the physical properties of the produced nanocomposite.

The experimental parameters of the reduction of Pd/CuBTC into PdCu/Cu_2O were varied in an attempt to optimise the ratio of Cu_2O to Cu^0 in the nanoparticle support. This involved altering the concentration of the $NaBH_4$ reducing agent, the temperature of reduction and the concentration of 4-nitrophenol present.

X-ray diffraction patterns of samples obtained at varying concentrations of $NaBH_4$ are shown in **Figure 55**. The patterns indicate that a higher concentration of $NaBH_4$ yields a greater amount of Cu_2O relative to Cu^0, evidenced by an increase in the Cu_2O (111) and (200) peaks at 36.3 and 42.3 degrees. This is caused by a particle size effect, since a higher concentration of reductant will yield a faster rate of reduction and thus produce smaller particles on average. Upon re-oxidation in air, they have a smaller relative amount of bulk Cu^0 compared to the oxidised surface layer of Cu_2O, which leads to the difference in XRD peak intensities.

In contrast, at lower $NaBH_4$ concentrations, the samples partly preserve the CuBTC features seen in the 20-30° region. This is attributed to the concentration being low enough that insufficient amounts of $NaBH_4$ were present to fully reduce the sample, yielding a hybrid of the Pd/CuBTC composite and PdCu/Cu_2O nanocomposite. Increasing the concentration of $NaBH_4$ further causes the CuBTC pattern to disappear, leaving only the NP-metal oxide nanocomposite product.

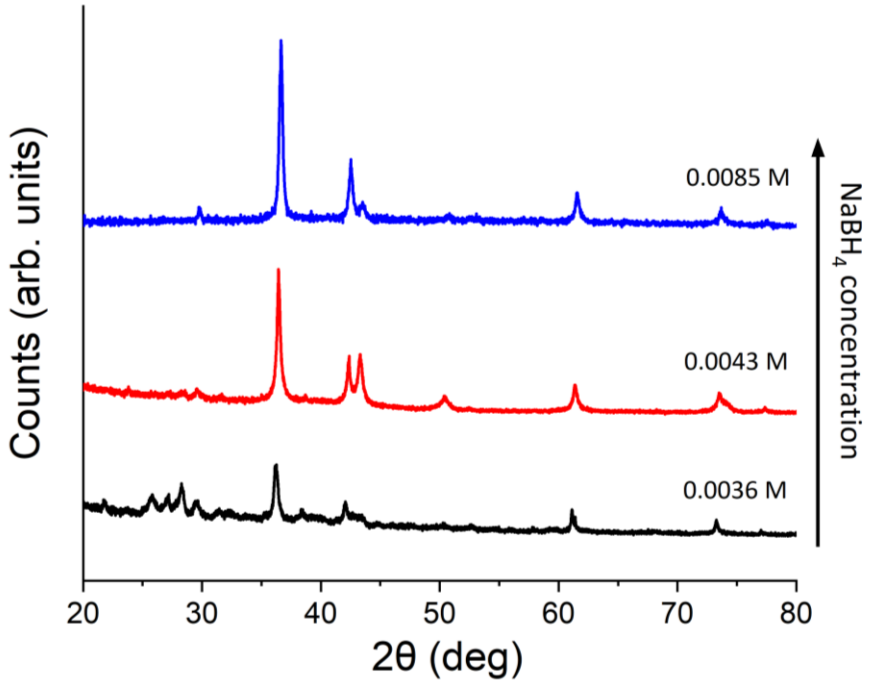

Figure 55: X-ray diffraction patterns of reduced PdCu/Cu_2O nanocomposites obtained with different concentrations of $NaBH_4$ and a 4-nitrophenol concentration of 0.16 mM.

The Pd/CuBTC reduction was also performed at a range of temperatures from 1-75 °C, by heating the water used to dissolve the $NaBH_4$ prior to adding the borohydride itself, whilst the Pd/CuBTC sample was in suspension. The resulting nanocomposites were characterised by XRD, with their diffraction patterns shown in **Figure 56**. The patterns demonstrate that the Cu_2O:Cu^0 ratio is essentially unaffected by a variation in temperature, since the major peaks for Cu_2O and Cu^0 remain in very similar ratios throughout. There is a subtle hint of the peak corresponding to the (111) plane of CuO at 38.7°, suggesting the material is not perfectly composed of Cu_2O and Cu^0, but none of the other peaks for CuO are visible above the background, suggesting that the CuO presence is very slight.

Applying the Scherrer equation for the most intense peaks corresponding to Cu_2O and Cu^0, using the common estimate of 0.9 for the crystallite shape factor[30], yielded estimates of crystallite size from 26-40 nm for Cu_2O and 30-34 nm for Cu^0, which are listed in **Table 8**. There is a slight decreasing trend in the observed crystallite sizes for Cu^0, which could be attributed to an increased rate of $NaBH_4$ reduction at the higher reduction temperatures. However, this trend is not perfectly observed for the Cu_2O crystallites, as the sample reduced at 25 °C displayed the largest crystallite size of 40 nm. In both cases, the sample prepared at 75 °C exhibited the smallest crystallite size.

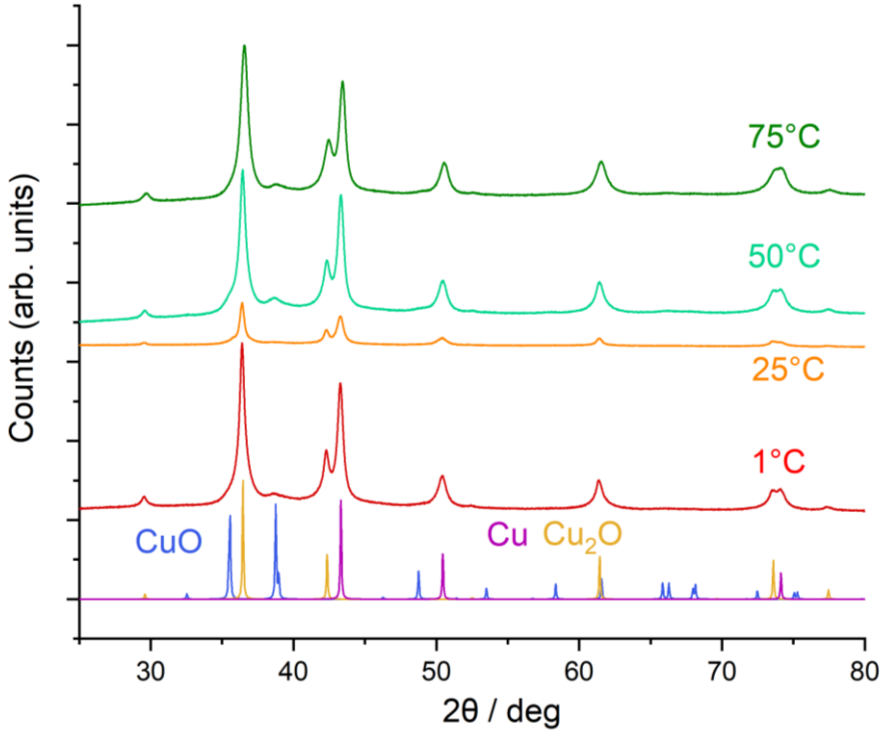

Figure 56: X-ray diffraction patterns of PdCu/Cu_2O nanocomposites formed from reduction of Pd/Cu-BTC using $NaBH_4$, with solvent temperature at reduction held at 1 °C, 25 °C, 50 °C and 75 °C. Reference patterns for Cu_2O (ICSD-180846)[39] and Cu^0 (ICSD-627114)[40] are also shown.

Table 8: Estimates of crystallite sizes for Cu_2O and Cu^0 in the PdCu/Cu_2O samples reduced at varying temperatures. All calculations were performed using the Scherrer equation with an estimate of 0.9 for the shape factor.

Sample ID	Cu_2O crystallite size estimate / nm	Cu^0 crystallite size estimate / nm
PdCu/Cu_2O 1 °C	34.1	34.2
PdCu/Cu_2O 25 °C	40.8	32.9
PdCu/Cu_2O 50 °C	31.5	31.6
PdCu/Cu_2O 75 °C	26.5	29.9

Varying the concentration of 4-nitrophenol present during reduction (**Figure 57**) was shown to have the greatest effect on the Cu_2O:Cu^0 phase ratio. 0.00018 M 4-NP is the standard concentration used in the UV-vis study of 4-NP reduction for testing Pd nanoparticles used in this report, and it can be seen that the sample prepared at this concentration exhibits the approximate Cu_2O/Cu^0 phase balance of the nanocomposites examined in **Section 4.3.1.1**, since the conditions from the catalytic reaction were kept the same for the initial nanocomposite study.

However, when the concentration of 4-NP is increased, to 0.001 M, 0.005 M and 0.01 M, there is a distinct shift in the intensity ratios for the main Cu_2O and Cu^0 diffraction peaks. The peaks at 36.3°, 42.3°, and 61.2°, the (111), (200) and (202) planes of Cu_2O, become notably less intense, with the (200) peak disappearing at the highest concentrations and the (202) peak being very weak. The Cu^0 (111) and (200) peaks, respectively located at 43.3° and 50.3°, increase in intensity, with the (111) peak becoming the most intense peak in the diffractogram. Finally, the two peaks at 73.6° and 74.1°, tend to merge into one another due to the line broadening associated with nanoscale crystallites. These represent the (113) planes in Cu_2O and the (022) planes in Cu^0, and close inspection reveals a clear increase in 2θ angle for the feature in that region when 4-NP concentration is increased, consistent with Cu^0 becoming the most populous phase at the expense of Cu_2O.

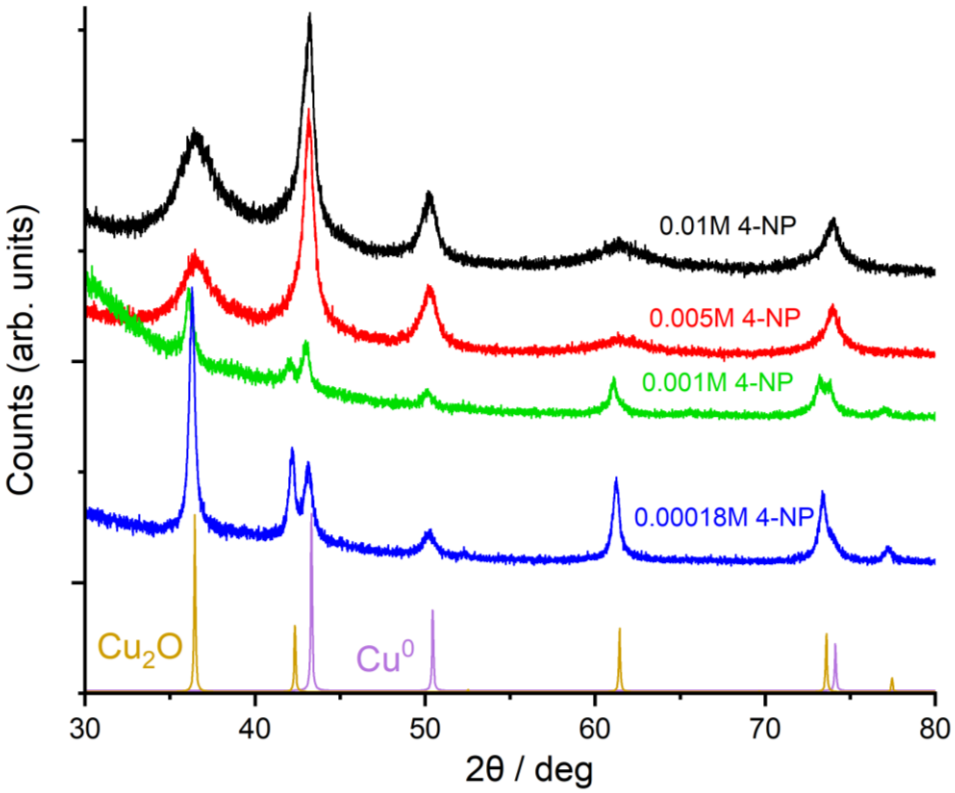

Figure 57: XRD patterns of $PdCu/Cu_2O$ samples reduced in the presence of varying concentrations of 4-nitrophenol. Reference patterns for Cu_2O and Cu^0 are also shown.

Figure 57 also shows clear evidence of increased line broadening in the XRD patterns for the higher concentrations of 4-NP. Applying the Scherrer equation to the Cu_2O peak at 36.3° suggested a crystallite size of ~7-9 nm for the 0.01 M and 0.005 M 4-NP samples, compared to 37 nm for the sample prepared at 0.00018 M 4-NP. This seems to be a very low value, given that the typical Pd nanoparticle size was determined as 5-10 nm in Chapter 3, and the sample is considered to be PdCu NPs supported on Cu_2O and Cu^0 nanodiscs. Applying the Scherrer equation to the Cu^0 peak at 43.3° suggests a crystallite size of 19 nm and 22 nm for Cu^0 at 0.01 M and 0.005 M respectively, and 27 nm at the original concentration of 0.00018 M.

In qualitative terms, it is clear that crystallite size decreases with increasing 4-NP concentration. It has already been discussed in **Sections 4.3.1.1** and **4.3.2.1** how the presence of the reduced product 4-aminophenol is hypothesised to coordinate to copper atoms and influence both local PdCu alloying and the average oxidation state of Cu atoms in the support. Here, the concentration of 4-NP is increased by a factor of ~55 over the experiment, and assuming a reasonable proportion of the 4-NP is catalytically converted to 4-AP by the Pd nanoparticles during nanocomposite reaction, there is a similarly-large increase in 4-AP presence between the 0.00018 M and 0.01 M samples.

Therefore, it is suggested that the increased presence of 4-AP contributes to the generation of smaller Cu_2O and Cu^0 NPs. Examining the literature, Deka *et al.* demonstrated that Cu NPs of average size 4-7 nm were produced by $NaBH_4$ reduction of a precursor copper chloride hydroxide compound, with the *in situ*-synthesised Cu NPs catalysing the reduction of 4-NP to 4-AP, and the precursor compound determined to be inactive for catalysis.[41] Whilst it is difficult to determine the precise timescales involved in the $NaBH_4$ reduction of Pd/CuBTC – i.e. whether 4-AP is being produced by the Pd nanoparticles before the bulk reduction of the CuBTC MOF and can be involved in controlling the formation of copper oxides – this paper does suggest that it is possible to produce very small Cu NPs in a similar manner, which supports the low crystallite sizes observed through use of the Scherrer equation.

One way to achieve these small particle sizes is for the nitrophenol/aminophenol to act as a capping agent during the synthesis, which will cause the samples reduced in the presence of the highest concentrations of 4-NP (such as 0.01M) to have their growth inhibited by this capping. The reduced particle size can clearly be seen in the line broadening, and if the 4-aminophenol product remains coordinated to the nanoparticle surface following the reaction, this will lead to a surface coordination layer that passivates the surface, largely preventing the formation of Cu_2O in air and reducing that peak's intensity relative to Cu^0. A similar example of this use of a coordinating ligand to induce passivation of a surface can be seen in Peng *et al.*[42], who used formate and alkanethiol ligands to prevent re-oxidation of copper in a similar manner.

In summary, the fine details of nanocomposite structure can be accessed and tailored by variation of the experimental parameters used during the reduction of Pd/CuMOF composites. A decrease in the amount of $NaBH_4$ used in the reduction would allow some retention of the original porous MOF structure, but the amounts used elsewhere in this chapter destroy that structure to yield a mixed Cu_2O/Cu^0 support. Additionally, increasing the concentration of $NaBH_4$ favours the formation of Cu_2O over Cu^0, due to an overall reduction in particle size. The temperature of reduction does not influence the oxidation state of the support, but could have an effect on Pd-Cu alloying, which is explored further in the next section. The most intricate changes occur when the concentration of 4-nitrophenol is varied, with large quantities pushing the oxidation state of the support in favour of Cu^0 and decreasing the crystallite size.

Combining these variations together, it is suggested that to obtain the highest possible ratio of Cu_2O:Cu^0 for a PdCu nanocomposite, or perhaps to eliminate the Cu^0 phase entirely, there would need to be a high concentration of $NaBH_4$ used in the reduction, ensuring complete reduction, a small particle size, and increased Cu_2O formation. This should be combined with a low concentration of 4-nitrophenol, but not so low as to prevent any Pd-Cu alloying in the first instance. However, this results in a large number of variables that all must be tightly controlled simultaneously, which makes the method quite intricate and complex, especially when compared to the alternative methods of nanocomposite synthesis from NP-MOF composite reduction, such as pyrolysis.

4.3.4 Effect of reduction temperature on Pd-Cu alloying

4.3.4.1 Sample preparation and XAFS data

A further XAS experiment was performed, again at beamline B18 at Diamond Light Source, to investigate whether the temperature of reduction of Pd/CuBTC by $NaBH_4$ in the presence of 4-NP influenced the structure within the resultant alloyed PdCu NPs. A series of 1 wt% PdCu/Cu_2O nanocomposites were prepared at four different reduction temperatures ranging from 1-75 °C, and were measured at the Pd K edge in transmission mode. The results were also compared to the Pd/CuBTC composite analysed in Chapter 3.

The experimental parameters and sample details for the analysed samples are summarised in **Table 9**. The XANES spectra, XANES derivative, and transformations into *k*-space and *R*-space (k^2-weighted, non-phase corrected) for the 1 °C and 25 °C samples are shown in **Figure 58**, and for the 50 °C and 75 °C samples in **Figure 59**.

Table 9: Preparation details for the Pd/CuBTC and PdCu/Cu_2O samples studied at the Pd K XAFS edge, including solvent of preparation, presence of 4-NP during reduction, and reduction conditions. All Pd loadings for the samples were calculated as 1 wt%.

Sample ID	Sol-immobilisation solvent	Nitrophenol (4-NP) present during reduction?	Reduction conditions	$NaBH_4$ concentration / mol dm^{-3}
Pd/CuBTC	H_2O	Not reduced	Not reduced	0.0397
PdCu/Cu_2O 1 °C	H_2O	Yes	Reduced at 1 °C using $NaBH_4$ with 4-NP present.	0.0397
PdCu/Cu_2O 25 °C	H_2O	Yes	Reduced at 25 °C using $NaBH_4$ with 4-NP present.	0.0397
PdCu/Cu_2O 50 °C	H_2O	Yes	Reduced at 50 °C using $NaBH_4$ with 4-NP present.	0.0397
PdCu/Cu_2O 75 °C	H_2O	Yes	Reduced at 75 °C using $NaBH_4$ with 4-NP present.	0.0397

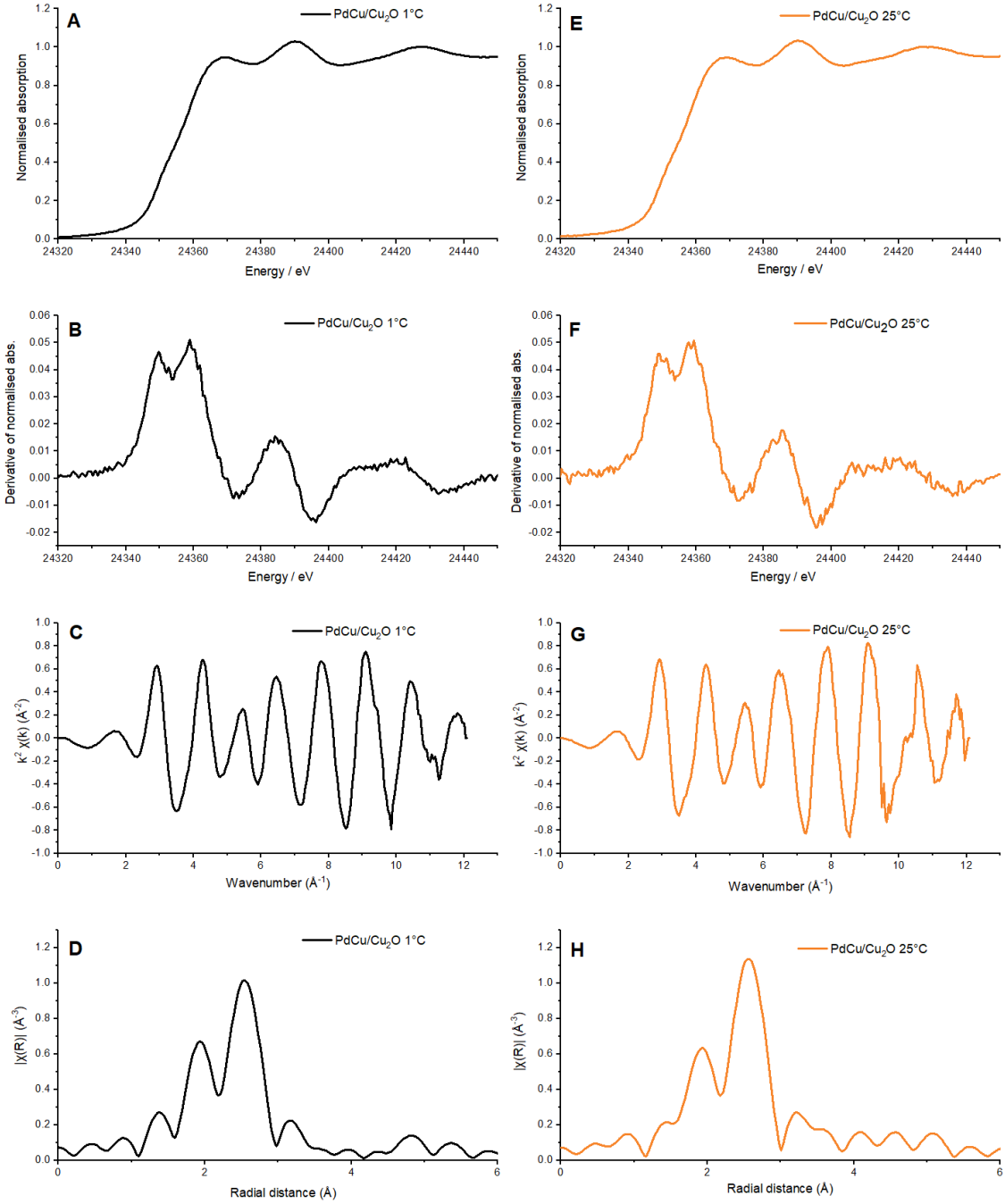

Figure 58: Pd K edge XAFS spectra for sample IDs PdCu/Cu_2O 1 °C (black) and PdCu/Cu_2O 25 °C (orange); where figures A-D represent for the sample PdCu/Cu_2O 1 °C a) the normalised absorption coefficient at the Pd K X-ray edge after background subtraction; b) the first derivative of that absorption coefficient; c) the transformation of the absorption signal into *k*-space, weighted by a k^2-term; and d) the Fourier transform of the k^2-weighted *k*-space function into *R*-space; figures E-H are analogous to figures A-D but for the PdCu/Cu_2O 25 °C sample.

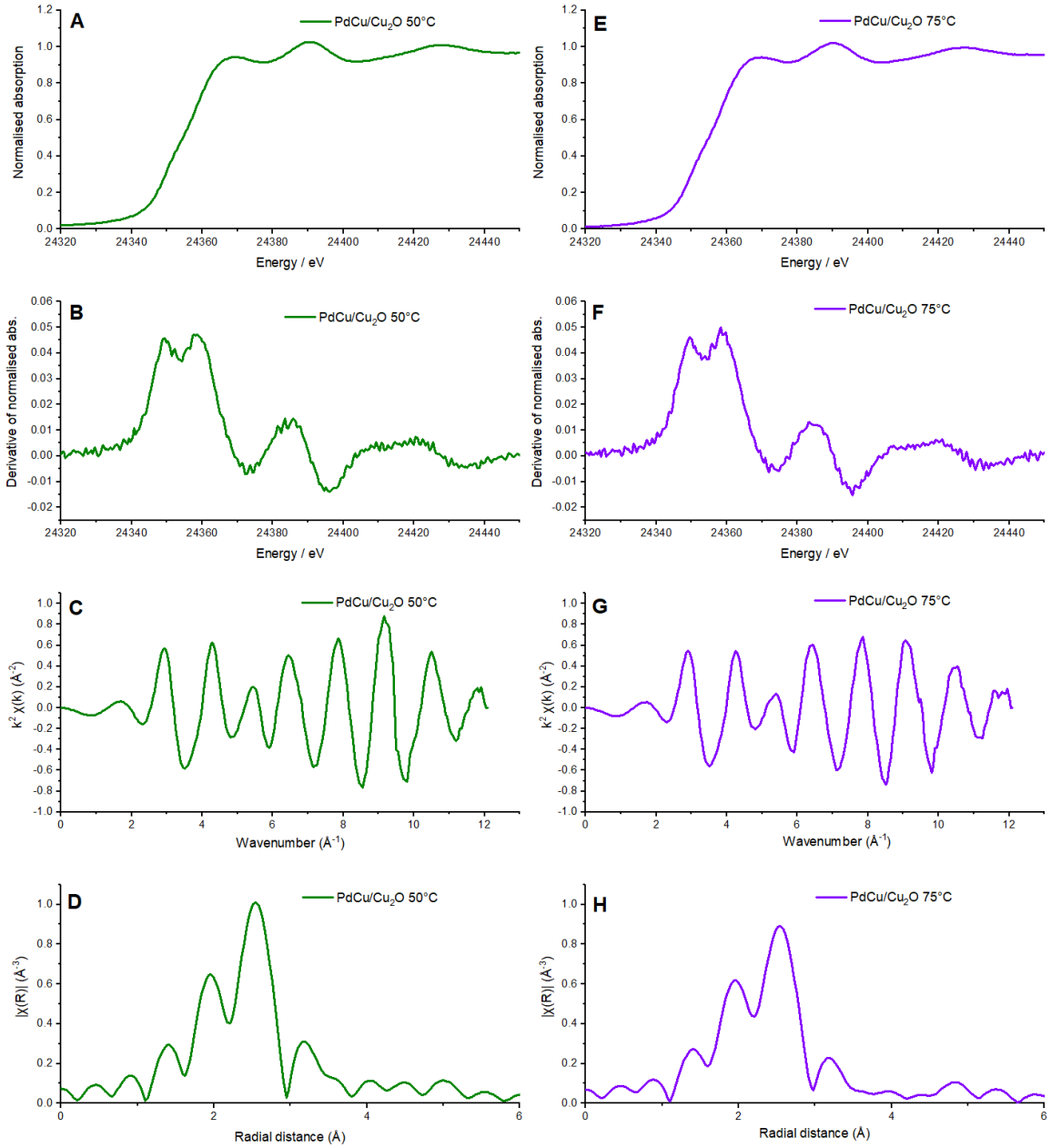

Figure 59: Pd K edge XAFS spectra for sample IDs PdCu/Cu_2O 50 °C (green) and PdCu/Cu_2O 75 °C (violet); where figures A-D represent for the sample PdCu/Cu_2O 50 °C a) the normalised absorption coefficient at the Pd K X-ray edge after background subtraction; b) the first derivative of that absorption coefficient; c) the transformation of the absorption signal into *k*-space, weighted by a k^2-term; and d) the Fourier transform of the k^2-weighted k-space function into *R*-space; figures E-H are analogous to figures A-D but for the PdCu/Cu_2O 75 °C sample.

As expected given the only altered variable was reduction temperature, the XANES spectra largely resemble one another, as do their derivatives, which indicates that the overall sample structure remains generally the same. However, a closer comparison of the *k*-space data for all samples, as shown in **Figure 60**, illustrates that there are some subtle differences. These are particularly highlighted by the zoomed plot in **Figure 60b**, which shows how the oscillations all

have a relative phase shift, particularly for the 75 °C sample. As discussed previously in **Section 4.3.2.1**, this phase shift could suggest Pd-Cu alloying, which can be determined by fits to the EXAFS data.

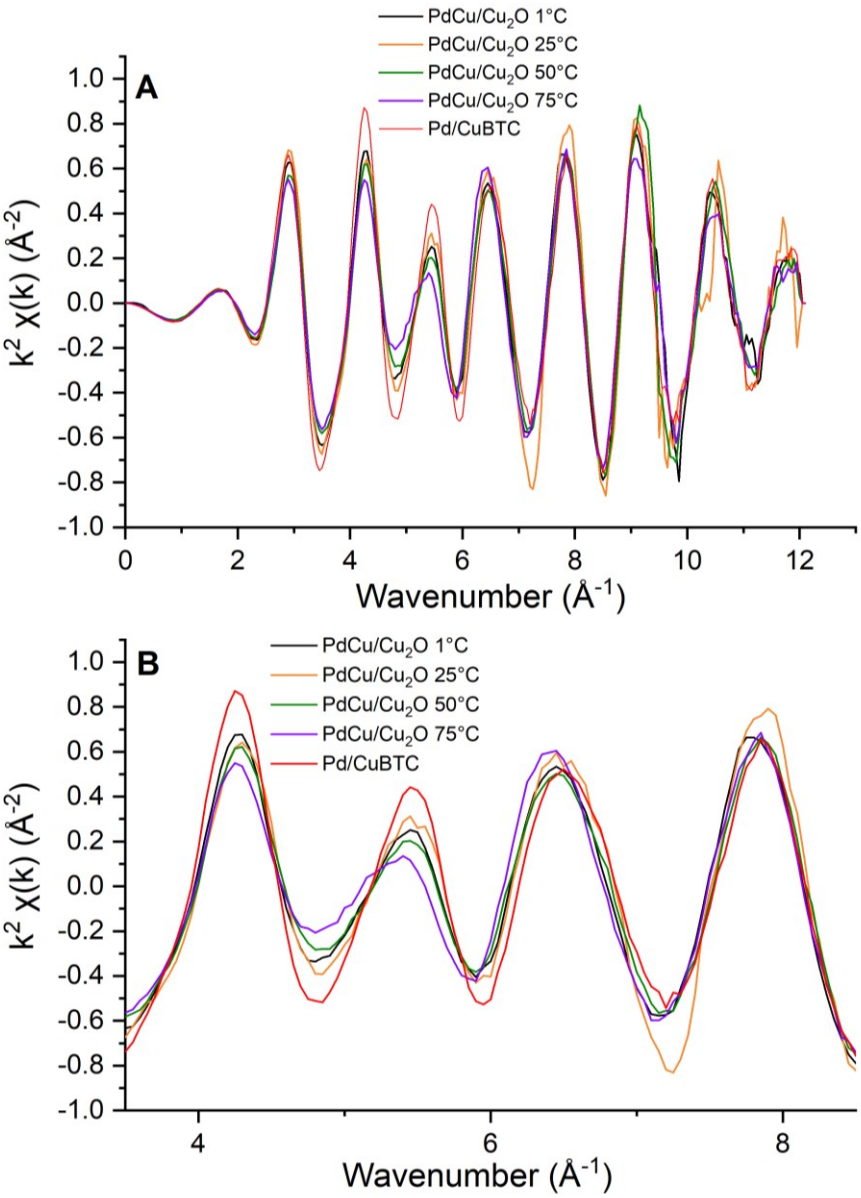

Figure 60: a) Comparisons of the k^2-weighted k-space functions of the Pd K edge XAFS spectra for PdCu/Cu_2O samples reduced at 1-75 °C, and non-reduced Pd/CuBTC; b) a zoomed version of the k^2-weighted k-space data for those samples highlighting the $3.5 < k < 8.5$ region.

The non-phase-corrected Fourier transform data for the reduced samples and Pd/CuBTC are also shown in **Figure 61**. Examination of the central feature at ~2.5 Å shows a subtle positive shift for the reduced samples compared to Pd/CuBTC, and there is also a notable increase in the dipped feature at ~2.2 Å, which in **Section 4.3.2.1** was attributed as evidence of Pd-Cu alloying. Additionally, this feature appears to become stronger as reduction temperature

increases, which suggests that the magnitude of PdCu alloying will increase at high temperature.

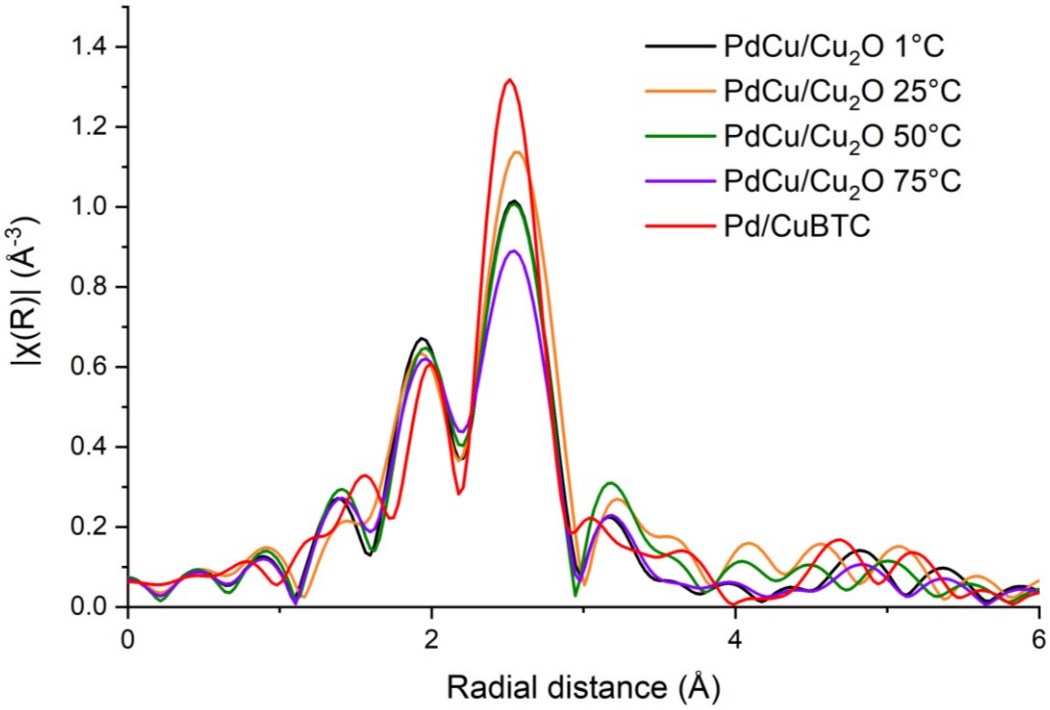

Figure 61: Comparisons of the non-phase-corrected Fourier transform (*R*-space) data of the Pd K edge XAFS spectra for PdCu/Cu_2O samples reduced at 1-75 °C, and non-reduced Pd/CuBTC.

4.3.4.2 EXAFS fits

To evaluate the subtle differences between the samples, the EXAFS data for each sample was fitted using a simple first shell model using the Artemis software from the Demeter software package. The fits for the four temperature-reduced samples are displayed in **Figure 62**, with the fitting parameters summarised in **Table 10**. The fitting parameters calculated for Pd/CuBTC in Chapter 3 have also been included for straightforward comparison.

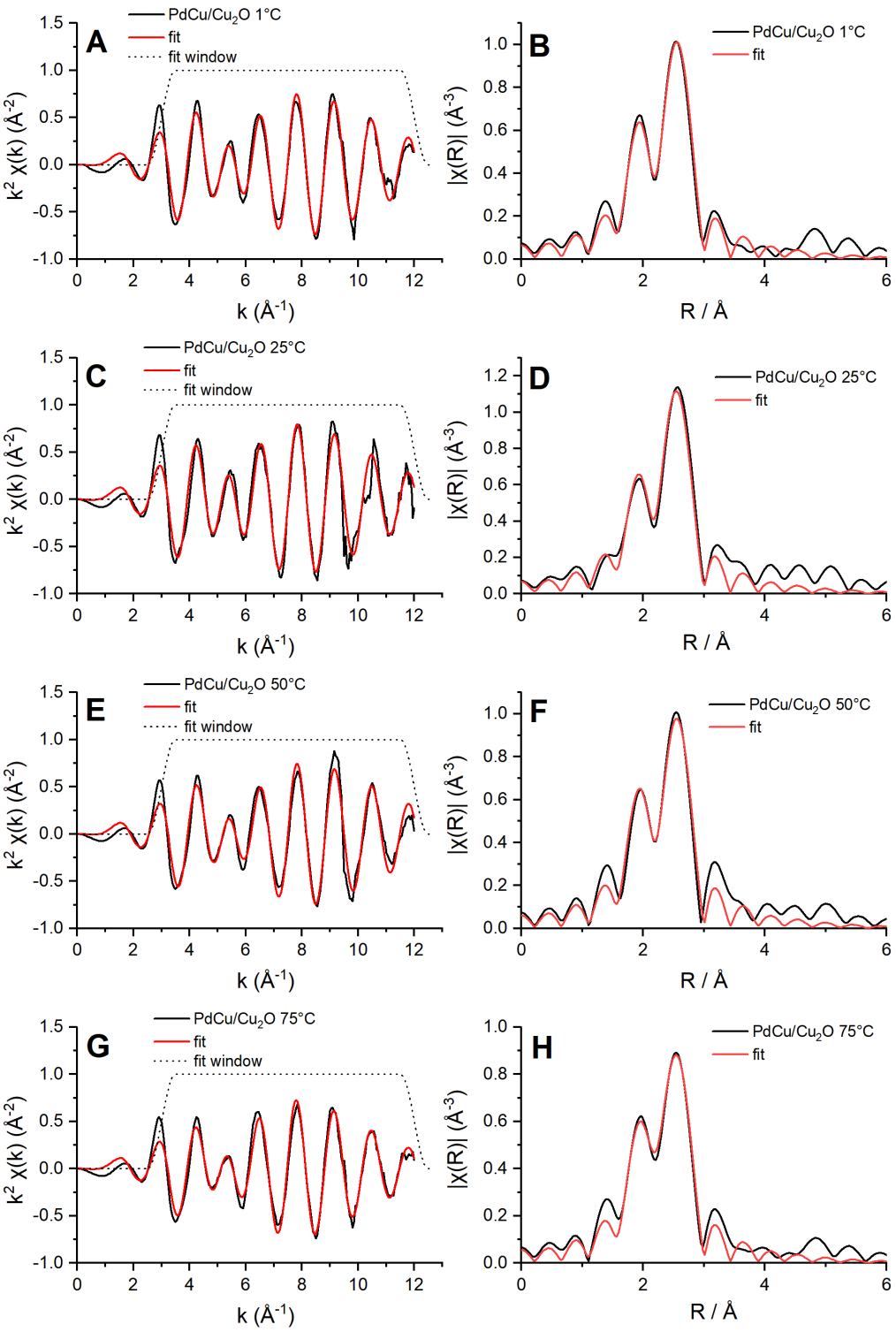

Figure 62: Fits of Pd K EXAFS data for PdCu/Cu_2O 1 °C, showing a) the k^2-weighted EXAFS signal (black) with a corresponding fit (red) and fit window (black dots); and b) the magnitude of the k^2-weighted non-phase-corrected Fourier transformed signal (black) with a corresponding fit (red). Figures c) and d) are analogous to a) and b) respectively, but for PdCu/Cu_2O 25 °C; in the same manner, e) and f) represent PdCu/Cu_2O 50 °C, and g) and h) represent PdCu/Cu_2O 75 °C.

Generally, it can be seen that the fits model the non-phase-corrected Fourier transform data well, particularly for the main features at ~1.9 Å, ~2.2 Å and ~2.5 Å. There is consistently small disagreement for the feature at ~1.3 Å, which could be due to a small percentage of oxide layer on the nanoparticles; however, implementing a Pd-O distance alongside Pd-Cu and Pd-Pd does not yield a successful fit. The 1 °C sample fit also does not perfectly model the feature at ~1.9 Å, but is a reasonable approximation.

Table 10: EXAFS fitting parameters for the Pd K edge for a Pd/CuBTC composite and samples of $PdCu/Cu_2O$ nanocomposites varied by reduction temperature. Fitting parameters: $S_0^2 = 0.85$, determined from Pd foil; fit range $3 < k < 12$ and $1.0 < R < 3.0$. The spectra were fitted using 9 independent points, and the values for E_0 and σ^2 for all samples were fixed with no associated error.

Sample	Bond (Absorber-scatterer)	Coordination number (C.N.)	E_0 (eV)	σ^2 / Å^2	R / Å	R-factor
$PdCu/Cu_2O$ 1 °C	Pd-Cu1	1.2(2)	-5	0.005	2.62(1)	0.01
	Pd-Pd1	7.4(4)		0.009	2.76(1)	
$PdCu/Cu_2O$ 25 °C	Pd-Cu1	1.4(3)	-5	0.007	2.60(2)	0.01
	Pd-Pd1	7.9(5)		0.009	2.76(1)	
$PdCu/Cu_2O$ 50 °C	Pd-Cu1	1.6(3)	-5	0.007	2.62(2)	0.01
	Pd-Pd1	6.7(5)		0.008	2.75(1)	
$PdCu/Cu_2O$ 75 °C	Pd-Cu1	1.8(3)	-5	0.006	2.60(1)	0.01
	Pd-Pd1	6.3(5)		0.009	2.77(1)	
Pd/CuBTC	Pd-Pd1	8.8(3)	-5	0.009	2.77(2)	0.02

Similarly to the sample reduced with $NaBH_4$ in the presence of 4-NP in **Section 4.3.2.1**, a combination of Pd-Pd and Pd-Cu scattering distances produces an effective model. The sample produced at a reduction temperature of 75 °C has the highest Pd-Cu and lowest Pd-Pd coordination number, suggesting that increased alloying of Cu at higher temperature is displacing Pd atoms from the first coordination sphere. However, a decreasing trend in Pd-Pd coordination number with increasing temperature is not entirely observed due to an increase to

7.9 for the sample reduced at 25 °C. The central Pd-Pd scattering peak in the *R*-space data is also increased in magnitude for this sample, suggesting a larger nanoparticle size on average.

One interesting result from the temperature-varied samples is the appearance of an apparent upward trend in Pd-Cu coordination number with increasing temperature Although there is a substantial amount of error present in measurements of coordination numbers via EXAFS, which limits how much can be concluded, the fact that the numbers correlate well with Sample B from the previous XAS study, which was also prepared at 25 °C and has an estimated Pd-Cu coordination number of 1.4, lends some validity to the trend. Additionally, the biggest difference in coordination number is observed between the 1 °C and the 75 °C samples, a difference which is larger than both the relative margins of error.

There are physical grounds for this trend, since the higher temperature of reduction will lead to a faster rate of reduction of the CuBTC MOF support with $NaBH_4$. As this reaction is quite exothermic itself, this will increase the solution temperature even further and increase the rate of diffusion of Cu atoms towards the Pd nanoparticles, facilitating increased alloying. The extent of this alloying can also influence the catalytic properties of the PdCu nanoparticles, which means that catalytic performance can be used as a proxy to confirm the extent of alloying. Therefore, the relative performances of these nanocomposites for CO oxidation will be explored in Chapter 5.

4.3.4.3 Removal of palladium carbide during alloying

In Chapter 3, there was discussion of how a small amount of palladium carbide was observed to form within the palladium nanoparticles in the Pd/CuBTC composite, arising from the sol-immobilisation synthesis. To investigate its presence in the reduced nanocomposites, the XANES regions of the Pd K edge XAFS spectra for PdCu/Cu_2O 75 °C, Pd/CuBTC, and various reference compounds are displayed in **Figure 63**.

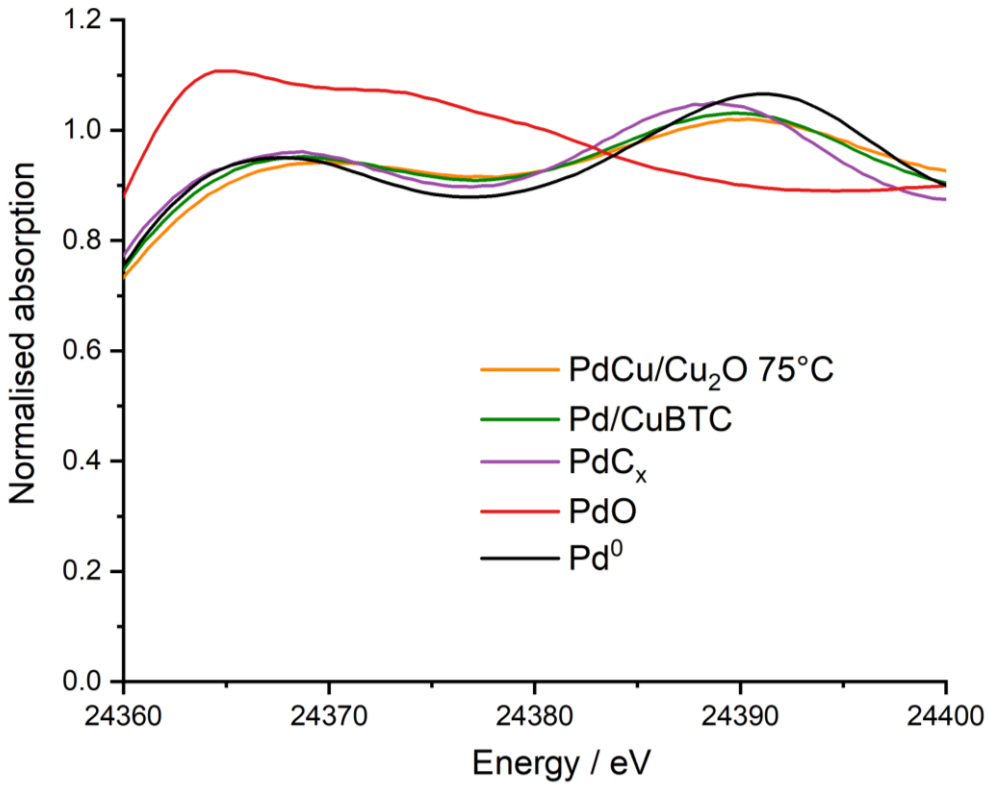

Figure 63: XANES spectra at the Pd K edge for PdCu/Cu_2O 75 °C (orange), Pd/CuBTC (green), and palladium foil (black), palladium oxide (red) and palladium carbide (purple) references.

The evidence for the formation of PdC_x in Pd/CuBTC discussed a subtle positive shift in the first main XANES feature at ~24368 eV, followed by a pronounced negative shift of the second main feature at ~24390 eV, compared to Pd^0. The reduced nanocomposite prepared at 75 °C, which features the most Pd-Cu alloying of the reduced samples, displays a similarity to the Pd/CuBTC XANES spectrum in the raised feature at ~24376 eV, but also features a downward rather than upward shift compared to Pd/CuBTC and PdC_x in the first main feature at ~24368 eV. Additionally, the reduced nanocomposite does not display the same amount of negative shift at ~24390 eV as the Pd/CuBTC sample, which itself was less than that of the PdC_x sample.

Tew *et al.*[43,44] report the formation of persistent palladium carbide during Pd-NP-catalysed hydrogenation of 1-pentyne, which was stable under the reaction conditions of 150 °C, but decomposed under exposure to a reductive atmosphere of H_2. Given that the XANES spectrum for PdCu/Cu_2O prepared at 75 °C does not show the distinctive features of PdC_x, the possibility of its removal must be considered, and it is likely that the harsh reaction conditions of the nanocomposite synthesis are removing the carbide from the Pd nanoparticle lattice.

The reduction process evolves a significant amount of local heat due to the exothermic reduction of the CuBTC MOF support, and given that alloying between Pd and Cu is observed to occur, the local temperature at the nanoparticle surface is expected to be extremely high.

Popov *et al*.[45] report a Cu-Pd phase diagram where alloying becomes accessible at annealing temperatures of over 300 °C, and these local temperatures are known to be accessible at the nanoparticle surface even in room-temperature catalysis. For example, Nagaoka *et al*.[46] were able to initiate the room-temperature oxidative decomposition of ammonia on RuO_2/γ-Al_2O_3 catalysts just by using the local heat of ammonia adsorption on to the catalyst. The overall reaction led to the temperature at the nanoparticle surface being estimated at over 300 °C despite there being no external heat source for the catalytic cycle. Ziemecki *et al*.[47] also reported that an interstitial palladium carbide phase can be removed via heating at temperatures of over 600 °C in an inert atmosphere, or at temperatures of above 150 °C in H_2 or O_2, so there is clearly a limit to the thermal stability of PdC_x phases.

Additionally, the large concentration of $NaBH_4$ reductant used in the nanocomposite preparation will yield a reductive environment similar to that of exposure to a H_2 atmosphere. The combination of the high temperature (enabling diffusion within the lattice) and reductive environment is likely to lead to the overall removal of the carbide. Furthermore, the Pd-Pd distances in the reduced nanocomposites, estimated by the EXAFS fits listed in **Table 10**, all remained less than or equal to that of the carbidised Pd/CuBTC sample (2.77 Å) despite the introduction of Cu into the lattice. Whilst carbon is significantly smaller than copper, the presence of both carbide and Pd-Cu alloying within the same nanoparticle would be expected to cause a greater distortion in the nanoparticle lattice than with just a small amount carbide alone. Finally, if the reductive environment led to the generation of palladium hydride in place of carbide, this is not expected to be persistent, and would require continued exposure to a H_2 environment to remain stable[48]; it would decompose under the atmospheric conditions used to record the above XANES spectra. In conclusion, the small amount of palladium carbide phase observed in the palladium nanoparticles in the Pd/CuBTC composite is expected to be removed following the reduction of the Pd/CuBTC composite to a PdCu/Cu_2O nanocomposite.

4.3.5 TEM of reduced nanocomposites

To further examine the structure of the nanocomposites produced by the reduction of Pd/CuBTC with $NaBH_4$ and 4-nitrophenol, transmission electron microscopy was performed. **Figure 64** shows the effect of partially reducing the Pd/CuBTC composite with insufficient quantities of $NaBH_4$. The rods of CuBTC MOF with an even dispersal of Pd nanoparticles, as analysed in Chapter 3, are clearly visible, but the foreground of the image shows a clustered structure composed of nanodiscs.

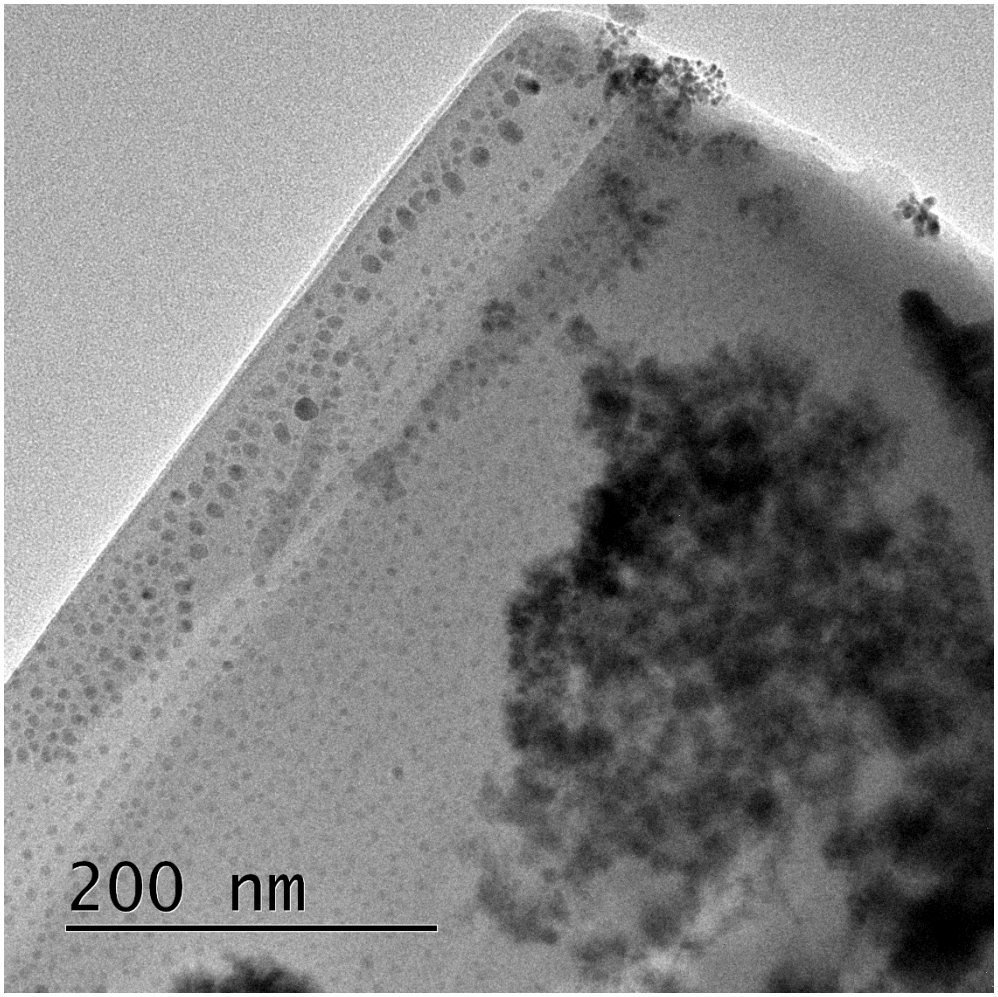

Figure 64: TEM image of partially-reduced Pd/CuBTC, showing rods of CuBTC MOF with a dispersion of Pd nanoparticles, and the clustered structure produced after $NaBH_4$ reduction.

This clustered structure produced on reduction is examined further in **Figure 65**, in which the structure of aggregated discs of mixed copper oxide is clearer. The individual discs measure approximately 15-20 nm in diameter, similar to that estimated by the Scherrer equation in **Section 4.3.3**. The alloyed PdCu NPs remain visible as darker black dots atop the copper support.

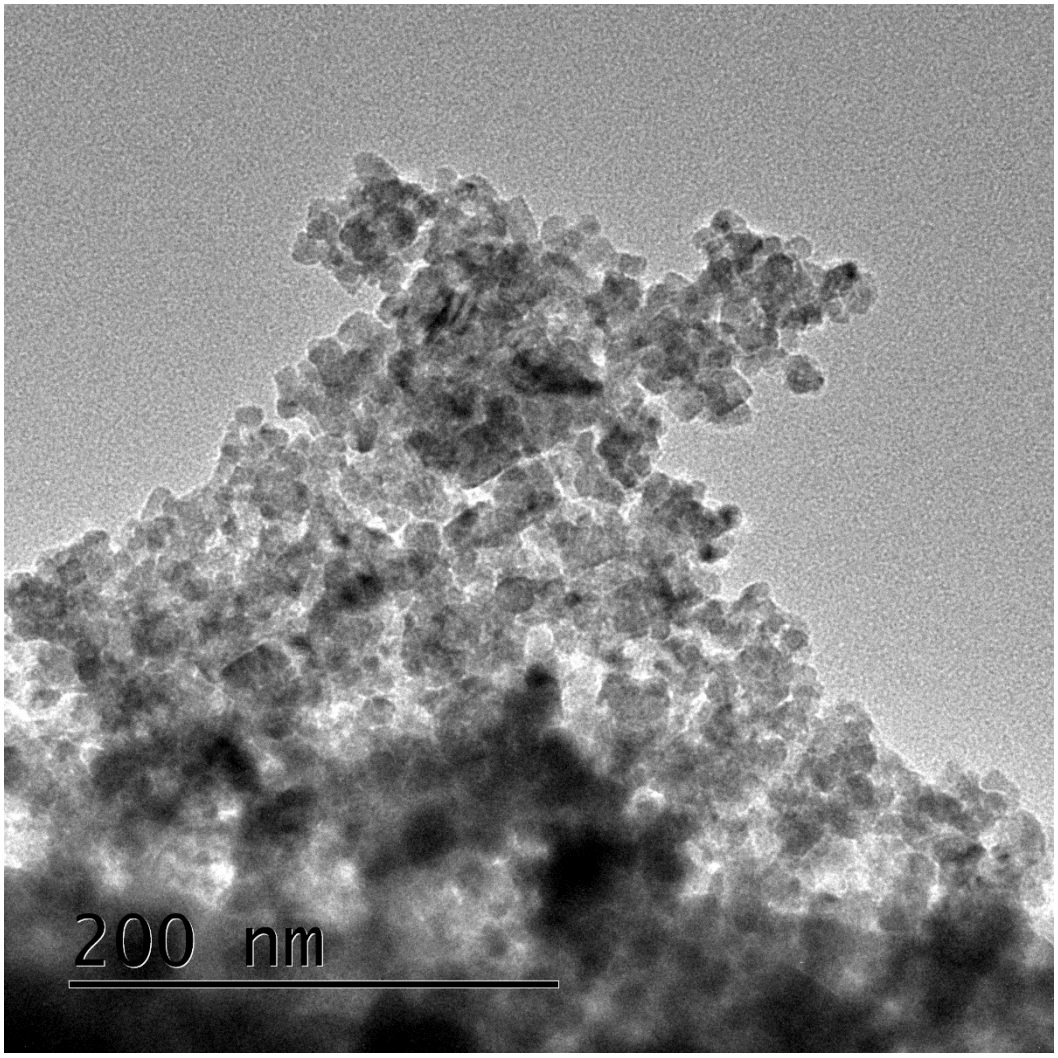

Figure 65: TEM image of PdCu/Cu_2O, produced by reduction of Pd/CuBTC with $NaBH_4$ in the presence of 4-NP, showing aggregated discs of copper oxide and supported PdCu NPs.

The nanodiscs seen above also morphologically resemble the Cu_2O nanoparticles synthesised by Lee *et al.*[49] using $NaBH_4$ reduction of copper (II) sulfate, which formed the same aggregated disc structure. They also appear very similar to mixed Cu/Cu_2O/CuO NPs produced by Fuku *et al.*[50], most resembling those formed after 200 °C and 400 °C calcinations.

This structure can be seen in further detail in **Figure 66**. The inset portion of the figure shows a zoomed view of a copper oxide nanodisc with approximate dimensions of 40 x 20 nm, clearly supporting a Pd nanoparticle of ~6 nm diameter. This structural motif recurs throughout the reduced nanocomposite, although it is clear that there is significant aggregation caused by the reduction process generally, and the ordered structure displayed by the Pd/CuBTC composite has generally been lost during the violent reduction. A snake-like rod structure is occasionally visible in this nanostructure and is seen here at the bottom of the image; this could be attributed to a small amount of local incomplete reduction of the Pd/CuBTC nanocomposite leaving a

larger nanostructure in place of the disc-like morphology seen elsewhere. However, the nanodisc morphology remains the predominant structure throughout the nanocomposite.

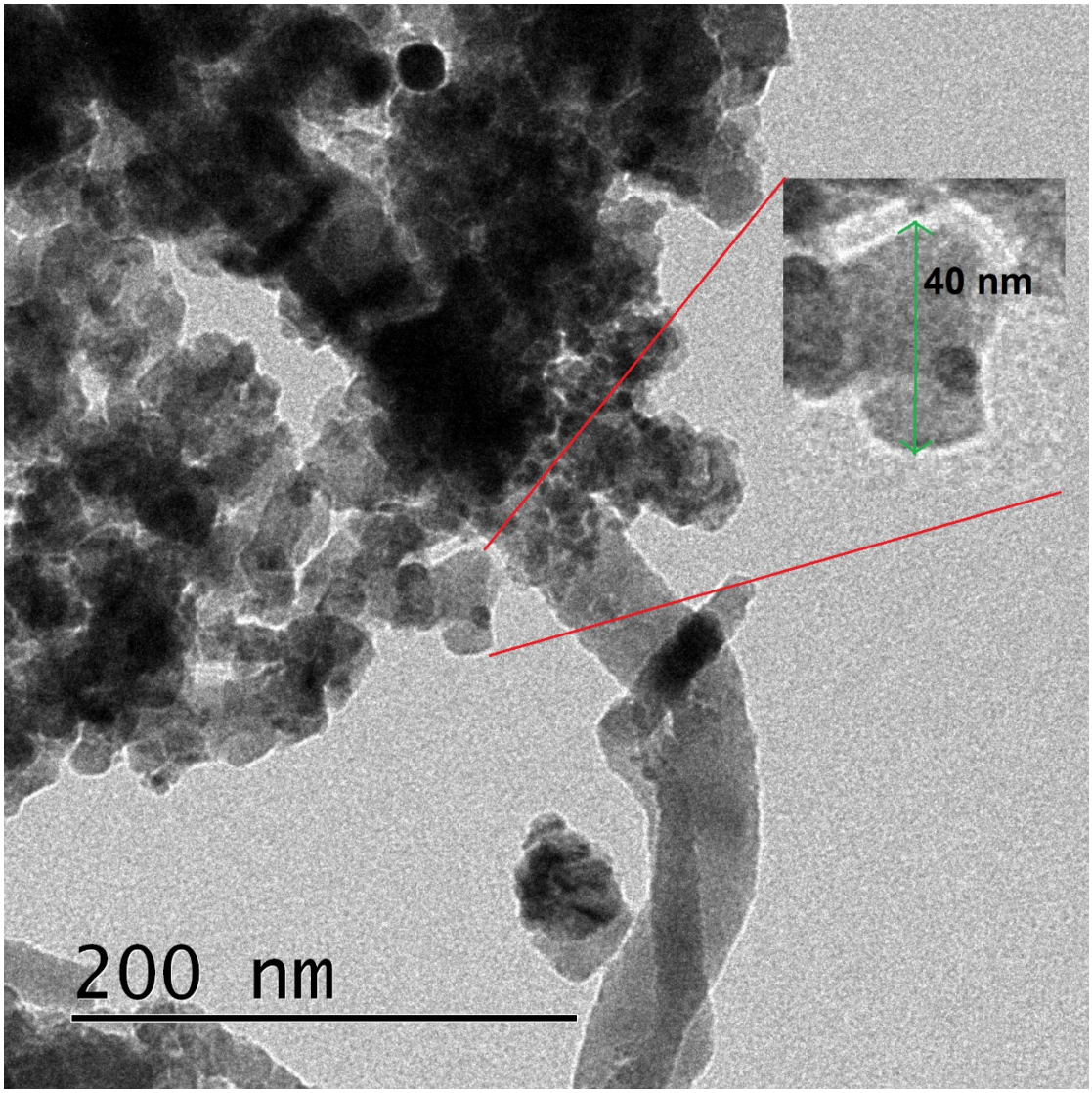

Figure 66: TEM image of PdCu/Cu_2O reduced nanocomposite, showing the disc-like nanostructure with supported PdCu NPs.

High-resolution TEM was also performed to examine the structure of the nanoparticles in more detail. The resolution is such that the lattice spacing within the PdCu NPs can be observed, and is displayed in **Figure 67a**. Taking a profile (**Figure 67b**) along the highlighted yellow line allows calculation of the lattice parameter as 0.241 nm, averaged over ten fringes.

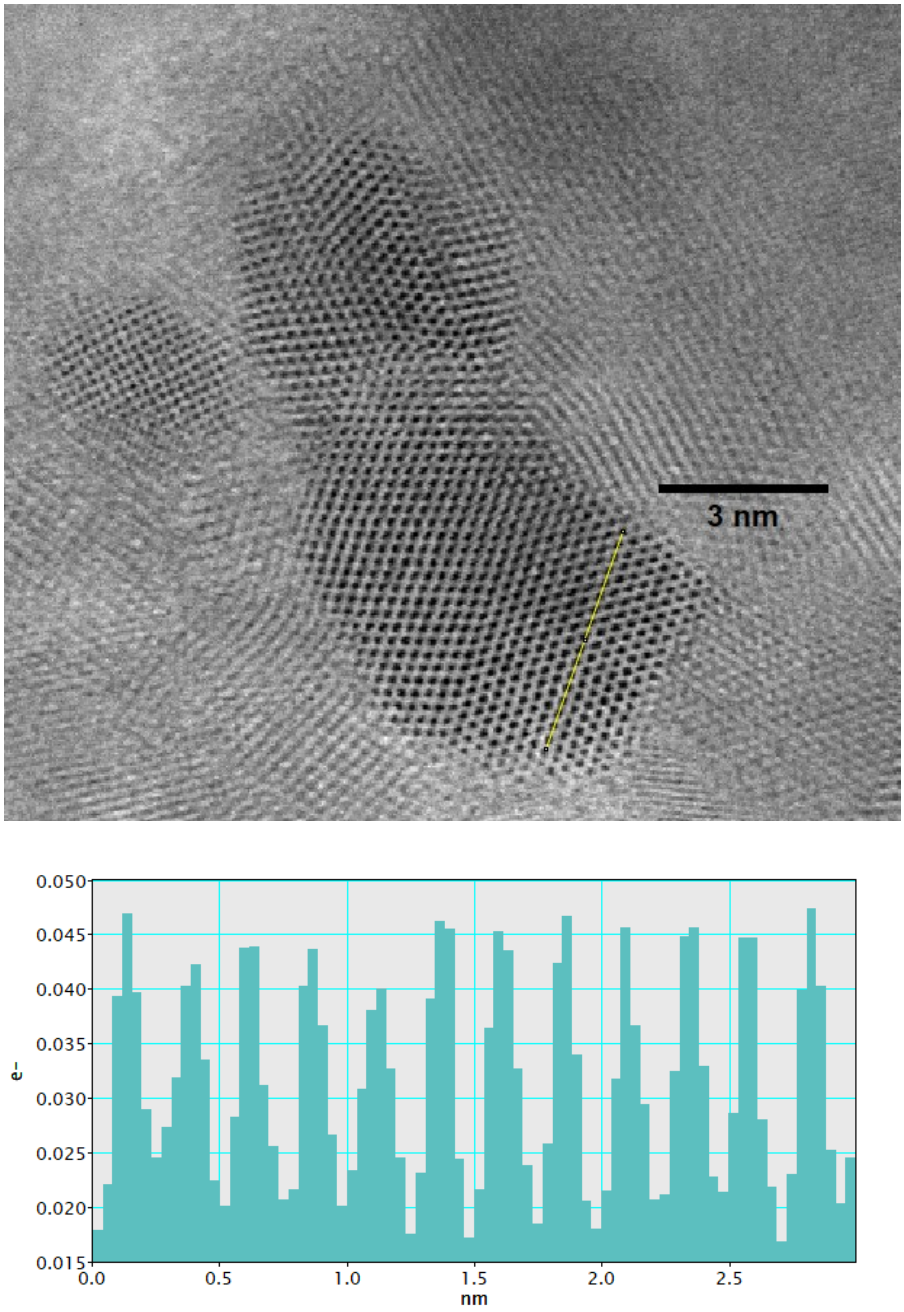

Figure 67: a) High-resolution TEM image of PdCu NPs on a mixed copper oxide support, showing atomic spacing within the nanoparticle. The yellow line indicates a line profile. b) The line profile taken to estimate the lattice parameter within the nanoparticle.

This calculated value compares well to the values of 0.22-0.23 nm exhibited by the (111) facets of various Pd and PdCu nanoparticles in literature.[51–53] The small extra expansion could be indicative of extra strain within the lattice arising from Pd-Cu alloying.

4.4 Conclusions

Overall, a novel chemical method has been developed to allow the generation of nanocomposites using the controlled reduction of nanoparticle-MOF composite structures. The additional experimental parameters available in this chemical method afford enhanced control in contrast to established thermal methods such as MOF pyrolysis, whilst being achievable using standard laboratory equipment at room temperature and pressure.

It was demonstrated that reducing the Pd/CuBTC composites with $NaBH_4$ in the presence of 4-nitrophenol causes a significant shift in the underlying structure of the support. The use of 4-nitrophenol controls the oxidation state of the support, producing a mixed Cu_2O/Cu^0 phase in its presence, suppressing the formation of CuO, which becomes the dominant phase in its absence. Further investigations with 4-aminophenol and ethanolamine suggest that the species responsible for this control is actually the reduced 4-aminophenol product, generated during the *in situ* reduction of 4-nitrophenol catalysed by the Pd NPs, with the control occurring via coordination of amine ligands to Cu atoms.

Further investigation via XAFS analysis suggested that Pd-Cu alloying within the nanoparticles occurred in a specific set of circumstances: using a water-based sol-immobilisation method to generate the Pd/CuBTC composite, and reducing the composite using $NaBH_4$ in the presence of 4-NP. The absence of 4-NP prevents Pd-Cu alloying, as does the use of a methanol-based sol-immobilisation method in Pd/CuBTC synthesis.

The initial key condition for this alloying to occur is the water-based sol-immobilisation method. Due to the relative instability of the CuBTC MOF in water, to which it is exposed for ~90 minutes during the sol-immobilisation process, copper is able to be abstracted from the MOF lattice, which then becomes available for Pd-Cu alloying during the reduction step. The copper can then diffuse across the MOF surface and into the adjacent Pd nanoparticles during reduction, which will be facilitated by the large amount of local heat generated by the $NaBH_4$ hydrolysis.

This observation is possible by comparison to the MeOH-based preparation method. The lack of Pd-Cu alloying for these samples, even after reduction in the presence of 4-NP, suggests that the MOF instability in water is vital for the abstraction of sufficient copper to be available for alloying; CuBTC's stability in MeOH prevents the same situation occurring in this alternate method. Additionally, EXAFS analysis indicates that the lack of a PVA capping agent in the MeOH-based method leads to a higher average Pd-Pd coordination number in the nanoparticles, likely due to the lower amount of NP stabilisation afforded by the MeOH solvent molecules compared to PVA.

The structure of the resultant nanocomposite can then be varied by modulating a series of different experimental parameters. For instance, it was demonstrated that changing the MOF support used to produce the nanocomposite does not have a significant effect on the resultant nanocomposite support structure, since the nanocomposites produced by reducing Pd/CuTPA MOF were shown to have the same XRD pattern and therefore crystal structure as those prepared via the reduction of Pd/CuBTC MOF.

Variation of $NaBH_4$ concentration was shown to not control the extent of Pd-Cu alloying alone, but it does have an influence on the structure of the support. It is possible to retain a NP-MOF-metal oxide hybrid structure by using low concentrations of $NaBH_4$ and forcing the reduction to be incomplete. Other experimental parameters varied include the temperature of reduction, which does not have an effect on the ratio of the copper oxide phases present in the support material, but does affect the extent of Pd-Cu alloying within the nanoparticle, as confirmed by further XAFS analysis, which suggested that an increased reduction temperature of 75 °C caused substantially-more alloying than those produced at 1 °C and 25 °C.

Most importantly, the concentration/amount of amine-based protecting agent used was demonstrated to have a significant influence over the Cu_2O:Cu^0 phase ratio, with high concentrations of 4-nitrophenol (and hence 4-aminophenol) favouring the formation of zero-valent Cu metal. Overall, this means that it is possible to synthesise a nanocomposite with a high Cu_2O:Cu^0 phase ratio and a maximal amount of Pd-Cu alloying by reducing a Pd-MOF composite with a high concentration of $NaBH_4$ and a low concentration of 4-nitrophenol, at a high temperature of reduction.

These level of control over the final properties of the nanocomposite would be significantly more challenging to achieve via a thermal annealing method. For instance, it has been demonstrated to be possible to achieve Pd-Cu alloying in nanoparticles supported on a carbon matrix after a 400 °C annealing step[54], and even after a 100 °C annealing step[55], and unsupported PdCu NPs have recently been generated at 80 °C via an aqueous synthesis[56], but the method described in this chapter is distinguished from these approaches by allowing simultaneous control of the nanoparticle structure and oxide support structure to generate both a Pd-Cu interface within the nanoparticles and a Pd-copper oxide interface between the nanoparticles and the support. The method is intricate and requires careful control of a number of variables, but presents a novel route to generating these PdCu nanocomposites with the overall aim of providing catalytic applications, which will be examined in the following chapter.

4.5 References

1 H. L. Wang, H. Yeh, Y. C. Chen, Y. C. Lai, C. Y. Lin, K. Y. Lu, R. M. Ho, B. H. Li, C. H. Lin and D. H. Tsai, *ACS Appl. Mater. Interfaces*, 2018, **10**, 9332–9341.

2 Q. Wang and D. Astruc, *Chem. Rev.*, 2020, **120**, 1438–1511.

3 K. L. Mulfort and J. T. Hupp, *J. Am. Chem. Soc.*, 2007, **129**, 9604–9605.

4 L. Oar-Arteta, T. Wezendonk, X. Sun, F. Kapteijn and J. Gascon, *Mater. Chem. Front.*, 2017, **1**, 1709.

5 J. Zhang, B. An, Y. Hong, Y. Meng, X. Hu, C. Wang, J. Lin, W. Lin and Y. Wang, *Mater. Chem. Front.*, 2017, **1**, 2405.

6 H. Yue, Y. Zhao, S. Zhao, B. Wang, X. Ma and J. Gong, *Nat. Commun.*, 2013, **4**, 2339.

7 R. V. Jagadeesh, K. Murugesan, A. S. Alshammari, H. Neumann, M. M. Pohl, J. Radnik and M. Beller, *Science (80-.).*, 2017, **358**, 326–332.

8 J. M. Zamaro, N. C. Pérez, E. E. Miró, C. Casado, B. Seoane, C. Téllez and J. Coronas, *Chem. Eng. J.*, 2012, **195–196**, 180–187.

9 B. Liu, S. Han, K. Tanaka, H. Shioyama and Q. Xu, *Bull. Chem. Soc. Jpn.*, 2009, **82**, 1052–1054.

10 S. Li, G. Liu, H. Lian, M. Jia, G. Zhao, D. Jiang and W. Zhang, *Catal. Commun.*, 2008, **9**, 1045–1049.

11 S. Mukherjee, S. Hou, S. A. Watzele, B. Garlyyev, W. Li, A. S. Bandarenka and R. A. Fischer, *ChemElectroChem*, 2022, **9**, e202101476.

12 V. P. Santos, T. A. Wezendonk, J. J. D. Jaén, A. I. Dugulan, M. A. Nasalevich, H. U. Islam, A. Chojecki, S. Sartipi, X. Sun, A. A. Hakeem, A. C. J. Koeken, M. Ruitenbeek, T. Davidian, G. R. Meima, G. Sankar, F. Kapteijn, M. Makkee and J. Gascon, *Nat. Commun.*, 2015, **6**, 6451.

13 A. Jalal, Y. Zhao and A. Uzun, *Ind. Eng. Chem. Res.*, 2022, **61**, 2068–2080.

14 J. Sun, D. Ma, H. Zhang, X. Liu, X. Han, X. Bao, G. Weinberg, N. Pfänder and D. Su, *J. Am. Chem. Soc.*, 2006, **128**, 15756–15764.

15 Y. Dai, P. Lu, Z. Cao, C. T. Campbell and Y. Xia, *Chem. Soc. Rev.*, 2018, **47**, 4314–4331.

16 J. A. Cahill and A. D. Kirshenbaum, *J. Phys. Chem.*, 1962, **66**, 1080–1082.

17 K. Ma, Y. Tian, Z. J. Zhao, Q. Cheng, T. Ding, J. Zhang, L. Zheng, Z. Jiang, T. Abe, N. Tsubaki, J. Gong and X. Li, *Chem. Sci.*, 2019, **10**, 2578–2584.

18 S. Q. Cheng, X. F. Weng, Q. N. Wang, B. C. Zhou, W. C. Li, M. R. Li, L. He, D. Q. Wang and A. H. Lu, *Chinese J. Catal.*, 2022, **43**, 1092–1100.

19 T. W. Hansen, A. T. Delariva, S. R. Challa and A. K. Datye, *Acc. Chem. Res.*, 2013, **46**, 1720–1730.

20 I. Yamane, K. Sato, R. Otomo, T. Yanase, A. Miura, T. Nagahama, Y. Kamiya and T. Shimada, *Nanomaterials*, 2021, **11**, 1040.

21 S. Li, M. Li, C. Zhang, S. Wang, X. Ma and J. Gong, *Int. J. Hydrogen Energy*, 2012, **37**, 2940–2949.

22 L. Santamaria, G. Lopez, A. Arregi, M. Amutio, M. Artetxe, J. Bilbao and M. Olazar, *Appl. Catal. B Environ.*, 2019, **242**, 109–120.

23 R. Li, S. Wu, X. Wan, H. Xu and Y. Xiong, *Inorg. Chem. Front.*, 2016, **3**, 104–110.

24 Y. Fu, X. Zhai, S. Wang, L. Shao, X. Bai, Z. Su, Y. Liu, L. Zhang and J. Chen, *Inorg. Chem.*, 2021, **60**, 16447–16454.

25 G. N. Glavee, K. J. Klabunde, C. M. Sorensen and G. C. Hadjipanayis, *Langmuir*, 1994, **10**, 4726–4730.

26 Q. M. Liu, D. B. Zhou, Y. Yamamoto, R. Ichino and M. Okido, *Trans. Nonferrous Met. Soc. China - English Ed.*, 2012, **22**, 117–123.

27 T. Aditya, A. Pal and T. Pal, *Chem. Commun.*, 2015, **51**, 9410–9431.

28 A. Khan, A. Rashid, R. Younas and R. Chong, *Int. Nano Lett.*, 2016, **6**, 21–26.

29 D. E. Diaz-Droguett, R. Espinoza and V. M. Fuenzalida, *Appl. Surf. Sci.*, 2011, **257**, 4597–4602.

30 U. Holzwarth and N. Gibson, *Nat. Nanotechnol.*, 2011, **6**, 534.

31 G. F. Tierney, S. Alijani, M. Panchal, D. Decarolis, M. B. de Gutierrez, K. M. H. Mohammed, J. Callison, E. K. Gibson, P. B. J. Thompson, P. Collier, N. Dimitratos, E. C. Corbos, F. Pelletier, A. Villa and P. P. Wells, *ChemCatChem*, 2021, **13**, 5121–5133.

32 M. Newville, *Rev. Mineral. Geochemistry*, 2014, **78**, 33–74.

33 M. J. Islam, M. Granollers Mesa, A. Osatiashtiani, J. C. Manayil, M. A. Isaacs, M. J. Taylor, S. Tsatsos and G. Kyriakou, *Appl. Catal. B Environ.*, 2021, **299**, 120652.

34 D. N. Olekszyszen, B. L. Albuquerque, D. D. O. Silva, G. L. Tripodi, D. C. De Oliveira and J. B. Domingos, *Nanoscale*, 2020, **12**, 1171–1179.

35 C. Sarkar, P. Koley, I. Shown, J. Lee, Y. F. Liao, K. An, J. Tardio, L. Nakka, K. H. Chen and J. Mondal, *ACS Sustain. Chem. Eng.*, 2019, **7**, 10349–10362.

36 B. Ravel and S. D. Kelly, *AIP Conf. Proc.*, 2007, **882**, 150–152.

37 H. T. Phan and A. J. Haes, *J Phys Chem C Nanomater Interfaces*, 2019, **123**, 16495–16507.

38 Y. Yang, P. Shukla, S. Wang, V. Rudolph, X. M. Chen and Z. Zhu, *RSC Adv.*, 2013, **3**, 17065–17072.

39 W. Wang, Z. Liao, Y. Wang, X. Wu, F. Qu and X. Zhang, *Cryst. Res. Technol.*, 2011, **46**, 300–304.

40 M. E. Straumanis and L. S. Yu, *Acta Crystallogr. Sect. A*, 1969, **25**, 676–682.

41 P. Deka, R. C. Deka and P. Bharali, *New J. Chem.*, 2014, **38**, 1789–1793.

42 J. Peng, B. Chen, Z. Wang, J. Guo, B. Wu, S. Hao, Q. Zhang, L. Gu, Q. Zhou, Z. Liu, S. Hong, S. You, A. Fu, Z. Shi, H. Xie, D. Cao, C. J. Lin, G. Fu, L. S. Zheng, Y. Jiang and N. Zheng, *Nature*, 2020, **586**, 390–394.

43 M. W. Tew, M. Janousch, T. Huthwelker and J. A. Van Bokhoven, *J. Catal.*, 2011, **283**, 45–54.

44 M. W. Tew, M. Nachtegaal, M. Janousch, T. Huthwelker and J. A. Van Bokhoven, *Phys. Chem. Chem. Phys.*, 2012, **14**, 5761–5768.

45 A. A. Popov, Y. V. Shubin, P. E. Plyusnin, M. R. Sharafutdinov and S. V. Korenev, *J. Alloys Compd.*, 2019, **777**, 204–212.

46 K. Nagaoka, T. Eboshi, Y. Takeishi, R. Tasaki, K. Honda, K. Imamura and K. Sato, *Sci. Adv.*, 2017, **3**, 1–8.

47 S. B. Ziemecki, G.A. Jones, D.G. Swartzfager, R.L. Harlow and J. Faber, *J. Am. Chem. Soc.*, 1985, **107**, 4547-4548.

47 T. Xie and R. M. Rioux, *Catal. Today*, 2021, **371**, 29–39.

48 J. H. Lee, S. K. Hong and W. B. Ko, *J. Ind. Eng. Chem.*, 2010, **16**, 564–566.

49 X. Fuku, M. Modibedi and M. Mathe, *SN Appl. Sci.*, 2020, **2**, 1–15.

50 A. Kumar, M. M. Mohammadi and M. T. Swihart, *Nanoscale*, 2019, **11**, 19058–19085.

51 F. Cai, L. Yang, S. Shan, D. Mott, B. Chen, J. Luo and C.-J. Zhong, *Catalysts*, 2016, **6**, 96.

52 O. Y. Sarıbıyık, G. Rupprechter, C. Weilach and S. Serin, *Catalysts*, 2020, **10**, 1–18.

53 Y. Luo, L. A. Estudillo-Wong, L. Cavillo, G. Granozzi and N. Alonso-Vante, *J. Catal.*, 2016, **338**, 135–142.

54 Z. P. Wu, S. Shan, Z. H. Xie, N. Kang, K. Park, E. Hopkins, S. Yan, A. Sharma, J. Luo, J. Wang, V. Petkov, L. Wang and C. J. Zhong, *ACS Catal.*, 2018, **8**, 11302–11313.

55 B. Cho, J. Lee, I. P. Roh, M. H. Lee and T. Yu, *J. Alloys Compd.*, 2022, **911**, 164990.

Chapter 5 Catalytic Testing of Pd/CuMOF and PdCu/Cu_2O Nanocomposites

5.1 Introduction

In this chapter, the Pd/CuBTC composites from Chapter 3 and the PdCu/Cu_2O nanocomposites produced in Chapter 4 are examined as catalysts for 4-nitrophenol reduction and CO oxidation, with their relative performances for both reactions evaluated. As discussed in **Section 1.5**, PdCu NP-based catalysts have been shown to be versatile and effective catalysts, and this report aims to investigate the utility of the synthesised PdCu/Cu_2O nanocomposites and whether it is possible to improve upon the performances of other PdCu-based catalysts reported in literature.

5.1.1 Reduction of 4-nitrophenol to 4-aminophenol

The reduction of 4-nitrophenol to 4-aminophenol is an important catalytic reaction, since the initial nitro compound is a harmful industrial by-product, and the product is a synthetically-useful pharmaceuticals precursor.[1] 4-nitrophenol is used in the creation of dyes and pesticides and is also useful as a fungicide on leather.[2] Nitrophenols serve as industrial pollutants within wastewater and are highly toxic, necessitating a method for their removal.[3] Previous methods used to dispose of this compound include adsorption with carbon nanotubes[4] or with nanoscale oxides[5], but there has also been recent research into the use of nanocomposites to catalyse the reduction of 4-nitrophenol to 4-aminophenol, including with ZnO/HZSM-5 zeolite[6] or Pd, Au or bimetallic PdAu NPs supported on magnetite.[7] Rogers *et al.* demonstrated that nanoparticle-metal oxide composites synthesised via sol-immobilisation can function as an effective catalyst for 4-nitrophenol reduction[8], a similar approach to that undertaken in this report.

The reduction of 4-nitrophenol to 4-aminophenol has also been exploited as a model catalytic reaction, as it is well-established as an effective screening method to characterise the availability of supported nanoparticles.[9] This is possible since the reaction happens very quickly and at room temperature, and can be easily monitored using UV/vis spectroscopy.[10]

Many metal nanoparticles are able to catalyse the reduction of 4-nitrophenol. For instance, there are recent examples of nanocomposite catalysts based on Au NPs stabilised by zeolites[11], polymeric resins[12], and cyclodextrins[13]. Catalysis is not limited to rare metals, however, since there are further examples of Cu^0 NPs supported on a carbon-based matrix[14],

copper-terephthalate-based MOFs[15], and metal-oxide-supported CuO nanoparticles[16] all demonstrating catalytic activity for the nitrophenol reduction. Additionally, Sasmal *et al.*[17] reported a mixed Cu_2O-Cu-CuO nanocomposite phase generated *in situ* as an explanation for the improved activity of Cu_2O NPs compared to Cu^0 NPs, and the mixed copper-oxide phase bears some similarities to the copper oxide nanocomposites derived in Chapter 4 of this report.

As with many other catalytic reactions[18], Pd nanoparticle-based catalysts persistently exhibit high performance for nitrophenol reduction with respect to turnover frequency and yield.[19] However, catalytic performance depends on being able to minimise the aggregation of Pd NPs on the support, maintaining a sufficient level of dispersion and available surface area. Methods to achieve this have included introducing strong metal-support interactions, using a Sn/S chalcogel[20]; using dendritic nanospheres of mesoporous silica and titania[21]; and the more common choice of using PVA as a polymeric capping agent.[22,23] There have also been reported examples of using metal-organic frameworks as a support for Pd NPs to generate a catalyst for 4-nitrophenol reduction, including Pd NPs dispersed on 2D Co-MOF heterostructures[24], and even a Pd/HKUST-1 composite similar to that produced in Chapter 3, through an alternative "spray synthesis" method, wherein an NP-MOF precursor solution is sprayed into droplets, heated to 200 °C and collected through centrifugation.[25]

In the first section of this chapter, the Pd/CuMOF composites synthesised in Chapter 3, and the resultant nanocomposites prepared from their reduction with $NaBH_4$, are tested as catalysts for the reduction of 4-nitrophenol into 4-aminophenol. The Pd/CuMOF composites include both those prepared using CuBTC (HKUST-1) and the terephthalate-based CuTPA MOF.

5.1.2 CO Oxidation

Carbon monoxide is a diatomic, colourless gas formed during the incomplete combustion of carbon-based fuels. It is both colourless and odourless, and is toxic when inhaled in sufficient amounts, due to its stronger affinity for haemoglobin than O_2, inhibiting oxygen transport in the body.[26,27] Its release into the atmosphere, as a pollutant arising from the exhaust fumes of automobiles and otherwise, presents a significant public health concern.[28] Oxidising CO to carbon dioxide is one possible solution to this, despite CO_2 itself being a greenhouse gas, since this reaction can be readily achieved using a range of established nanoparticle and noble metal catalysts[29,30].

The equation for CO oxidation is simply $2CO + O_2 \rightarrow 2CO_2$.[31] The ability to perform this reaction using standard testing equipment and common laboratory gases makes it a useful test reaction for supported nanoparticle catalysts.[32]

A range of nanoparticle-MOF composites have been tested for CO oxidation. For example, Jiang *et al.*[33] supported Au nanoparticles on a ZIF-8 MOF support, determining a decrease in light-off temperature from 225 °C to 170 °C by increasing the gold loading from 0.5 wt% to 5 wt%. CuBTC MOF has also been employed as both a catalyst and a support, according to Ye *et al.*[34], who claimed that conventional CuBTC, an amorphized variant prepared by plasma treatment, and a sample with PdO_2 nanoparticles loaded on to the amorphized MOF all exhibited activity for CO oxidation, with light-off temperatures over 200 °C. This was followed up by Zamaro *et al.*[35], who showed that CuBTC MOF actually thermally decomposes at those reaction temperatures to yield an active catalyst based on CuO nanoparticles, a process which they exploited to synthesise nanocomposites of CuO-CeO_2.

Due to the wide applicability of palladium to many catalytic reactions, many catalysts based on supported Pd nanoparticles have been evaluated for CO oxidation. Murata *et al.*[36] used 2 nm-sized Pd NPs supported on alumina to demonstrate that Pd corner sites and (111) facets are most active for CO oxidation, supported by a similar pattern seen in Pd/$SrTiO_3$ catalysts prepared by Chen *et al.*.[37] Pd NPs supported on MOFs have also been studied for the reaction, such as the Pd/rGO@CuBTC catalysts prepared by Altass *et al.*[38], where reduced graphene oxide was used as part of a nanocomposite to improve the dispersion of Pd NPs on the MOF support, achieving CO light-off temperatures as low as 71 °C.

There has been some interest in the use of bimetallic PdCu nanoparticles for CO oxidation, aiming to exploit electronic interactions between the two atoms that serve to improve their catalytic properties relative to unalloyed Pd nanoparticles. Computational studies have determined that for PdCu nanoparticles, the adsorption energy of O_2 reaches a minimum for Pd:Cu 50:50 alloys, which was the ratio that provided an optimal predicted activity level for CO oxidation.[39] The PdCu alloying also causes the energies of centres of the electronic *d*-bands for Pd and Cu to shift towards each other, reducing the overall binding strength of CO for Pd and increasing it for Cu.[40] One problem faced by Pd-based catalysts is poisoning by CO molecules[41], binding too strongly to the metal and blocking the active sites, so causing an overall reduction in CO binding strength by alloying Pd with Cu is likely to help alleviate this issue. PdCu NPs supported on oxides such as titania, ceria, and alumina were prepared by Cai *et al.*[42], which displayed large differences in light-off temperature between supports, attributed to a combination of metal-support interactions and the oxygen storage capacity of the material.

In the second section of this chapter, the Pd/CuBTC composite from Chapter 3 and the reduced PdCu/Cu_2O nanocomposites generated in Chapter 4 are evaluated for CO oxidation and their catalytic performances analysed.

5.2 Experimental Details

Pd/CuMOF composites: All Pd/CuMOF composites examined in this chapter were prepared using the water-based sol-immobilisation method outlined in Chapter 3, using PVA as a capping agent. The metal-organic frameworks used as a support were synthesised using the hydrothermal synthesis based on a 1:1:1 solvent mix of DMF:H_2O:EtOH, also described in Chapter 3.

PdCu/Cu_2O nanocomposites: All PdCu/Cu_2O nanocomposites studied in this chapter were prepared using the $NaBH_4$ reduction method in the presence of 4-nitrophenol, as described in Chapter 4. Where appropriate, samples are labelled with their temperature of reduction, either 1 °C, 25 °C, 50 °C, or 75 °C, where the water used to dissolve the $NaBH_4$ for the reduction is stabilised at that temperature prior to the addition of $NaBH_4$ powder to begin the reaction. Samples were prepared using an $NaBH_4$ concentration of 0.0397 M and a 4-NP concentration of 0.00018 M.

MP-AES: MP-AES spectra were recorded on an Agilent 4100 spectrometer. Samples were digested in an aqueous solution of 10% aqua regia. The instrument was calibrated using Pd and Cu atomic absorption standards of 1000 µg / mL, using wavelengths of 324.754 nm and 510.554 nm for Cu, and 340.458 nm and 360.955 nm for Pd.

Reduction of 4-nitrophenol: 1 mg of catalyst was weighed out and added to a polystyrene cuvette. $NaBH_4$ (0.3 mL, 0.0397 M) was added by pipette prior to the addition of aqueous 4-nitrophenol solution (2.7 mL, 0.00018 M). The quantities of $NaBH_4$ and 4-NP were calculated to give an $NaBH_4$/4-NP molar ratio of ~25. The reaction was monitored using UV/vis spectroscopy, using a Shimadzu UV-1800 spectrophotometer, with polystyrene cuvettes with a path length of 1 cm. Scans from 600-300 nm were repeated every 15 seconds until the reaction was observed to be complete. Due to variations in the baseline of the UV/vis spectra arising from absorbance of the suspended catalyst within the mixture, the UV/vis spectra were translated to set the identified crossing point at ~470 nm as equal to zero absorbance.

CO oxidation: Catalytic testing for CO oxidation was undertaken using a Hiden CATLAB microreactor, using a 5 °C min^{-1} temperature ramp rate across the range 40-200 °C for the reduced PdCu/Cu_2O nanocomposites. Pd/CuBTC composites were also measured, but at the temperature range 40-350 °C. A pellet press and sieve set were used to obtain 100 mg of catalyst in the 125 – 250 μm sieve fraction, which was used to form a catalyst bed in a quartz capillary packed at both ends with quartz wool. Catalytic testing was performed using a total gas flow rate of 70 mL min^{-1}, using 50 mL min^{-1} of 10% CO/He, an excess of 5 mL min^{-1} O_2, and 15 mL min^{-1} Ar. Exhaust gases were fed into a Hiden QGA mass spectrometer, allowing tracking of outlet composition for CO at m/z = 28, O_2 at m/z = 32, Ar at m/z = 40, He at m/z = 4, and CO_2 at m/z = 44.

5.3 Results and Discussion

5.3.1 Pd- and PdCu-based catalysts for the reduction of 4-nitrophenol to 4-aminophenol

As previously mentioned, UV/vis spectroscopy can be used to track catalytic activity for 4-nitrophenol reduction. This is achieved by examining the characteristic absorbance at $\lambda = 400\ \mathrm{nm}$ for the 4-nitrophenolate ion, which is produced *in situ* upon deprotonation by the $NaBH_4$ reducing agent and forms a bright yellow solution. Its decrease over time is proportional to the rate of the reaction, as the 4-nitrophenol is converted to 4-aminophenol, which in turn leads to an increase in a peak at $\lambda = 300\ \mathrm{nm}$ arising from the 4-aminophenol.

Conventionally, supported NP catalysts are briefly pre-treated with $NaBH_4$ to remove any surface oxide component from the nanoparticles, and provide a maximum amount of zero-valent metal available to transfer electrons to the nitrophenolate ion.[43] This generates a short induction period in which the $NaBH_4$ has a stronger affinity for dissolved oxygen than the nitrophenolate ion, and the 4-NP reduction begins once the dissolved oxygen concentration is depleted below a critical value.[44] However, as discussed in Chapter 4, the addition of $NaBH_4$ to the CuMOF support will cause a degradation of the MOF structure, particularly in this case, where $NaBH_4$ is used in significant excess compared to 4-NP, in order to simplify the kinetics of the reaction to be pseudo-first-order with respect to 4-NP concentration.[45] Additionally, the presence of 4-NP during the reduction of the NP-MOF composite was shown to influence Pd-Cu alloying, so for the studies in this chapter, the $NaBH_4$ was added immediately after the addition of 4-NP, to maintain the same conditions as during nanocomposite synthesis via $NaBH_4$ reduction.

The UV/vis spectra produced during 4-nitrophenol reduction using the initial composites of 1 wt% Pd/CuBTC as a catalyst are displayed in **Figure 68**, using three independent testing runs. It is apparent that there is significant variability between the times taken to deplete the 4-nitrophenolate peak. Correcting for small differences in mass of the ~1 mg testing samples does not sufficiently account for this, but the likeliest explanation is that the reaction takes place in an unstirred cuvette in a spectrophotometer, and the reduction of the Pd/CuBTC composite after addition of $NaBH_4$ produces a significant amount of heat to locally distort the rate of reaction. This local exotherm significantly influences the results presented in this chapter, although the test reaction has been repeated to minimise some possible variation.

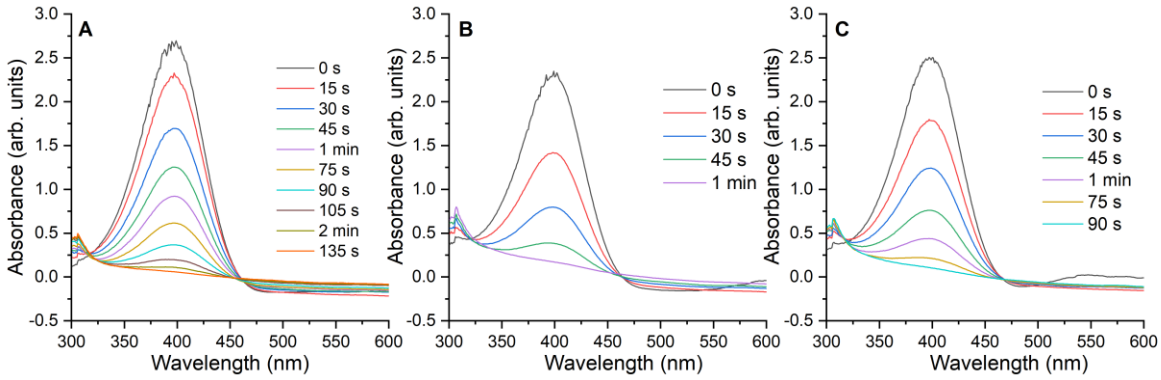

Figure 68: UV/vis spectra of 4-nitrophenol reduction using 1 wt% Pd/CuBTC as a catalyst, showing three separate testing runs in a)-c). Testing performed using a 4-NP/Pd ratio of 5.1 and an $NaBH_4$/4-nitrophenol molar ratio of 24.5.

Plots for the conversion of 4-nitrophenol over time and the change in $ln(C_t/C_0)$ over time, where C_t is the concentration of 4-NP at a given time t and C_0 is the initial concentration of 4-NP, are shown in **Figure 69**. All testing runs exhibited 4-NP conversion of over 90%.

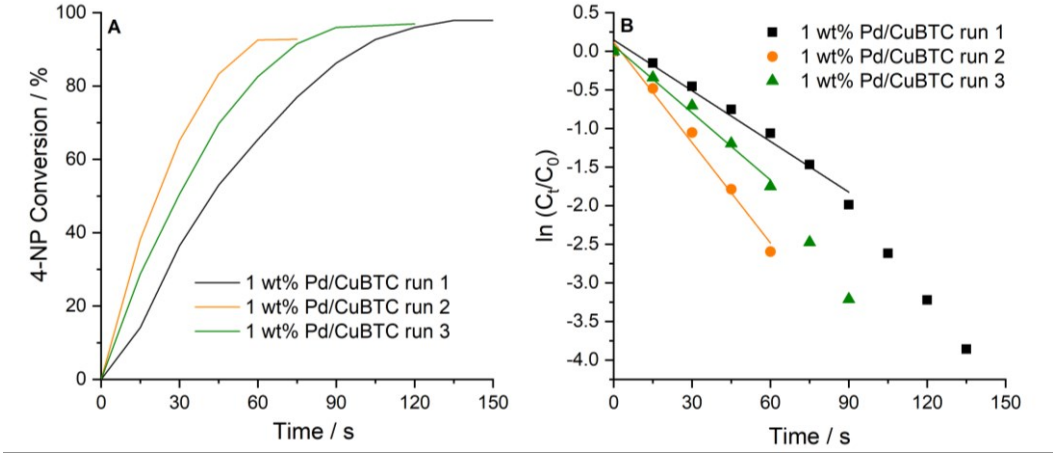

Figure 69: a) Plot of 4-NP conversion against time for the 1 wt% Pd/CuBTC catalyst on three separate testing runs; b) plot of ln(C_t/C_0) for 4-nitrophenol for the same 1 wt% Pd/CuBTC catalyst and testing regime.

It should be noted that the plots of $ln(C_t/C_0)$ against time show a break from linearity as time increases. The kinetic analysis of the reaction is discussed in **Section 2.7.1**, and the assumption that the reaction is pseudo-first-order with respect to 4-NP is only valid when the concentration of $NaBH_4$ is in significant excess. As discussed in Chapter 4, the MOF support in the catalyst can itself be reduced by $NaBH_4$, and it is likely that the concentration of $NaBH_4$ decreases sufficiently during the reaction, through reaction with both 4-NP and the MOF, to cause the pseudo-first-order assumption to break down. Therefore, the trendlines and corresponding rate constants have only been calculated across the region that displays linearity; including further points would overestimate the rate constant. Additionally, the local

exotherm caused by reduction of the Pd/CuBTC composite will cause an initial fast reaction rate, which will then begin to decrease as the reaction vessel cools. It is likely that a combination of temperature effects and $NaBH_4$ concentration effects causes the observed departure from linearity.

Testing was repeated for samples of Pd/CuBTC with calculated Pd loadings of 0.5 wt% and 0.25 wt%, with similar UV/vis spectra shown in **Figure 70** and **Figure 71** respectively, again for three testing runs.

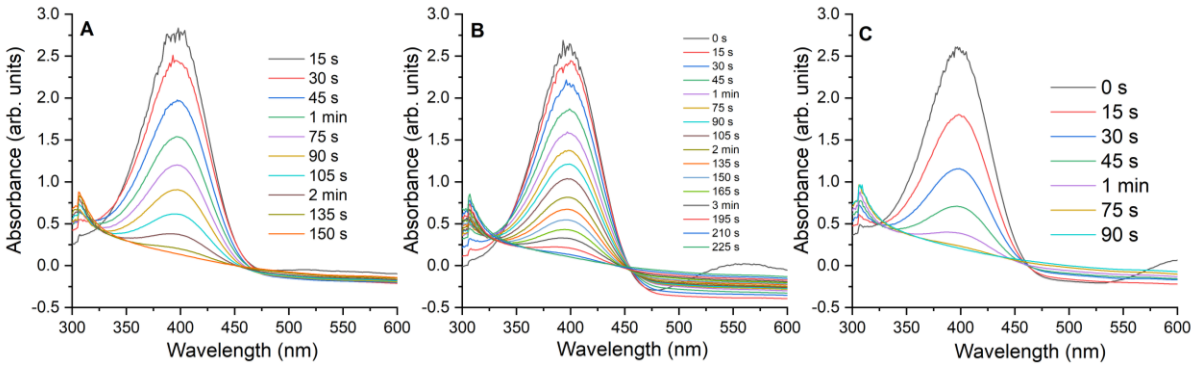

Figure 70: UV/vis spectra of 4-nitrophenol reduction using 0.5 wt% Pd/CuBTC as a catalyst, showing three separate testing runs in a)-c). Testing performed using a 4-NP/Pd ratio of 10.3 and an $NaBH_4$/4-nitrophenol molar ratio of 24.5.

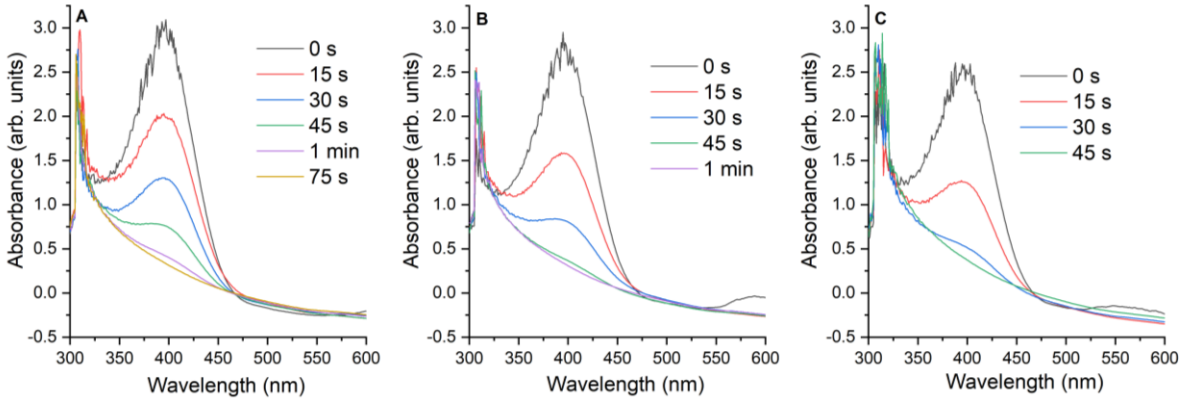

Figure 71: UV/vis spectra of 4-nitrophenol reduction using 0.25 wt% Pd/CuBTC as a catalyst, showing three separate testing runs in a)-c). Testing performed using a 4-NP/Pd ratio of 20.7 and an $NaBH_4$/4-nitrophenol molar ratio of 24.5.

The total amount of 4-nitrophenol being reduced was held constant across testing of all the above Pd/CuBTC samples, which causes the 4-NP/Pd ratio to increase when the Pd loading is reduced; from an ideal ratio (assuming perfect loading) of 5.1 for the 1 wt% sample, 10.3 for the 0.5 wt% sample, and 20.7 for the 0.25 wt% sample. Given the amount of 4-NP per nanoparticle is doubling, it might be expected that the time taken to reduce the 4-NP in the testing batch would also increase. This is observed somewhat for the 0.5 wt% sample, which converts the batch of 4-NP more slowly than the 1 wt% sample, but in contrast, the 0.25 wt% sample displays the best performance of all samples analysed, reducing the 4-NP batch fastest on average and notably faster than the 1 wt% sample.

It is possible that this increased rate reflects an improved dispersion of Pd nanoparticles on the support, but XRD analysis in **Section 3.3.4** indicated that the 0.25 wt% sample exhibited significant quantities of Cu_2O in its diffraction pattern, produced by degradation of the CuBTC MOF during the sol-immobilisation process. As discussed in **Section 5.1.1**, Cu_2O NPs can themselves display activity for the conversion of 4-nitrophenol, so it is possible that both Pd NPs and the Cu_2O nanodiscs observed in these nanocomposites are contributing to the reduction. This would be observed to a lesser extent in the 0.5 wt% sample, which shows a smaller amount of Cu_2O present in its diffraction pattern; the 1 wt% sample does not display significant quantities of Cu_2O and is observed to degrade to a lesser extent during the preparation method.

The conversion and $ln(C_t/C_0)$ data for the 0.5 wt% and 0.25 wt% Pd/CuBTC samples are displayed in **Figure 72**. Like the 1 wt% samples, the 0.5 wt% samples consistently display over 90% conversion of 4-NP; the 0.25 wt% samples approach 87-88% conversion. There is a slight systematic error that will be magnified for the 0.25 wt% samples; they convert 4-NP so quickly that by the time the spectrometer has scanned the first peak (designated as time = 0), a small proportion of the 4-NP has already been converted. This is likely to underestimate the conversion by 2-3 percentage points, determined by correcting the initial absorbance to the maximum 4-NP absorbance possible, but even after this correction, the 0.25 wt% samples still reach a lower peak conversion than the 0.5 wt% and 1 wt% samples.

Calculated pseudo-first-order rate constants for the tested Pd/CuBTC catalysts are listed in **Table 11**, along with average turnover frequencies, expressed as the moles of 4-nitrophenol converted per moles of Pd per hour. Turnover frequencies were calculated after 30 seconds for all samples, to approximate the initial rate of reaction whilst accounting for any time differences in activating the spectrometer after addition of 4-NP and $NaBH_4$.

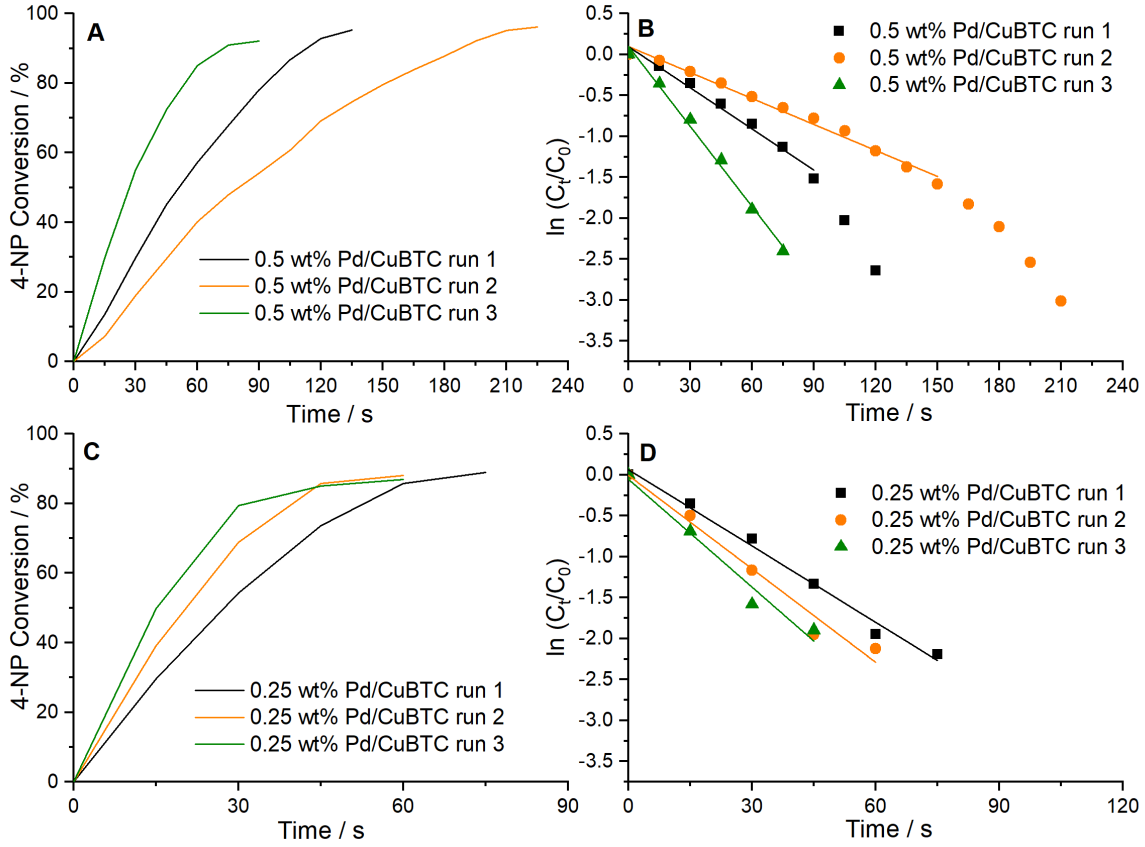

Figure 72: a) Plot of 4-NP conversion against time for the 0.5 wt% Pd/CuBTC catalyst on three separate testing runs; b) plot of ln(C_t/C_0) for 4-nitrophenol for the same 0.5 wt% Pd/CuBTC catalyst and testing regime; c) and d) are analogous to a) and b) but for the 0.25 wt% Pd/CuBTC catalyst.

Table 11: Calculated pseudo-first-order rate constants and turnover frequencies for the 1 wt%, 0.5 wt% and 0.25 wt% Pd/CuBTC catalysts, averaged across the 3 testing runs. Pd loading was measured via MP-AES spectroscopy. Turnover frequencies were calculated after 30 seconds for all samples, to approximate the initial rate of reaction under the local exotherm, and the standard deviation is provided for all samples.

Sample ID	Pd loading	4-NP Conversion	k_{app} / min^{-1}	TOF / hr^{-1}
1.0 wt% Pd/CuBTC	0.991 wt%	96%	1.884	282 ± 76
0.5 wt% Pd/CuBTC	0.354 wt%	94%	1.198	587 ± 241
0.25 wt% Pd/CuBTC	0.178 wt%	88%	2.260	2248 ± 346

The Pd/CuBTC composite performs similarly to other Pd NP-based catalysts in literature. For example, Deng *et al.*[46] reported a TOF for 4-NP of 989 hr^{-1} for a 2.11 wt% Pd NP sample supported on a covalent organic framework, albeit with only 61% conversion, and TOFs of 600-700 hr^{-1} for samples at a lower 0.67 wt% loading. Additionally, Gu *et al.*[47] supported 1.69 wt% Pd NPs on carbon nanotubes, reporting a TOF of 1080 hr^{-1}. The standard deviations of the turnover frequency calculations in **Table 11** further demonstrate the variability in catalytic performance exhibited by these Pd/CuBTC samples, but the 0.25 wt% sample particularly remains a high-performing catalyst even when accounting for these variations.

It is evident that the overall turnover frequency of the catalyst increases with decreasing Pd loading. However, this turnover frequency is calculated relative to the moles of Pd, as Pd NPs are assumed to be the dominant species catalysing the reaction. If Cu_2O nanodiscs, or even a similar Cu^0 species formed in the support material, are also involved in catalysing the 4-NP reduction, this could explain the observed boost in catalytic activity.

To investigate this, two of the PdCu/Cu_2O nanocomposites produced from reducing the Pd/CuBTC composite fully, using $NaBH_4$ in the presence of 4-NP, as discussed in Chapter 4, were tested as catalysts for the nitrophenol reduction. This is effectively the species generated *in situ* during the Pd/CuBTC-catalysed reduction of 4-NP, but the PdCu/Cu_2O catalysts tested here have experienced extra centrifugation and drying steps during their large-scale synthesis.

PdCu/Cu_2O samples reduced at temperatures of 25 °C and 50 °C were tested, and the resultant UV/vis spectra are displayed in **Figure 73**. Conversion and $ln(C_t/C_0)$ data for both samples are shown in **Figure 74**, and peak 4-NP conversions, estimated pseudo-first-order rate constants and turnover frequencies are listed in **Table 12**.

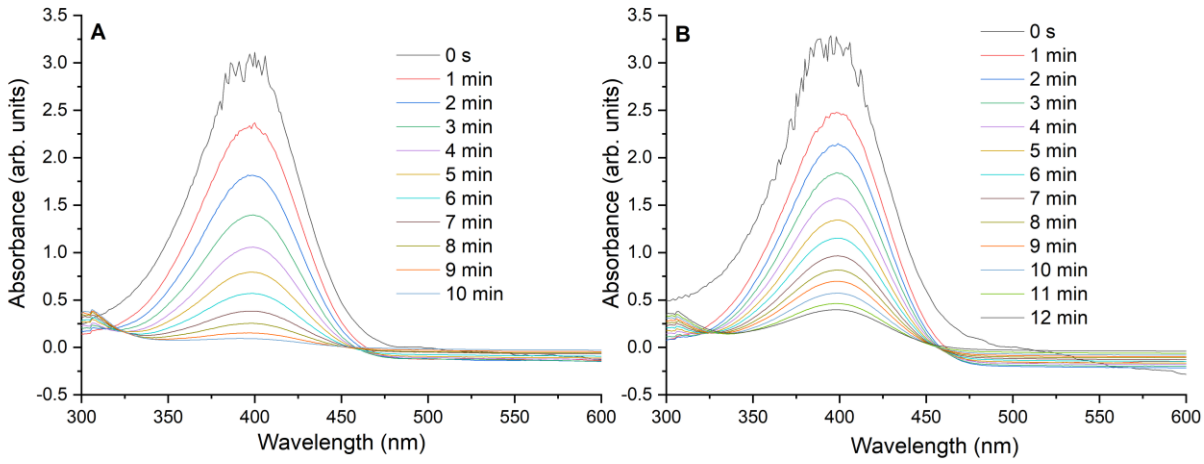

Figure 73: UV/vis spectra of 4-nitrophenol reduction using PdCu/Cu_2O catalyst samples reduced at a) 25 °C and b) 50 °C. Testing performed using a 4-NP/Pd ratio of ~2 and an $NaBH_4$/4-nitrophenol molar ratio of 24.5.

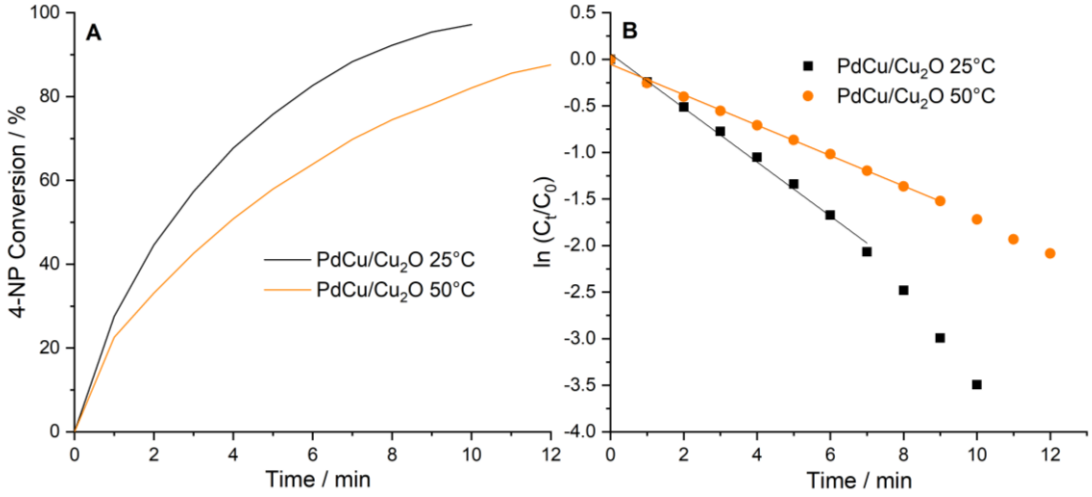

Figure 74: a) Plot of 4-NP conversion against time for PdCu/Cu_2O catalysts prepared at reduction temperatures of 25 °C and 50 °C; b) plot of ln(C_t/C_0) for 4-nitrophenol for the same PdCu/Cu_2O catalysts and testing regime.

Table 12: Calculated pseudo-first-order rate constants and turnover frequencies for the PdCu/Cu_2O catalysts prepared at reduction temperatures of 25 °C and 50 °C. Pd loading was measured via MP-AES spectroscopy. Turnover frequencies were calculated after 30 seconds of reaction for both samples, to approximate the initial rate.

Sample ID	Pd loading	4-NP Conversion	k_{app} / min^{-1}	TOF / hr^{-1}
PdCu/Cu_2O 25 °C	2.03 wt%	97%	0.290	38
PdCu/Cu_2O 50 °C	2.65 wt%	88%	0.163	28

The PdCu samples display a significantly reduced activity for 4-NP reduction. These samples are essentially spent catalysts, having already been exposed to 4-NP during their own reduction step, and there are multiple possible explanations for their lack of activity compared to the Pd/CuBTC samples. Firstly, since these samples have already been reduced from the original Pd/CuBTC composite, the local exotherm present from reduction of the MOF will not be present, which will lead to a marked drop in their catalytic performance, since the reactions are essentially being conducted at different temperatures. Additionally, the surface area of the reduced catalyst is drastically lower than the Pd/CuBTC composite, due to the collapse of the porous MOF structure, which could limit the ability of 4-NP to access the nanoparticles. Furthermore, as discussed in Chapter 4, Pd-Cu alloying is observed to occur during reduction of

the Pd/CuBTC composite, which would change the overall electronic character of the nanoparticles and affect their catalytic performance. Whilst there is evidence in literature of PdCu nanoparticle catalysts being active for 4-NP reduction[48,49], the reported turnover frequencies of 61 hr^{-1} and 14 hr^{-1} are closer in magnitude to those reported here for PdCu/Cu_2O rather than those for Pd/CuBTC.

The relative lack of activity for the PdCu/Cu_2O samples suggests that the Cu_2O nanodiscs are not involved with catalysing the 4-NP reduction, and that the high performance exhibited by the Pd/CuBTC composites arises from a combination of a local exotherm from Pd/CuBTC reduction, increased accessibility of the Pd nanoparticles, and excellent Pd NP dispersion, particularly for the 0.25 wt% Pd/CuBTC sample.

Finally, a 0.25 wt% sample of Pd/CuTPA, as discussed in Chapter 3, was tested for 4-NP reduction, with the resulting UV/vis spectra shown in **Figure 75**.

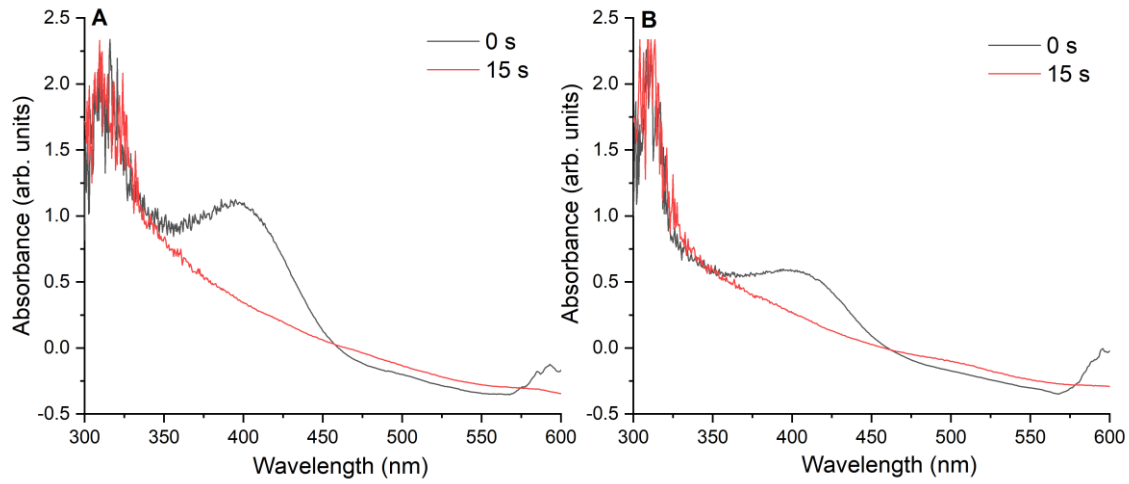

Figure 75: UV/vis spectra of 4-nitrophenol reduction using a 0.25 wt% Pd/CuTPA catalyst, showing two separate testing runs in a) and b). Testing performed using a 4-NP/Pd ratio of ~20.7 and an $NaBH_4$/4-nitrophenol molar ratio of 24.5.

The Pd/CuTPA sample displays remarkable activity for the reduction of 4-NP, rapidly depleting the 4-NP peak even within the short timescale required to initiate the reaction and scan the spectrum. This does not generate enough data points for a reliable calculation of the rate constant; a faster scanning method would be required to further examine the reduction kinetics for this sample. However, the fact that 0.25 wt% Pd samples for both CuBTC and CuTPA MOF reduce the test's batch of 4-NP faster than the higher Pd loadings tested for Pd/CuBTC supports the idea that 0.25 wt% Pd produces a more suitable dispersion of nanoparticles for catalytic performance.

5.3.2 PdCu-based catalysts for CO oxidation

The PdCu/Cu_2O nanocomposites generated in Chapter 4 were investigated as potential catalysts for CO oxidation, with the 1 wt% Pd/CuBTC nanocomposite tested as a control sample. The samples were tested using a CATLAB microreactor, which allows the temperature of the sample to be ramped at a constant rate. The CATLAB was connected to a mass spectrometer to measure the composition of gases leaving the reactor bed. Mass spectrometer responses for mass-to-charge ratios corresponding to CO, O_2 and CO_2 are shown in **Figure 76** for PdCu/Cu_2O samples prepared from Pd/CuBTC at reduction temperatures of 1 °C and 25 °C, and in **Figure 77** for reduction temperatures of 50 °C and 75 °C.

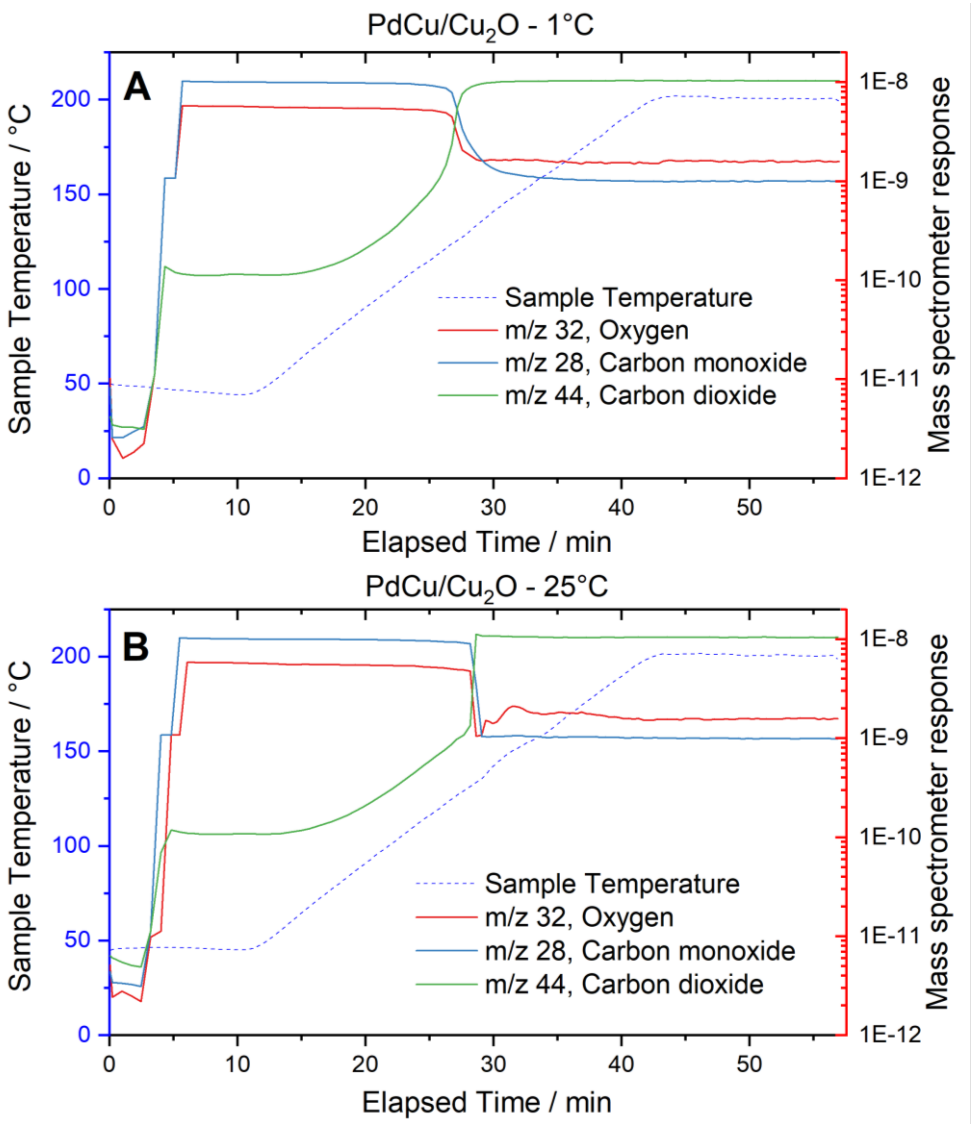

Figure 76: Sample temperature readings and mass spectrometer responses for reactants and products of CO oxidation over PdCu/Cu_2O catalysts prepared at reduction temperatures of a) 1 °C; b) 25 °C.

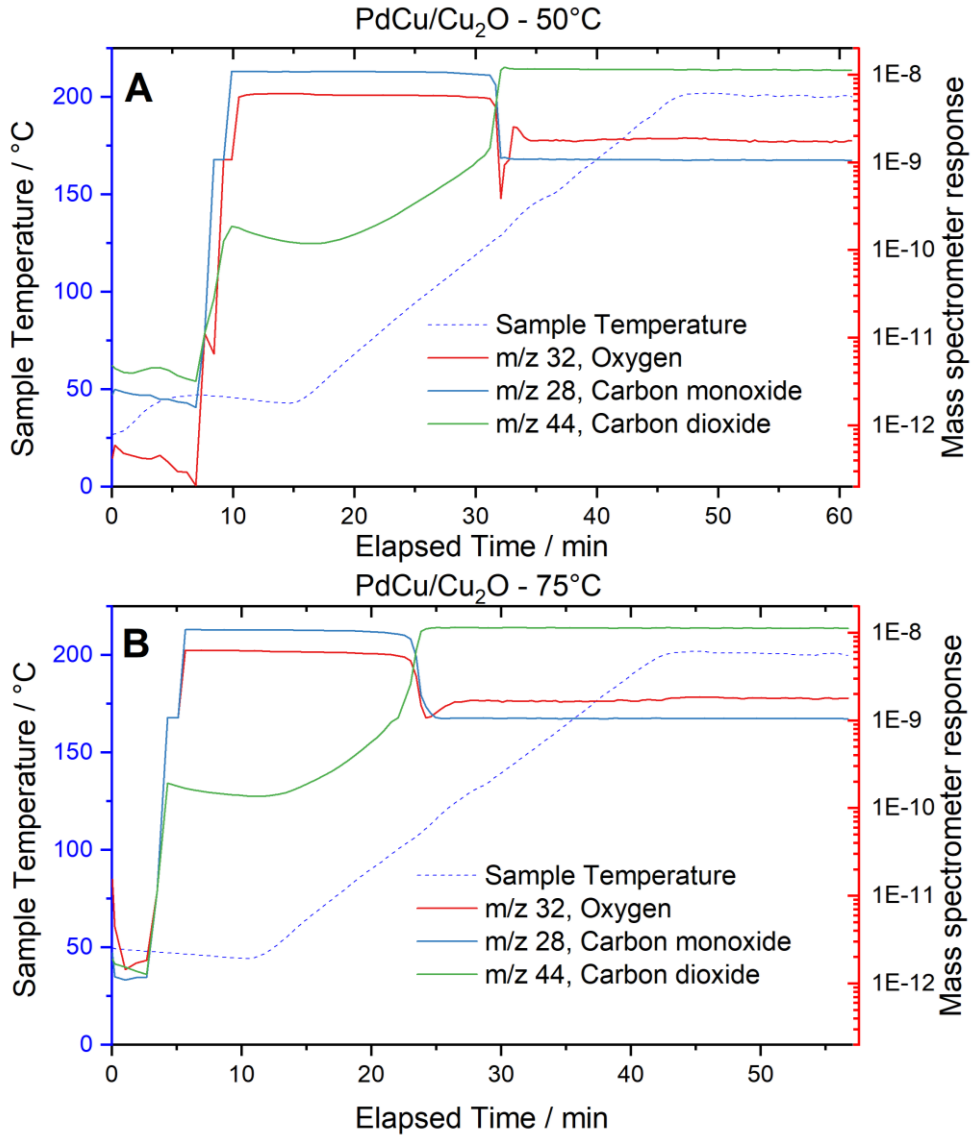

Figure 77: Sample temperature readings and mass spectrometer responses for reactants and products of CO oxidation over $PdCu/Cu_2O$ catalysts prepared at reduction temperatures of a) 50 °C; b) 75 °C.

All the $PdCu/Cu_2O$ samples display activity for CO oxidation, with an initial increase in the CO_2 mass spectrometer response indicating a small amount of catalytic conversion in the 55-60 °C temperature range. Light-off curves were generated for the four $PdCu/Cu_2O$ samples by measuring CO conversion with temperature, with the corresponding light-off temperature, T_{50}, defined as the temperature at which CO conversion reaches 50%. The light-off curves are displayed in **Figure 78**. All the samples display a rapid increase in conversion to 100% shortly after catalytic activity begins, but the light-off temperatures vary by 26 °C across the range of synthetic reduction temperatures. Estimated light-off temperatures, peak CO conversion temperatures (T_{100}), and percentages of CO conversion for all PdCu catalysts tested are listed in **Table 13**.

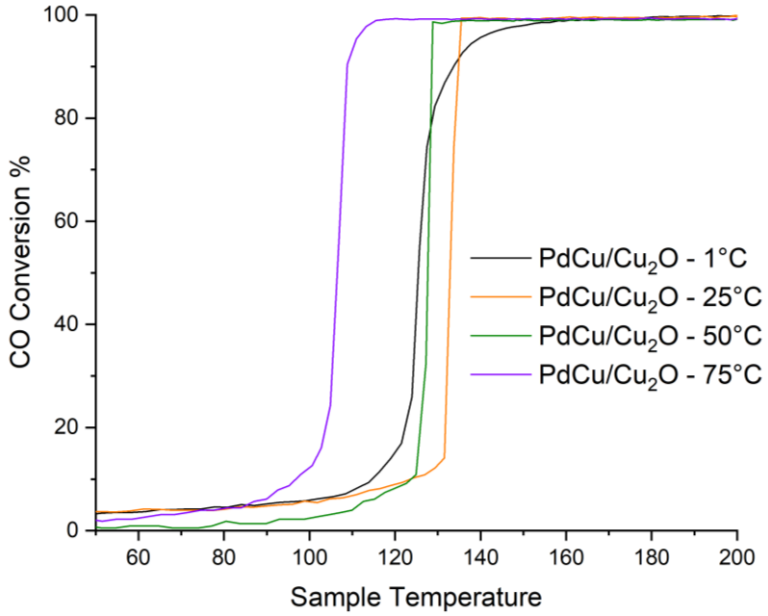

Figure 78: Plots of CO conversion against temperature for $PdCu/Cu_2O$ catalysts prepared at reduction temperatures of 1-75 °C.

Table 13: Estimated light-off temperatures, peak CO conversion temperatures and percentages of CO conversion for $PdCu/Cu_2O$ catalysts prepared at reduction temperatures of 1-75 °C. All samples underwent no pre-treatment procedure and were tested to a peak temperature of 200 °C. Gas flows across the catalyst bed during the reaction were 50 mL / min of 10% CO in helium, 5 mL / min of O_2, and 15 mL / min of Ar.

Catalyst	Light-off temperature (T_{50})	Peak CO conversion temperature (T_{100})	Estimated CO % conversion
$PdCu/Cu_2O$ – 1 °C	125 °C	164 °C	99%
$PdCu/Cu_2O$ – 25 °C	133 °C	135 °C	99%
$PdCu/Cu_2O$ – 50 °C	128 °C	129 °C	99%
$PdCu/Cu_2O$ – 75 °C	107 °C	115 °C	99%

The PdCu/Cu_2O sample prepared at a reduction temperature of 75 °C shows a clear decrease in T_{50} light-off temperature compared to the other samples, becoming active at 107 °C. However, there is no indication of a trend in decreasing light-off temperature with increasing reduction temperature, since the sample prepared at 25 °C shows the highest light-off temperature of 133 °C, with the 1 °C and 50 °C samples having similar but slightly lower values. Comparing this to the EXAFS fitting parameters for these samples in **Section 4.3.4.2**, the 25 °C sample displayed the highest value for Pd-Pd coordination number, at 7.9, compared to 6.3 for the 75 °C sample. Whilst there is a substantial amount of error in coordination number estimates, a lower Pd-Pd coordination number could suggest that more of the nearest neighbours around the absorbing Pd atom have been replaced by Cu atoms, increasing Pd-Cu alloying. Since synergistic effects between Pd and Cu are known to decrease the binding strength of O_2 when the metals are alloyed, providing a boost to CO oxidation activity[39], a lower light-off temperature for the PdCu/Cu_2O sample reduced at 75 °C supports the finding in Chapter 4 that that sample had the highest Pd-Cu coordination number. The hypothesis that PdCu alloying increases with reduction temperature is also supported by a correlation between sample reduction temperature and the temperature at which peak conversion is reached, designated T_{100}, since the 1 °C sample reaches peak conversion more slowly than the others.

The estimated light-off temperatures compare favourably to similar catalysts in literature. For example, Dann *et al.*[50] report a 3 wt% Pd NP catalyst supported on alumina that displayed a light-off temperature of 114 °C. Additionally, Shan *et al.*[51] demonstrated that the alloying within a $Pd_{56}Ni_{44}$/C nanoparticle catalyst caused its light-off temperature for CO oxidation to decrease to around 130 °C, compared to ~160 °C for a Pd/C control sample. Furthermore, Jiang *et al.* prepared unsupported PdCu NPs for CO oxidation, which displayed a decreased light-off temperature of ~215 °C compared to ~255 °C for unalloyed Pd NPs.

Interestingly, some of the PdCu/Cu_2O nanocomposites show oscillations in the mass spectrometer response for O_2 following catalyst light-off. This is most noticeable in **Figure 76b** and **Figure 77a**, for the samples reduced at 25 °C and 50 °C respectively, but there is also a sharp initial drop in O_2 level for the 75 °C sample at light-off – only the 1 °C sample displays a smooth O_2 response. These oscillations are similar in character, albeit present to a lesser extent, to those reported for Pd NPs by Dann *et al.*[50], who used *operando* XAFS to demonstrate that the large spikes in O_2 consumption occurred in tandem with surface oxidation of the Pd nanoparticles. In that example, the Pd/Al_2O_3 catalyst was confirmed to exist as metallic Pd nanoparticles poisoned by CO until the light-off temperature, at which point sufficient CO desorbs from the surface to allow dissociative adsorption of O_2 across the Pd NPs. The oscillations in CO oxidation activity then arose from competition between storage of CO on the catalyst surface, and surface oxide formation on the nanoparticle.

Since these nanocomposites only have a limited amount of Pd-Cu alloying, as seen by the lower Pd-Cu coordination numbers arising in EXAFS analysis compared to Pd-Pd coordination, they are likely to behave somewhat similarly to Pd NPs in this situation, but with the potential for a lower overall binding strength of CO due to synergetic effects arising from Pd-Cu alloying. As oxygen is present in excess during the reaction, there is a sufficient quantity of O_2 to react with both CO from the gas stream and sequestered CO on the nanoparticle surface simultaneously, which leads to rapid consumption and a large drop in O_2 response. However, it is not clear why the sample reduced at 1 °C does not exhibit this behaviour. One possibility could be a relative lack of sequestered CO on the nanoparticles at the point of light-off, leading to a smoother consumption of O_2. However, this would likely necessitate a larger amount of Pd-Cu alloying within the nanoparticles of this sample than is predicted by both EXAFS analysis and light-off temperature, since the alloying is predicted to confer some resistance to CO poisoning by reduction of CO binding strength.[40]

There is also a subtle increase in sample temperature for the samples reduced at 25 °C, 50 °C and 75 °C, occurring shortly after the reaction light-off and the beginning of the oscillations in the O_2 mass spectrometer response. As the CO oxidation reaction and the adsorption of oxygen on PdCu nanoparticles are both exothermic[31,52], the heat evolved by the rapid consumption of the sequestered CO and readsorption of reactant gases will propagate through the catalyst bed and reach the thermocouple, which could explain the slight delay in the temperature increase. Additionally, Ghosh *et al*.[53] suggest that Pd nanoparticles undergo some surface restructuring during CO oxidation, also producing a small amount of heat. Since the proportion of Cu in the PdCu nanoparticles presented here is likely to be quite small due to its method of incorporation from the MOF lattice during catalyst synthesis, it is feasible that the PdCu nanoparticles in these measured samples could behave in a similar manner, further contributing to this observed bump in sample temperature.

A 1 wt% Pd/CuBTC composite was also evaluated for CO oxidation, with its testing data displayed in **Figure 79**. The pattern of mass spectrometer responses appears broadly similar to that of the PdCu-based nanocomposites, but at significantly higher temperatures – light-off is not observed until ~210 °C, and peak CO conversion is only achieved just below 350 °C, which is also the temperature to which the sample was ramped to. TGA analysis of the MOF in Chapter 3 did not indicate thermal decomposition of the ligands until ~360 °C, but those measurements were recorded in inert atmosphere rather than in this oxidative atmosphere. The mass spectrometer responses below indicate a spike in CO_2 at 205 °C, just before the reaction light-off, which is significantly higher than the peak CO_2 conversion for the reaction and suggests that the MOF lattice has been pyrolysed into a new nanocomposite that is active for the reaction, likely to be some form of Pd/CuO nanocomposite analogous to the thermal decomposition

behaviour for CuBTC shown by Zamaro *et al.*.[35] This new catalyst still reaches 98% conversion of CO, comparable to the PdCu-based samples, but it is likely that the Pd-Cu alloying within the reduced nanocomposites serves to lower the light-off temperature for CO oxidation.

There is a complicating factor in the analysis, since the mass and sieve fraction of each catalyst within the bed was kept the same for each testing run, to ensure that the entire catalyst bed experiences an even gas flow rate and contact time. However, the removal of the organic linkers during the formation of the PdCu/Cu_2O nanocomposites serves to increase the relative weight percentage of palladium within the material. This means that 100 mg of Pd/CuBTC catalyst has a substantially-lower loading of Pd than an equivalent 100 mg of PdCu/Cu_2O. Taking an average of all the PdCu/Cu_2O nanocomposites prepared from 1 wt% Pd/CuBTC measured using MP-AES yields a Pd loading of 2.7 wt% in the reduced nanocomposites, with the 1 wt% Pd/CuBTC nanocomposites demonstrating Pd loadings of 0.9 – 0.99 wt%. This means that on average, there is three times as much Pd present during CO oxidation for the PdCu-based nanocomposites than there is for Pd/CuBTC. It was discussed in **Section 5.1.2** how Jiang *et al.*[33] were able to reduce light-off temperature for Au-based catalysts by 55 °C simply by increasing Au loading from 0.5 to 5.0 wt%.

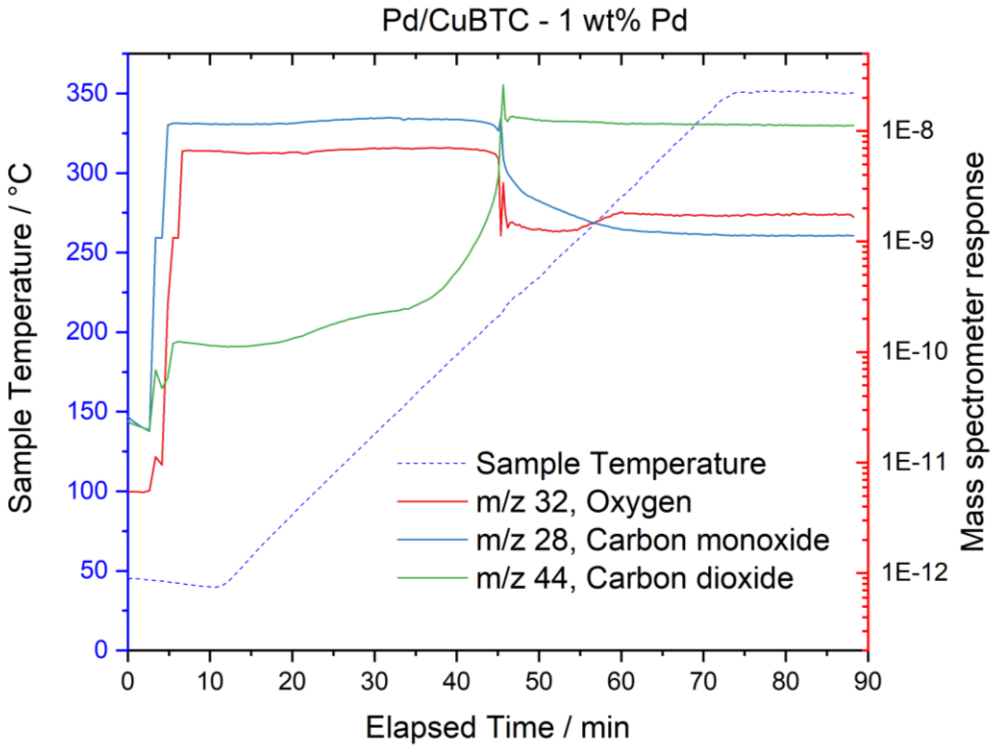

Figure 79: Sample temperature readings and mass spectrometer responses for reactants and products of CO oxidation over a 1 wt% Pd/CuBTC catalyst.

This means that it is likely that some of the reduction in light-off temperature is caused by a significant increase in Pd nanoparticle loading compared to 1 wt% Pd/CuBTC. However, the

75 °C-reduced sample still displayed a large further reduction in T_{50} compared to the other PdCu-based nanocomposites, suggesting that using CO oxidation as a proxy to investigate Pd-Cu alloying still has some validity.

Whilst it is challenging to generate an accurate light-off curve for the 1 wt% Pd/CuBTC catalyst, due to the large spike in gas partial pressures occurring at both the moment of light-off and the decomposition of the MOF structure, removal of this somewhat-anomalous data point generates a smooth light-off curve similar to the PdCu-based samples, as seen in **Figure 80**. From this, the light-off temperature of CO oxidation on the Pd NP can be more accurately-estimated as 212 °C, over 100 °C higher than the PdCu/Cu_2O sample prepared at 75 °C.

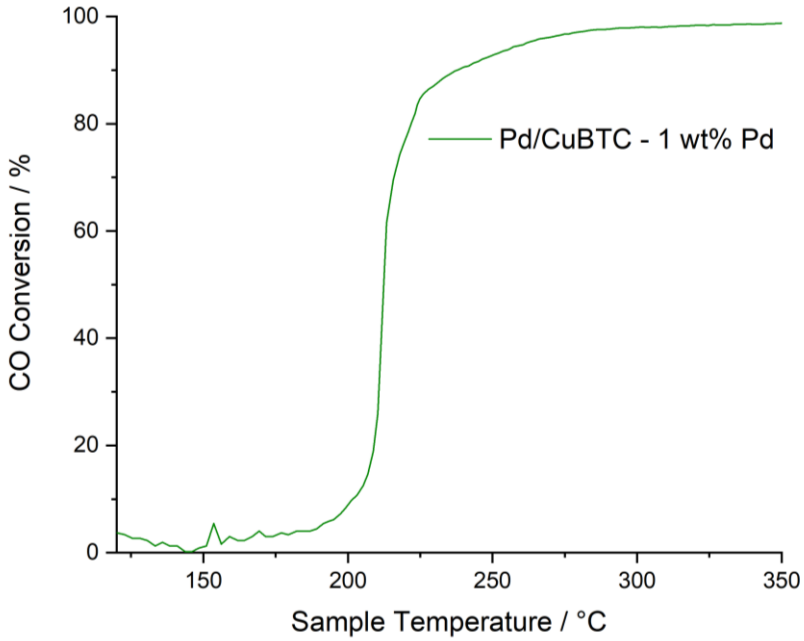

Figure 80: Plot of CO conversion against temperature for a PdCu/BTC composite catalyst.

5.4 Conclusions

The Pd/CuMOF composites and PdCu-based reduced nanocomposites generated in this report have been demonstrated as active catalysts. When applied to the reduction of 4-nitrophenol, the Pd/CuBTC composites perform comparably to other NP-based catalysts for the same reaction in literature, particularly when the loading is reduced to 0.25 wt% Pd. This increase in performance with lowered loading is attributed to improved dispersion of Pd on the rods of the MOF support.

However, the 4-nitrophenol reduction is carried out under the same conditions used to generate the PdCu/Cu_2O nanocomposites studied in Chapter 4. This is an inherent and irreversible transformation of the catalyst structure, destroying the porous MOF structure, modifying the support into a mixed copper oxide phase, and inducing Pd-Cu alloying within the Pd NPs. This means that Pd/CuBTC is not effectively reusable as a catalyst for 4-NP reduction, especially since the PdCu/Cu_2O nanocomposites exhibit a significantly reduced activity for the reaction, with at least an order-of-magnitude decrease in turnover frequency compared to the Pd/CuBTC composites. This decrease is also affected by the exothermic nature of the reduction of the Pd/CuBTC composite, as its occurrence in the unstirred cuvette leads to both variability between individual testing runs from the presence of a local exotherm, and to significant variability between the results measured for Pd/CuBTC and PdCu/Cu_2O, since the latter sample cannot generate significant heat from a reduction of the catalyst itself.

A composite prepared with CuTPA MOF in place of CuBTC displayed even higher activity for the conversion of 4-nitrophenol to 4-aminophenol, also at the 0.25 wt% loading that proved effective for Pd/CuBTC. However, precise quantification of the rate constant and turnover frequency is not possible with the experimental setup used here due to the 4-NP being reduced too quickly to collect enough data points.

Although the Pd-based NP-MOF composites are significantly better catalysts for 4-NP reduction than their PdCu-based counterparts, the reverse is true when the catalysts are used for CO oxidation. Both the Pd/CuBTC and PdCu/Cu_2O samples displayed very high conversions for CO, but the light-off temperature for the PdCu-samples is up to 100 °C lower than for Pd/CuBTC, with the lowest light-off temperature observed being 107 °C. This is relevant to their potential industrial applications, since present catalysts used in car exhausts perform well at temperatures above 200 °C, but have limited activity in the initial warming-up period after starting an engine, meaning that the majority of pollutant gases are emitted in that initial period.[54] Development of catalysts with lower light-off temperatures would therefore target the main source of pollution from automobiles not presently addressed.

The PdCu/Cu_2O nanocomposite prepared at a higher reduction temperature of 75 °C demonstrated the best performance of the reduced nanocomposites, supporting the increased amount of Pd-Cu alloying present within that sample identified by EXAFS analysis in Chapter 4. This indicates that the method of nanocomposite synthesis presented in this report does have some ability to influence the level of alloying induced within Pd nanoparticles. However, there was not a consistent trend between reduction temperature and catalyst light-off temperature, which could suggest that the alloying influence only becomes tangible at high reduction temperatures. Given that the solvent used for the reduction of Pd/CuBTC to PdCu/Cu_2O was water, the method is already operating close to the possible ceiling of reduction temperature due to water's boiling point being 100 °C. However, future work could examine a reduction temperature of 90 °C to investigate whether Pd-Cu alloying increases further, or the solvent used for the reduction step could be altered to one with a higher boiling point.

Even without this additional optimisation, the PdCu/Cu_2O samples prepared at or below room temperature still display a significant improvement over the Pd/CuBTC composite, with decreases of 85 °C and 77 °C in light-off temperature for the samples reduced at 1 °C and 25 °C respectively. These gaps in light-off temperature must be offset somewhat due to the increased weight percentage of Pd in the reduced nanocomposites compared to Pd/CuBTC, the relative differences in light-off temperature within the PdCu/Cu_2O series itself also supports small changes in Pd-Cu alloying with reduction temperature.

Given that one of the goals of this project was to explore a synthetic method that avoided high-temperature calcination steps and thermal treatments, the successful inducement of Pd-Cu alloying in standard laboratory conditions to produce active catalysts represents a significant achievement.

5.5 References

1 N. K. Reddy Bogireddy, Y. R. Mejia, T. M. Aminabhavi, V. Barba, R. H. Becerra, A. D. Ariza Flores and V. Agarwal, *J. Environ. Manage.*, 2022, **316**, 115292.

2 G. Xue, M. Gao, Z. Gu, Z. Luo and Z. Hu, *Chem. Eng. J.*, 2013, **218**, 223–231.

3 N. You, J. Y. Li, H. T. Fan and H. Shen, *J. Adv. Res.*, 2019, **15**, 77–86.

4 Y. X. Yao, H. B. Li, J. Y. Liu, X. L. Tan, J. G. Yu and Z. G. Peng, *J. Nanomater.*, 2014, 1–9.

5 Q. Jing, Z. Yi, D. Lin, L. Zhu and K. Yang, *Water Res.*, 2013, **47**, 4006–4012.

6 M. Khatamian and Z. Alaji, *Desalination*, 2012, **286**, 248–253.

7 Y. Tuo, G. Liu, B. Dong, J. Zhou, A. Wang, J. Wang, R. Jin, H. Lv, Z. Dou and W. Huang, *Sci. Rep.*, 2015, **5**, 13515.

8 S. Rogers, R. Catlow, D. Gianolio, P. Wells and N. Dimitratos, *Faraday Discuss.*, 2018, 1–12.

9 T. Aditya, A. Pal and T. Pal, *Chem. Commun.*, 2015, **51**, 9410–9431.

10 M. J. Vaidya, S. M. Kulkarni and R. V. Chaudhari, *Org. Process Res. Dev.*, 2003, **7**, 202–208.

11 J. He, C. Lai, L. Qin, B. Li, S. Liu, L. Jiao, Y. Fu, D. Huang, L. Li, M. Zhang, X. Liu, H. Yi, L. Chen and Z. Li, *Chemosphere*, 2020, **256**, 127083.

12 P. Cyganowski, *Colloids Surfaces A Physicochem. Eng. Asp.*, 2021, **612**, 125995.

13 S. Noël, H. Bricout, A. Addad, C. Sonnendecker, W. Zimmermann, E. Monflier and B. Léger, *New J. Chem.*, 2020, **44**, 21007–21011.

14 S. Xie, Z. Xu, C. Yu, X. Yu, Z. Zhang and J. Li, *ChemistrySelect*, 2021, **6**, 13572–13576.

15 A. A. Kassem, H. N. Abdelhamid, D. M. Fouad and S. A. Ibrahim, *J. Environ. Chem. Eng.*, 2021, **9**, 104401.

16 B. Coşkuner Filiz, *Adv. Powder Technol.*, 2020, **31**, 3845–3859.

17 A. K. Sasmal, S. Dutta and T. Pal, *Dalt. Trans.*, 2016, **45**, 3139–3150.

18 N. Joudeh, A. Saragliadis, G. Koster, P. Mikheenko and D. Linke, *Front. Nanotechnol.*,

2022, **4**, 1–24.

19 Y. R. Mejía and N. K. Reddy Bogireddy, *RSC Adv.*, 2022, 12, 18661–18675.

20 X. Shan, N. Sui, W. Liu, M. Liu and J. Liu, *J. Mater. Chem. A*, 2019, **7**, 4446–4450.

21 Y. Wang, J. Tao, Y. Wang, L. Huang and X. Ding, *Appl. Surf. Sci.*, 2022, **574**, 151702.

22 K. Alshammari, Y. Niu, R. E. Palmer and N. Dimitratos, *Philos. Trans. R. Soc. A Math. Phys. Eng. Sci.*, 2020, **378**, 20200057.

23 S. Chatterjee and S. K. Bhattacharya, *ACS Omega*, 2021, **6**, 20746–20757.

24 X. Duan, A. Liu, L. Zhou and S. Wei, *Environ. Sci. Pollut. Res.*, 2023, **30**, 97936–97947.

25 M. Kubo, T. Matsumoto and M. Shimada, *Adv. Powder Technol.*, 2022, **33**, 103701.

26 Y. Zhou, Z. Wang and C. Liu, *Catal. Sci. Technol.*, 2015, **5**, 69–81.

27 I. Blumenthal, *J. R. Soc. Med.*, 2001, **94**, 270–272.

28 J. M. Graber, S. C. Macdonald, D. E. Kass, A. E. Smith and H. A. Anderson, *Public Health Rep.*, 2007, **122**, 138–144.

29 C. Feng, X. Liu, T. Zhu and M. Tian, *Environ. Sci. Pollut. Res.*, 2021, **28**, 24847–24871.

30 J. Gustafson, O. Balmes, C. Zhang, M. Shipilin, A. Schaefer, B. Hagman, L. R. Merte, N. M. Martin, P. A. Carlsson, M. Jankowski, E. J. Crumlin and E. Lundgren, *ACS Catal.*, 2018, **8**, 4438–4445.

31 M. A. Van Spronsen, J. W. M. Frenken and I. M. N. Groot, *Chem. Soc. Rev.*, 2017, **46**, 4347–4374.

32 B. Brandt, T. Schalow, M. Laurin, S. Schauermann, J. Libuda and H. J. Freund, *J. Phys. Chem. C*, 2007, **111**, 938–949.

33 H. Jiang, B. Liu, T. Akita, M. Haruta, H. Sakurai, K. U. V and N. Ku, *J. Am. Chem. Soc.*, 2009, **2**, 11302–11303.

34 J. Y. Ye and C. J. Liu, *Chem. Commun.*, 2011, **47**, 2167–2169.

35 J. M. Zamaro, N. C. Pérez, E. E. Miró, C. Casado, B. Seoane, C. Téllez and J. Coronas, *Chem. Eng. J.*, 2012, **195–196**, 180–187.

36 K. Murata, E. Eleeda, J. Ohyama, Y. Yamamoto, S. Arai and A. Satsuma, *Phys. Chem. Chem. Phys.*, 2019, **21**, 18128–18137.

37 B. R. Chen, L. A. Crosby, C. George, R. M. Kennedy, N. M. Schweitzer, J. Wen, R. P. Van Duyne, P. C. Stair, K. R. Poeppelmeier, L. D. Marks and M. J. Bedzyk, *ACS Catal.*, 2018, **8**, 4751–4760.

38 H. M. Altass, M. Morad, A. E. R. S. Khder, M. A. Mannaa, R. S. Jassas, A. A. Alsimaree, S. A. Ahmed and R. S. Salama, *J. Taiwan Inst. Chem. Eng.*, 2021, **128**, 194–208.

39 W. Zhang, S. Shan, J. Luo, A. Fisher, J.-F. Chen, C.-J. Zhong, J. Zhu and D. Cheng, *J. Phys. Chem. C*, 2017, **121**, 11010–11020.

40 N. Lopez and J. K. Nørskov, *Surf. Sci.*, 2001, **477**, 59–75.

41 F. Schiller, M. Ilyn, V. Pérez-Dieste, C. Escudero, C. Huck-Iriart, N. Ruiz Del Arbol, B. Hagman, L. R. Merte, F. Bertram, M. Shipilin, S. Blomberg, J. Gustafson, E. Lundgren and J. E. Ortega, *J. Am. Chem. Soc.*, 2018, **140**, 16245–16252.

42 F. Cai, L. Yang, S. Shan, D. Mott, B. Chen, J. Luo and C.-J. Zhong, *Catalysts*, 2016, **6**, 96.

43 R. D. Neal, Y. Inoue, R. A. Hughes and S. Neretina, *J. Phys. Chem. C*, 2019, **123**, 12894–12901.

44 E. Menumerov, R. A. Hughes and S. Neretina, *Nano Lett.*, 2016, **16**, 7791–7797.

45 Y. Mei, G. Sharma, Y. Lu, M. Ballauff, M. Drechsler, T. Irrgang and R. Kempe, *Langmuir*, 2005, **21**, 12229–12234.

46 X. Deng, L. Zhu, H. Zhang, L. Li, N. Zhao, J. Wang, S. M. Osman, R. Luque and B. H. Chen, *Environ. Res.*, 2022, **214**, 114027.

47 X. Gu, W. Qi, X. Xu, Z. Sun, L. Zhang, W. Liu, X. Pan and D. Su, *Nanoscale*, 2014, **6**, 6609–6616.

48 Y. Duan, Y. Ma, Y. Xie, D. Li, D. Deng, C. Zhang and Y. Yang, *Chem. - An Asian J.*, 2021, **16**, 165–173.

49 H. Saikia, B. J. Borah, Y. Yamada and P. Bharali, *J. Colloid Interface Sci.*, 2017, **486**, 46–57.

50 E. K. Dann, E. K. Gibson, C. R. A. Catlow, V. Celorrio, P. Collier, T. Eralp, M. Amboage, C.

Hardacre, C. Stere, A. Kroner, A. Raj, S. Rogers, A. Goguet and P. P. Wells, *J. Catal.*, 2019, **373**, 201–208.

51 S. Shan, V. Petkov, L. Yang, J. Luo, P. Joseph, D. Mayzel, B. Prasai, L. Wang, M. Engelhard and C. J. Zhong, *J. Am. Chem. Soc.*, 2014, **136**, 7140–7151.

52 J. Liu, X. Fan, C. Q. Sun and W. Zhu, *Materials (Basel).*, 2017, **11**, 18–20.

53 T. Ghosh, J. M. Arce-Ramos, W. Q. Li, H. Yan, S. W. Chee, A. Genest and U. Mirsaidov, *Nat. Commun.*, 2022, **13**, 1–10.

54 E. J. Peterson, A. T. DeLaRiva, S. Lin, R. S. Johnson, H. Guo, J. T. Miller, J. H. Kwak, C. H. F. Peden, B. Kiefer, L. F. Allard, F. H. Ribeiro and A. K. Datye, *Nat. Commun.*, 2014, **5**, 4885.

Chapter 6 Conclusions and Future Work

With the continued onset of industrialisation worldwide, the need for effective catalysts grows in parallel, to minimise the impacts that our industrial processes have on the environmental stability of the planet. Both the physical and chemical properties of catalysts can be influenced through careful design, but within the field of catalyst design itself, there can appear to be a colossal array of possibilities to consider or control. These include the elements used within a catalyst or support, the physical structure of the catalyst, the nature of the active sites, possible interactions between the metal and support, the experimental conditions used in catalyst synthesis, and the many applicable chemical reactions that could be catalysed, both within a laboratory and in wider industry.

There is a clear need for well-established, reproducible methods of catalyst synthesis that can deliver fine control of this wide range of variables and properties. To that end, the work presented within this thesis can be divided into three major themes: 1) the extension of the successful sol-immobilisation method of catalyst design towards metal-organic framework supports, yielding nanoparticle-MOF composites; 2) the development of an alternate route to allow generation of nanocomposite materials, via chemical reduction rather than thermal annealing methods; and 3) the evaluation of the catalytic behaviour of these nanocomposites. To investigate these topics, a range of characterisation techniques were employed, including XRD, electron microscopy, UV/vis, MP-AES, and synchrotron-based X-ray absorption spectroscopy.

Chapter 3 examined the synthesis of a CuBTC MOF support and its use as the underlying structure for a composite material produced by adding palladium nanoparticles to the MOF surface through sol-immobilisation. The size of the Pd nanoparticles was controlled by using polyvinyl alcohol as a capping agent, and the nanoparticles were demonstrated to be well-dispersed atop the rod-like structure of CuBTC. The stability of the CuBTC support was also evaluated, since this MOF was selected as a support because of its inherent lack of long-term stability when exposed to water. The crystal structure of CuBTC was observed to degrade to a slight extent upon contact with water for ~1 hour during the sol-immobilisation, with the resultant Pd/CuBTC composite displaying some signs of Cu_2O in its diffraction pattern. This is a key consideration for the subsequent generation of nanocomposites, since PdCu alloying can be caused upon reduction with $NaBH_4$, but requires readily-accessible copper atoms already abstracted from the MOF lattice prior to reduction. Analysis of the local coordination environments of Pd and Cu in the Pd/CuBTC composite using XANES and EXAFS supported the formation of a small amount of copper oxide during the sol-immobilisation and suggested that a

small amount of interstitial carbide is formed within the Pd nanoparticles during composite synthesis.

Within that chapter, there is already scope for variation and control in the properties of the synthesised materials. The Pd/CuBTC composite was also synthesised using a methanol-based variant of the sol-immobilisation method, which did not exhibit the same level of support degradation as the same composite produced in water. Additionally, the loading of Pd nanoparticles on CuBTC was varied from 0.25-1 wt% Pd, and the identity of the MOF support itself was examined, with the benzene tricarboxylate ligand in CuBTC being replaced with a similar benzene dicarboxylate ligand to generate 0.25 wt% and 1 wt% Pd/CuTPA MOF composites. There are thousands of examples of synthesised MOFs in literature, varying in surface area, porosity, stability and secondary building unit.[1] While composites derived from CuBTC MOF remained the prime focus of this thesis, there is great potential to extend the methods developed here to other classes of MOF, with a view to controlling the formation of various other metal-support interfaces: for example through the choice of metals present in either the immobilised nanoparticles or the MOF support.

In Chapter 4, a novel method was developed to generate nanocomposite structures through the chemical reduction of nanoparticle-MOF composites, rather than the conventional method of thermal treatment. It was demonstrated that whilst reduction with $NaBH_4$ alone yields Pd nanoparticles supported on a mixed $CuO/Cu_2O/Cu^0$ support, the presence of 4-nitrophenol during the reduction step allows some control over the oxidation state of the copper support, preventing the formation of CuO and leaving a mixed Cu_2O/Cu^0 structure. This level of control was found to also be possible when 4-nitrophenol was replaced with its own reduction product, 4-aminophenol, and also with the unrelated ethanolamine, suggesting that coordination of amine ligands to the copper produced by reduction of the MOF is influencing speciation of the nanoparticle support.

Additionally, EXAFS analysis confirmed that a specific set of conditions, namely a water-based sol-immobilisation method, and reduction of the resultant Pd/CuBTC composite with $NaBH_4$ in the presence of 4-nitrophenol, was able to induce Pd-Cu alloying within the resultant nanocomposites. Further optimisation of the synthetic method demonstrated that the temperature of reduction influences the extent of Pd-Cu alloying, with the greatest extent being observed at a 75 °C reduction temperature. It was also shown that variation of other synthetic parameters such as $NaBH_4$ concentration and 4-NP concentration could control the physical properties of the underlying copper support, such as particle size and the phase ratio of Cu_2O:Cu^0.

This represents a different level of synthetic control to that reported in current thermal methods of nanocomposite generation from MOFs, which are also able to exert some control over nanocomposite properties through variation of maximum calcination temperature[2], ramp rate[3], and calcination atmosphere[4], but to the author's knowledge, there has not yet been a reported method within the field of the generation of nanocomposites from NP-MOF composites that yields simultaneous and precise control of both a Pd-Cu interface within the nanoparticle and a Pd-copper oxide interface between the nanoparticles and support. Furthermore, this synthetic method is accessible using standard laboratory equipment, reagents, and experimental conditions, avoiding the need for a calcination step, especially one in an inert, oxidative, or reductive atmosphere.

There is again potential for future work in this area, such as through applying the concepts from NP-MOF generation in Chapter 3 to alternative MOFs, then applying this chemical reduction method to investigate the possibility of generating and controlling other Pd-metal interfaces, or indeed other nanoparticle-Cu interfaces. This research focused primarily on the samples shown to undergo Pd-Cu alloying, with a view to generating PdCu nanoparticle catalysts, but the unalloyed Pd/CuO-based nanocomposites generated from $NaBH_4$ reduction without the presence of nitrophenol could also be examined in further detail. Without the control of copper oxidation state afforded by the variation in nitrophenol concentration, the structure of the support becomes increasingly messy, with three different copper phases present, but as an example, alternative chemical protecting agents playing the same role as nitrophenol/aminophenol could potentially be found to favour the formation of CuO in the support.

Whilst the methanol-based sol-immobilisation method was also observed to generate nanocomposites with a larger Pd-Pd coordination number and particle size upon reduction, which could have an impact upon their potential utility as catalysts, there is also scope for investigating how the extra MOF stability afforded by using methanol as the sol-immobilisation solvent alters the properties of potential nanocomposites. Given that the chemical reduction method deliberately destroys the MOF structure, and that the test reactions evaluated in Chapter 5 also degraded the Pd/MOF composite, the extra stability from the MeOH-based approach is somewhat redundant for this class of generated nanocomposites. However, there are many potential catalytic applications of NP-MOF composites that prioritise the nanoparticle dispersion on the MOF surface, the stability of the underlying support, and the porosity and surface area afforded by the MOF, for which these MeOH-prepared composites could be better suited.[5–7]

In Chapter 5, the Pd/CuBTC composites and the PdCu/Cu_2O nanocomposites were evaluated as catalysts for the reduction of 4-nitrophenol to 4-aminophenol, and for CO oxidation. Whilst it is clear that the Pd/CuBTC composites are highly active for the reduction of 4-nitrophenol, they are unlikely to be useful catalysts on a larger scale, since they are themselves transformed by interaction with the $NaBH_4$ reducing agent to yield the PdCu/Cu_2O nanocomposites, which are considerably less active for the reduction, with the original porous structure of the NP-MOF composite unable to be simply regenerated. It was shown that nanoparticle dispersion on the MOF surface is a prime consideration for catalytic activity, with samples prepared at 0.25 wt% Pd loading demonstrating greatly-improved activity even when compared to the active catalysts at 1 wt% Pd. Fast-scanning UV/vis spectroscopy allows monitoring of the catalytic activity *in situ*, but there are two problems with this approach. Firstly, there is a limit to the size of the batch of 4-nitrophenol that can be converted without saturating the detector in the spectrophotometer; testing catalytic activity for a larger batch of nitrophenol could eliminate some of the perceived variability in performance between different testing runs of the same catalyst type. Additionally, the 0.25 wt% Pd/CuTPA composites were seen to be too active for accurate determination of catalytic activity, depleting the 4-NP batch in under 30 seconds, so either a faster scanning method or a larger batch of nitrophenol, perhaps through use of a full batch reactor setup rather than a cuvette, is required to obtain sufficient data for analysis.

The Pd/CuBTC composite was also shown to not be a useful catalyst for CO oxidation, since the catalyst does not become sufficiently active within the thermal stability range of the sample. Similarly to the nitrophenol reduction, the composite is transformed during the reaction into a new nanocomposite species, analogous to the thermal methods of nanocomposite generation discussed above. However, the PdCu/Cu_2O nanocomposites generated using the chemical reduction method all displayed good activity and conversion for the reaction, displaying a significant decrease in light-off temperature compared to the initial Pd/CuBTC composite. The best performance was observed for the sample prepared at a reduction temperature of 75 °C, providing additional support to the hypothesis that a higher reduction temperature increases the amount of Pd-Cu alloying induced within the nanoparticles.

With the sheer quantity of variables and choices available in the design of these nanocomposites, one future direction for research in this area is to develop rapid screening methods to evaluate which variables are most consequential for controlling the final properties of the catalyst. Test reactions such as 4-nitrophenol reduction and CO oxidation make up part of the way towards this, allowing examination and quantification of nanoparticle availability and Pd-Cu alloying by proxy, since it is not realistic on a cost- or time-based level to be able to screen every prepared nanocomposite for potential alloying using synchrotron-based techniques.

However, synchrotron-based techniques could be employed to investigate the true mechanism of Pd-Cu alloying upon nanocomposite reduction, evaluating how the composition of the nanoparticles varies over the timescale of the reduction, and also how the oxidation state of the copper support evolves. It is likely that this would be a challenging experiment to perform, since the reduction reaction is vigorous and generates hydrogen bubbles that would complicate beamline investigations; however, it is possible that a slower, flow-based method of reduction, perhaps even using a weaker reducing agent than $NaBH_4$, could modulate the reaction rate sufficiently to allow resolution of the alloying mechanism.

Overall, this chemical reduction method to synthesise nanocomposites has a high potential utility, but significant trade-offs come with this. The introduction of the additional experimental parameters associated with a solution-based method, rather than a thermal method, both serve to provide additional control of the synthesised nanocomposite and act as complicating factors that must be carefully accounted for, which can make the overall method quite intricate. The level of control possible through a thermal method of preparing nanocomposites from nanoparticle-MOF composites has also itself advanced over the duration of the project.[8–10] This notwithstanding, the approach presented in this thesis is a novel and innovative method of nanocomposite generation demonstrated to facilitate and tailor local nanoparticle alloying whilst only using common chemicals and equipment. This approach also represents a contrast to much of the present research into metal-organic frameworks, which commonly focuses on maximising the stability and surface area of a MOF rather than treating it as a precursor to another nanomaterial, immediately destroying this ordered structure to yield more effective catalysts.

In conclusion, this thesis provides new insight into the generation of nanocomposite materials from metal-organic frameworks, demonstrating how a chemical reduction method can provide careful control of nanocomposite properties at nanoscale dimensions, with consequent implications for the catalytic properties of the nanocomposites.

6.1 References

1 S. M. Moosavi, A. Nandy, K. M. Jablonka, D. Ongari, J. P. Janet, P. G. Boyd, Y. Lee, B. Smit and H. J. Kulik, *Nat. Commun.*, 2020, **11**, 1–10.

2 Q. Wang and D. Astruc, *Chem. Rev.*, 2020, **120**, 1438–1511.

3 V. P. Santos, T. A. Wezendonk, J. J. D. Jaén, A. I. Dugulan, M. A. Nasalevich, H. U. Islam, A. Chojecki, S. Sartipi, X. Sun, A. A. Hakeem, A. C. J. Koeken, M. Ruitenbeek, T. Davidian, G. R. Meima, G. Sankar, F. Kapteijn, M. Makkee and J. Gascon, *Nat. Commun.*, 2015, **6**, 6451.

4 L. Oar-Arteta, T. Wezendonk, X. Sun, F. Kapteijn and J. Gascon, *Mater. Chem. Front.*, 2017, **1**, 1709.

5 W. Xiang, Y. Zhang, H. Lin and C. Liu, *Molecules*, 2017, **22**, 2103.

6 L. Jiao, Y. Wang, H. L. Jiang and Q. Xu, *Adv. Mater.*, 2018, **30**, 1703663.

7 B. Li, J. G. Ma and P. Cheng, *Small*, 2019, **15**, 1–16.

8 Z. Xie, W. Xu, X. Cui and Y. Wang, *ChemSusChem*, 2017, **10**, 1645–1663.

9 Y. Z. Chen, R. Zhang, L. Jiao and H. L. Jiang, *Coord. Chem. Rev.*, 2018, **362**, 1–23.

10 M. Z. Hussain, Z. Yang, Z. Huang, Q. Jia, Y. Zhu and Y. Xia, *Adv. Sci.*, 2021, **8**, 1–30.